UNIVERSITÉ DE NEUCHÂTEL

Hydraulics and sedimentary processes in the karst aquifer of Milandre (Jura Mountains, Switzerland)

Thesis submitted at the

Faculty of Sciences

Center for Hydrogeology and Geothermics (CHYN)

University of Neuchâtel

for the degree of

PhD

presented by

Cécile Vuilleumier

accepted on the recommendation of

Prof. Pierre-Yves Jeannin
Prof. Pierre Perrochet
Prof. Franci Gabrovšek
Prof. Nico Goldscheider
Dr Michiel Pronk

University of Neuchâtel
Defended on December 8, 2017

UNIVERSITÉ DE NEUCHÂTEL

Faculté des Sciences
Secrétariat-décanat de Faculté
Rue Emile-Argand 11
2000 Neuchâtel – Suisse
Tél : + 41 (0)32 718 21 00
E-mail : secretariat.sciences@unine.ch

IMPRIMATUR POUR THESE DE DOCTORAT

La Faculté des sciences de l'Université de Neuchâtel autorise l'impression de la présente thèse soutenue par

Madame Cécile VUILLEUMIER

Titre:

“Hydraulics and sedimentary processes in the karst aquifer of Milandre (Jura Mountains, Switzerland)”

sur le rapport des membres du jury composé comme suit:

- Prof. Pierre-Yves Jeannin, directeur de thèse, UniNE
- Prof. Pierre Perrochet, co-directeur de thèse, UniNE
- Prof. Nico Goldscheider, Karlsruhe Institute of Technology, Allemagne
- Prof. Franci Gabrovsek, Karst Research Institute, Postojna, Slovénie
- Dr Michiel Pronk, UniNE

Neuchâtel, le 01.02.2018

Le Doyen, Prof. R. Bshary

Abstract

This thesis aims at characterizing the sedimentary processes taking place in the karst aquifer of Milandre (Switzerland) both by direct observation inside the conduit network and through numerical modeling. A physics based pipe flow model of the downstream part of the karst system is developed on the basis of measurements of hydraulic heads, flow rates and flow velocities performed in the speleological network. The flow simulations allow to compute the mean boundary shear stress and the shear velocity in the conduits, which are used to assess when and where erosion and deposition of sediments are likely to occur. The model predictions are compared to various field observations. In the Milandre cave stream, a sedimentation monitoring station has been in operation for 11 years. The turbidity and the suspended sediment composition have been monitored at three locations in the underground system and at the perennial outlet over the same time period. Furthermore, the evolution of the grain size and fecal bacteria content of the suspended solids discharged at the spring has been analyzed over the course of a flood event. The simulations are in good agreement with the available data. Overall, the following conceptual model of sedimentary fluxes in the Milandre system is proposed: during low intensity flood events (maximum discharge at the outlets of $\sim$400 L$\cdot$s^{-1}), the bulk of the turbidity observed at the springs comes from the remobilization of karstic sediments (autochthonous turbidity). Soil derived (allochthonous) turbidity may reach the saturated zone with a delay of up to 3 days, but is often not detected at the spring. As the peak discharge of the event increases, the delay between the flood peak and the allochthonous turbidity peak shortens and the intensity of the allochthonous turdibity peak increases. Moderate to intense flood events thus yield a mixed autochthonous and allochthonous turbidity response at the springs, while the turbidity signal is mostly shaped by the processes of sediment remobilization in the karst system. The model highlights the fact that the mean boundary shear stress reaches a maximum during the flooding and the emptying of the different levels of conduits of the karst network. This leads to the generation of secondary turbidity peaks during flow recession, which are observed both in the cave stream and at the outlets of the system. In the medium term, the model suggests that both the accumulation and the erosion of sediments are frequent along the cave stream. In contrast, the uppermost epiphreatic passages are predicted to act as effective sediment traps. From the observed data, it appears that the sediment fluxes are mainly controlled by the hydrodynamics of the karst system. There is however a seasonal component in the variations of the sediment concentration at the spring. This annual cycle is attributed to an enhanced soil sediment availability during fall. In terms of composition, there is a pluriannual increase in the phyllosilicate content in the suspended sediment. The phyllosilicate concentration was found to be well correlated with groundwater temperature, both on a seasonal and on a pluriannual scale.

Keywords

karst, turbidity, particles, sediment transport, hydraulic modeling, SWMM5, Milandre, Jura Mountains

Résumé

Cette thèse vise à caractériser les processus sédimentaires s'opérant dans l'aquifère karstique de Milandre (Suisse), à la fois grâce à des observations de terrain à l'intérieur du réseau de conduits et à l'aide de la modélisation numérique. Un modèle de tuyaux, qui reproduit la physique du système, est développé sur la base de mesures de charges hydrauliques, de débits et de vitesses d'écoulement mesurés dans le réseau spéléologique. Les simulations d'écoulement permettent de calculer la contrainte de cisaillement limite moyenne et la vitesse de cisaillement dans les conduits, qui sont utilisées pour évaluer où et quand l'érosion et le dépôt de sédiment sont probables. Les prédictions du modèle sont comparées à des observations de terrain variées. Dans la rivière souterraine de Milandre, une station de surveillance de la sédimentation a été en fonction pendant 11 ans. La turbidité et la composition des sédiments en suspension ont été surveillées à trois sites dans le système souterrain et à l'exutoire pérenne au cours de la même période. De plus, l'évolution de la granulométrie et de la teneur en bactéries fécales de la charge sédimentaire à la source a été analysée au cours d'un événement de crue. Les simulations sont en ligne avec les observations disponibles. Le modèle conceptuel suivant est proposé : lors d'événements de faible intensité (débit maximal aux exutoires d'environ 400 $L \cdot s^{-1}$), l'essentiel de la turbidité observée aux sources provient de la remobilisation de sédiments karstiques (turbidité autochtone). La turbidité provenant de la surface (allochtone) peut atteindre la zone saturée avec un délai allant jusqu'à 3 jours, mais dans la plupart des cas elle n'est pas détectée à la source. Quand le pic de débit augmente, le délai entre le pic de crue et le pic de turbidité allochtone diminue, alors que l'intensité du pic de turbidité allochtone augmente. Les événements de crue d'intensité modérée à forte induisent donc une réponse mixte, à la fois autochtone et allochtone aux sources, alors que le signal de turbidité est fortement influencé par les processus de remobilisation de sédiment dans le système karstique. Le modèle a mis en évidence le fait que la contrainte de cisaillement limite est maximale durant le remplissage et la vidange des différents niveaux de conduits du réseau karstique. Cet effet conduit à la génération de pics secondaires de turbidité durant la phase de récession de la crue. Ces pics secondaires de turbidité ont été observés tant dans la rivière souterraine qu'aux exutoires du système. À moyen terme, le modèle prédit que les processus d'érosion et d'accumulation de sédiment sont tous les deux fréquents aux abords de la rivière souterraine. Par contre, dans les galeries épiphréatiques les plus hautes, une accumulation nette de sédiment est prévue par le modèle. D'après les observations, les flux sédimentaires sont principalement contrôlés par l'hydrodynamique du système karstique. Cependant, une composante saisonnière apparaît dans les variations de la concentration de sédiment à la source. Ce cycle annuel est attribué à une disponibilité accrue de sédiments de surface durant l'automne. En terme de composition, une augmentation pluriannuelle de la teneur en phyllosilicate dans les sédiments en suspension est observée. La concentration en phyllosilicate apparaît bien corrélée avec la température des eaux souterraines, autant à l'échelle saisonnière qu'à l'échelle pluriannuelle.

Mots clés

karst, turbidité, particules, transport de sédiment, modélisation hydraulique, SWMM5, Milandre, Jura

Remerciements

En premier lieu je tiens à remercier Prof. Pierre-Yves Jeannin, qui m'a ouvert le chemin vers la boue de Milandre, et dont j'ai beaucoup appris tant sur le terrain que lors du développement du modèle hydraulique et de l'interprétation des données. Merci à lui pour sa disponibilité, ses conseils et nos discussions animées tout au long de ce travail de thèse.

Merci à Prof. Pierre Perrochet pour la confiance qu'il m'a accordée et pour sa disponibilité tant pour les questions théoriques que pour donner un coup de main sur le terrain.

Merci aux rapporteurs de thèse, Dr Michiel Pronk, Prof. Franci Gabrovšek et Prof. Nico Goldscheider pour leur relecture et leurs précieux commentaires.

Ce travail de thèse a énormément bénéficié des travaux réalisés dans le cadre de l'étude d'impact et du suivi environnemental du chantier de l'A16. Dans ce contexte, j'adresse mes sincères remerciements à Pierre Xavier Meury (Géo Environnement) et à Philip Häuselmann (ISSKA) qui, à mes débuts, m'ont emmenée avec eux à Milandre lors de leurs tournées et m'ont initiée au travail souterrain. Merci également à Marc Hessenhauer (MFR) et à Florence Boesch (RWB) pour m'avoir aimablement renseignée et transmis des données.

Au CHYN, j'ai eu la chance de bénéficier des conseils de Dr Michiel Pronk concernant les essais de traçages, le suivi des sources, les analyses microbiologiques et de PSD. Merci également à Dr Pierre Schnegg, qui a mis à disposition deux fluorimètres pour cette étude et a répondu à mes nombreuses questions, et à Roberto Costa pour ses conseils au sujet des diverses sondes que j'ai pu utiliser aux sources et pour son coup de main sur le terrain. Un merci particulier également à Dr Andrea Borghi qui a été d'un précieux conseil sur des sujets aussi variés que la compilation en C et la stratégie de rédaction de la thèse.

Merci aux collaborateurs de l'ISSKA pour leur accueil lors de mes passages à la Chaux-de-Fonds, en particulier à Dr Urs Eichenberger, Demian Rickerl et Eric Weber pour leurs conseils.

Merci à Joël Stalder, fontainier à Boncourt, qui a aimablement partagé avec moi ses connaissances des sources et des captages de la commune.

Merci aux courageux qui sont venus me donner un ou plusieurs coup de main sur (sous) le terrain : Alain, Alizée, Celia, Guillaume, Martin, Louis et Stéphane.

Ça a été un plaisir de travailler au CHYN ces quatre années, et je tiens à remercier tout spécialement Lorienne, Lucien, Claire, Violaine, Greg et Dan pour leurs divers conseils et leur amitié.

Merci à ma famille pour leur soutien tout au long de mes études. Un merci particulier à mon père pour son œil avisé.

Et enfin j'exprime tout ma gratitude à Jacques, qui a été un compagnon essentiel dans les méandres de la Milandrine comme dans ceux de la thèse.

Contents

Chapter 1

Introduction

1.1 Introduction

Rapid flow through karst aquifers makes them prone to convey particulate matter. Most remarkable evidence for the transport of sediments are the intense turbidity peaks frequently observed at karst springs during storm flow, as well as the piles of clastic deposits found in caves throughout the world. Sediment yields at karstic springs may be of similar magnitude as in surface catchments (Drysdale et al., 2001). Clastic sediment fluxes through karst aquifers can thus be a significant geomorphic agent (Bosch and White, 2004; Dogwiler and Wicks, 2004; Herman et al., 2012), e.g. by shaping the landscape (Gillieson, 1986) or by influencing cave solution (White and White, 1968; Jones, 1971). More recently, suspended particles transported through karst aquifers have also been pointed out as a vector for contaminant transport, because they may act as sorbents towards pathogens, metals and other hydrophobic contaminants (Mahler et al., 2004). However, due to the lack of direct access to the conduits in most karst catchments, the sedimentary processes occurring inside karst aquifers are poorly characterized.

This thesis aims at improving the understanding of the physical processes controlling sediment fluxes inside the karst system of Milandre, in the Jura Mountains (Switzerland). In this introductory chapter, a literature review on particle transport in karst aquifers is presented (Sec. 1.2). This review serves as a basis for the motivations and goals of this thesis (Sec. 1.3). A description of the Milandre site is then proposed in Sec. 1.4. Finally, the structure of the thesis is described in Sec. 1.5.

1.2 State of the research

1.2.1 Mechanisms of sediment transport

Karst aquifers are generally much more effective at conveying suspended solids than porous media. Massei et al. (2002) gave the example of the Bébec sinking stream–Hannetôt spring system in Upper Normandy (France). They compared the particle transport between the swallow hole and the spring (3 km distance) and between the spring and a well 130 m downstream in the alluvial aquifer. The transport through the karst system appeared to be fairly conservative, with a slight attenuation of the turbidity signal, and a similar evolution of the particle size distribution in the sinking stream and at the spring. In contrast, the turbidity signal was dramatically attenuated in the well, reaching values ~ 50 smaller than at the spring. Moreover, the particle size distribution showed considerable size sorting between the spring and the well, demonstrating the filtration capacity of the porous aquifer. This example is somewhat extreme, being a well developed sinking stream–spring system. Toran et al. (2006), by comparing three catchments from the Appalachians, found that the most mature karst system (according to their reactivity to storm events) yielded much higher sediment concentrations than the least developed one.

The mechanisms of particle transport in karst aquifers have been investigated by means of tracer tests in several studies. Fluorescent polystyrene microspheres are commonly used as a particulate tracer (Goldscheider et al., 2003; Auckenthaler et al., 2002; Göppert and Goldscheider, 2008; Sinreich et al., 2009; Schiperski et al., 2016) as well as biological tracers such as bacteriophages (Auckenthaler et al., 2002; Flynn and Sinreich, 2010), spores (Goldscheider et al., 2003) and bacteria (Sinreich et al., 2009). These experiments generally aim at characterizing the mobility of pathogenic microorganisms through karst. Mahler et al. (1998) introduced the use of lanthanide-labeled clay as a sediment tracer. Goldscheider et al. (2008) and Luhmann et al. (2012) used natural mud. In those experiments, a solute tracer is introduced together with the particulate tracer. Two effects are commonly reported: (1) the recovery rate of the particulate tracer is significantly lower than the solute one (often designated as *attenuation*) and (2) the particulate tracer appears to travel faster in terms of first detection at the observation point and/or of dominant flow velocity (*early breakthrough*). This behaviour was previously observed and studied in porous media (e.g. Zhang et al. (2001)). Authors also reported the importance of the physico-chemical properties of the injected particles on their transport through the karst media. Finally, once introduced into the phreatic zone, sediments may be deposited and subsequently eroded. These mechanisms are reviewed in this section.

Attenuation

McDowell-Boyer et al. (1986) listed three mechanisms that can contribute to particle filtration in porous aquifers, depending on the relative size of the particles with respect to the grain size of the porous media. For particle sizes similar to the aquifer grain size, a filter cake of particles is produced on the surface of the porous media. When the particle size is somewhat smaller than the aquifer grain size, straining can contribute to particle attenuation – i.e., particles getting trapped in smaller pores. Finally, for particles that are much smaller than the porous media grain size, attachment can occur – i.e., the adsorption of particles on the porous media by physical and chemical forces. In karst aquifers, gravitational settling of particles in fissures and conduits can also participate in particle attenuation.

In their experiment, Göppert and Goldscheider (2008) injected a solute (uranine) and a particulate

(1 µm microspheres) tracer in a cave stream and observed their breakthrough at a spring 2 km downstream. Uranine recovery was very close to 100% both during low and high flow. Microspheres recovery varied from 75% (low flow) to 42% (high flow). They attributed this difference in attenuation to the increased turbulence during flow, which boosts the frequency and the intensity of collisions between particles and conduit walls, enhancing particle attachment. Mahler et al. (1998) also injected their tracers in an active conduit and monitored their breakthrough at a spring 200 meters away. However, in this case, the particulate tracer was completely attenuated at low flow, but was detected at higher flow. They explained theses observations by particle deposition or flow diversion at low flow, as the recovery rates of the solute tracer were in both cases very low. Goldscheider et al. (2003) reported an almost complete attenuation of 1 µm microspheres and 30 µm spores over a 2-km distance, despite significant solute tracer recoveries. They hypothesized that sedimentation, filtration and adsorption processes in this confined karst aquifer with low flow velocities were effectively preventing particle transport. As a comparison, dominant flow velocities were 25 and 145 $m \cdot h^{-1}$ in Göppert and Goldscheider (2008) and 30–50 $m\ d^{-1}$ in Goldscheider et al. (2003). On the contrary, both Sinreich et al. (2009) and Flynn and Sinreich (2010) reported a higher recovery for particles than iodide through 10 m of epikarst. In this case, the particles travelled faster than the solute, and a significant amount of iodide remained in the system at the end of the experiments.

Early breakthrough

In porous media, the early breakthrough of particles compared to solutes is attributed to exclusion processes. Two phenomenons have been identified: (1) size exclusion, in which particles follow faster streamlines in the center of pore spaces and (2) pore exclusion, in which particle only travel through larger pores and thus at faster velocities (Schiperski et al., 2016). Zhang et al. (2001) warned that an apparent early breakthrough of a particulate tracer does not necessarily imply a faster advection velocity. First arrival of particles prior to first arrival of solute can be an artefact caused by lower detection limits of particles (down to a few occurrences per mL) than of solutes. Moreover, the particle attenuation tends to shift the breakthrough curve (BTC) earlier in time. This is due to the higher probability of late particles to become attached as they follow slower and/or longer flow paths.

Goldscheider et al. (2008) compared the breakthrough of uranine and mud through 30 m of epikarst covered with 2 m of soil. Turbidity and uranine started to increase simultaneously, but the turbidity BTC has a steeper rising limb, peaking and receding earlier than uranine. They explained it by exclusion processes and/or attenuation. At another site, through 10 m of epikarst covered by thin soil, early BTC of bacteriophages (Flynn and Sinreich, 2010) and bacteria (Sinreich et al., 2009) compared to solute tracer were observed. In this case, the authors were able to attribute it to exclusion processes, as the recovery rates were higher for particles than for solute.

Similarly, an early particle BTC is reported by Luhmann et al. (2012), who injected multiple tracers into a dry sinkhole connected by a saturated conduit to a spring 100 m downstream. They favour the hypothesis of deposition as an explanation for the steep rising limb and the early peak in sediment, as the discharge was decreasing during the tracer breakthrough. In their cave stream experiment, Göppert and Goldscheider (2008) also observed shorter transit times for 1 µm microspheres than for uranine under low flow conditions, but this time shift was not visible during high flow. They hypothesized that size exclusion processes are most efficient during low flow because during high flow, turbulences homogenize the velocity profile in the conduits. Early breakthrough of particles through a saturated conduit are also reported by Mahler et al. (1998).

Schiperski et al. (2016) injected multiple tracers into a dry sinkhole connected to a spring. They also observed an earlier breakthrough of particles. They attributed it to pore exclusion processes both in the unsaturated and saturated zones. Indeed, they were able to rule out attenuation, because the recovery was close to that of uranine. Furthermore, size exclusion is expected to have an effect on the tracer dispersion, which was not observed in their experiment. Auckenthaler et al. (2002) injected uranine, bacteriophages and 1 µm microspheres into a trench and monitored a spring 1.25 km away. First arrival times yield maximum transport velocities of 770, 846 and 6113 $m \cdot d^{-1}$, respectively. The surprisingly fast breakthrough of microspheres may arise from an analytical artefact, their detection limit being much lower than that of bacteriophages. They attribute the faster maximum velocity of bacteriophages — with respect to uranine — to exclusion processes in the soil and the underlying quaternary deposits. However, this could as well arise from the attenuation of bacteriophages, their recovery rate being one order of magnitude lower than that of uranine. Moreover, the exclusion processes might as well take place in the epikarst (Sinreich et al., 2009; Flynn and Sinreich, 2010) or in the saturated zone (Mahler et al., 1998; Göppert and Goldscheider, 2008). Some authors (Auckenthaler et al., 2002; Pronk et al., 2006) also report this differential breakthrough with natural tracers: UV extinction, a proxy for dissolved organic carbon originating from

soils, and fecal microorganisms — although in such cases it could be due to differences of origin or of their recharge mechanisms (Pronk et al., 2006). In contrast, Personné et al. (1998) observed an increase in NH^{4+} slightly preceding *E. coli* increases at a point-source polluted karst spring.

Physico-chemical properties of particles

The physical properties of particles affect the way they are transported. Goldscheider et al. (2003) and Göppert and Goldscheider (2008) injected at the same time particulate tracers of different sizes (1 µm vs. 30 µm and 1 µm vs. 5 µm). Both studies highlighted a much stronger attenuation of larger particles. This is probably caused by mechanical processes such as sedimentation and straining. Schiperski et al. (2016) compared the transport of 1 µm particles of different density: silica (2 $g{\cdot}cm^{-3}$) and polystyrene (1.05 $g{\cdot}cm^{-3}$) microspheres. They concluded that the surface properties of the particles have a stronger control on the attenuation than their density: attenuation was greater for polystyrene microspheres than for the silica ones, which had a recovery rate similar to that of uranine. Mechanical attenuation, e.g. particle sedimentation, was hence unlikely to have taken place. Rather, the hydrophobicity of polystyrene particles explains their greater attenuation by adsorption processes.

The influence of particle surface properties have been pointed out by several studies. Sinreich et al. (2009) compared the recovery of 1 µm polystyrene microspheres and 0.5 × 2 µm bacteria of similary density through an epikarst: the recovery of the microspheres was 2% of that of the bacteria. They suspected that this was caused by the microspheres being more hydrophobic than the bacteria. This argues against the use of polystyrene microspheres in tracer tests as a surrogate for microorganisms. At the same site, Flynn and Sinreich (2010) compared the recovery of two type of phages, H40/1 and T7, of similar sizes (some tens of nm). The H40/1 recovery rate was 5 times that of T7. Again, they emphasize the influence of surface properties — H40/1 having a more negatively charged surface and being less hydrophobic than T7. In constrast, in their experiment with four different types of 1 µm microspheres, Schiperski et al. (2016) found that more negatively charged particle were more attenuated than neutral ones. This points out also the effects of the natural environment in adsorption processes. Sinreich et al. (2009) investigated those effects in a lab experiment: they compared microsphere and bacteria attenuation in three types of environments — soil, pure crushed limestone and biofilm-coated limestone. They found that soil and biofilm-coated limestone had a strong adsorption capacity for microspheres, but not for the bacteria. Pure limestone, on the other hand, attenuated both microspheres and bacteria at similar rates. Both Sinreich et al. (2009) and Schiperski et al. (2016) field experiments lead to the hypothesis of a significant effect of a biofilm coating the aquifer limestone on the attenuation of small (up to 1 µm) particles.

Observations of naturally occurring suspended particles in karst waters also point out the existence of physico-chemical processes affecting their transport. Mavrocordatos et al. (2000), in their study at a swallow hole–spring system, found that iron rich colloids were mostly retained by the karst system, although clay particles were mostly transferred. Shevenell and McCarthy (2002) found in some wells that turbidity variations were well correlated with large pH changes, implying that chemical effects, although not exclusively, played a role in small particles mobilization. Investigating particle-size distribution and its dynamics at a karst spring, Atteia and Kozel (1997) highlighted the different behaviour of colloids (smaller than 4–5 µm) and particles (larger than 5 µm). Spring discharge is the most important control on particles concentration, and pH, on colloid concentration. They were thus able, for this particular swallow hole–spring system, to identify the particle size threshold at which chemical processes have a stronger control on transport than hydrodynamic processes. Reed et al. (2010), who also analyzed the suspended sediment grain size distribution at two karst springs, found a jump in the concentration of particles larger than ≈ 10 µm for a certain discharge value. They also conclude to a transition between chemically and hydrodynamically controlled transport processes.

Sediment remobilization

As in surface streams, fluvial sediment in karst conduits may be transported as bedload or as suspended load. Sediment may be deposited on the conduit bed and subsequently eroded under certain flow conditions. Sediment movement starts when the boundary shear stress exerted by flowing water on the channel bed exceeds a critical value. The boundary shear stress in an open channel can be expressed as (Baker and Ritter, 1975):

$$\tau_0 = \rho g R_h \frac{\mathrm{d}h}{\mathrm{d}L} \tag{1.1}$$

where τ_0 ($N{\cdot}m^{-2}$) is the mean boundary shear stress, ρ the fluid density ($kg{\cdot}m^{-3}$), g the gravitational acceleration ($m{\cdot}s^{-2}$), R_h the hydraulic radius (m) and $\frac{\mathrm{d}h}{\mathrm{d}L}$ the friction slope (-). This equation is valid for open, low slope channels. It results from the balance between the gravitational force acting on the fluid and the resistance force exerted by the bottom boundary. In karst studies, some authors (White and White, 1997; Dogwiler and Wicks, 2004) use flow depth rather than the hydraulic radius in Eq. 1.1, but this approximation should only be applied when the

conduit is considerably wider than deep. The relation between boundary shear stress and flow velocity is not straightforward: mean channel velocity is not easily converted to bottom velocities, and bottom velocities depend on bed roughness factors (White and White, 1968). Gale (1984); Bosch and White (2004); Herman et al. (2012) suggest the following relation, valid in circular conduit under pipe-full conditions:

$$\tau_0 = \frac{f\rho}{8} v^2 \tag{1.2}$$

where f is the Darcy-Weisbach friction factor (-) and v is the flow velocity at the bottom of the channel ($\mathrm{m{\cdot}s^{-1}}$). In their study on surface streams, Jamieson et al. (2005) combined Eq. 1.1 with Manning's formula to express the boundary shear stress as a function of flow and hydraulic geometry:

$$\tau_0 = \rho g \left(\frac{\mathrm{d}h}{\mathrm{d}L}\right)^{1/4} \left(\frac{n}{A}\right)^{3/2} Q^{3/2} \tag{1.3}$$

where n is the Manning roughness coefficient ($\mathrm{s{\cdot}m^{-1/3}}$), A is the flow cross-sectional area ($\mathrm{m^2}$) and Q is the flow rate ($\mathrm{m^3{\cdot}s^{-1}}$). The relationship between critical boundary shear stress τ_c and grain size is expressed as follows (White and White, 1968; Dogwiler and Wicks, 2004; Herman et al., 2012):

$$\Theta = \frac{\tau_c}{(\rho_s - \rho) g d_{50}} \tag{1.4}$$

where Θ is the Shields parameter, a dimensionless critical shear stress, ρ_s is the density of the sediment ($\mathrm{kg{\cdot}m^{-3}}$) and d_{50} the median grain size (m). Using measurements of grain size distributions in cave sediment published in the literature, Herman et al. (2012) found the following empirical relation between grain size and critical shear stress

$$\tau_{c90} = 0.341 d_{90}^{1.021} \tag{1.5}$$

for d_{90} between 0.02 and 100 mm. d_{90} is the diameter which 90 % of the sediment mass is smaller than and τ_{c90} the critical boundary shear stress of sediment of size d_{90}. Theses equations are all expressions of the threshold required for sediment to be transported as bedload. For sediment to be transported as suspended load, not only must the shear stress be sufficient to initiate movement, but the gravity pull on the grains must be compensated by upwards forces created by the turbulence of the flow. For small particles, adhesive forces play a more important role than gravitational forces. Empirical relationships between critical boundary shear stress, for both bed and suspended load, and sediment grain size are mentioned by several authors; they are grouped altogether in so-called Shields diagrams (White and White, 1968; Herman et al., 2012). However, these relationships are not valid for fine sediments, e.g. in the silt and clay range size, because they are subject to interparticle forces. A numerical model of the entrainment and attachment of $< 50\,\mu\mathrm{m}$ particles in karst conduit is presented by Hauns (1999).

1.2.2 Cave deposits

Lithofacies of cave sediments

Cave sediments often display poor lateral correlation and much reworking. They may be subject to extreme variations in rate of deposition, and the law of superposition may be violated (Ford and Williams, 2007b). Classifications for theses complex deposits have been proposed by several authors. An early and very detailed one was proposed by Gillieson (1986) on the basis of his observations in New Guinea caves. Deposits were classified according to the water flow type and the depositional energy. Springer and Kite (1997) classified the deposits they observed in the caves of Cheat River (West Virginia) in three classes: phreatic, vadose (or slackwater) and residuals. A somewhat more general classification, with distinct lithofacies sorted according to stream power, was presented by White and White (1997) and later revised in Bosch and White (2004). It is based on two parameters: particle size and size sorting. All this can be summarized the following way:

Channel facies Most common facies. It consists in sorted or partially sorted silts, sands and gravels transported as bedload and deposited in distinct beds by an active stream.

Thalweg facies Produced by an active stream cutting through the channel facies. It consists in well sorted gravels, cobbles and boulders. Silts and sand have been winnowed. As boundary shear stress increases with the square of flow velocity (Eq. 1.2), it can be an efficient process under specific flow conditions. The thalweg facies hence correspond to a higher stream power than the channel facies.

Slackwater facies Laminated, well-sorted clays and silts deposited from the suspended load. They can be deposited in semi-active passages that get flooded by muddy, slowly flowing waters during storm events, or as a final layer on top of channel facies sediments.

Diamicton facies Unsorted, chaotic deposits containing all particle sizes, from clay to boulder. They correspond to debris flow occuring in extreme, rare events. They seem to be associated with tropical (Gillieson, 1986; McFarlane and Lundberg, 2004) or periglacial conditions (White and Hess, 1982).

Backswamp facies Poorly sorted clays to silts originating from bedrock weathering or from the overlying soils, with little lateral transport.

Field examples for each lithofacies are presented in Bosch and White (2004); Chess et al. (2010); Herman et al. (2012).

Hydraulics reconstruction

Sedimentary structures and textures are records of the hydrodynamic conditions at the time of their deposition, be it regular or extreme flow conditions. An early attempt of linking sediment grain size with flow velocity is presented by Schroeder and Ford (1983). They found an accumulation of rounded pebbles at the bottom of an 8 m vertical shaft, seemingly transported up to the top of the shaft during floods. By estimating the force required to prevent the settling of similar-sized spherical particles, they obtained flow velocities of ∼1 $m{\cdot}s^{-1}$. These are compatible with the measured discharge and the conduit cross section, confirming the capacity of normal flood flows to lift the pebbles up the shaft. An example of local hydraulic reconstruction of extreme flow conditions is given by Palmer and Palmer (2006): sandstone boulders of metric dimensions moved uphill in a Virginian cave, indicating flow velocities faster than 3.5 $m{\cdot}s^{-1}$.

Gale (1984) presented a systematic study of flow velocity estimation on the basis of cave sediment grain size. He analyzed grain size distributions for several samples in a cave and subdivided them in several subpopulations. The coarsest grain size subpopulation is assumed to have been transported as bedload. The critical boundary shear stress corresponding to this subpopulation (using d_{50}, the median grain size) is evaluated by means of a Shields diagram. The mean flow velocity is estimated using a relation expressed in Eq. 1.2. The resulting velocities lie between 0.1 to 0.3 $m{\cdot}s^{-1}$. He found this to be consistent with flow velocity estimates from a range of caves he calculated using scallop wavelengths (0.01–1 $m{\cdot}s^{-1}$). He also noted that these velocities are mostly representative of high stage conditions, and are faster that the typical velocities estimated from tracer tests.

Another systematic study of sediment mobility is provided by Dogwiler and Wicks (2004). They measured or estimated water depth and hydraulic gradient during base flow and high flow at several stations in two cave streams. Bed sediment samples from these locations were analysed for grain size distribution, and were mostly of cobble size. They calculated the corresponding critical boundary shear stress for d_{50} and d_{85} (cf. Eq. 1.4). They compared it to the boundary shear stress inferred from the water depth and slope (cf. Eq. 1.1, but approximating R_h by water depth). They found that the stream bed sediment is mostly not mobile during base flow, but that the critical shear stress for movement of 85% of the sediment mass is reached generally at stages lower than bankfull. For one station, the return periods of events capable of entraining d_{50} and d_{85} was estimated at 2.4 and 12 months, respectively, implying that the system is generally at equilibrium regarding channel bed movement.

Sedimentation rates

Because of the episodic nature of karst sediment accumulation and erosion, sedimentation rates in caves are generally difficult to estimate. A few case studies of contemporary sedimentation rate estimations are found in the literature, but no measuring method really stands out. Murray et al. (1993) analysed ^{137}Cs in sediment cores from an Australian cave. They associate detectable concentrations of ^{137}Cs with deposition during or after the late 1950s. This yields sedimentation rates of 3 to 5 $mm{\cdot}y^{-1}$, although a specific flood event in this period is known to have deposited ∼20 mm of sediment. Sasowsky et al. (2004) extrapolated the observed sediment accumulation for specific events (3 mm) in a Pennsylvanian cave and found that the total sediment pile could have been deposited in ∼1500 y — probably an underestimation, as the cave is likely older than 100 ky.

In the coastal karst of the Yucatan peninsula, high organic content in the sediment enables the use of radiocarbon dating. A compilation of such dating in Collins et al. (2015b) indicates rates in the order of 0.2 $mm{\cdot}y^{-1}$ over the last 4–6 ky. In this coastal karst, sediment fluxes are controlled by primary productivity in and around the *cenotes* rather than by hydrological events (Collins et al., 2015a) and hence are probably steadier than in continental caves.

Chédeville et al. (2016) realized a detailed study of contemporary sedimentation dynamics in an active cave stream in the chalk of Normandy (France). A sediment trap revealed that each turbidity event corresponds to a sequence of one lighter, coarser sediment layer followed by a darker, finer layer deposited during flow recession. On this basis, a sediment core of ∼25 cm was correlated with the corresponding 22 year turbidity time series. The overall sedimentation rate is 1.1 $cm{\cdot}y^{-1}$, but several individual events deposited 1 to >2 cm in one go. They pointed out a periodicity of 5–8 y in the meteorological and sedimentary activity which they linked to the North Atlantic Oscillation.

1.2.3 Sediment sources

Classification

A classification of the different types of sediment input into karst aquifers has been developed by W. B. White and co-authors (White and White, 1968; Bosch and White, 2004; Herman et al., 2012). In its most recent form, it consists in five categories:

1. allogenic sediments carried by sinking streams;
2. soil piping, sinkhole collapse and injection into vertical shafts;
3. soil washdown through the epikarst;
4. backflooding of base level surface stream;
5. and insoluble bedrock residue.

Sediments may also enter caves by being pushed in by glaciers.

Suspended sediment discharged at karst springs is often categorized between *autochthonous*, e.g. coming from the aquifer, and *allochthonous*, e.g. coming from the surface. This distinction is of particular interest in terms of catchment vulnerability assessment, since most contaminants originate from the surface. Earlier authors used the term *autochthonous* to describe exclusively sediment derived from carbonate dissolution in the aquifer (Mahler et al., 1999; Mahler and Lynch, 1999; Massei et al., 2002). Lately the term has been used to describe any material that originates from the resuspension of intrakarstic deposits, while *allochthonous* corresponds to the material that is eroded from soils and transported to the spring over the course of one flood event (Massei et al., 2003; Pronk et al., 2007, 2009; Schiperski et al., 2015a). This later classification will be used throughout this thesis. Other authors used the terms *resuspension* and *direct transfer* (or *direct transport*) to describe the processes generating, respectively, autochthonous and allochthonous turbidity (Valdes et al., 2005; Fournier et al., 2007b,a).

Determining the origin of sediments from their composition

Earlier works on karst sediment origin have focused on cave deposits. A pioneer study is provided by White (1977) on the sediments of Mammoth Cave. He suggested the use of near infrared and visible spectroscopy as a way to quantify the perceived differences in the color of sediments. He found that the amount and the hydration state of iron were the dominant controls on sediment color and was able to discriminate the three types of surface soils based on their spectral reflectance. Lower passage deposits appeared to contains less iron than upper levels — either, their was a shift in sediment source along the cave history, or, as mentioned as well by Davies and Chao (1959), the lower passages are provided in sediment by the backflooding of Green River. Another study on cave deposits (Murray et al., 1993) used the relative concentrations of ^{226}Ra and ^{232}Th to assess the contributions of two surface subcatchments and how they evolved through time. Other authors have used mineralogical XRD analysis (Schroeder and Ford, 1983; Knapp et al., 2004).

More recently, many authors have been interested in characterizing the nature of the sediment discharged at karst springs — for instance, through mineralogical (XRD) and morphological (SEM) analyses. The presence of quartz grains and other silicates is usually associated with a provenance from surface loam formations. It was found to be the dominant component of the discharged sediment at several karst springs (Massei et al., 2002; Vesper and White, 2003; Herman et al., 2007; Reed et al., 2010). Calcite and dolomite are usually associated with erosion or precipitation inside the aquifer (Mahler et al., 1999; Vesper and White, 2003; Herman et al., 2007). Lynch et al. (2004) pointed out the potential of clay mineralogy to identify sediment origin in their study at Barton springs (Edwards aquifer, Texas). They found distinct clay mineral suites in the potential sediment supplies and stated that the sediment discharged at the spring originates from the distant (tens of km) allogenic recharge zone. SEM imagery reveals information on the composition and morphology of the grains that can by useful in assessing their origin. For instance, Mahler et al. (1999) identified organic matter and coloured fibres of unambiguously allochtonous origin. Herman et al. (2007) found particular morphologies of calcite grains that indicates that they were formed by precipitation inside the aquifer itself. Drysdale et al. (2001) were able to differentiate aquifer derived carbonate grains from the debris issued by a quarry exploitation, thanks to the distinguishable texture produced by the cutting tools.

Particle size distribution (PSD) techniques have yielded promising results in the identification of the source of discharged sediment, although it requires first to characterize the signature of the sediment inputs. On the plus side, instruments now allow instantaneous, on site PSD measurements (Pronk et al., 2007; Schiperski et al., 2015a). A nice example in a chalky aquifer of Normandy (France) is given by Lacroix et al. (2000). Analyses of surface formations (Tertiary to Quaternary loams) and the decalcified residues of the aquifer chalk formations (epikarst, unsaturated and saturated zones) yielded distinct, well sorted unimodal PSD for each component. This enables the decomposition of the microgranulometric spectra of the suspended sediment in the underground stream. Under low flow conditions, suspended sedi-

ment composition is dominated by decalcified loam from the epikarst and the saturated zone, and also contains a significant portion of surface loams. The high flow suspended sediment is, on the other hand, entirely composed of silts originating from surface formations.

Another example is given by Pronk et al. (2007) in a sinking stream–spring system of the Swiss Jura Mountains. In this case, allochthonous turbidity at the spring was identified using the timing of the arrival of *E. coli* contaminated sinking stream water. For two different storm events, they found that, by comparison with the pre-storm PSD, a relative decrease in smaller particles is associated with autochthonous turbidity. Conversely, a relative increase in smaller particles appears to be consistently associated with the arrival of allochthonous turbidity. Massei et al. (2002) found comparable PSD in a sinking stream and in its outlet spring in Normandy, and concluded to a conservative particle transport through the aquifer.

Determining the origin of sediments through time series analysis

The relative timing of sediment breakthrough compared with freshly-infiltrated water arrival is probably the most commonly used method to distinguish allochthonous and autochthonous turbidity at springs at the event scale. That is, sediment arriving before event water is considered to be issued by resuspension of sediment inside the aquifer, and sediment arriving simultaneously with event water is assumed to originate from surface soil erosion. An early example of storm event monitoring is provided by Ryan and Meiman (1996) at a spring in Mammoth Cave National Park. The spring catchment, with a mostly allogenic recharge, is forested close to the spring and agricultural in its distal part. They monitored rainfall, spring discharge, specific conductance, turbidity and fecal coliform concentration. They decomposed the two monitored events in three phases: (1) discharge increases, specific conductance and other spring parameters are constant. The antecedent water stored in the aquifer is flushed to the spring. Discharged volume corresponds to the volume of the conduit system. (2) Decrease of the specific conductance, other parameters are stable (discharge may further increase or decrease). It corresponds to the arrival of proximal event water from the forested area. (3) Specific conductance remains low, turbidity and fecal coliforms peak. It reflects the arrival of distal event water from the agricultural area. The transit times between the different recharge areas and the spring were confirmed by tracer injections simultaneous with the recharge events. Throughout the literature, typical natural tracers that are used to identify the arrival of allochthonous turbidity are the decrease in specific conductance (Mahler and Lynch, 1999; Vesper and White, 2003; Massei et al., 2003; Toran et al., 2006; Pronk et al., 2006, 2007; Herman et al., 2008; Reed et al., 2010; Butscher et al., 2011), breakthrough of *E. coli* (Auckenthaler et al., 2002; Pronk et al., 2007; Knierim et al., 2015) and of total or dissolved organic carbon, often estimated by UV extinction or UV fluorescence (Auckenthaler et al., 2002; Pronk et al., 2006, 2007; Schiperski et al., 2015b).

The association between the decrease in specific conductance (or electrical conductivity) and the breakthrough of allochthonous turbidity is the most commonly used methods. The earlier studies such as Ryan and Meiman (1996) simply made visual comparison of the different times series. In the early 2000s, some authors started using signal processing methods on spring parameter time series. Bouchaou et al. (2002) suggested autocorrelation as a way to investigate sediment dynamics in karst aquifers. It consists in calculating the correlation of a variable with itself for a range of time lags, thus quantifying the memory effect, or inertia, of a system with respect to this variable. The inertia of a variable is quantified by the time lag needed for the autocorrelation coefficient to reach a value of 0.2. In their study on a spring in the middle Atlas, Bouchaou et al. (2002) found that discharge had a much higher inertia than turbidity: the correlation coefficient reaches 0.2 with a time lag of 75 days, while only 4 to 5 days are needed in the case of turbidity. Similar observations are reported by Amraoui et al. (2003) in the same area. They explained this by sediment mobilization and deposition being threshold controlled processes. In contrast, Massei et al. (2006), who studied a sinkhole–spring system in Upper Normandy, also found a low inertia for turbidity (autocorrelation of 0.2 after 2.5 days), but the inertia of the spring water level was similarly low (3 days). Valdes et al. (2005, 2006); Massei et al. (2006) compared the autocorrelograms of turbidity and specific conductance (SC) rather than discharge to study sediment transport in the karst of Normandy. They use SC as a proxy for event water recharge. Massei et al. (2006) introduced the idea of using a logarithmic fit rather than a single cut-off value for autocorrelogram comparisons. While the memory effect of SC is always longer than that of turbidity, Valdes et al. (2006) found significant differences in the memory effect of SC throughout similar size catchments. They stated that it reflects the throughflow capacity of the system: long SC memory effect means that water storage takes place, and is associated with sediment deposition. Conversely, a short SC memory effect means a fast solute transport with a more conservative particle transport. Bouchaou et al. (2002); Amraoui et al. (2003); Massei et al. (2006) computed cross-correlation of different time series. These studies pointed out that the turbidity is more closely cor-

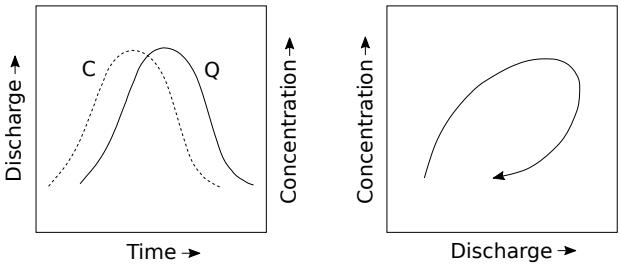

Figure 1.1: Example of a clockwise loop in the sediment concentration (C) vs discharge (Q) relationship (modified from Williams (1989)).

related with rainfall than with spring discharge or water level, but the interpretation for this observation differs depending on the context: in the 200 km^2, mixed auto- and allogenic catchment studied by Bouchaou et al. (2002), this correlation between rainfall and turbidity is thought to arise from threshold effects in the processes controlling sediment resuspension in the karst conduits. On the other hand, Massei et al. (2006), in their small sinkhole–spring system, saw the correlation of turbidity with rainfall to be an indication of surface soil erosion. Massei et al. (2003) suggested to decompose the turbidity signal in distinct peaks by a peak fitting method. A comparison with the SC time series was used to distinguish allochthonous peaks from autochthonous ones. This method was also applied by Schiperski et al. (2015a). Fournier et al. (2007a) decomposed the histograms of SC, discharge and turbidity to identify subpopulations which they associated to hydro-sedimentary processes — e.g. low SC, high discharge and high turbidity corresponds to direct transfer of surface-derived sediment, etc. Massei et al. (2006) also used wavelet analysis on their time series. Wavelet filtration on the water level time series highlighted two main components: quick flow (high frequency) and slow flow (lower frequency). They show that turbidity events are synchronous with quick flow peaks — i.e. turbidity is linked with rapid, concentrated infiltration and fast flow through the conduit system. Wavelet analysis was also used by Chédeville et al. (2016) in a karst system of Normandy, and highlighted the influence of the North Atlantic Oscillation on the turbidity dynamics.

In the past decade, the comparison between the temporal variations of the electrical conductivity and of the turbidity has been extensively used. Starting with the study of Valdes et al. (2005), authors have been using surrogates to the sediment concentration (C) vs discharge (Q) curves first drawn by Williams (1989). He developed a classification of the possible shapes of the C–Q relation for single events in surface streams, which gives insight into the transport processes at stake. C–Q relations are plotted on a log-log scale and graphically classified. He described 5 classes; only the first 3 are mentioned by karst authors:

Single-valued line Synchronous discharge and sediment peaks

Clockwise loop The discharge peak lags behind the sediment peak (Fig. 1.1)

Counter-clockwise loop The sediment peak lags behind the discharge peak

The karst authors use turbidity as a proxy for sediment concentration, and the decrease in electrical conductivity, ΔEC, as a proxy for the contribution of event water to the spring discharge. The resulting turbidity–ΔEC curves are graphically or analytically classified in categories inspired from those of Williams (1989) and re-interpreted to the karst context. Valdes et al. (2005, 2006), in their studies of the chalky karst of Upper Normandy, found mostly clockwise hysteresis turbidity–ΔEC curves, which they explained by resuspension of autochthonous sediment at the beginning of the event, and deposition in the conduit system at the start of the recession. Turbidity–ΔEC curves with overlapping rising and falling limbs — i.e. turbidity and electrical conductivity have synchronous responses — were interpreted as a direct transfer of allochthonous sediments. The few counter-clockwise loops were interpreted as a limitation of sediment supply inside the system. Fournier et al. (2007b) suggested to normalize turbidity and ΔEC over the range of values reached for each event. They also separated each event between rising and falling limb, e.g. several events showed a constant slope of 1 during the rising phase, attributed to direct transfer, and an initial decrease in turbidity higher than the increase in EC at the beginning of recession, explained by sediment deposition. Schiperski et al. (2015b) further formalized the approach and suggested to compute the instantaneous slope at each time step of normalized turbidity–ΔEC curves, which they called the δ function. They can thus identify the different phases of sedimentary processes for each event. They use a range of values rather than one single cut-off value: instantaneous slopes of values between 0.5–1.5 are associated to direct transport. Resuspension is indicated by a slope >1.5 before recession. Sediment deposition or sediment supply depletion are indicated by slopes <0.5 until recession and slopes >1.5 during recession.

1.2.4 Anthropogenic impacts

Implications of particle transport on contamination

While suspended sediment may itself be considered as a contaminant (Currens, 2002; Mahler et al., 2004), it is also an effective carrier for various unwanted substances. The large specific surface area of small

particles enhance their capacity to adsorb contaminants (Atteia and Kozel, 1997). Mahler et al. (2004) pointed out the tendency of hydrophobic contaminants, such as trace elements, organochlorine compounds and polycyclic aromatic hydrocarbons, to sorb onto suspended sediments. Indeed, authors have reported the presence of sediment-attached arsenic and metals (Vesper and White, 2003; Mahler et al., 2004; Cholet et al., 2016) as well as pathogenic microorganisms (Mahler et al., 2000; Dussart et al., 2003) at karst springs and wells. Attached bacteria may be stored in the aquifer and subsequently resuspended or detached, adding a dimension to the prediction of microbial transport (Marshall et al., 1998; Mahler et al., 2000). Microorganisms are themselves particles that can be freely transported through karst aquifers — Mahler et al. (2000), in their study in southern France, found that the proportion of free vs total bacteria varied temporally between 0 and 100%. Fecal bacteria are the most commonly reported contamination of karst waters, with the infamous example of the Walkerton *E. coli* outbreak (Worthington et al., 2002). These aspects are of public health concern, as karst waters are widely used as drinking water supply and for recreational purposes (Mahler and Lynch, 1999; Knierim et al., 2015).

Fecal contamination

Contamination by enteric bacteria is mostly reported in agricultural and urban catchments. Comparisons with forested catchments showed that those are generally unaffected (Pasquarell and Boyer, 1995; Ryan and Meiman, 1996), although wild life may also constitute an input of fecal bacteria. Some identified contamination sources are pastures (Pasquarell and Boyer, 1995; Ryan and Meiman, 1996; Gunn et al., 1997; Reed et al., 2011), spread manure (Davis et al., 2005), dairies (Boyer and Pasquarell, 1999), waste water plants (Personné et al., 1998; Mahler et al., 2000), sewer leakages (Reed et al., 2011) and septic tanks (Knierim et al., 2015). Pasquarell and Boyer (1995) found no strong relation between the portion of agricultural land use and the fecal bacteria concentrations. Moreover, small inputs of bacteria contaminated water can significantly deteriorate groundwater quality (Pronk et al., 2006). Best management practices, such as manure and animal waste containment (Boyer and Pasquarell, 1999) and exclusion of cattle from stream and karst windows (Currens, 2002), are however expected to improve the groundwater microbial quality.

Fecal contamination affects both in allogenic and autogenic catchments. Soils attenuate the migration of fecal bacteria, but they do not provide a complete protection against groundwater contamination. Indeed, they may store and subsequently release fecal bacteria to the aquifer. *E. coli* has been found to persist for months or years in agricultural soils (VanderZaag et al., 2010; Brennan et al., 2010). Storage may also take place at the base of the epikarst. From there, they are transferred to the saturated zone and to springs by flood pulses. As a result, bacteria concentrations in groundwater may show a seasonal pattern — with storage and release during spring and summer; recovery during winter — but also exhibit a strong control from hydrological conditions (Pasquarell and Boyer, 1995; Gunn et al., 1997; Reed et al., 2011; Knierim et al., 2015).

Evidence for fecal bacteria storage in the aquifer have also been pointed out. The cool temperatures slow down their metabolism, prolonging their survival, and attachment to sediment may shelter them from predation (Davis et al., 2005). Marshall et al. (1998) studied the temporal variations of *E. coli* and fecal coliforms at karst springs in Northwest Arkansas during flood events. The timing of fecal bacteria breakthrough, occurring during the rising limb of the hydrograph, indicates that they originate from the resuspension of sediment, after being stored in the aquifer for up to several months. There is however no direct observation of fecal coliform storage inside karst aquifers. Enterococci, on the other hand, are in some cases reported to be more persistent than coliforms, or even endemic (Personné et al., 1998; Mahler et al., 2000). Overall, bacteria that are sediment-bound are of specific concern, as they exhibit longer survival, resistance to water treatments and may be stored and released by resuspension or detachment (Mahler et al., 2000; Dussart-Baptista et al., 2003). Mahler et al. (2000), in their study on karst wells in southern France, found that a substantial portion of the total fecal coliforms and enterococci concentrations was sediment-bound, at times up to 90%.

The water microbial quality may vary quickly in karst springs and wells, and this constitutes a challenge for drinking water supply. Several authors have been interested in finding real time monitored parameters that could effectively be used as an early warning for microbial contamination. Turbidity is generally discounted, because its increase may appear up to several hours after the rise in bacteria concentrations (Auckenthaler et al., 2002) and because contaminations may occur even during low turbidity periods (Dussart-Baptista et al., 2003; Pronk et al., 2006). Proxy for organic matter concentration such as UV extinction or UV fluorescence are generally well correlated but slightly preceded by fecal contaminations (Auckenthaler et al., 2002; Pronk et al., 2006). Pronk et al. (2007) found that PSD meets all the requirements to be an early warning indicator in their studied sinkhole–spring system. But the technique did not succeed at another site (Schiperski et al., 2015a). Schiperski et al. (2015b) stated that the electrical con-

ductivity vs. turbidity curves (see Section 1.2.3) have the potential to succeed in fecal contamination prediction. Butscher et al. (2011) suggested a numerical modelling method for the same purpose, which computes the contribution of conduit flow to the spring discharge. It was successfully applied to their field study in the Jura Mountains. Auckenthaler et al. (2002) suggested to use discharge as an early warning signal, as it is generally the first parameter to response to flood pulses.

Sediment fluxes

A few studies have tried to quantify the effects of human activities on sediment fluxes through karst aquifers, and some authors report that they can be significant. Murray et al. (1993) reported historical evidence for an increase in the sedimentation rate at the Jenolan Cave (Australia) starting from the 1950s on, which is coincident with the establishment of a pine plantation in the catchment. They estimated that about 35% of the contemporary sedimentation in the cave is attributable to wood exploitation. Drysdale et al. (2001) compared the sediment discharged at two neighbouring springs in Italy, one of which hosts marble quarries in its catchment. They showed that this spring, which exhibits turbidity peaks that frequently exceed 1000 NTU, mostly conveys sediment produced by marble cutting.

Currens (2002) assessed the efficiency of best management practices in an agricultural catchment in Kentucky. The median total suspended solids in groundwater went from 127 to 48 $mg{\cdot}L^{-1}$ after the best management practice implementation — mostly conservation crop rotation and crop residue use. This highlights the potential effects of agriculture on soil erosion. Also in Kentucky, Reed et al. (2010) compared two neighbouring catchments, one mostly urbanized and the other consisting mainly of grassland. They found sediment fluxes up to 3 to 50 times greater for the rural catchment than for the urban one. They explained this difference by the important portion of impervious cover in the urban catchment, which limits the sediment yield. These few examples tend to indicate that agriculture enhances sediment fluxes, and that urbanisation may restrict them.

1.3 Motivations and aim of the thesis

On the topic of sediment transport in karst aquifers, a number of studies focused on the identification of the sources of the sediment discharged at springs, and, more specifically, on the distinction between autochthonous and allochthonous turbidity. Many authors used XRD and/or SEM techniques to analyze the composition of the discharged sediments and infer their origin. A major shortcoming of this approach is that these methods are time consuming, as they require sampling and subsequent analyzes in the lab. Also, apart from specific material that can unambigously be indentified as allochtonous (Mahler et al., 1999; Drysdale et al., 2001), there is no general rule to link sediment composition to a particular source. Even in the case of Mahler et al. (1999), who did an extensive study of the mineralogy of the superficial formations in the catchment and of the aquifer compartments, the identification of the sediment origin was not always possible. Authors who performed XRD and/or SEM analysis of spring suspended sediment at karst springs tend in the end to rely more on the timing of freshly infiltrated water tracers to identify the arrival of allochthonous sediment (Mahler and Lynch, 1999; Vesper and White, 2003).

Several studies successfully used particle size distribution to identify the origin of suspended sediments (Lacroix et al., 2000; Massei et al., 2002; Pronk et al., 2007). This technique has the benefit that it may be used as a real time, in situ monitoring system (Pronk et al., 2007; Schiperski et al., 2015a). But again, this method requires a prior assessment of the PSD in the potential sources of sediment. In the case of a simple sinkhole–spring system, the characterization of the allochthonous sediment PSD is straightforward, whereas it is not easily feasible in purely autogenic catchments. It also seems to be very site specific — other authors did not find grain size distribution to be linked with sediment sources (Mahler et al., 1999; Schiperski et al., 2015a). Furthermore, some authors emphasized the strong control of hydrodynamic processes and chemical conditions on PSD variations at springs, which may interfere with this method (Atteia and Kozel, 1997; Mahler and Lynch, 1999; Dussart-Baptista et al., 2003; Reed et al., 2010).

Many authors analyzed time series of spring turbidity, rainfall and spring discharge to infer on the physical processes triggering sediment mobilization (Sec. 1.2.3). There are however limitations in how much information can be gained on a system's functioning through a single observation point. For instance, a series of papers focusing on the chalky aquifers of Upper Normandy advocates the use of turbidity vs electrical conductivity curves as a method to distinguish between autochthonous and allochthonous suspended sediments (Valdes et al., 2005, 2006; Fournier et al., 2007b). One benefit of this method is its straightforward data acquisition and processing. However, this approach relies on several assumptions which cannot always be verified. For instance, it implies that particles and solutes are identically advected. As described in Sec. 1.2.1, exclusion processes may lead to an apparent early breakthrough of particles compared to solutes, even in the saturated zone. For instance, in the multitracer test of Schiperski et al. (2016), a plot of Si^0 particle concentration

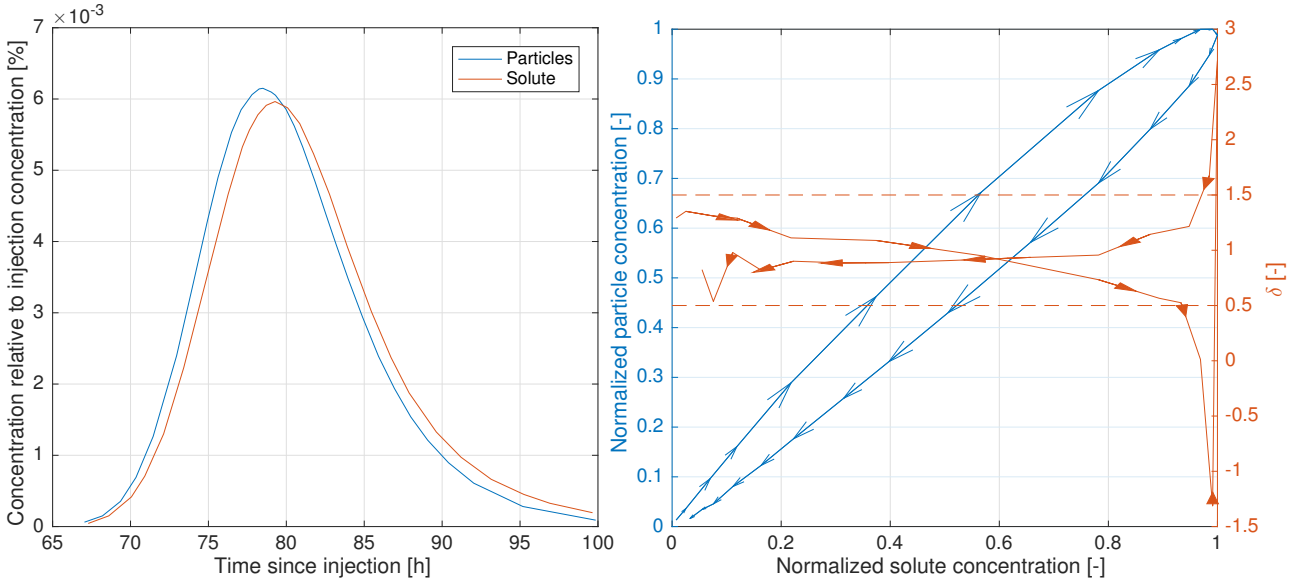

Figure 1.2: Left: tracer test recovery curves, from Schiperski et al. (2016). Right: Corresponding normalized particle concentration vs solute concentration curve and δ function, which is defined by Schiperski et al. (2015b) as the derivative of the normalized particle vs solute concentration curve. The dashed lines are the bounding values of δ for direct transfer of particles from the surface given by Schiperski et al. (2015b).

vs uranine concentration gives a clockwise loop (Fig. 1.2). The method of Valdes et al. (2005, 2006) would thus conclude to a resuspension of intrakarstic sediment during the rising limb of the loop, and a deposition of sediment in the conduit network during the falling limb. However, the particles and the dye tracer were injected simultaneously and injection was completed in 10 minutes, so that, considering the overall transit times, it is equivalent to a Dirac input. Moreover, resuspension is not possible, since the particulate tracer is artificial, while deposition is unlikely or very limited, since the recovery rates of both tracers were similar (61.5 vs 60.9%). This is thus a case of direct transfer of material from the surface to the spring. The range of slope values of the turbidity vs electrical conductivity curve (δ function) for direct transfer given in another paper from Schiperski et al. (2015b) seems however to be appropriate in this case (Fig. 1.2, right). Nonetheless, these slope values lack some physical justification in order to be generalizable to other systems or experiments. Furthermore, the turbidity vs electrical conductivity approach assumes that the variations in electrical conductivity at springs are thoroughly explained by a linear mixing between the water stored in the aquifer and the freshly infiltrated water. While this can be verified in sinkhole–spring system, additional processes may affect the electrical conductivity at karst springs in other catchments (Perrin et al., 2007; Jeannin et al., 2017). Finally, this method, or any method based on peak timing analysis, assumes that when freshly infiltrated water and turbidity have simultaneous breakthrough, they have the same origin. It is not straightforward to prove that this is always the case.

There also has been a growing interest regarding the characterization of the transport of fine particles (10 µm and smaller) in karst media. Because of their great sorption potential for a variety of substances, these particles are of particular concern in terms of contaminant transport (Atteia and Kozel, 1997; Mahler et al., 2004). Using artificial particulate tracers, a number of studies pointed out the dominant control of the surface properties of fine particles on their attenuation rate when circulating underground (Sinreich et al., 2009; Flynn and Sinreich, 2010; Schiperski et al., 2016). However, the interactions between particles, groundwater and the aquifer substrate may change depending on the prevailing physico-chemical conditions. Indeed, Atteia and Kozel (1997); Shevenell and McCarthy (2002) found a link between pH variations and fine particle concentration in karst groundwater. By contrast with surface water studies, the influences of physico-chemical processes on the transport of fine sediment in karst media are not well characterized. Indeed, there is a prolific literature on the effects of sediment concentration, water mineralization and temperature on fine particle transport both in lab experiments and in surface water (e.g. the early works of Mattson (1928); Owen (1976); Jianwei (1981) and Mehta et al. (1989) and the recent works of Debnath and Chaudhuri (2010); Naghipour et al. (2014) and Wan et al. (2015)). To determine to which extent these processes also affect sediment transport in karst aquifers, in situ observations of the variations of fine particle concentration and their relationships with other variables are required.

Overall, while the dynamics of particle transport in karst aquifers have been a topic of marked interest for karst scientists, it appears that the physical processes that control these variations are poorly characterized. This is demonstrated by the fact that most studies rely on the observations made at a spring to infer the sedimentary processes taking place inside its feeding aquifer (Sec. 1.2.3). While other authors (Gale, 1984; Dogwiler and Wicks, 2004; Sasowsky et al., 2004; Collins et al., 2015b; Chédeville et al., 2016) were able to give quantitative estimates of intrakarstic sedimentary fluxes through direct observation, these estimates are mostly based on geomorphological observations and sediment dating. The modeling techniques currently available to simulate flow in karst aquifers should allow to enhance the spatial and temporal resolutions of these estimates.

The aim of this thesis is thus to bridge gaps in the understanding of the processes that mobilize sediment and generate turbidity in karst systems, both through physically based numerical modeling and by field observations. The investigations are focused on the Milandre study site, which has the major advantage that a great portion of the epiphreatic conduit network is accessible by caving. This allows the direct observation of flow and sedimentary processes in the karst conduits. One goal of this work is to build a hydraulic pipe flow model of the downstream part of the Milandre system which can be used to infer the sedimentary processes occurring in the conduits.

Another advantage of the Milandre study site is that an extended data set regarding sediment fluxes inside the karst system, collected within the framework of a highway construction, is already available. For instance, 4 monitoring stations, among which 3 were located underground, have been continuously measuring turbidity at a 15 minute time interval over the 2003 to 2015 period. These stations were also equipped with cumulative sediment traps which allowed to analyze the grain size and mineralogical content of the suspended sediment load. Furthermore, an innovative setup for the monitoring of sedimentary processes allowed to gather systematic observations of the sediment deposits and their evolution at one location in the cave stream. The locations of these stations are shown in Fig. 1.3. Additionally, more data on the suspended load composition was collected at the Milandre springs through PSD and *E.coli* content analyzes within the present work. Another goal of this thesis is thus to examine these observations and compare them with the model predictions and with other environmental variables in order to characterize the sedimentary dynamics in the Milandre system.

1.4 Study site

The Milandre catchment is located in the Table Jura, in the northwestern part of the Jura Mountains. The system discharges to the perennial Saivu spring (20 – 200 $L{\cdot}s^{-1}$, 373 m.a.s.l) and to the overflow Bâme spring (0 – ∼3 $m^3{\cdot}s^{-1}$, 375 m.a.s.l.), which are located on the left bank of the valley of the Allaine river (Fig. 1.3). The karst system is fed by a recharge area of 13.3 km^2 (Favre, 2001) which consists in a dry limestone plateau at an altitude of ∼550 m.a.s.l. This area is occupied by forests, pastures and cultivated lands. The recharge is purely autogenic and diffuse. The mean annual precipitation is 1070 mm and the mean annual effective precipitation (precipitation minus evapotranspiration) is 520 mm, as measured by the MeteoSwiss weather station at Fahy, located 2.5 km away from the southern catchment boundary. An overview of the hydrogeological settings of the area is provided by Kovács and Jeannin (2003). The aquifer is hosted by Upper Jurassic limestone and is underlain by the Oxfordian marls, which act as a regional aquiclude. As the active conduits lie almost directly above this impervious formation, there is no deep phreatic zone and the system is qualified as a shallow karst system (Perrin, 2003). The Upper Jurassic limestone series contains three marl levels which do not seem to act as hydraulic barriers at the regional scale. In terms of structure, the geological formations are slightly folded and are affected by normal faults of NS, NW-SE and NE-SW orientation. The first orientation is associated with the Rhine Graben formation, while the latter are caused by the Jura folding (Kovács and Jeannin, 2003).

The downstream part of the catchment contains a 12 km speleological network, the Milandre cave. The Bâme spring flows out of a ∼100 m cave which lies some 20 meter below the Milandre cave historical entrance, but no speleological junction is know between these two cavities. The upstream end of the Milandre cave is accessible by an artificial shaft. The speleological network develops sub-horizontally and hosts a perennial cave stream, the Milandrine, which is the main drainage axis of the catchment. The stream is lost into a sump around ∼500 m upstream from the Saivu spring. Upstream from this sump, the cave stream can be followed for 4 kilometers. Two important underground tributaries feed the Milandrine and each of them contributes to 25 to 30% to the cumulative discharge of the Saivu and Bâme springs (Grasso and Jeannin, 1994). According to Favre (2001), the *Droite* tributary drains an area of 3.8 km^2 and the *Bure* tributary, an area of 3.7 km^2. The catchment area feeding the Milandrine upstream from the cave is estimated at 4.6 km^2. Tributaries of smaller importance are also found along the Milandrine, contributing to 10% of the Saivu and Bâme spring discharge

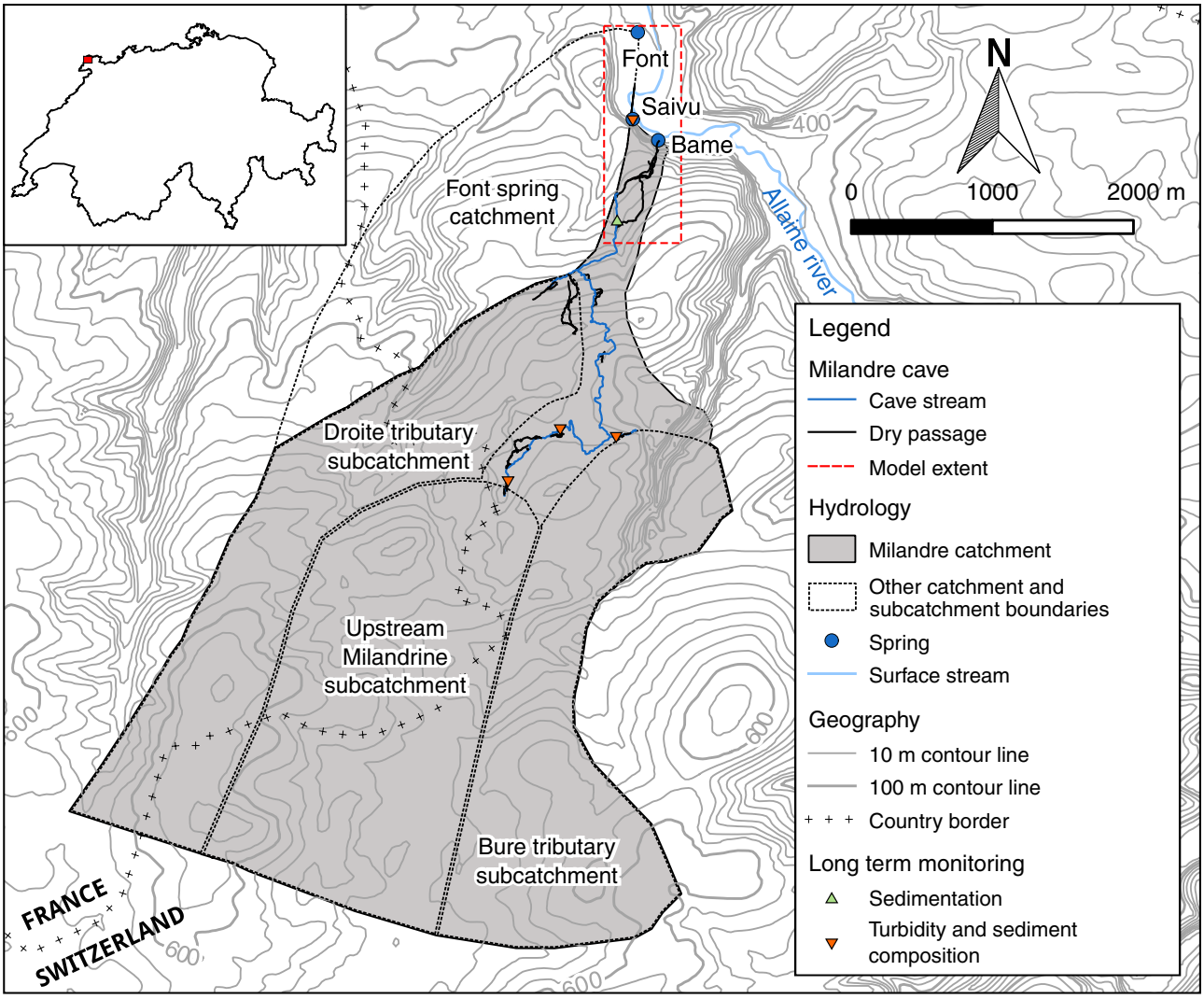

Figure 1.3: Catchment area of the Milandre karst system. Catchment boundaries are from Favre (2001), cave survey from Gigon and Wenger (1986) and background data from the Swiss Federal Office of Topography.

(Grasso and Jeannin, 1994). The extent of the Milandre catchment and the second order catchments (*subcatchments*) are depicted in Fig. 1.3. Grasso and Jeannin (1994) mention the existence of a flow loss of 10 to 15 $L \cdot s^{-1}$ of the Milandrine towards the Font spring. The Font spring is also fed by a catchment area of its own, which is shown in Fig. 1.3.

Perrin (2003) provided a detailed study of the hydrogeological functioning of the Milandre system. He showed that the soil and the epikarst act as a reservoir which collects recharge water and continuously releases it toward the deeper parts of the aquifer. During moderate to extreme storm events (effective precipitation greater than 15 to 20 mm), recharge water may directly reach the phreatic zone. He also found a marked spatial heterogeneity in the water chemistry of the tributaries feeding the cave stream. This heterogeneity is linked with the land use of the recharge areas of the different tributaries. For instance, agriculture was shown to have a significant impact on groundwater quality. These effects are both direct, through fertilizer spreading, and indirect, by enhancing limestone dissolution because of relatively high CO_2 pressure in cultivated soils, thus increasing dissolution related ion concentrations in groundwater. Conversely, forested areas yield water with generally lower ion concentrations. These contributions are mixed in the phreatic zone and the Saivu spring chemistry is the result of this mixing. Perrin (2003) further showed that during moderate flood events, the chemograph variations at the spring can be explained thoroughly by the mixing of underground tributaries, because, while their respective chemistry is constant, their relative contribution to the total discharge changes temporally.

The hydraulic model developed in this thesis focuses on the downstream part of the Milandre catchment. It includes the downstream part of the Mi-

Figure 1.4: Sediment accumulation on the banks of the cave stream (Photo: P.-Y. Jeannin).

landrine, the phreatic zone between the cave and the three outlets of the catchment (Saivu, Bâme and Font springs) and the associated epiphreatic passages, i.e. conduits that may get flooded during storm events. This area is delimited by the red dashed line in Fig. 1.3. The downstream part of the Milandre cave is of particular interest in terms of sedimentary processes. Indeed, in this area, piles of clastic sediments are found on the banks of the cave stream. An example is shown in Fig. 1.4. Moreover, epiphreatic passages are partly filled with clastic sediment. There is also anecdotal evidence for a net accumulation of sediment at some locations (Hessenauer et al., 2004).

On the basis of mineralogical analysis, Rodriguez (1996) and Schmassmann (2006) showed that these cave deposits are mainly the product of surface soil erosion, and, to a lesser extent, of limestone dissolution. This material is likely deposited at high stage by storm water. Rodriguez (1996) also studied the turbidity variations at the Saivu spring. He suggested that, for flood events of peak discharge lower than $\sim$700 L$\cdot$s^{-1}, there is a linear relationship between the peak turbidity value and the peak discharge value, because turbidity is mainly produced by sediment remobilization in the conduits. For more intense flood events, a sudden increase in turbidity is often observed, which he attributed to the arrival of surface derived turbidity.

1.5 Structure of the thesis

The first step of this work is the building of a pipe flow model of the downstream part of the Milandre system, which is described in Chap. 2. This hydraulic model is developed on the basis of the cave survey and calibrated using hydraulic head monitoring, salt dilution gauging and tracer tests that were carried out in the speleological network. It aims at reproducing the physics of the system in terms of flow rates, flow velocities and hydraulic heads.

The resulting flow simulations are used in Chap. 3 to estimate the mean boundary shear stress and shear velocity in the conduits, which are key parameters controlling sediment erosion and deposition. The model predictions are compared to the observations gathered by the sedimentation monitoring station. Furthermore, the model is used to infer on the overall dynamics of the sediment fluxes over a $\sim$10 year period.

In Chap. 4, the evolution of the turbidity, PSD and *E.coli* content at the system's perennial spring throughout a flood event is described. This data is used to identify the breakthrough of autochthonous and allochthonous turbidity. Results are compared with the hydraulic model simulation. Further investigations on turbidity variations at the event scale are also realized by analyzing the long term time series of turbidity in the cave stream and at the spring.

Chap. 5 presents the results of the grain size and mineralogical content analysis of the sediment trap cumulative samples. Relationships between sediment fluxes and and environmental variables as well as their evolution on a pluriannual time scale are analyzed.

Finally, the conclusions of this thesis are presented in Chap. 6.

Chapter 2

Hydraulic modeling

2.1 Introduction

Because of its strong heterogeneity and anisotropy, it is challenging to model flow in karst aquifers. Most of the flow occurs in high conductivity solution channels, the location, dimensions and topology of which are rarely directly observable. Worthington (2003) estimated for four different carbonate aquifers that 94% to 99.7% of the groundwater flow is conduit flow. Several studies showed the necessity of integrating high conductivity channels into distributed groundwater flow models in order to reproduce both the observed hydraulic heads and the spring discharges (Kiraly, 1995; Kovács and Jeannin, 2003; Worthington, 2009). However, these models consider the conduits to be a high conductivity equivalent porous media where flow is laminar and governed by Darcy's law. As flow in karst conduits is often turbulent (White, 1969), they fail to reproduce the observed flow velocities. Accurate flow velocity simulation is of primary importance when addressing transport and vulnerability issues, as well as sedimentary processes. Moreover, the existence of variably saturated epiphreatic conduits implies a strongly non-linear response of karst aquifer to recharge events. Variably saturated pipe flow models can accurately reproduce this behaviour (Jeannin, 2001).

This chapter describes the building and the calibration of a hydraulic flow model for the downstream part of the Milandre karst system. The use of a turbulent pipe flow model seems the most suitable to this site, as in this part of the system, the entire flow is conveyed by the conduits and is in the turbulent regime (Jeannin and Maréchal, 1995). Furthermore, as the main karstic drain and several epiphreatic conduits are accessible, the geometry of the conduit network can be well characterized. The aim is to obtain a distributed, physically based model, which reproduces the hydraulic behaviour of the system — flow rates, hydraulic heads and transit times — and which can thus be used, thanks to the simulated flow velocities, to assess the sedimentary processes taking place inside the karst system.

2.2 Conceptual model

The downstream part of the Milandre speleological network consists in several superimposed epiphreatic passages which give access to the main karstic drain of the system (Fig. 2.1). At its downstream end, the Milandrine stream reaches a sump which discharges to the Saivu spring (20 – 200 $L{\cdot}s^{-1}$, 373 m.a.s.l, Fig. 2.1a), the perennial outlet of the system. A flow loss of the Milandrine towards the Font spring (369.5 m.a.s.l.) has been identified in previous studies (e.g. Grasso and Jeannin (1994)), but its location was so far unknown. Unexplored phreatic conduits likely exist between the speleological network and the Saivu and Font springs. A first step in the building of the hydraulic model is thus to characterize their geometry and position.

During precipitation events, the epiphreatic passages get flooded and the overflow Bâme spring (0–3 $m^3{\cdot}s^{-1}$, 375 m.a.s.l.) starts discharging (Fig. 2.1b). A great length of epiphreatic passages has been explored, but it is clear from field observations that other inaccessible conduits participate in groundwater flow. The characterization of those conduits constitutes the second step in the development of the model.

Lastly, under extreme hydrological conditions, the hydraulic head may be high enough for the cave entrance (402 m.a.s.l.) to act as a temporary outlet (Fig. 2.1c). Only two relatively recent instances are reported, respectively in 2006 and in 2007.

2.3 Methodology

The hydraulic modeling is achieved using the SWMM5 code from the US EPA. This software has been increasingly used in karst hydrology modeling in the past years (Campbell and Sullivan, 2002; Peterson and Wicks, 2006; Wu et al., 2008; Chen and Goldscheider, 2014; Jeannin et al., 2015; Kaufmann et al., 2016). It is well suited to this purpose, as it simulates turbulent flow in variably saturated pipes. Head losses are computed using the Manning-Strickler formula:

$$Q = \frac{1}{n} R_h^{2/3} \left(\frac{\Delta H}{L} \right)^{1/2} A \tag{2.1}$$

where Q is the conduit discharge ($m^3{\cdot}s^{-1}$), n the Manning roughness coefficient ($s{\cdot}m^{-1/3}$), R_h the hydraulic radius (m), ΔH the head loss (m), L the conduit length (m) and A the flow cross sectional area (m^2).

The dynamic wave flow routing option is selected. This method solves the 1D Saint-Venant equations of continuity (Eq. 2.2) and momentum (Eq. 2.3) (James et al., 2010):

$$\frac{\partial A}{\partial t} + \frac{\partial Q}{\partial x} = 0 \tag{2.2}$$

$$\frac{\partial Q}{\partial t} + \frac{\partial Q^2/A}{\partial x} + gA\frac{\partial H}{\partial x} + gAS + gAh_L = 0 \tag{2.3}$$

where t is time (s), x is the distance along the conduit (m), g is the gravitational acceleration ($m{\cdot}s^{-2}$), H is the hydraulic head in the conduit (m) and h_L the local energy loss per unit length of conduit (-). Eq. 2.2 expresses the conservation of mass. Eq. 2.3 is the equation of the conservation of momentum. The terms are, respectively, the local acceleration term, the convective acceleration term, the pressure force

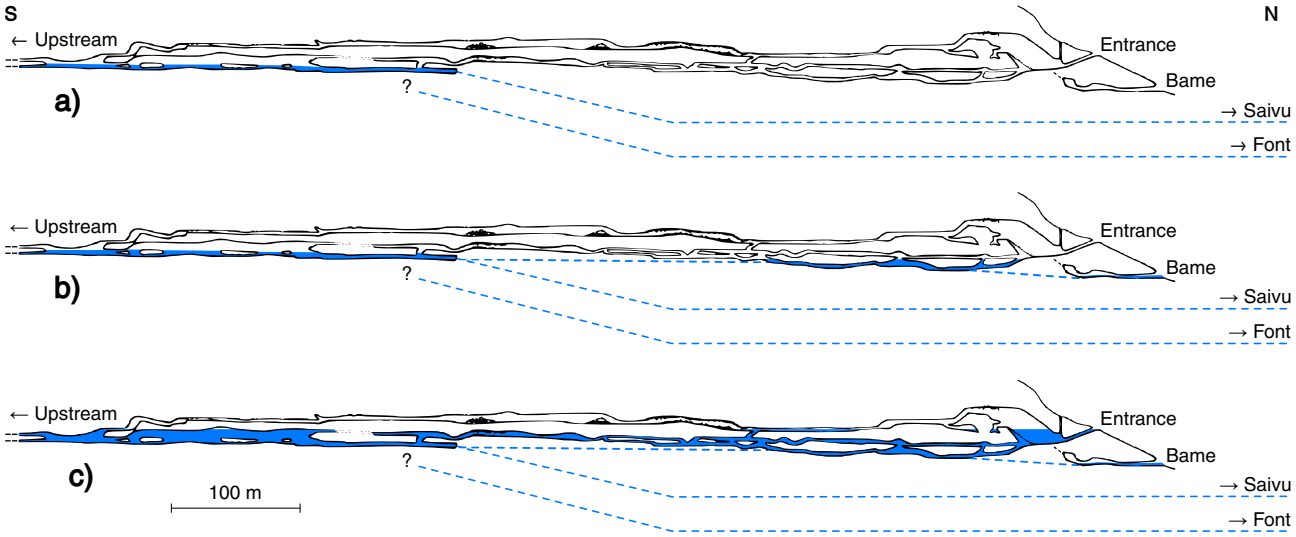

Figure 2.1: Cross sectional, schematized view of groundwater flow in the downstream part of the Milandre speleological network (cave survey modified after Gigon and Wenger (1986)) under low (a), intermediate (b) and extreme (c) hydrological conditions. Dashed blue lines indicate hydraulic connections through unexplored conduits.

term, the friction loss term and the local energy loss term.

The karst network is thus represented as a set of nodes connected by conduits. The network geometry is based on the cave survey of the downstream part of Milandre system, which has been re-surveyed as part of this study. The calibration process consists in gradually adding new conduits and adjusting their geometry from bottom to top, starting from the phreatic zone, in order to reproduce the hydraulic functioning of the system. As the Manning roughness coefficient is coupled with the conduit geometry, a constant n is used throughout the model (Kaufmann et al., 2016). A value of 0.05 s·m$^{-1/3}$ is used, following the observations of Jeannin (2001) in the Hölloch system, and their adaptation to the Manning-Strickler formula by Jeannin et al. (2015). Conduits in the saturated zone are mainly calibrated on the basis of tracer test results (Section 2.3.1). For the calibration of epiphreatic conduits, hydraulic heads and spring discharges have been simultaneously monitored at a 15 minutes time interval during a little over a year in order to define the head–discharge relationships at 10 different locations in the speleological network (Section 2.3.2). Two measuring points are used for the model calibration. One is located in the perennial cave stream and the other, on the epiphreatic flow path discharging to the overflow spring. The performance of the model is then assessed by comparing the simulations with the observed head–discharge relationships at the 8 other points. Flow rates at the different outlets and transit times through the model are also tested against observed data (Section 2.4).

2.3.1 Phreatic zone

Under low to medium flow conditions, the Milandrine stream discharges to the Font and Saivu springs. To gain insight on groundwater flow in the phreatic zone, a series of 7 tracer tests was conducted in 2014–2015. Table 2.1 presents a summary of the set-ups and results of these tracer tests. The tracer recovery curves at the Saivu spring are shown in Fig. 2.2. Fluorescent dyes were injected at different locations in the Milandrine stream and under varying flow conditions — i.e. very low (20 L·s^{-1} discharge at the Saivu spring) to intermediate (84 L·s^{-1}). Tracer concentrations were monitored with a GGUN-FL30 field fluorometer at a 1 to 5 mn time interval at the Saivu spring, and, for experiment a) to f) in Fig. 2.2, by lab analyzes of water samples taken every 30 mn to 1 h during the tracer recovery. Concentrations obtained by lab analysis were used for the calibration of the field fluorometer. For experiment g), the calibration of the field fluorometer was done in the lab. Tracer tests were performed under stable flow conditions and the Saivu spring discharge was estimated in each experiment by salt dilution gauging and continuous stage monitoring. At the Font spring, the tracer concentration was monitored on two instances and the flow rate was estimated using an existing rating curve. Additional information on these tracer experiments can be found in App. I.

In first order, the recovery curves at the Saivu spring of each of the seven tracer tests can be separated into two main peaks, whose relative amplitudes vary with spring discharge (Fig. 2.2). Two conduits between the underground stream and the Saivu spring are thus introduced in the model. A single

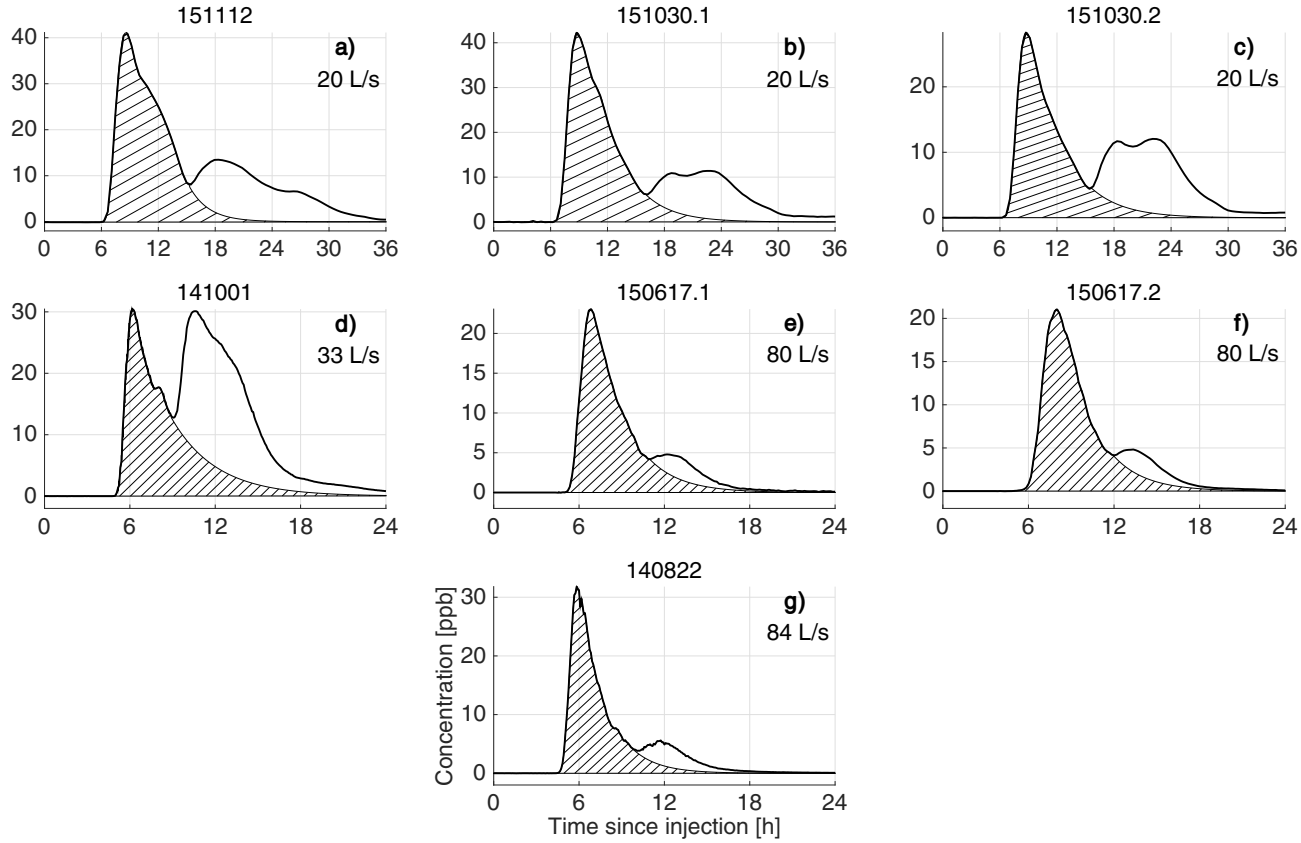

Figure 2.2: Recovery curves at the Saivu spring of fluorescent tracers injected in the downstream part of the Milandrine in 2014 and 2015. Top right of each plot is the discharge of the spring during the tracer recovery. Each plot corresponds to a specific injection. The recovery curves are separated into two peaks by fitting an exponential function to the falling limb of the first peak.

Table 2.1: Summary of the results of the tracer tests.

Test ID	**Distance [m]**	**Discharge [L·s^{-1}]**		**Recovery rate [%]**				**Transit time [h:min]**	
	Saivu	Milandrine	Saivu	Saivu	Bâme	Font	Total	Peak 1	Peak 2
151112	551	*35*	20	85.0	0.0	>0	>85.0	08:40	19:20
151030.1	640	36	20	80.9	0.0	>0	>80.9	08:49	23:04
151030.2	666	36	20	61.0	0.0	>0	>61.0	08:44	22:34
141001	640	60	33	93.9	0.0	n.m.	>93.9	06:12	10:45
150617.1	666	111	80	84.4	1.2	15.6	101.2	06:49	13:09
150617.2	816	111	80	84.3	0.8	14.1	99.2	07:57	13:43
140822	581	110	84	97.3	n.d.	n.m.	97.3	05:50	11:45

Table 2.2: Milandrine flow contribution to the Font spring derived from tracer test recovery rates. Each line represents one tracing experiment. The flow rate of the Milandrine was determined by salt dilution gauging; the flow rate of the Font spring by a rating curve.

Test ID	Flow rate of Milandrine upstream of loss [L·s^{-1}]	Flow rate of Font spring [L·s^{-1}]	Tracer recovery at Font spring	Milandrine contribution to Font spring [L·s^{-1}]
150617.1	110	25	15.6%	17.2
150617.2	110	25	14.1%	15.5

Table 2.3: Milandrine flow contribution to the Font spring derived from salt dilution gauging upstream and downstream from the loss. Each line corresponds to one survey.

Flow rate of Milandrine upstream of loss [L·s^{-1}]	Flow rate of Milandrine downstream of loss [L·s^{-1}]	Milandrine contribution to Font spring [L·s^{-1}]
34.6	22.3	12.4
36.4	27.6	8.8

conduit is considered for the Font spring, as single peak recovery curves were obtained at this spring.

The length of each conduit is approached by multiplying the distance between its start and its end by the mean tortuosity of the Milandre cave system, 1.67, calculated by Maréchal (1994) on the basis of the 12 km survey of the whole Milandre system. The terminal sump of the Milandrine is considered to be the start of the saturated conduit towards the Saivu spring, as tracer injections there yielded high recovery rates under low and intermediate flow conditions: 93.9% and 97.3% for tracer tests d) and g) in Fig. 2.2. Both Saivu conduits thus have equal lengths of approximately $480 \cdot 1.67 \approx 800$ m. To locate the starting point of the conduit flowing towards the Font spring, the injections of the tracers during the tracer test campaign have been made at varying locations in the cave stream. A map of the injection points is shown in App. I and the distance between each injection point and the Saivu spring are listed in Table 2.1. The different recovery rates at the Saivu spring allowed to identify the existence of one main flow loss located at a distance of ∼650 meters from the spring. Its precise location was then confirmed by direct observation in the cave stream and by stream gauging. The resulting estimated conduit length, again obtained by multiplying the distance between the flow loss (1170 m) and the spring by the tortuosity of the cave network, is almost 2 km.

The overall slopes of the conduits are deduced from the head differences between the sumps — known from the cave survey — and the springs. The parameters to calibrate are thus the conduit diameters, and the constraining data are the flow rate, transit time and head loss through each conduit. In addition, conduit volumes are estimated on the basis of tracer tests in order to gain insight on the conduit geometries. The following sections describe how the conduit flow rates, transit times and volumes are determined, as well as the calibration process for the phreatic zone.

Flow rates

The discharge rate lost by the Milandrine stream towards the Font spring was so far never directly measured, as the spring is also fed by its own catchment and the flow loss in the cave stream had not been localized. Grasso and Jeannin (1994) estimated it to 10 to 15 L·s^{-1} under low flow conditions. In this study, the stream losses towards the Font spring were measured by gauging the stream and by conducting several tracing experiments in low and medium flow conditions. During one tracing experiment where two tracers were injected, the flow rate of the cave stream was measured by salt dilution gauging and the flow loss was estimated by multiplying the measured flow rate by the tracer recovery rates at the Font spring. Results are shown in Table 2.2. After the swallow hole had been precisely localized in the stream conduit, two stream gauging surveys were carried out under low flow conditions, and flow rate was measured upstream and downstream from the swallow hole. Results are shown in Table 2.3. The resulting estimations of the flow loss are in line with the values given by Grasso and Jeannin (1994), with ∼9 L·s^{-1} when the Milandrine flow rate is around 35 L·s^{-1} and ∼16 L·s^{-1} when the Milandrine flow rate is 110 L·s^{-1}.

For the Saivu spring, the flow contribution of each conduit is derived from the tracer recovery curves. The separation of the curves into two peaks is achieved by extrapolating an exponential decay fit to the falling limb of the first peak. The flow contribution of each conduit is estimated by the relative tracer recovery rate for each peak, following

$$Q_c = Q_s \cdot \int_{t_0}^{t_{max}} \frac{C_c(t)}{C_s(t)}\,\mathrm{d}t \tag{2.4}$$

where Q_c is the conduit discharge (L·s^{-1}), Q_s the spring discharge (L·s^{-1}) (constant during each tracer test), t_0 and t_{max} the start and end time of recovery (s), t is the time since injection (s), C_c the tracer concentration attributed to the conduit and C_s the total tracer concentration (ppb) as measured by the calibrated field fluorometer.

Results are shown in Fig. 2.3a. It appears that the second peak, the slowest one, always contributes to roughly 10 L·s^{-1} to the Saivu spring discharge. It is interpreted as a lower, always saturated conduit. The first peak is attributed to an upper variably saturated conduit, taking the excess flow from 10 to 70 L·s^{-1}. For larger flow rates, the Bâme overflow spring starts discharging.

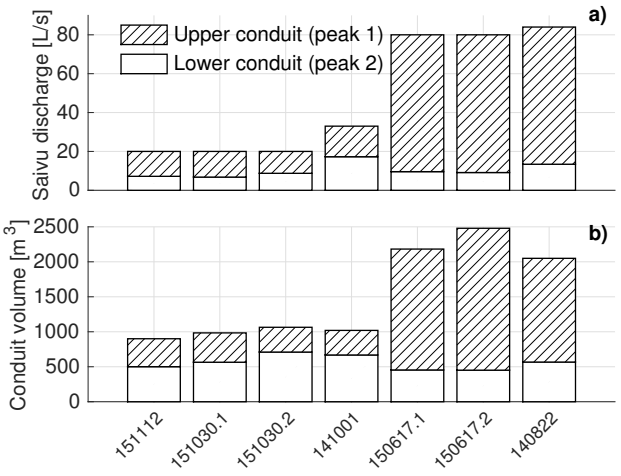

Figure 2.3: a) Flow contribution of each peak of the tracer recovery curves (Fig. 2.2) calculated with Eq. 2.4. Each bar represents a different tracer injection. b) Corresponding volume of each conduit calculated with Eq. 2.5

Transit times

Transit times through the phreatic conduits were estimated using the tracer recovery curves — considering that the arrival time of the tracer concentration peak is equivalent to the mean water transit time. Transit times for each tracer test are listed in Table 2.1. They vary with the system's discharge, and, to a lesser extent, with the distance between the injection and the spring. At the Font spring, under low flow conditions (Milandrine discharge before loss of 36 $L{\cdot}s^{-1}$), the tracer peak time arrives approximately 87 h after the injection. Under medium flow conditions (Milandrine discharge before loss of 110 $L{\cdot}s^{-1}$), the mean transit time is 42 hours. At the Saivu spring, the first peak time ranges from 9 to 6 hours, from low to medium flow conditions. The second one, from 23 to 12 hours.

Volumes

Knowing the transit time and the flow rate for each conduit, its volume, if the conduit is saturated, can be approached by

$$V_c = Q_c \cdot t_{peak} \tag{2.5}$$

where V_c is the conduit volume (m^3), Q_c is the estimated conduit discharge ($m^3{\cdot}s^{-1}$) and t_{peak} (s) the time between the injection and the arrival time of the tracer peak at the spring — approximately, the mean flow transit time through the conduit. The estimated volume for the Font conduit is of ~2500 m^3. Values obtained for the Saivu conduits are given in Fig. 2.3b. The lower conduit (peak 2) has an estimated volume of approximately 560 m^3. For the upper conduit (peak 1), only the values for higher discharges should be taken into account, as for lower discharge the conduit is probably only partially saturated and this would lead to an underestimation of the conduit volume. The obtained value is approximately 1750 m^3.

Table 2.4: Geometries satisfying Eq. 2.8 and 2.7 for a fictitious conduit of total length 600 m, volume 2435 m^3, head loss 15 m and flow rate 83 $L{\cdot}s^{-1}$. Each conduit is made of two segments defined by a length L (m) and a diameter ⌀ (m).

	L_1	L_2	⌀$_1$	⌀$_2$
1.	10	590	0.18	2.29
2.	100	500	0.28	2.49
3.	100	500	5.50	0.38
4.	200	400	3.90	0.37
5.	200	400	0.32	2.78
6.	300	300	3.20	0.35
7.	300	300	0.35	3.20

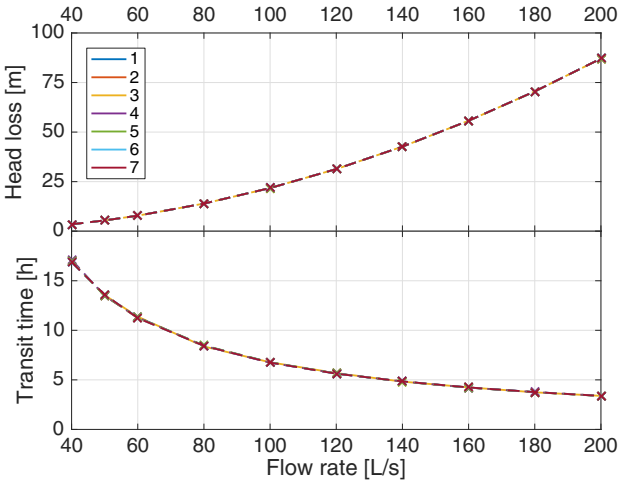

Figure 2.4: Simulated head losses and transit times for various flow rates in the conduits presented in Table 2.4. All conduits are clearly equivalent.

Calibration

In the phreatic zone, the aim is to reproduce both the flow distribution and the transit times for each of the identified flow paths (Font, lower and upper Saivu) by calibrating the conduit diameters. No adequate solution is found using circular conduits of uniform diameter: the simulated flow velocities are much faster than the estimations obtained by tracer testing. Conduits are thus divided in a series of segments of different diameters. By testing a series of segment combinations, two effects appear: (1) the smallest segment diameter of each conduit is the main control on the head loss, i.e. the flow rate taken by this conduit, and (2) the overall volume of each conduit is the main control on the transit time through the conduit (following Eq. 2.5). For a conduit of two segments and of given head loss (ΔH), total length (L_c)

and volume (V_c), the length (L_1, L_2) and cross sectional area (A_1, A_2) can be expressed by the following equation system:

$$L_c = L_1 + L_2 \tag{2.6}$$

$$V_c = L_1 \cdot A_1 + L_2 \cdot A_2 \tag{2.7}$$

$$\Delta H = 2^{4/3} \cdot \pi^{2/3} \cdot n^2 \cdot Q^2 \cdot \left(\frac{L_1}{A_1^{8/3}} + \frac{L_2}{A_2^{8/3}}\right) \tag{2.8}$$

Eq. 2.8 follows the Manning-Strickler formula in a saturated circular pipe (Eq. 2.1). By setting L_1, the other parameters L_2, A_1 and A_2 can be analytically found. An example is shown in Table 2.4 for a fictitious conduit of length 600 m, volume 2435 m^3, head loss 15 m and flow rate 84 $L{\cdot}s^{-1}$. These values are arbitrary but in the range of magnitude of the phreatic conduits of the Milandre system. L_1 is set to 10, 100, 200 and 300 meters. In Table 2.4, the resulting conduits are presented in terms of L_i (length of segment i) and $\oslash_i$ (diameter of segment i). These conduits are then used for flow simulation with SWMM5, for a range of flow rates going from 40 to 200 $L{\cdot}s^{-1}$ as shown in Fig. 2.4. The simulated head losses and transit times through these synthetic conduits are identical. As SWMM5 does not account for punctual head losses caused by changes in cross sectional area, they are also hydraulically equivalent to any conduit which is a combination of segments of diameter $\oslash_1$ totalling a length L_1 and of segments of diameter $\oslash_2$ totalling a length L_2. Furthermore, an infinity of other conduits satisfying the given total length, volume and head loss do exist for other values of L_1 and for a number of segments greater than 2.

As there is no unique solution, for the sake of simplicity, each phreatic conduit (lower Saivu, upper Saivu and Font) in the model is divided in only two segments of same length but of distinct diameters. Volumes are taken from the tracer test results and lengths are obtained by multiplying the straight line distance between the conduit ends with the tortuosity of the Milandre speleological network (1.67 according to Maréchal (1994)). Final conduit geometry for the phreatic zone in terms of L_1, L_2, $\oslash_1$ and $\oslash_2$ for each conduit are presented in Table 2.5. The head losses and transit times simulated by SWMM5 in each conduit under low and medium flow conditions are also shown. The final model geometry is shown in Fig. 2.5.

Table 2.5: Geometry of the phreatic conduits after calibration and comparison between observed and simulated discharges ($L{\cdot}s^{-1}$) and transit times (h:min), observed values are averages of measurements under similar flow conditions) under low (1.) and medium (2.) flow conditions.

			Font	Saivu lower	Saivu upper
	Segment 1	L_1	977	395	395
		$\oslash_1$	1.78	1.45	2.15
	Segment 2	L_2	977	395	395
		$\oslash_2$	0.20	0.20	0.40
1.	Discharge	Sim.	10	10	11
		Obs.	11	8	12
	Transit time	Sim.	70:30	18:55	09:05
		Obs.	87:00	21:40	08:45
2.	Discharge	Sim.	10	13	67
		Obs.	16	11	71
	Transit time	Sim.	67:05	14:40	06:10
		Obs.	42:00	12:50	06:50

2.3.2 Epiphreatic zone

The backbone of the model pipe network in the epiphreatic zone is a survey of the cave which has been conducted as part of this study. The pipe network is discretized according to the survey line-of-sights, which have an average length of 6.7±3.6 m. The cross sections of the resulting conduits are schematically represented as rectangular. Rather than using the dimensions measured at each survey station, an average height and width for each conduit are read from the hand drawn cave survey. This is to prevent a sampling bias which may arise from the fact that cave surveyors tend to avoid tight passages when they select a station location. The resulting pipe network is shown through a map and a cross sectional view in Fig. 2.5. The conduits built from the survey are shown in white.

The model calibration is based on the relationships between hydraulic head measured in the speleological network and the corresponding discharge at the outlets. The process consists in adding new conduits were necessary and adjusting their cross sectional shape and area and the elevation of their end nodes. Conduits are first assumed to have a circular cross section. If no adequate diameter is found in order to fit the observed head–discharge relationships, a rectangular cross section is used and its width and depth are calibrated. The present section describes this calibration process in more details.

Head and discharge monitoring took place during parts of the years 2014, 2015 and 2016. The resulting time series are shown in Fig. 2.6. Heads were monitored at 10 locations by Reefnet Sensus Ultra pressure probes (resolution: 1.27 cm, accuracy: 30.5 cm) at a 15 minute time interval. The probe positions were determined during the cave survey and are shown in Fig. 2.5. The estimated error on the

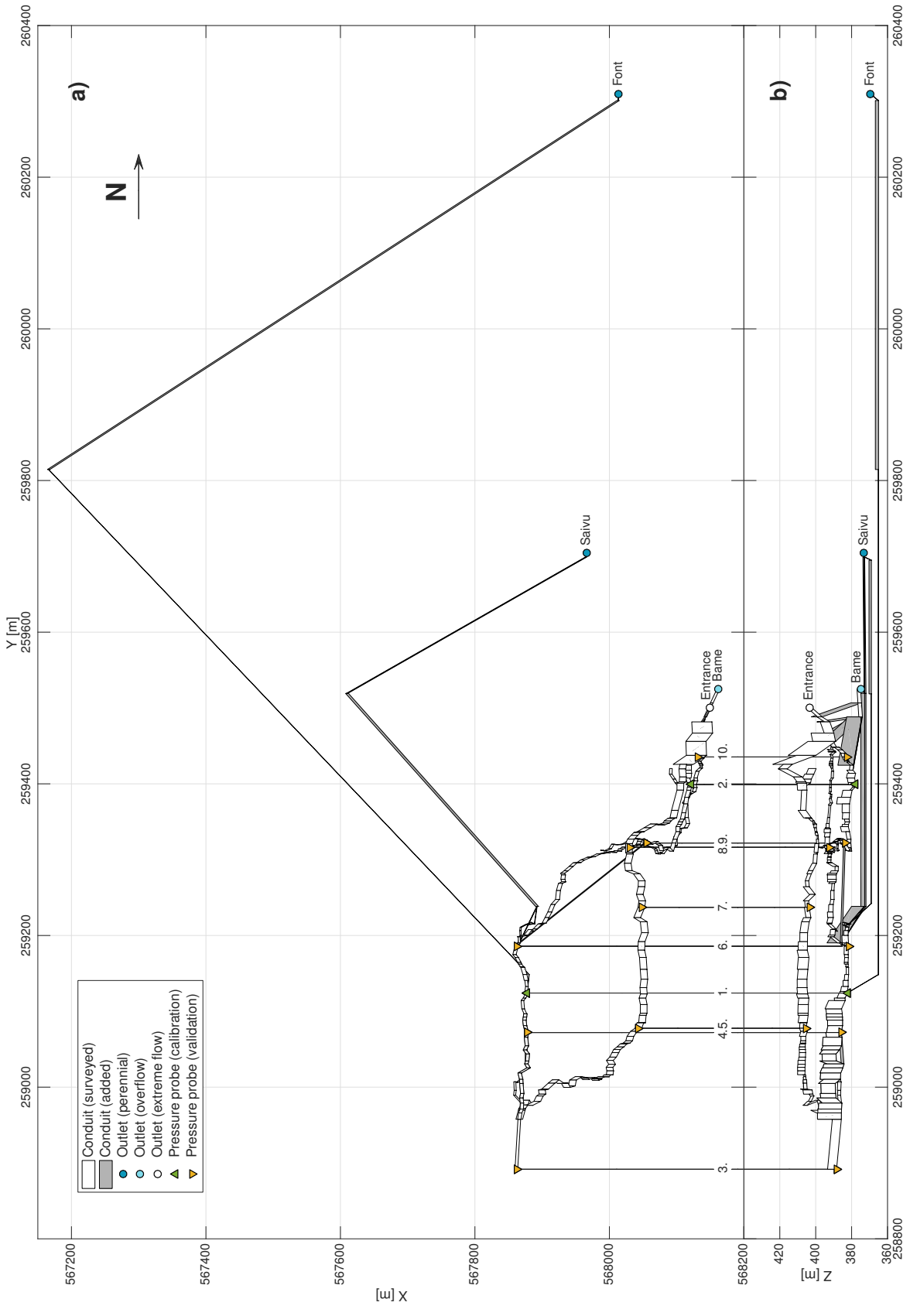

Figure 2.5: a) Map and b) cross-sectional view (vertical exaggeration of 2.5) of the pipe network of the hydraulic model. X and Y are easting and northing in the Swiss coordinates system (CH1903) [m]. Z is the elevation above sea level [m]. White filled rectangles are conduits that were introduced on the basis of the cave survey and the gray filled ones are the ones that were added in the calibration process. Circles are the outlets of the system and the triangles are the pressure probes. Probes 1. and 2. were used for the model calibration and probes 3.-10. for the model assessment.

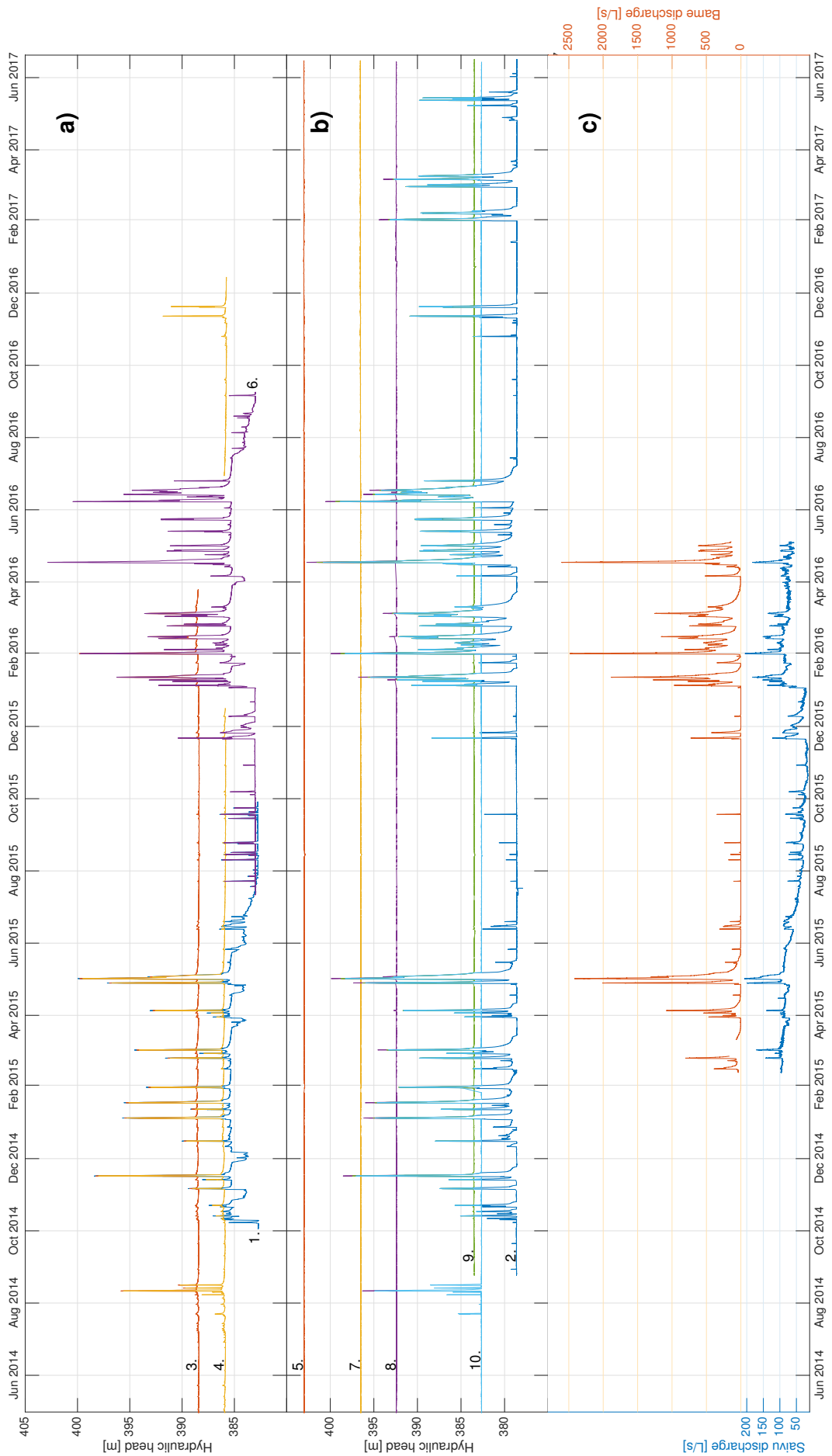

Figure 2.6: Hydraulic head time series (15 minute time interval) in the perennial stream (a), in the epiphreatic passages flowing toward the Bâme spring (b) and flow rate time series (5 minute time interval) at the Saivu and Bâme spring (c). Continuous lines in the hydraulic head curves indicate the probe elevation.

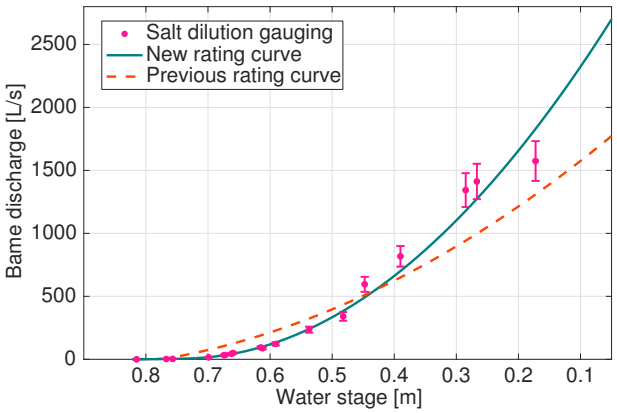

Figure 2.7: Bâme spring rating curves. The dashed curve is the previous rating curve and the continuous one is obtained by fitting a curve to measurements realized within this study (dots) by salt dilution gauging with an estimated uncertainty of 10% (vertical bars). The water stage is the value read on the staff gauge at the spring.

vertical position of the probes is ∼0.5 m for the ones that are the farthest from the entrance, according to the closure of the survey loops. Barometric compensation is done with the atmospheric pressure record of a Cave-Link monitoring station located in the upstream part of the cave (data from the A16 highway environmental impact study). Since this device has a better accuracy, this data was used to reduce the systematic error of the Reefnet probes. Assuming a constant atmospheric pressure in the speleological network, the pressure recorded by the Reefnet probes during no flow periods are shifted to fit the Cave-Link station data. Discharge data at the Saivu and Bâme springs are obtained from stage monitoring (Solinst Levelogger and Barologger Edge Model 3001, overall accuracy of 6 mm) at a 5 minute time interval, converted to flow rates using rating curves. Rating curves had been previously established in the 1990s and 2000s for both springs and were assessed within this study by a series of flow rate measurements by salt dilution gauging. For the Saivu spring, which is equipped with a weir, the existing rating curve was used as no discrepancy was observed when comparing it with the recent measurements. In contrast, a new rating curve was established at the Bâme spring as a poor fit was obtained between the old and the recent measurements (Fig. 2.7). This change might arise from an evolution of the stream bed.

Hydraulic head and discharge increase considerably in reaction to recharge events (Fig. 2.6). The most intense event was recorded in April 2016. The total discharge peaked at 2.8 m^3. Hydraulic head reached 402.8 m in the perennial stream (probe 6.) and 400.8 m at the probe closest to the cave entrance (probe 10.). The rise in water level is rather quick and simultaneous throughout the different measuring points. An example is shown in Fig. 2.8 for an event in January 2016. Hydraulic head increased by twenty meters in twelve hours (probe 2.). There is a slight delay of one to three hours between the reaction in the perennial stream and in the epiphreatic conduits (continuous vs dashed lines in Fig. 2.8). A small hydraulic gradient seems to exist during the event maximum: for instance, for the January 2016 event, the upstream probes 3. and 6. recorded hydraulic heads 1 meter higher than the downstream probes 9., 2. and 10.

Probes 1. and 2. were used for the model calibration (Fig. 2.5). To try to reproduce the hydraulic functioning of the karst system, the calibration is achieved with regard to the observed head–discharge relationships. Probe 1. is located in the perennial stream and probe 2. in an epiphreatic passage discharging towards the Bâme spring. Thus, head at probe 1. is plotted against the simultaneous discharge at the Saivu spring (Fig. 2.9a), and head at probe 2. against the discharge at the Bâme spring (Fig. 2.9b). The calibration of the model is realized at steady state. While this is true at low flow, high flow conditions, in contrast, are met during transient flood events. This is probably the cause of the dispersion observed in the head–discharge relationship at probe 1. (Fig. 2.9a), as this probe is located further upstream than probe 2. (Fig. 2.9b). Part of the dispersion in the head–discharge relationship is explained by hysteresis loops occurring at the event scale (Fig. 2.9c-2.9f). The variability seems to be especially high for the rising limb of the hysteresis loop, which may take slightly different paths for different events, showing the influence of the system initial hydrological conditions. On the other hand,

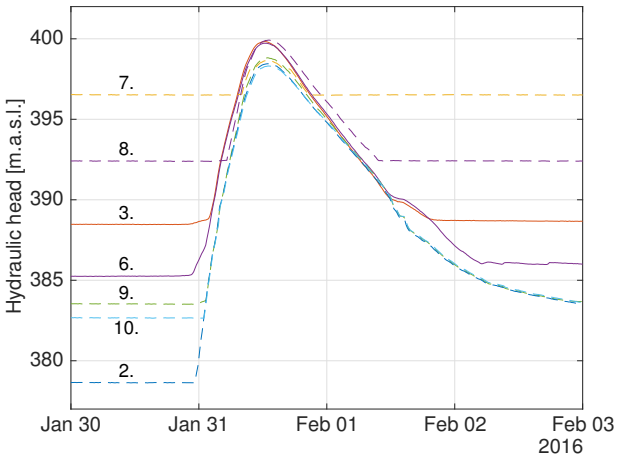

Figure 2.8: Hydraulic head variations during a flood event in early 2016. Continuous lines are probes in the perennial stream and dashed ones are in epiphreatic passages.

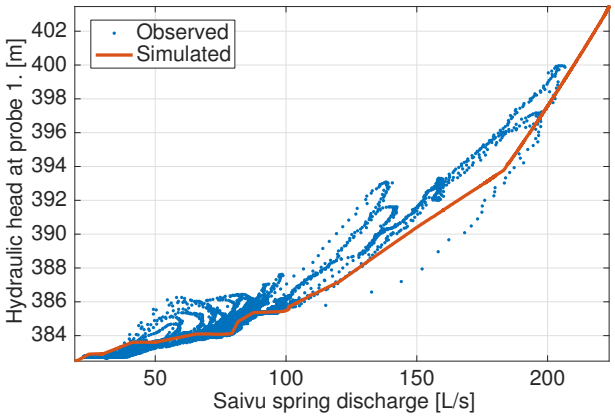

(a) Measured hydraulic head at pressure probe 1. (Fig. 2.5) compared with the measured discharge at the Saivu spring (dots). The continuous line are the simulated values after model calibration.

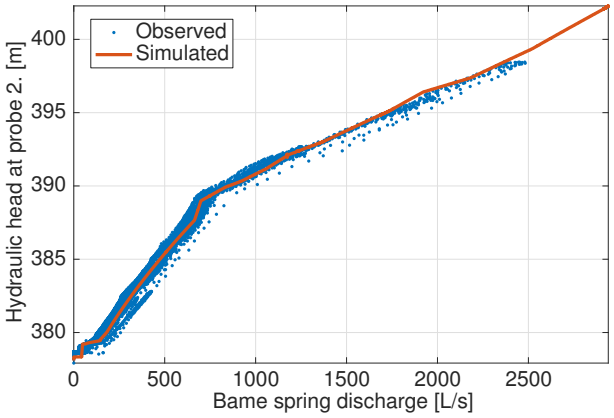

(b) Measured hydraulic head at pressure probe 2. (Fig. 2.5) compared with the measured discharge at the Bâme spring (dots). The continuous line are the simulated values after model calibration.

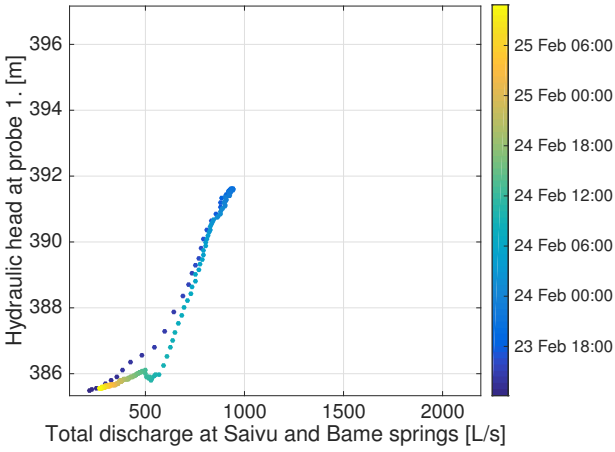

(c) Storm event in February 2015

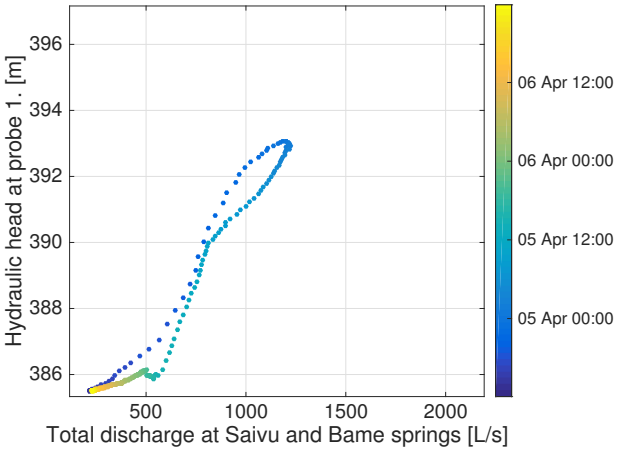

(d) Storm event in April 2015 (1)

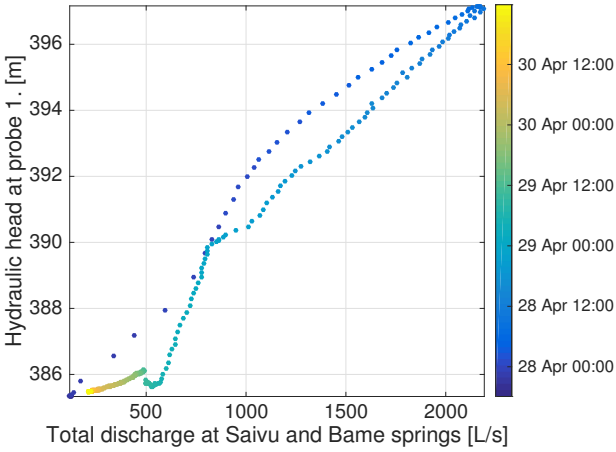

(e) Storm event in April 2015 (2)

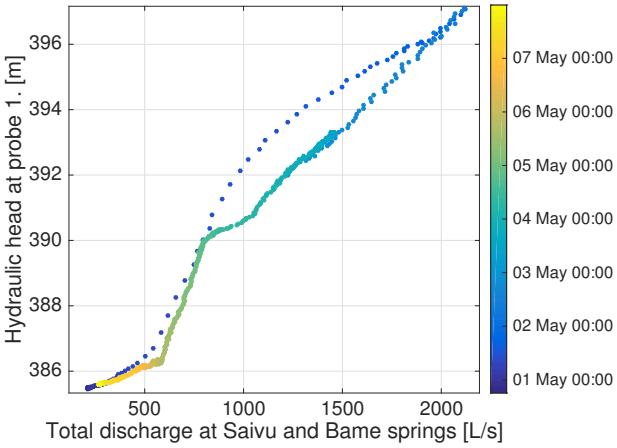

(f) Storm event in May 2015

Figure 2.9: Head–discharge relationships at pressure probe 1. and 2. Measurement time interval is 15 minutes. Plots c-f: zoom on selected storm events in 2015 at probe 1. Dot colors indicate the measurement time.

the head–discharge relationship for the falling limb appears to be more consistent between events, thus carrying more information on the system geometry. This is also confirmed by the greater density of data points during the falling limb of the loop (the time interval being constant), indicating that the system is closer to steady state conditions during recession than at rising water. For these reasons, the model is calibrated according to the recession data points.

The hydraulic head recorded by probe 1. in the perennial underground stream shows two threshold values with respect to the Saivu spring discharge (Fig. 2.6a and 2.9a). The first one, at around 384 m, is likely due to an overflow conduit located above the terminal sump and explored for a few meters during the cave re-surveying. The passage ended on a seemingly perched sump every time it has been visited. A conduit is thus added between the end of this passage and the start of the Saivu phreatic conduits in order to reproduce the hydraulic threshold. The second threshold, at around 385.5 m, is linked to the overflow conduit activating the Bâme spring (Fig. 2.6). Another pipe is thus added, connecting the main flow passage with the passage flowing towards the Bâme spring, at one point were a water inlet was observed under medium flow conditions (Fig. 2.5).

At probe 2., located a few meters upstream from the temporary sump flowing toward the Bâme spring, the main features are the linear relationship between hydraulic head and the Bâme spring discharge, and a smaller slope for heads greater than 389 m (Fig. 2.9b). The latter is caused by the flooding of the chamber located near the cave entrance, whose floor is located at around 389 m.a.s.l. (Fig. 2.5b). This part of the network is close to the Bâme spring cave, both being superimposed at some point (Fig. 2.5), but no junction passage is known between them. Their hydraulic connection is made through a massive boulder deposit which is found both on the floor of the entrance chamber and at the end of the Bâme spring cave. The steady increase of head with discharge in this part of the system is likely caused by the gradual flooding of the boulder deposit. To simulate flow in this medium, a series of vertical fissures was added between the two caves (Fig. 2.5). This proved successful in reproducing the linear head–discharge relationship.

After calibration, a good fit between the observed and simulated head–discharge relationships is reached, as shown in Fig. 2.9a and 2.9b. The final model is shown in Fig. 2.5. The unexplored conduits which were added during the calibration process are shown in gray. In total, the model consists in 306 nodes connected by 325 conduits. The software version used is 5.0.019 and the operating system is Ubuntu 12.04.5 LTS. The program code has been edited to output text files with the simulated flow rates, hydraulic heads and flow velocities. The computer used has an Intel® Core™ i3-2120 CPU with 3.30 GHz clock cycle and 4 GB of RAM. The routing time step used during calibration was 1 second. For a simulation of 24 hours, the computational time was 4 minutes.

2.4 Model assessment

2.4.1 Flow rates

An overview of the simulated flow rates, transit times and hydraulic head along the main flow paths and under varying flow conditions is depicted in Fig. 2.10. A first assessment of the model is performed by comparing the simulated and observed flow rates at the different outlets under varying flow conditions: the perennial Saivu spring, the Bâme overflow spring and the cave entrance, which can act as an overflow outlet during extreme hydrological events. Results are shown in Table 2.6. The evolution of the water distribution between the outlets under increasing flow conditions is well reproduced by the model: up to $\sim$100 L·s^{-1} in the Milandrine stream, the main outlet is the Saivu spring and the Bâme spring is dry. For higher flow rates in the Milandrine, the Saivu spring has a flow rate plateau at around 100 L·s^{-1} and the Bâme spring discharges the excess flow. The cave en-

Table 2.6: Observed and simulated (steady state) discharges in L·s^{-1} in the Milandrine stream (upstream from Font loss) and at the system outlets under varying flow conditions after model calibration. Lines 1. and 2. are salt dilution gauging measurements, each one realized within the same day. Line 3. are the average values of 3 different surveys under similar flow conditions. Lines 4. and 5. (italicized values) are estimates based on stage monitoring and extrapolation of the spring rating curves (discharge peak for one specific event. This data is from the A16 highway environmental impact study).

		Mil.	Saivu	Bâme	Entrance
1.	Observed	31	20	0	0
	Simulated	30	20	0	0
2.	Observed	85	64	0	0
	Simulated	85	74	0	0
3.	Observed	136	98	16	0
	Simulated	136	93	30	0
4.	Observed	196	89	101	0
	Simulated	196	100	84	0
5.	Observed	n.d.	*134*	*1962*	>0
	Simulated	2173	197	1956	0
6.	Observed	n.d.	*215*	*3000*	>0
	Simulated	3649	224	2939	471

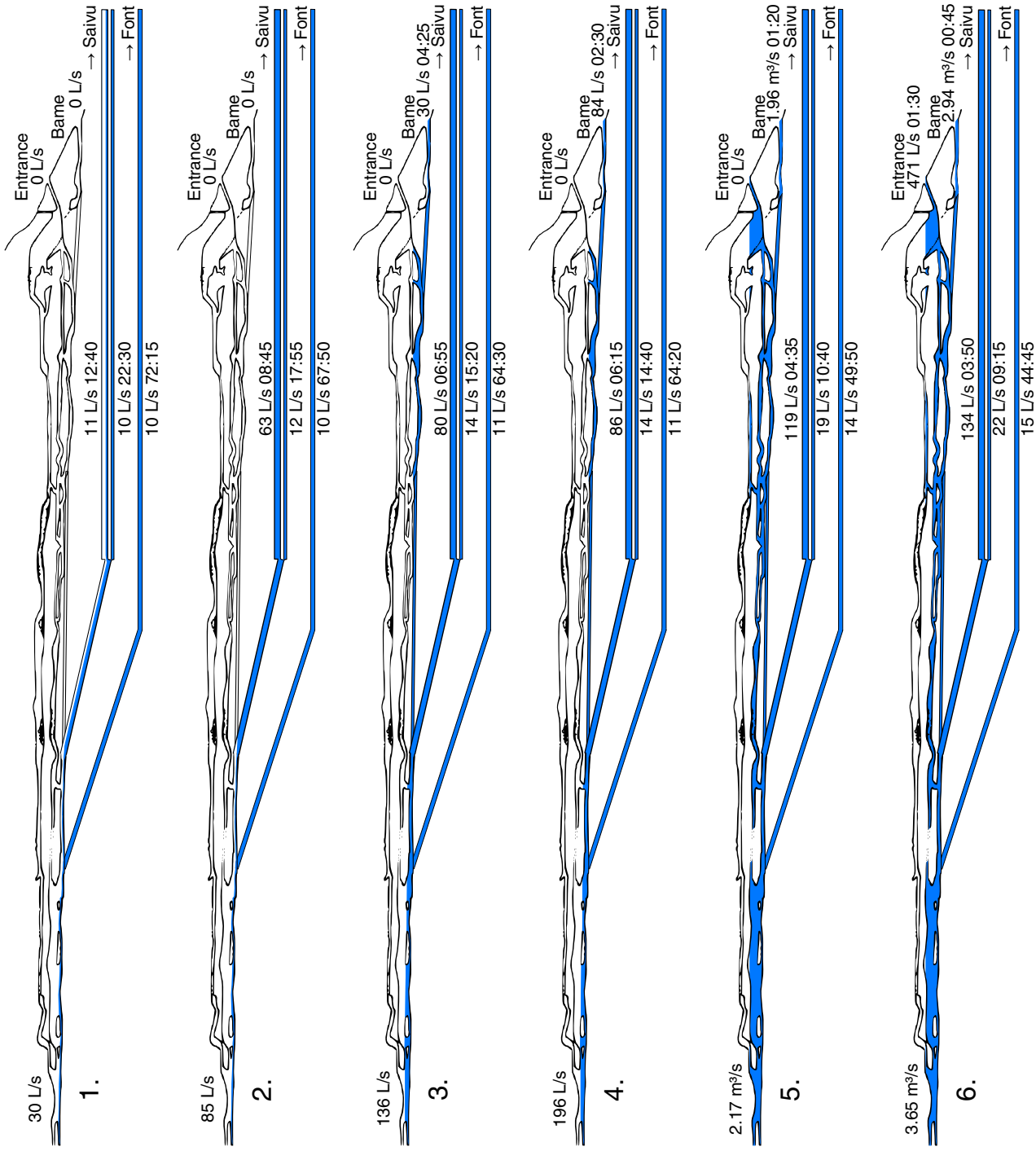

Figure 2.10: Cross sectional schematized view of flow simulations under varying hydrological conditions

trance flows when the Bâme discharge reaches values between 2 to 3 $m^3 \cdot s^{-1}$.

2.4.2 Hydraulic heads

A further evaluation of the model is made by comparing the simulated and observed head–discharge relationships measured by pressure probes at different locations in the speleological network (Fig. 2.5 and 2.6). Pressure probes 3., 4. and 6. are located in the perennial stream, thus the recorded hydraulic heads are plotted against flow rate at the perennial Saivu spring. Pressure probes 5., 7.-10. are set in epiphreatic passages flowing towards the Bâme spring, and their records are compared with the overflow spring discharge. Head–discharge relationships are shown in Fig. 2.11.

In the perennial stream (probes 3., 4., 6.), a lot of scatter is observed in the measured head–discharge relationships compared to the epiphreatic passages (probes 5., 7.-10.). At probes 3., 4. and 6., simulated values are mostly within the range of variability of the observations, although hydraulic heads are sometimes underestimated, and are generally in the lower range of the observed values. The scatter in the observation data is probably caused by the greater distance from the measuring points to the spring in the perennial stream than in the epiphreatic passages, which implies greater effects from transient processes in the head–discharge relationships, as seen at probe 1. (Fig. 2.9a). For instance, probe 3., which is ∼300 m upstream from probe 6., has a greater variability than probe 6. Probe 4. cannot be compared in this respect as this probe did not record during spring 2016, when most of the flood events occurred. At probe 3., the spring flow rate at which the head starts to increase varies from 100 to 130 $L \cdot s^{-1}$. The former corresponds to flood events in spring 2016, and the latter to events in spring 2015. The model is calibrated with respect to the 2015 events (Fig. 2.9a). Spring 2015 has been much drier than spring 2016 (Fig. 2.6), so for each of these flood events, some of the inflow first contributes to the flooding of voids before contributing to the spring discharge. In contrast, during spring 2016, the hydraulic head in the stream rarely dropped below 385.5 meters, the threshold level at which the overflow spring is active. It means that the bulk of the conduit volume participating in the overflow was already flooded, thus the head increase in the stream is initiated rather quickly at the event scale. In this sense, the model results are consistent with the data, as the calibration was made for 2015 events recorded by probe 1. However, it is not clear why the head–discharge relationships between the two years differ also during the falling limb of flood events.

In the epiphreatic passages, the simulated values are well in line with the records provided by probes 9. and 10., located in the lowermost explored epiphreatic passage. In the uppermost passage, probe 5. was never flooded, as predicted by the model. Probe 7., on the other hand, was reached by the water table on 5 different occasions, while it was never flooded in the simulation. This suggests the existence of an unexplored conduit linking this passage to a lower one. Probe 8., located in an intermediate epiphreatic passage, has been flooded several times during the monitored period. The head–discharge relationship obtained with the model, with a marked plateau at 393 m.a.s.l., is a bit different than the observed one. This plateau is caused by the flooding of this intermediate epiphreatic passage, which has a bottom elevation of 392-393 m.a.s.l. It is also present, but on a much shorter range of discharge rates, in the observed data. Hydraulic heads at larger flow rates are generally a bit overestimated. This shift could arise from an instrumental systematic error, as this probe recorded heads 1 m higher than the other ones located in the epiphreatic passages (Fig. 2.8). Overall, the hydraulic heads in the epiphreatic zone are well reproduced in the lowermost passage, a bit underestimated in the intermediate passage, and partly reproduced in the uppermost one. However, since the outlet flow rates are rather well reproduced, the passage does not seem to be a major contributor to the overall system flow. It rather acts as an overflow reservoir.

In summary, the hydraulic heads computed by the model are within the range of the observed data for 6 out of 8 observation points which were not used for the model calibration. The largest discrepancy between the model and the data is observed in the uppermost epiphreatic passage, which gets flooded only during major flood event and does not seem to be an important flow path. The performance of the model is thus quite good, although probably more insight into the hydraulic functioning of the model could be gained by trying to reproduce the hysteresis loops observed in the head–discharge relationships with a transient simulation. This is however beyond the scope of this chapter.

2.4.3 Transit times

With regards to flow velocities and transit times in the epiphreatic zone, few data are available. For logistical reasons, tracer tests in this study were performed under low to intermediate flow conditions. There is however one tracer test reported in the literature (Hessenauer et al., 2005) in October 2002 for which the injection took place in the downstream part of the Milandrine during the initial stage of a moderate flood event. Discharge rates went from 66 $L \cdot s^{-1}$ at the Saivu spring and 0 at the Bâme spring to 102 and

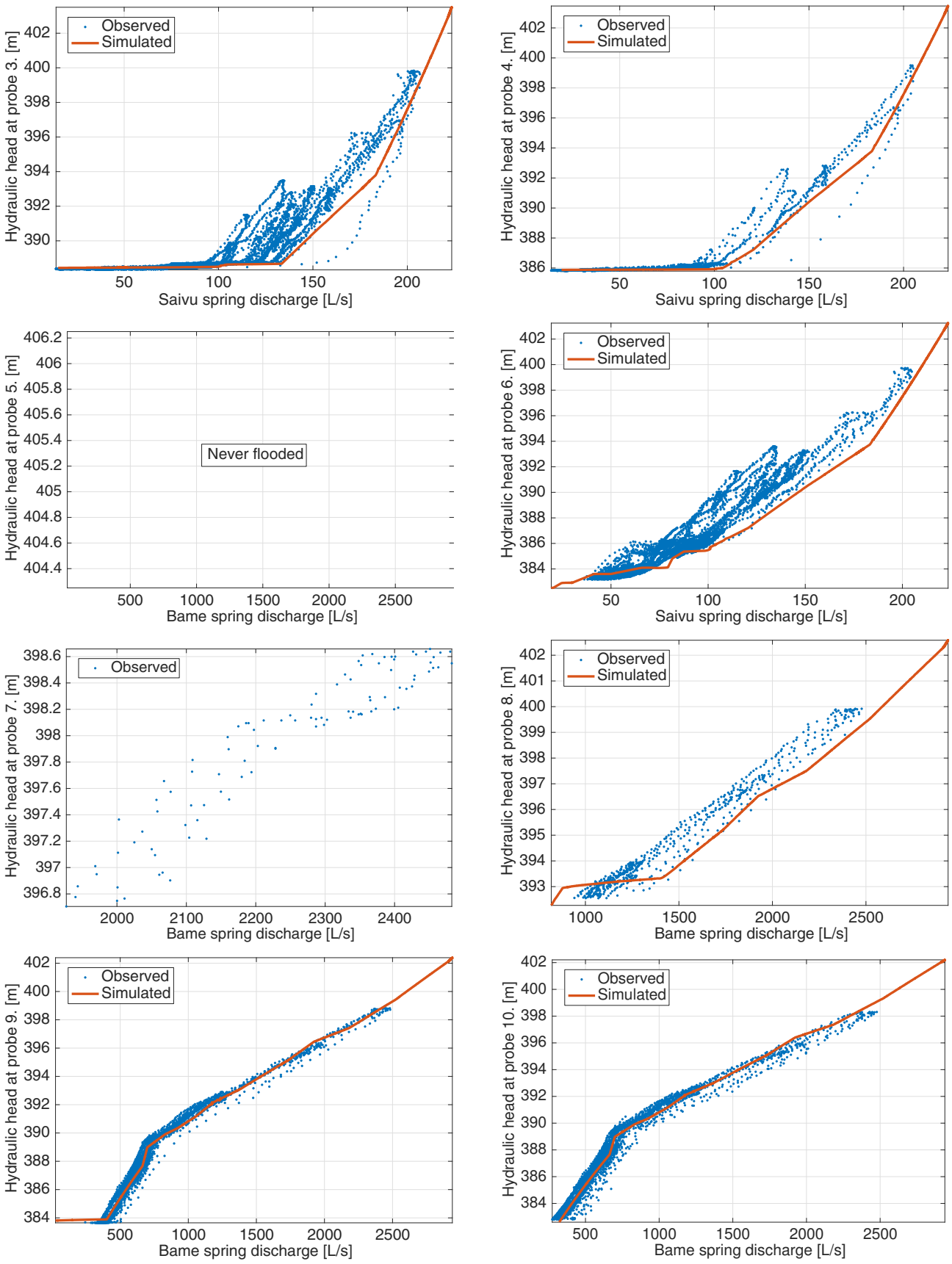

Figure 2.11: Model validation: Observed and simulated head–discharge relationships. Probes 3., 4. and 6. are located in the perennial stream, probes 5. and 7. in the uppermost epiphreatic passages and probes 8., 9. 10. on the flow path towards the Bâme spring (see map on Fig. 2.5).

345 L·s^{-1}, respectively, in less than 24 hours. Injection took place just as discharge rates were starting to increase at the gauging station at the upstream end of the cave stream and at the Saivu spring. The injection point corresponds to the second most upstream node of the model (Fig. 2.5). To compare the observed tracer transit times, the tracer concentration peak time at the Saivu and Bâme springs are considered. For each spring, the simulated transit time is computed from the simulated conduit flow velocities for a constant inflow equal to the mean system's discharge during the time between the injection and the peak in tracer concentration at the spring. This corresponds to 337 L·s^{-1} for the Saivu spring and 268 for the Bâme spring. Results are shown in Tab. 2.7. The tracer concentration peaked at the Bâme spring first, 4 hours and 10 minutes after the injection. The model gives a transit time of 4 hours and 30 minutes. The tracer peak time at the Saivu spring was observed 8 hours and 30 minutes after the injection. The simulated transit time for the Saivu spring is 7 hours. The simulated transit times are thus very realistic, although a bit overestimated for the Bâme spring and underestimated at the Saivu spring. This is only a quick and simple comparison to check the model consistency, as the results come from a steady state simulation. A transient simulation would require to infer the inflow function at the upstream of the model and to try and simulate solute transport in the conduits, which is beyond the scope of this chapter.

Table 2.7: Comparison between tracer transit times during a moderate flood event (total peak discharge: 450 L·s^{-1}, from Hessenauer et al. (2005)) and the simulated transit times.

	Observed	Simulated
Saivu	08:30	06:55
Bâme	04:10	04:30

2.4.4 Conduit geometry and roughness coefficient

The chosen geometry for the phreatic conduits in the model is as simple as possible, with each conduit being constituted of two circular segments of same length and of different diameters. In an attempt to create a more realistic geometry, the cave survey of the whole Milandre speleological network (12 km) is considered. The cave survey is treated as a set of segments, each of them defined by a length and a cross sectional area. A series of subsequent line-of-sights of equal cross sectional area is considered as a unique segment. The conduit is built by putting together randomly drawn segments from the set. When the aimed volume, estimated from tracer tests (Section 2.3.1), is reached, the conduit building is stopped. However, by doing so, the obtained conduits were too short by far to be integrated in the model. For instance, the upper Saivu conduit has an estimated volume of 1750 m^3 and a length of 800 m. The obtained mean length after 1000 conduit realizations is of 203±72 m. This indicates that the phreatic conduits have significantly smaller cross sectional area than the epiphreatic ones. Thus the geometry of the saturated conduits can be directly inferred from the conduit geometry in the speleological network. A possibility would be to scale the conduit cross sectional area distribution down to the mean conduit diameter found by calibrating the hydraulic model. The segment directions would also need to be somehow simulated. Overall, the resulting conduits would be hydraulically equivalent to the simplest one (Section 2.3.1) and this would not improve the performance of the model in reproducing the physics of the system.

A spatially constant Manning roughness coefficient of 0.05 s·m$^{-1/3}$ is set in the model. As the head losses and flow velocities are well reproduced by the flow simulation, this value appears to be appropriate for the downstream Milandre system. For instance, along the flow path from probe 9. to 10. via probe 2., the head–discharge relationships are well in line with the observations. The conduit geometry is well characterized since it is an explored and surveyed conduit. This implies that the Manning roughness coefficient is suitable, at least for this conduit. Further insight could be gained into roughness coefficient estimation and local flow velocities by direct measurement of flow velocities inside the system under different hydrological conditions.

2.5 Conclusions

This chapter describes the building and calibration of a hydraulic model of the downstream part of the Milandre system on the basis of sound observed data from the inside the karst network. The data presented here include the monitoring of hydraulic heads in the active karst conduits at high spatial and temporal scales. This gives very detailed and novel information on how flood pulses are transmitted through a karst system.

The resulting model reproduces well the physics of the system in terms of hydraulic heads, flow rates and flow velocities when compared to the available observations. In the phreatic zone, tracer test recovery curves allowed to identify two main flow paths between the underground stream and the perennial spring and to estimate the volume of the karst conduits. This enables the simulation of realistic transit time through the phreatic zone.

In the epiphreatic zone, hydraulic heads are well reproduced at several test points in the main flow paths. Simulated flow velocities are consistent with dye tracer transit times. The model is also almost fully distributed, the majority of the geometry of conduit network being characterized using cave surveying techniques or by tracer testing. This contrasts for instance with Wu et al. (2008) and Chen and Goldscheider (2014), who also used the SWMM flow simulator, but, working in catchments with no direct access to the karst network, subdivided their study area into subcatchments that are each drained by one hypothetical conduit. The main advantage of the present approach over a non-physically based or semi-distributed approach is that the model provides spatial and temporal information on the hydrodynamics — heads, flow rates, velocities — of the system, at any point in the speleological network. The model can thus further be used to infer the sedimentary processes that are likely taking place in the karst system under the observed hydrological conditions.

Chapter 3

Sedimentary processes in the karst network

3.1 Introduction

Water quality at karst springs varies very rapidly during flood events. The most striking change is the increase in turbidity which can reach several orders of magnitude along the course of a single event. Classical models attributes this excess sediment concentration to the arrival of soil particles washed by the flood water (Ford and Williams, 2007a; Goldscheider and Drew, 2007). As seen in Chap. 1, some of the increase in turbidity may also be caused by the remobilization of sediment that was previously deposited inside the karst system.

The breakthrough of resuspended (also called autochthonous) sediment at a karst spring is generally recognized when there is an increase in sediment concentration before the first indication of the arrival of freshly infiltrated water (Massei et al., 2003; Valdes et al., 2006; Pronk et al., 2006; Fournier et al., 2007b,a; Herman et al., 2008; Schiperski et al., 2015b). Similarly, the breakthrough of surface derived (allochthonous) suspended sediment is identified by its simultaneity with the decrease in electrical conductivity and in carbonate derived ion concentrations, which indicates the arrival of event water (Ryan and Meiman, 1996; Mahler and Lynch, 1999; Vesper and White, 2003). Some authors use the breakthrough of fecal bacteria, which in general originate from agricultural soils or septic tanks, as a tracer for the direct transfer of surficial material (Ryan and Meiman, 1996; Mahler et al., 2000; Pronk et al., 2006; Knierim et al., 2015). Mineralogical composition and grain shape of the discharged sediment are also widely used to distinguish sediment sources inside the aquifer and on the surface (Mahler et al., 1999; Mahler and Lynch, 1999; Drysdale et al., 2001; Lacroix et al., 2000; Lynch et al., 2004; Herman et al., 2007). Overall, these methods are solely based on the analysis of water quality and of suspended sediment composition at the outlet of a karst system.

Fewer studies focused on the hydrodynamics of the remobilization of sediment inside karst aquifers. In an early study, Gale (1984) analyzed the grain size distribution of sediment deposited in active conduits and was able to derive local flow velocities during high stage conditions. More recently, Dogwiler and Wicks (2004) investigated sediment mobilization along a cave stream. They estimated the water slope during flood events and systematically measured the sediment grain size distribution in order to assess the frequency at which the cave stream is able to erode its bed.

In the Milandre cave, there is evidence for active fluvial sedimentary processes. Thick deposits of clastic sediments are observed along the Milandrine stream and in the epiphreatic passages. In the downstream part of the system, these deposits are mostly composed of fine particles (silt to clay) and can reach several tens of centimeters to a few meters in thickness. There is anecdotal evidence for a net accumulation of sediment in some locations. For instance, the large passage which opens below the cave entrance is a former show cave which has been closed in the 1980s due to recurring cases of fine sediment deposition by flood waters (Hessenauer et al., 2004).

In this chapter, the ongoing sedimentary processes in the Milandre karst system are investigated both by direct observation and through flow modelling. A semi-quantitative approach for the modelling of sediment transport in this karst system is proposed. The approach is based on the SWMM5 hydraulic model developed in Chap. 2, which is used to compute mean boundary shear stress and shear velocity in the conduits. These parameters are used to infer whether erosion or deposition of sediment is likely to occur in the karst conduits. Further, the results of a 11 year temporal monitoring of sedimentary processes in the cave stream is presented. These observations are then compared with the flow simulations. Finally, the model results are also used to assess the overall dynamics of sediment transport along the cave stream and in the epiphreatic passages of the downstream part of the Milandre karst system.

3.2 Methodology

3.2.1 Sedimentation monitoring

To gain insight on the sedimentary processes taking place in the Milandre cave, a monitoring station was set up along a cross section in the underground stream conduit. The station consists in a set of twelve horizontal wooden plates of dimension 10 × 10 cm. They are positioned at different heights (0 to 3.65 m) above the stream. Heights are referenced to the stream level under base flow conditions. A schematized view of the conduit cross section with the sedimentation plates is shown in Fig. 3.1. The location of this station is shown in Fig. 3.2.

Monitoring took place from September 2004 to December 2015 within the framework of the A16 highway environmental impact study (Hessenauer et al., 2004). On average, the plates were visited once every three months. In this chapter, the interval between two visits will be referred to as an observation period. The aim was to obtain qualitative data on sedimentary processes. Thus, at each visit, each plate was photographed and half of the plate area was cleaned from the deposited sediment, if any. The pictures were compared with the ones from the previous visit to assess if any sedimentary processes are observable.

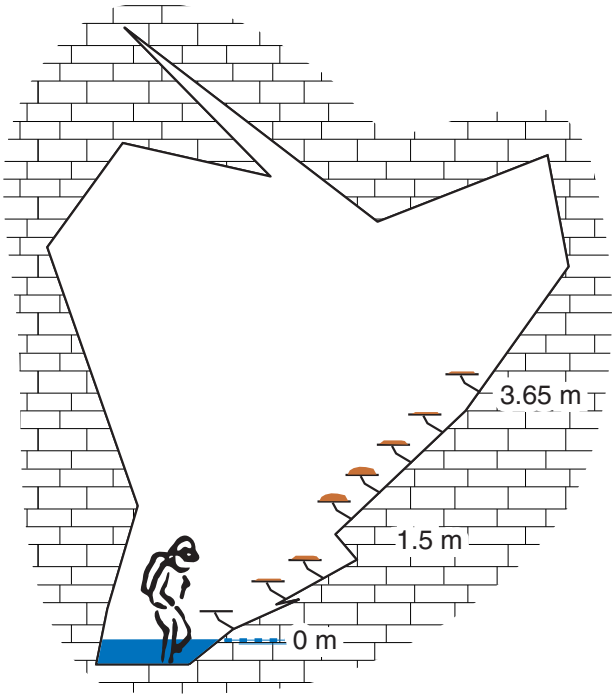

Figure 3.1: Schematized cross sectional view of the sedimentation monitoring station. The sedimentation plates are positioned at different heights along the conduit cross section. Heights are referenced to the stream level under base flow conditions.

Each plate was then classified as one of the following categories:

Flooded The plate is underwater at the time of the observation. No observation of sedimentary process.

Deposited A net accumulation of sediment is observed compared to the last visit.

Smoothed There is no observable accumulation or erosion, but the sediment has been reworked by flow since the last visit.

Stable No evidence of flow or sedimentary processes.

Eroded A net erosion of sediment is observed compared to last visit.

The station is located at a point where the main cave stream conduit forks into one upper and one lower passage. The lower passage consists in a 20 meter long sump while the upper passage is dry under base flow conditions. The floor of the upper passage is ∼2 meters above base flow level, so flooding above this height is caused by backflooding from the downstream part of the system. Between 0 and 2 meters of height, it is not clear if the flooding is primarily caused by the lower passage or by backflooding from further downstream constrictions.

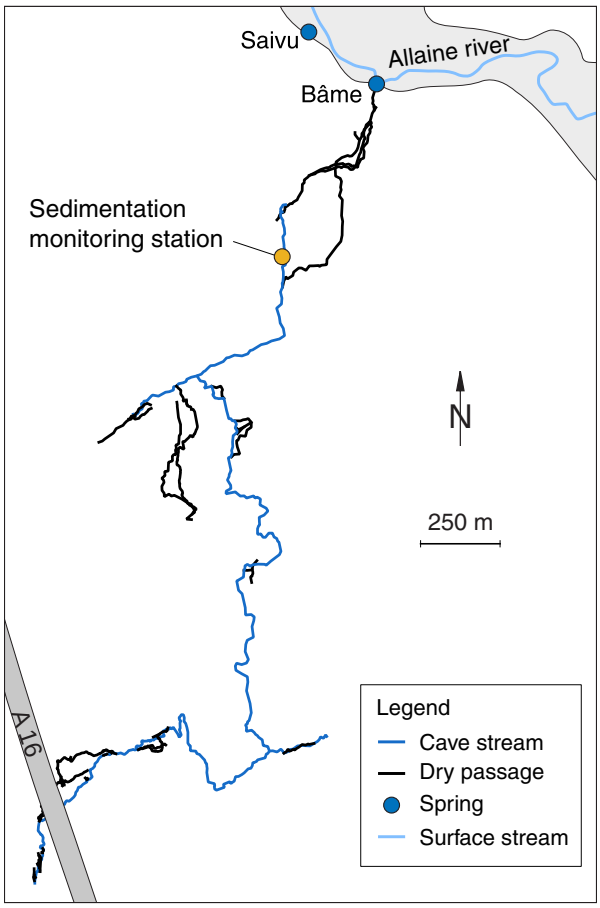

Figure 3.2: Location of the sedimentation monitoring station.

3.2.2 Modelling

Erosion

In a channel, sediment mobilization and transport is made possible by the shear stress exerted on the channel bed by the water flow. According to Herman et al. (2012), the mean boundary shear stress τ_0 (N·m^{-2}) in a karst conduit is

$$\tau_0 = \rho g R_h \frac{\Delta H}{L} \tag{3.1}$$

where ρ is the density of water (kg·m^{-3}), g the gravitational acceleration (m·s^{-2}), R_h the hydraulic radius (m) and $\frac{\Delta H}{L}$ is the friction slope (-). In the SWMM5 hydraulic model (Chap. 2), conduit flow is computed using the Manning-Strickler formula:

$$v = \frac{1}{n} R_h^{2/3} \left(\frac{\Delta H}{L}\right)^{1/2} \tag{3.2}$$

where v is the flow velocity in the conduit (m·s^{-1}) and n is the Manning roughness coefficient (s·m$^{-1/3}$). Combining Eq. 3.1 and 3.2, the mean boundary shear

stress can be reformulated as

$$\tau_0 = \rho g (nv)^{3/2} \left(\frac{\Delta H}{L} \right)^{1/4} \tag{3.3}$$

In this chapter, this formula is used to determine the mean boundary shear stress in the speleological network on the basis of the flow simulation yielded by the hydraulic model. Mean boundary shear stress is computed at each simulation time step in each surveyed conduit. As described in Chap. 2, the conduit network is discretized according to the cave survey lines-of-sight. The average conduit length is 6.7±3.6 m. In the model, conduit cross sections are rectangular, and their dimensions are read from the hand drawn plan and developed profile of the cave survey. Since their geometry is not well constrained, the unexplored conduits that were added during the calibration phase of the model are not considered for the sediment transport calculations. They are however also included in flow simulations.

The critical shear stress, which is the mean boundary shear stress above which sediment movement is initiated, depends on the nature of the sediment. In their study of sediment mobilization in karst conduits, Gale (1984) and Dogwiler and Wicks (2004) used the Shields parameter to estimate the critical shear stress (Chap. 1). The Shields parameter determines the value of the flow shear stress required to counterbalance the gravitational forces acting on the sediment grains. As a result, the critical shear stress is estimated from the grain size distribution and the grain density. However, this relation holds only for coarse, non cohesive sediment. For sediment in the silt–clay range size, such as in Milandre, the attractive forces between the particles have more influence on the erodability of the sediment bed than the gravitational ones (Knighton, 1998). As a result, several other factors influence the critical shear stress of fine sediment, such as the sediment bulk density, water and clay content (Debnath and Chaudhuri, 2010).

In this chapter, an experimental value of critical shear stress taken from the literature is used. The overall sediment grain size distribution in the Milandre system is assumed to be close to the suspended sediment mean grain size distribution as obtained from the cumulative sediment traps (Chap. 5). This gives a median grain size d_{50} of 29 µm, a d_{95} of 102 µm and a clay content of 9% (Fig. 3.3). Laflen et al. (1960) provided critical shear stress values for a variety of soil sediments, among which one is not too far from the Milandre sediments in terms of d_{50} (20 µm) and clay content (14%). He measured the minimum shear stress at which the bed starts to dismantle for different water depths. On average, the observed critical shear stress is of 0.65±0.17 N·m^2. This value is thus set as the threshold for sediment erosion in the semi-quantitative approach developed here.

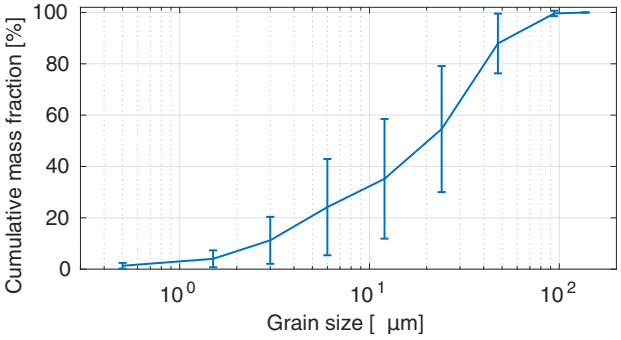

Figure 3.3: Mean suspended sediment size distribution in the Milandre system (measured from cumulative samples covering the 2003 to 2007 period at 4 different stations in the underground stream and at the Saivu spring). d_{50} is 29 µm and d_{95}, 102 µm.

Deposition

Once their remobilization is initiated, silt and clay particles are transported by the stream as suspended load, in contrast with sand and coarser material which are mostly transported as bed load. Particles will stay in suspension as long as the eddies of the turbulent flow are sufficient to balance the gravitational effects. This relation can be expressed in terms of the ratio between shear velocity and particle settling velocity (Julien, 1998). Shear velocity (u_*, in m·s^{-1}), a reformulation of the shear stress, is

$$u_* = \sqrt{g R_h \frac{\Delta H}{L}} \tag{3.4}$$

Similary to the mean boundary shear stress, shear velocity is reformulated in terms of flow velocity, by substituting R_h in Eq. 3.4 using the Manning-Strickler formula (Eq. 3.2):

$$u_* = \sqrt{g} (nv)^{3/4} \left(\frac{\Delta H}{L} \right)^{1/8} \tag{3.5}$$

This formulation allows the computation of shear velocity in the conduits directly from the results outputted by SWMM5. As for the settling (or terminal) velocity of a particle (w, in m·s^{-1}), it is reached when gravitational and viscosity forces (from Stokes' law) balance each other and can be expressed as

$$w = \frac{2 r^2 g (\rho_s - \rho)}{9 \mu} \tag{3.6}$$

where r is the particle radius (m), ρ_s is its density (kg·m^{-3}) and μ is the dynamic viscosity of water (kg·m^{-1}·s^{-1}). A value of 2650 kg·m^{-3}, representative of silicate minerals, is used for the particle density while the dynamic viscosity is set at 0.001308 kg·m^{-1}·s^{-1}, which is characteristic of water at 10°C.

Julien (1998), compiling experimental data from coarse to very fine sand, states that turbulent mixing entirely overcomes gravitational effects when $\frac{u_*}{w} > 2.5$. This is used here to determine the threshold for sediment deposition: when $u_* < 2.5w$, the deposition of particles is possible. For the d_{95} of the suspended grain size distribution in Milandre (Fig. 3.3), this gives $u_{*cd_{95}} = 0.0179$ m·s^{-1}.

Simulating the sedimentation plates

A first step is to test the semi-quantitative approach on the data gathered by the sedimentation plate monitoring. In order to compare the model output with the observations, the sedimentary state (flooded, deposited, smoothed, stable or eroded — see Sec. 3.2.1) has to be evaluated for each plate and for each of the ∼3 month observation period.

The surveyed cross section of the plate conduit is introduced in the model (Fig. 3.1). This contrasts with the rest of the model where the conduit cross sections are rectangular (Chap. 2). A more detailed section is introduced in this conduit in order to reproduce more accurately the variations of shear stress and shear velocity with respect to the water depth. Flow is simulated for the sedimentation monitoring period (2004–2015). The model inflow is constructed by adding up the Saivu and Bâme flow rate records (15 minutes time step), the two main outlets of the system. To ensure numerical stability, the routing time step is reduced to 0.1 second. The modified SWMM5.0.019 is used (Chap. 2). The overall computational time for this 12 year period was ∼3 weeks with a Intel® Core™ i3-2120 CPU at 3.30 GHz clock cycle and 4 GB of RAM. The report time step is 15 minutes. From the simulation results, the mean boundary shear stress (τ_0) and the shear velocity (u_*) are computed at each report time step in the conduit where the sedimentation plates are located. Sedimentary processes are then evaluated at each time step: if $\tau_0 > \tau_c$, erosion is active, while if $u_* < u_{*cd_{95}}$, deposition is occurring. For intermediate flow conditions, it is considered that the plates are getting smoothed. Finally, if the plate is above water level, it is considered stable. For one given time step, since flow is simulated in 1D, the active sedimentary process is the same for all the flooded plates. But since plates are flooded at different times (e.g. lower plates are flooded longer and more often than higher plates) and since the shear stress varies with the water level, each plate can experience its own succession of sedimentary processes. The last step is thus to determine the final state of the plate, i.e. its state at the time of the observation. After a short trial-and-error process, and so that each of the sedimentary plate state is simulated at least once in the data set, two adjustments are performed:

- erosion is dominant over other process — i.e. if erosion occurred at some point during the observation period, the final plate state is set as eroded;
- deposition is observable if it was active for at least 24 hours during the observation period.

This is consistent with the fact that erosion is a threshold, catastrophic-like process, while sedimentation is much slower and more time dependent.

3.3 Results

3.3.1 Sedimentation monitoring

Overall sedimentary dynamics

The monitoring of the sedimentation plates ran from September 2004 to December 2015. Over this period, several plates underwent a net downwards displacement due to the slumping of the stream bank. The displacement mostly took place between 2006 and 2008 (Häuselmann et al., 2016). Plate heights were surveyed at the beginning and at the end of the monitoring. The maximum displacement is observed at plate 3 (plate numbering goes from low to high height), which went from 1.00 meter above the stream base level to 0.46 m. Since no further data has been collected on the vertical position of the plate, it is here considered that the displacement occured at once in the beginning of 2007.

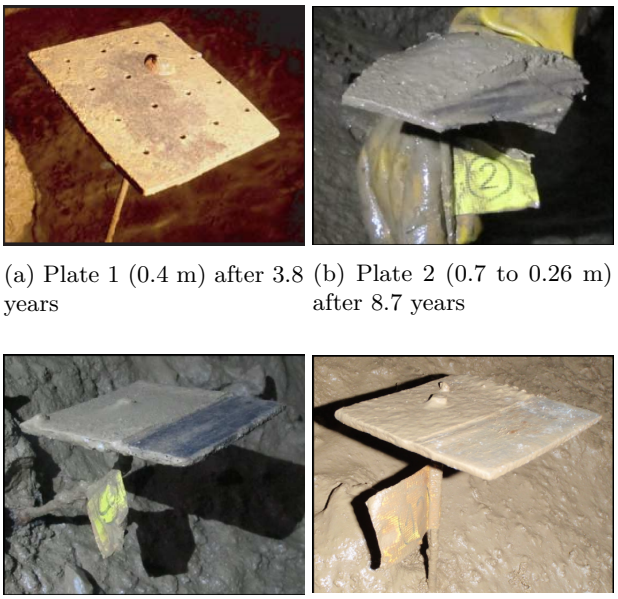

(a) Plate 1 (0.4 m) after 3.8 years

(b) Plate 2 (0.7 to 0.26 m) after 8.7 years

(c) Plate 9 (2.71 m) after 11.3 years

(d) Plate 12 (3.65 m) after 10.8 years

Figure 3.4: Low sedimentation rates: plates lower than 1 m and higher than 2 m (Blant et al., 2009; Häuselmann et al., 2014a, 2016)

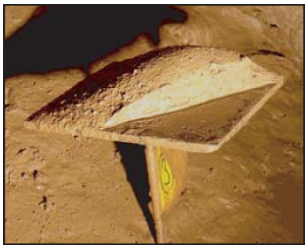

(a) Plate 3 (height of 1 to 0.46 m)

(b) Plate 4 (height of 1.3 to 1 m)

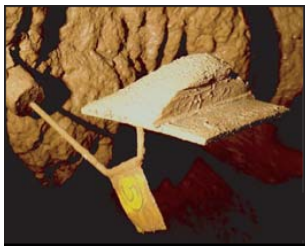

(c) Plate 5 (height 1.5 m)

Figure 3.5: High sedimentation rates: accumulation of sediment on plates 3, 4 and 5 after 3.8 year (18 June 2008) (Blant et al., 2009)

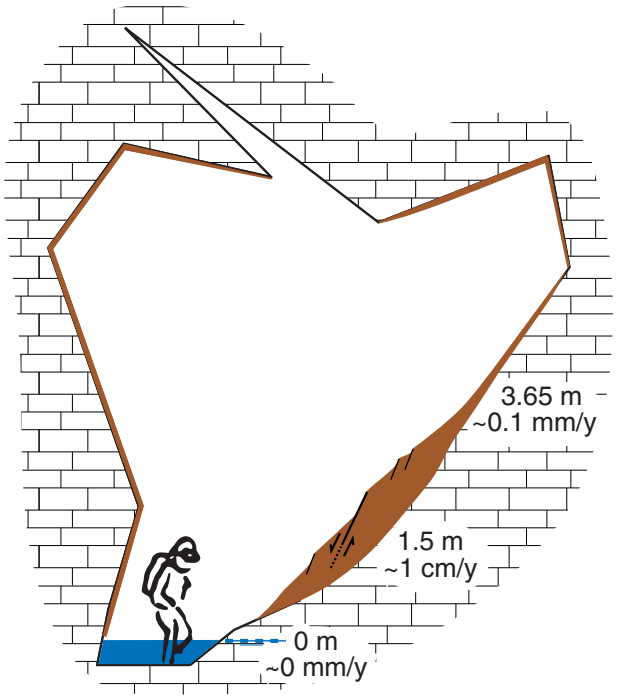

Figure 3.6: Schematized summary of the observations made at the sedimentation monitoring station. The station was active from 2004 to 2015. Heights are referenced to the base level of the stream. Italicized values are estimated overall accumulation rates.

The rate of sediment accumulation observed on the plates varies greatly depending on the plate height: on the plates lower than 0.7 m, the overall sedimentation rate goes from zero to roughly 1 mm·y^{-1} (Fig. 3.4a,b). Moreover, these plates are the ones that are the most subject to erosion. Indeed, erosion is never observed above 1.5 m. In contrast, relatively high accumulation rate are found on plates between 1 to 1.5 m (Fig. 3.5). For instance, plate 5 (Fig. 3.5c), at a stable height of 1.5 m, had already accumulated approximately 4 cm of sediment after 4 years of monitoring. The plate was saturated with sediment since then and did not show much change in the following years. Further upwards, the accumulation rate diminishes until approximately 0.1 mm·y^{-1} on the highest plate, at 3.65 m above base level (Fig. 3.4c,d). The observations are schematically summarized in Fig. 3.6 and compiled in Fig. 3.7b.

In summary, the monitoring of sedimentary processes in the Milandrine stream points out a net sediment accumulation on the banks of the conduit (Fig. 3.6). The accumulation is most effective at around 1.5 m above the stream base level, where it reaches ∼1 cm·y^{-1}. In the direct neighbourhood of the stream, deposition is less active and is counterbalanced by erosion processes. The upper parts of the stream conduit also display a net sediment accumulation, but the rate is two orders of magnitude less than the observed maximum (∼0.1 mm·y^{-1} vs ∼1 cm·y^{-1}). On the other hand, the sliding of the stream banks, which lowered by several tens of centimetres within a few years, may somehow compensate the particle accumulation in the long run by displacing the sediment bed into the zone where erosion may take place.

Temporal variations

There is an important temporal variability in the observed sedimentary processes (Fig. 3.7b). In Fig. 3.7a, the total discharge of the system (sum of Saivu and Bâme spring discharge) is plotted for comparison with the observations of the sedimentation plates. In Fig. 3.8a, the maximum peak discharge during the observation period is plotted against the height of the highest plate reached by water (e.g. on which deposition or smoothing was observed), as well as the highest deposited and eroded plate for the same time period. In all three cases, the scattering of the data shows that the height of the highest affected plate is not strongly correlated with the maximum peak discharge. For instance, the height of the highest plate showing evidence of flow (smoothing or deposition) does not systematically increases with higher maximum discharge. However, links between the hydrodynamics of the karst system and the sedimentary processes can be pointed out:

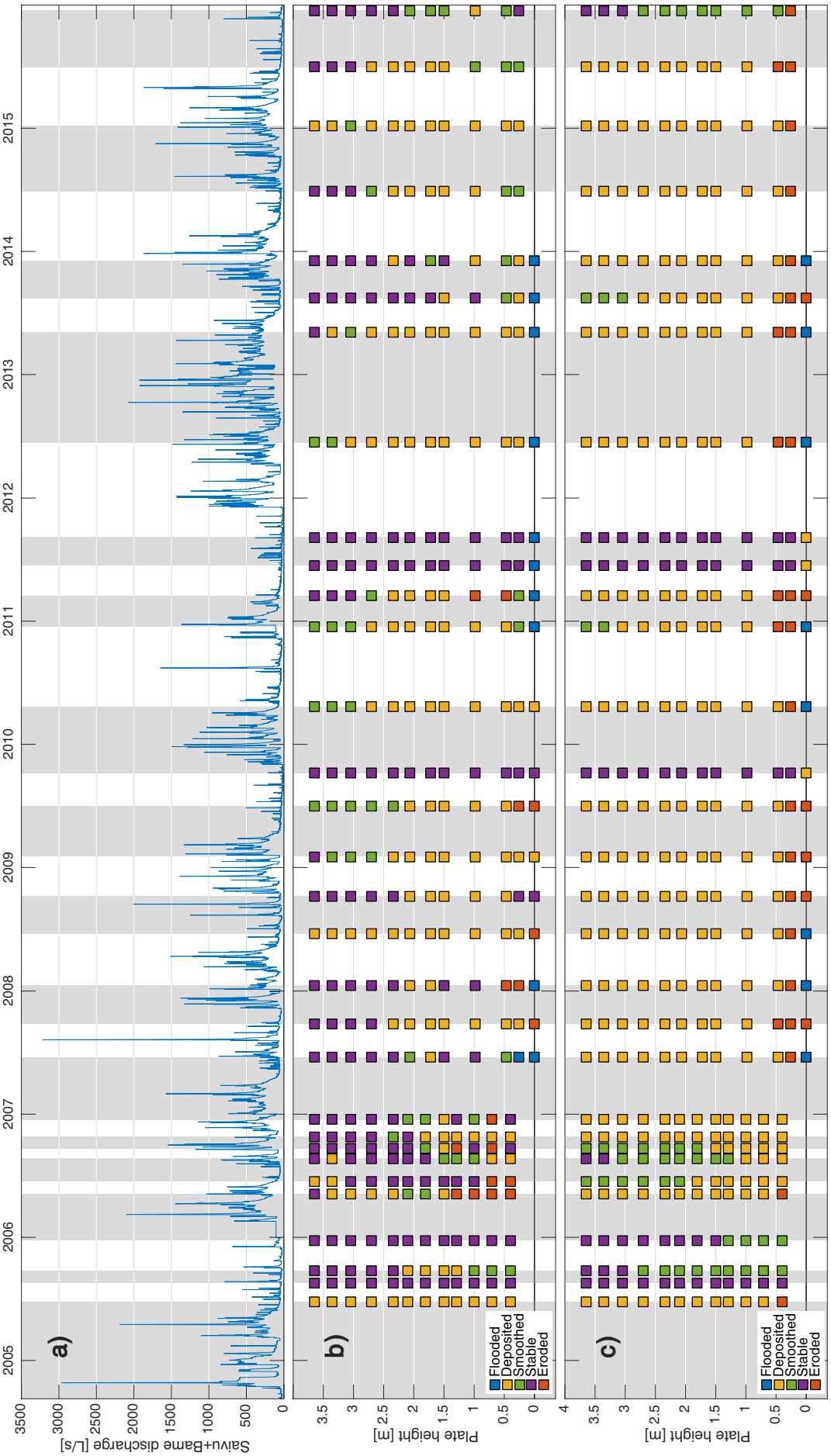

Figure 3.7: a) Cumulative discharge of the Saivu and Bâme springs. b) Observed sedimentary processes on the sedimentation plates. c) Simulated sedimentary processes on the sedimentation plates. The height of the plates refers to the stream level under base flow conditions.

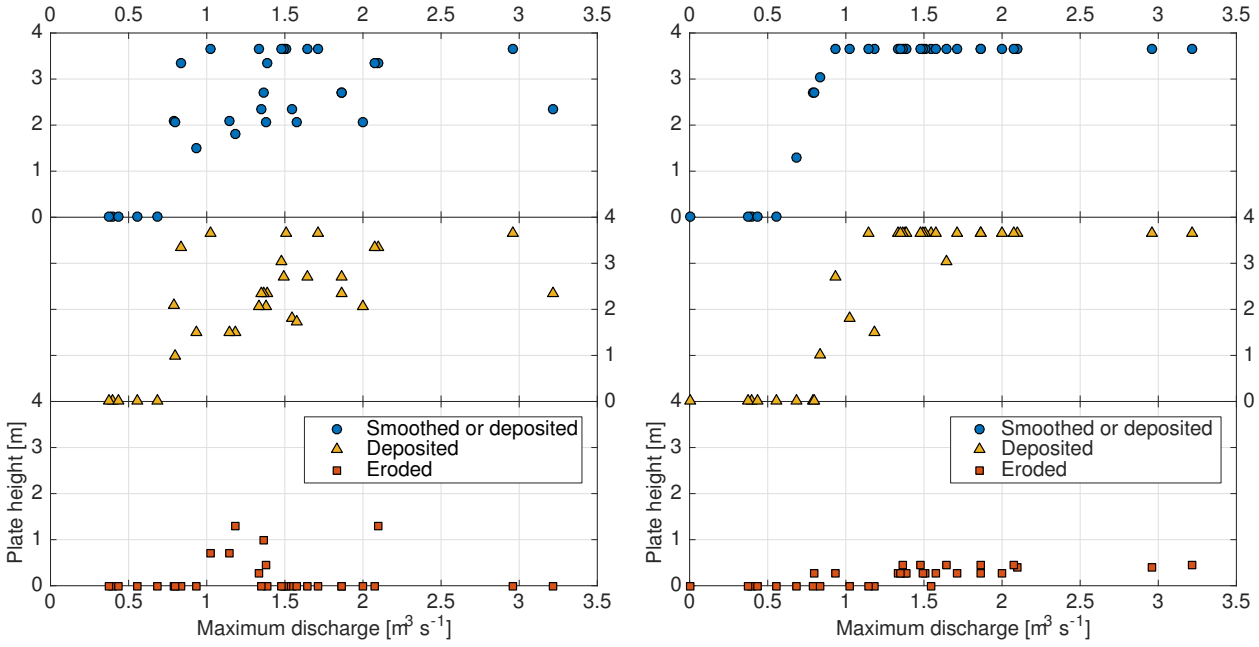

(a) Observed (b) Simulated

Figure 3.8: Scatter plots of the maximum discharge vs the height of the highest plate reached by water (smoothed or deposited), the highest deposited and eroded plate for each observation period (Fig. 3.7).

- For maximum discharges smaller than 0.7 $m^3 \cdot s^{-1}$, no effect of sedimentary processes were observed.
- For maximum discharges between 0.7 to 1 $m^3 \cdot s^{-1}$, the maximum height of deposition generally increases with discharge.
- Finally, above 1 $m^3 \cdot s^{-1}$, erosion may occur on the plates lower than 1.5 m and deposition may occur up to the highest plate, at 3.65 m. However, the height of the highest plate showing evidence for sedimentary processes is variable, and erosion is not always observed.

3.3.2 Modelling

Sedimentation plates

The results of the modelling of the sedimentation plate observations are shown in Fig. 3.7c. The general sedimentary dynamics is well captured by the model, as the extreme cases are quite well reproduced: when none of the plates show evidence of sedimentary processes, or when all plates accumulate sediments, the model prediction is almost accurate. For intermediate cases, there is some discrepancy between the observations and the simulations. For instance, deposition is overrepresented in the simulation. Erosion is limited to the lower plates, which is well in line with the observations. However, erosion is sometimes predicted when it was not observed, and vice versa. Overall, the model prediction of the plate states is accurate for 54% of the observations.

Similarly to Fig. 3.8a, Fig. 3.8b shows the maximum peak discharge against the highest plate reached by water (smoothed or deposited), the highest deposited and the highest eroded plate for each observation period according to the model prediction. Again, it appears that the general sedimentary dynamics is well reproduced: the plates show no effects of sedimentation for peak discharges below 0.7 $m^3 \cdot s^{-1}$ and are gradually deposited upwards for discharge between 0.8 and 1.2 $m^3 \cdot s^{-1}$. However, the simulated relationship between discharge and highest deposited plate is much smoother than in the data (Fig. 3.8a). Simulated erosion is triggered at 0.8 $m^3 \cdot s^{-1}$ (vs. 1 $m^3 \cdot s^{-1}$ in the data) and never reaches plates higher that 0.5 m (vs. 1.3 m in the data).

To explore these processes at a finer time scale, Fig. 3.9 shows the simulated values over the course of one sample event in June 2012. Values are taken for the conduit in the model where the sedimentation monitoring station is located. The discharge and the water level show a steady increase until their peak value is reached (Fig. 3.9a). Afterwards they decrease steadily towards their pre-event value. Flow velocity and mean boundary shear stress have a different evolution: they have a sharp peak when the water level is rising, and another one when it decreases. In between, they are relatively low. This indicates an initial erosive phase during the onset of the event, a depositional phase during the event maximum (if there is suspended sediment to deposit) and a secondary erosive phase during the conduit emptying.

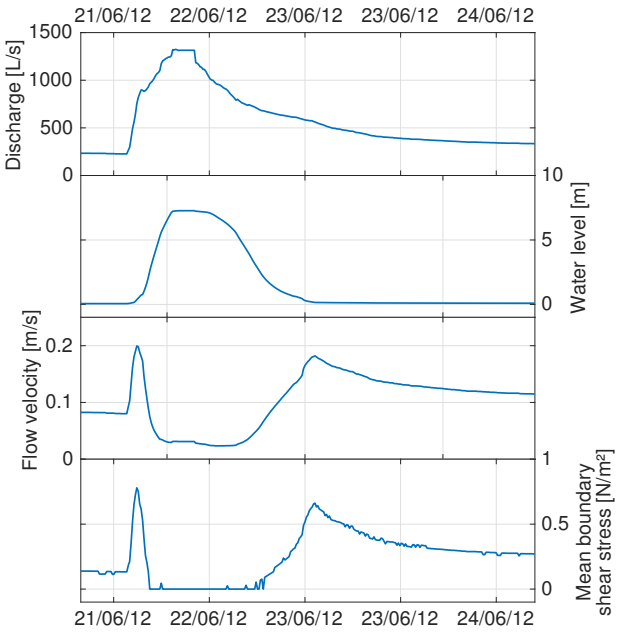

(a) Simulated discharge, water level (zero is the stream base level), flow velocity and shear stress.

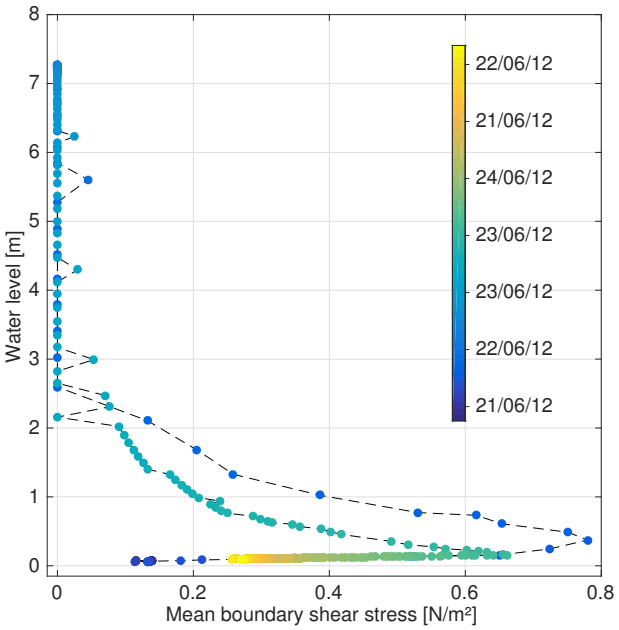

(b) Scatter plot of the water level vs the mean boundary shear stress. Dot colors indicate time.

Figure 3.9: Example of a simulated flood event. Both plots show values simulated at the location of the sedimentation monitoring station for the same event in June 2012. As for the plate height in previous figures, the zero of the water level corresponds to the base level of the stream.

Fig. 3.9b shows the mean boundary shear stress as a function of the water level at the same location for the same event. This shows again that low water levels are associated with high shear stress. Conversely, high water levels are associated with low shear stress values.

Spatial variations

To assess the sedimentary dynamics over the whole model, i.e., the downstream part of the Milandre system, mean boundary shear stress (τ_0) and shear velocity (u_*) are computed in each conduits for the whole simulation period which runs from September 2004 to December 2015. The maximum τ_0 in each surveyed conduit over the entire simulation period is shown in Fig. 3.10. The median and maximum u_* (for the total time during which the conduit was flooded) are shown in Fig. 3.11 and 3.12.

As mentioned in the previous section (3.2.2), the erosion of cohesive sediment is a threshold process. Below the critical shear stress (τ_c), erosion is negligible, while it becomes very effective once the threshold is exceeded. Thus, even if the critical shear stress is rarely reached at a certain location in the conduit network, erosion can still have a significant effect on the sediment mass balance at this location. Conversely, if the maximum τ_0 ever reached at a specific location is far from the critical shear stress, it is likely that erosion never occurs there. The maximum τ_0 in each conduit on a pluriannual (11 years) time scale, depicted in Fig. 3.10, is thus a good indicator of medium term erosion dynamics in the speleological network.

The maximum τ_0 in each conduit of the speleological network reaches values between $1.4{\cdot}10^{-4}$ to 285 $\mathrm{N{\cdot}m^{-2}}$. This range includes the estimated critical shear stress τ_c for the erosion of Milandre sediments of 0.65 $\mathrm{N{\cdot}m^{-2}}$. There is a spatial organization in the maximum τ_0: the conduits hosting the perennial stream (SW lowest path in Fig. 3.10) and the lowest epiphreatic passage flowing toward the Bâme spring have values of order 1 to 100 $\mathrm{Nm^{-2}}$. These are higher than τ_c, meaning that erosion can occur in theses passages under the observed flow conditions. In the intermediate epiphreatic passage (NE in Fig. 3.10), the maximum simulated τ_0 are a little lower but still generally above τ_c. In contrast, the highest flooded passages (the former show cave and the passage called *Galerie des Fistuleuses*) have very low maximum τ_0, generally below 0.1 $\mathrm{N{\cdot}m^{-2}}$. This indicates that the shear stress was never high enough to erode sediments in these passages over the 11 year study period.

To gain insight into deposition processes, the median simulated shear velocity in every surveyed conduit (u_*) is illustrated in Fig. 3.11. This corresponds to the shear velocity that was exceeded half of the time during which the conduit was flooded. The max-

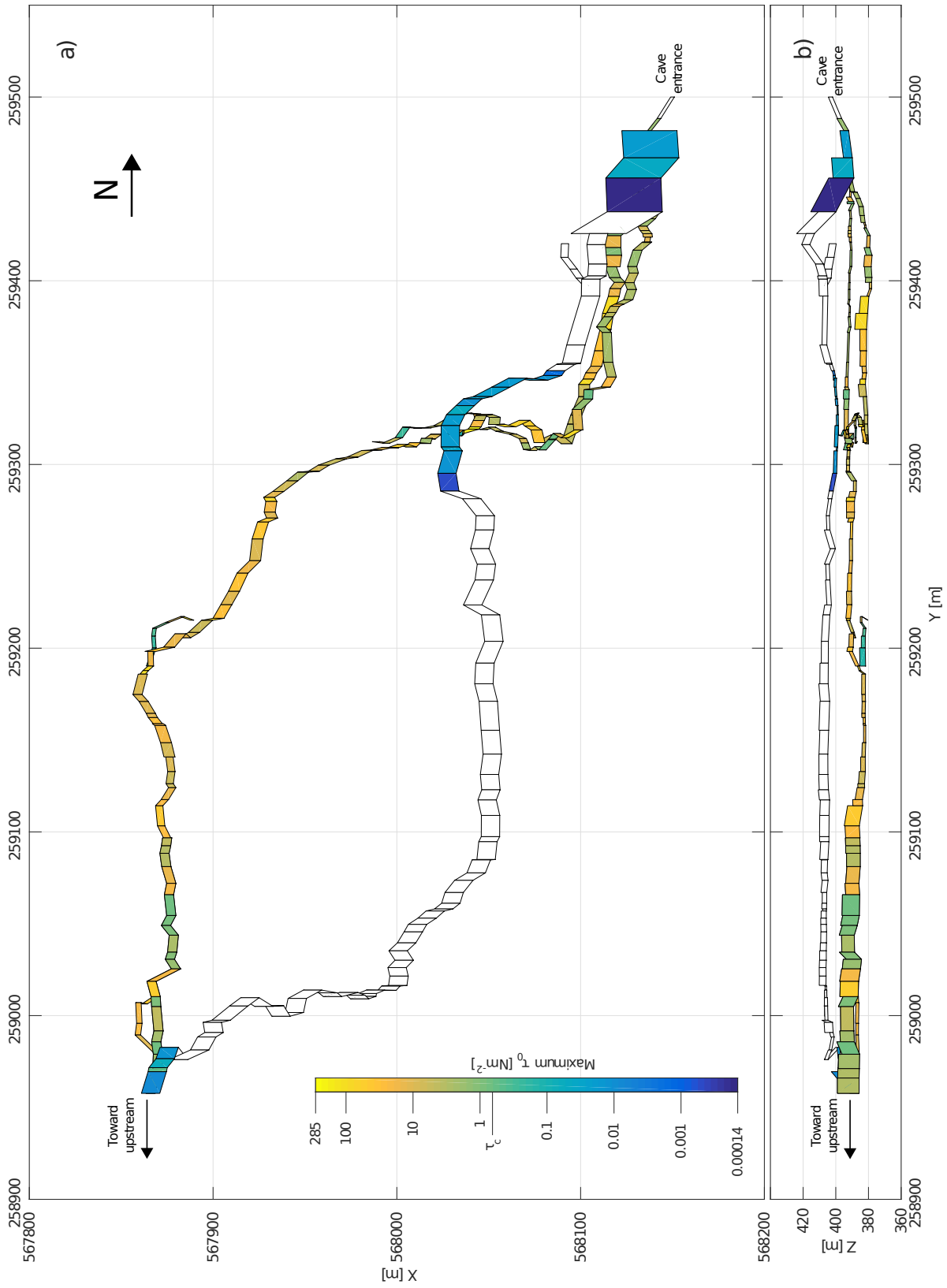

Figure 3.10: Map and cross section of the maximum simulated mean boundary shear stress (τ_0) in the conduits of the model over the 2004–2015 period. The critical shear stress (τ_c) of erosion for Milandre cave sediment is estimated at 0.65 $\mathrm{N \cdot m^{-2}}$. The color scale is in log scale.

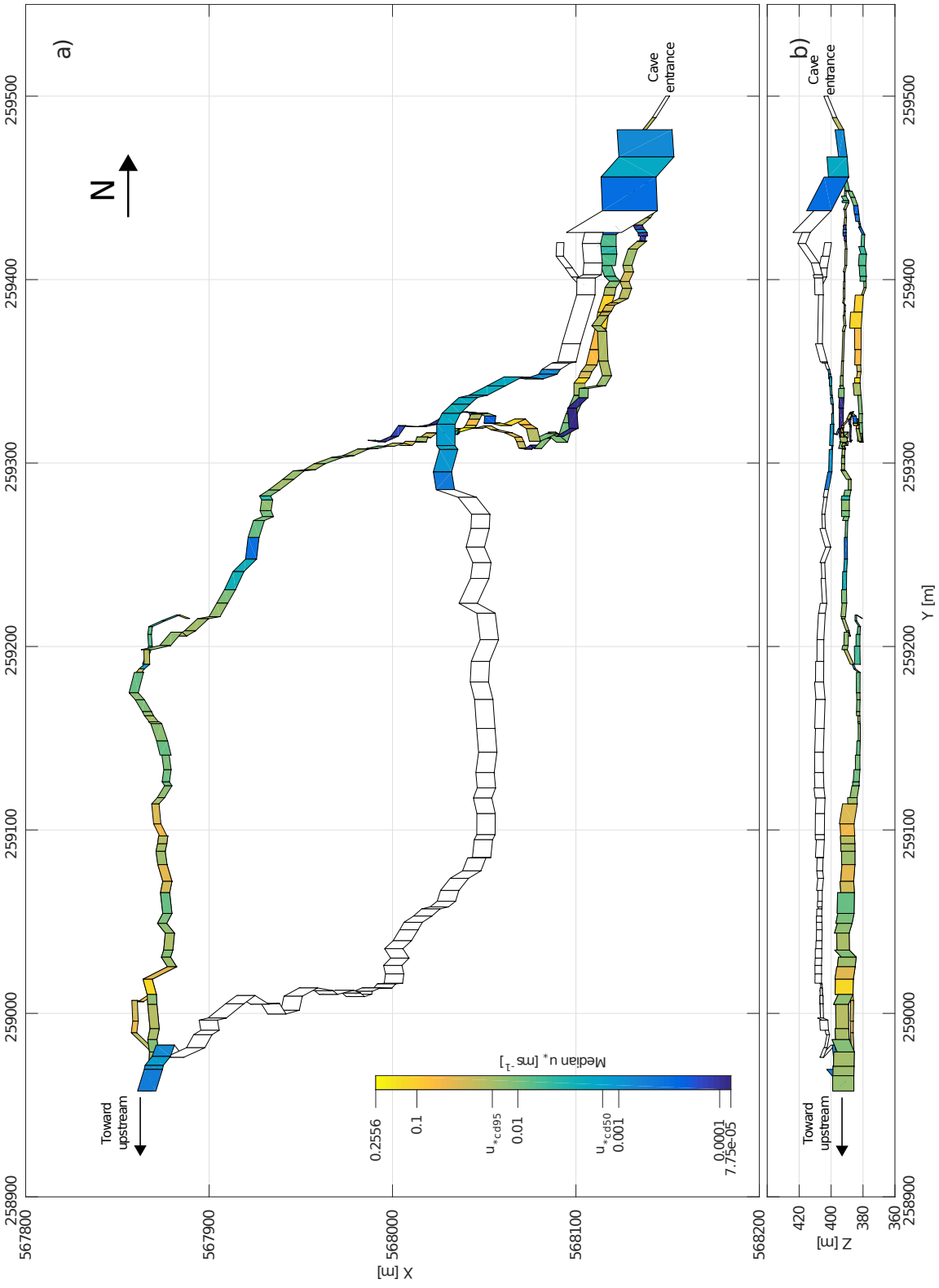

Figure 3.11: Map and cross section of the median simulated shear velocity (u_*) in the conduits of the model over the 2004–2015 period. $u_{*cd_{95}}$, the minimum shear velocity required for the full suspension of d_{95} size sediment, is 0.0179 m·s^{-1}. $u_{*cd_{50}}$, the minimum shear velocity required for the full suspension of d_{50} size sediment, is 0.0014 m·s^{-1}. The color scale is in log scale.

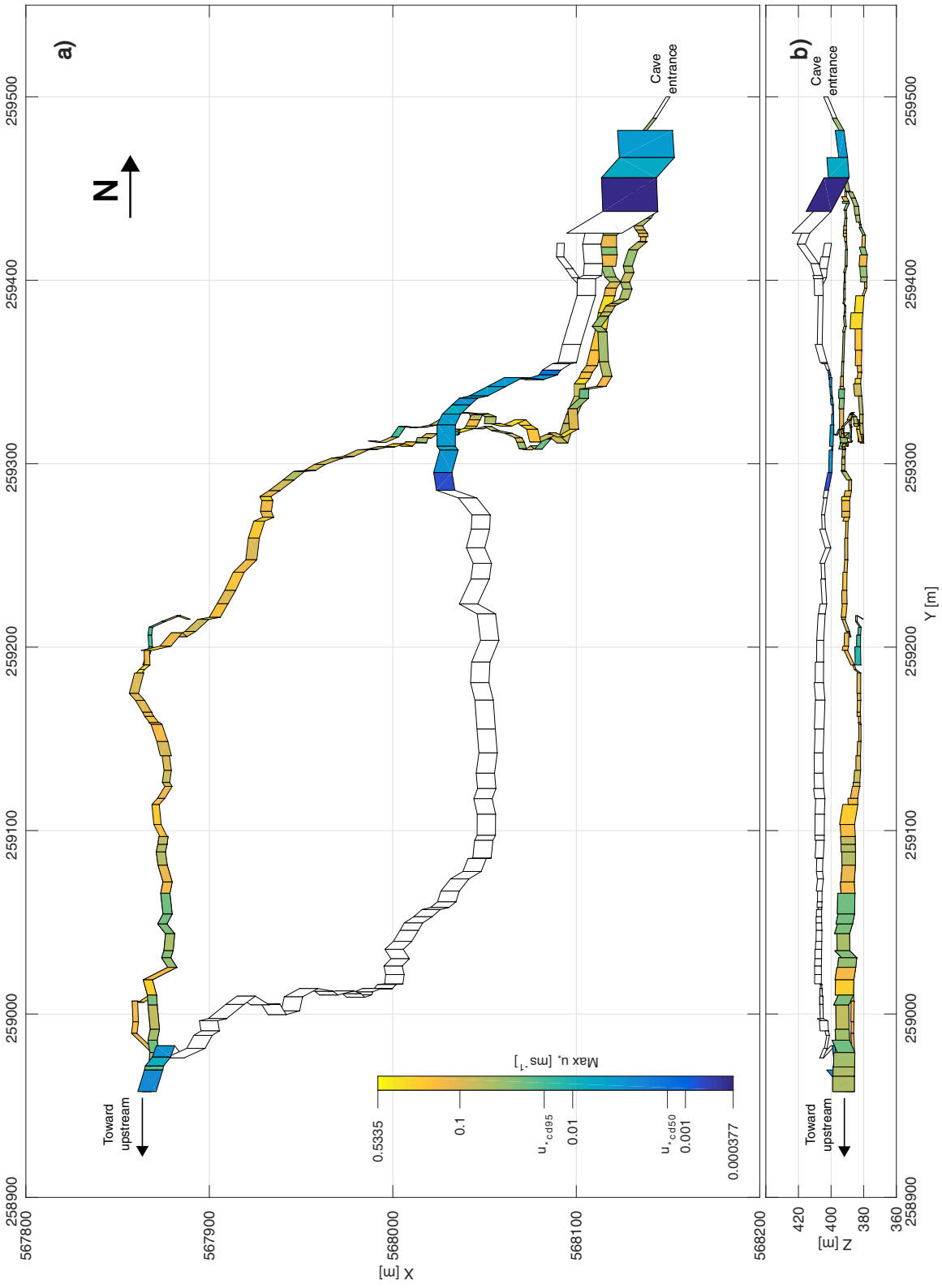

Figure 3.12: Map and cross section of the maximum simulated shear velocity (u_*) in the conduits of the model over the 2004–2015 period. $u_{*cd_{95}}$, the minimum shear velocity required for the full suspension of d_{95} size sediment, is 0.0179 m·s^{-1}. $u_{*cd_{50}}$, the minimum shear velocity required for the full suspension of d_{50} size sediment, is 0.0014 m·s^{-1}. The color scale is in log scale.

imum simulated u_* is shown in Fig. 3.12. In the perennial stream conduit, the maximum u_* are generally higher than 0.0179 m·s^{-1}, the minimum velocity required for the full suspension of particle of d_{95} size ($u_{*cd_{95}}$). This means that under high flow conditions, the underground stream has the capacity to transport the full suspended load. The median u_* are in the range of $u_{*cd_{50}}$ (minimum velocity required for the full suspension of particle of d_{50} size) to $u_{*cd_{95}}$, meaning that both transport and deposition are fairly common along this flow path. It also implies that deposition is active mostly for larger particles ($> d_{50}$). Again, this contrasts with the flow dynamics of the uppermost passages (*Fistuleuses* passage and former show cave): median u_* are close to or lower than $u_{*cd_{50}}$ and maximum u_* never reaches $u_{*cd_{95}}$. This implies a continuous deposition of larger particles — when the passages are flooded — and frequent deposition of d_{50} or smaller particles.

3.4 Discussion and conclusions

On the basis of both field observation and hydraulic modeling, this chapter presents an improved understanding of the ongoing fluvial sedimentary dynamics in the downstream part of the karst system of Milandre. The qualitative monitoring of sedimentary processes in the underground stream over 11 years reveals an important spatial variability: the accumulation rate varies from 0 to ∼1 cm·y^{-1} between sedimentation plates that are distant by only 1 m in height. Erosion processes are observed only in the direct neighbourhood of the stream. As for the rate of sediment accumulation, it reaches a maximum at a height of 1.5 m above the stream base flow level and diminishes upwards. This highlights the key role played by the hydrodynamics in the sedimentary processes: the shear stress is sufficient to erode the sediment only when the water depth is relatively low, i.e. during the initial and final stages of a flood event. Furthermore, the overall sediment accumulation rate at a certain height depends on how frequently it is reached by the flood waters. However, the sediment pile resulting from this accumulation appears to be unstable, as a net vertical displacement of up to >40 cm was measured.

The relationship between the system's hydrodynamics and the transport of sediment in the conduits is further investigated through numerical modeling. A simple, semi-quantitative approach for sedimentary process modeling is developed on the basis of flow simulations. Mean boundary shear stresses and shear velocities are computed in the conduit network from the SWMM5 hydraulic model output. Threshold values for erosion and deposition are used but sediment mass transfer and mass balance are not taken into account. The resulting model reproduces well the general sedimentary dynamics observed on the plates. At the scale of one flood event, the model predicts an initial erosive phase when the water level is increasing in the conduit. During the event maximum, the mean boundary shear stress decreases towards values compatible with sediment deposition. The model also suggests a secondary erosive phase when the conduit is emptied at the end of the event. This is in line with the observations made on the sedimentation plates, where erosion is visible only on the lowest plates, while deposition is frequent on mid-height plates. There are however some discrepancies between the model and the observations. For instance, deposition occurs more frequently in the simulation than in the data set: the model considered that deposition is active when the flow velocity is sufficiently low. It does not take into account whether there actually is a sediment load to deposit, nor the potential changes in the grain size of the sediment load which changes the sediment settling velocity. Also, in the model, deposition is considered to be significant (i.e. visible to the naked eye) if it occurred during a minimum of 24 hours. This time threshold is found by compromising so that both deposition and smoothing may occur during the simulation period, as observed during the monitoring. Quantitative observations at a finer spatial and temporal scale could help to model more accurately the smoothing and deposition processes. Similarly, the erosion processes are not exactly reproduced. Indeed, erosion is never simulated on the plates located between 0.8 and 1.5 meter above base level, in constrast to the observations. This would suggest that the chosen critical shear stress for erosion is too high. However, there are also many cases where erosion is simulated on the 0.5–0.7 plates while it was not observed. Setting a lower critical shear stress would lead to a greater overrepresentation of this process. It is possible that, as sediment deposits are not homogenous along the banks, the critical shear stress is variable in time and space. Again, a better constrain of this parameter by field measurements is required to improve the model. Finally, due to eddies and to the irregular shape of the conduit cross sections, flow velocities are also spatially variable even at small scale. However the model simulate a mean flow velocity a the scale of each conduit. Overall, considering that the model is a simplified implementation of competing, complex processes, it predicts plausible outcomes.

The conduit shear stress and velocity fields, computed for a period of 11 year following the flow rate time series recorded at the outlets of the system, give insight into the sedimentary dynamics over the entire modeled area. In the perennial stream conduit and in the lowest epiphreatic conduit, shear stress and velocity are sufficient under high flow conditions for both erosion and full suspension of the sediment. In-

Figure 3.13: The scarp of a sediment slump is visible on the left bank of the stream in the above picture. (Photo: M. Covington)

put from both remobilized (autochthonous) and soil derived (allochthonous) turbidity is thus expected at the springs during flood events. Deposition of larger particles (d_{95}) is also predicted by the model in these conduits. Piles of sediment are indeed visible on the banks of the stream. But, similarly to what was observed at the sedimentation monitoring station, these piles seems unstable over the medium term, as slumps are found elsewhere along the cave stream (Blant et al. (2010) and Fig. 3.13). These slumps could have a significant effect on the overall sediment mass balance in the system by enhancing sediment availability in the neighbourhood of the stream, where they are more easily eroded. Because of this, and as the model predicts that the conditions required for erosion are frequent, it is possible that there is a balance between accumulation and erosion of sediment in the medium term.

In contrast, in the uppermost epiphreatic passage, the shear stress never reached the threshold for erosion. Furthermore, in the simulation, there was a constant deposition of larger (d_{95}) particles and frequent deposition of medium size (d_{50}) particles. These passages thus act effectively as sediment traps in the medium term. This is consistent with the anecdotal evidence of net sediment accumulation, especially in the former show cave.

Chapter 4

Suspended sediment evolution at the event scale

4.1 Introduction

At karst springs, the suspended sediment concentration may rise quickly in response to storm events. The origin of the discharged particles and the timing of their breakthrough have been for a long time of interest to karst scientists. In particular, in the context of spring vulnerability assessment, many methods aiming at differentiating aquifer derived (autochthonous) from soil derived (allochthonous) turbidity have been proposed.

Autochthonous turbidity is created by the resuspension of previously deposited sediment in the karst conduits. It precedes the arrival of allochthonous material, which is eroded from the surface and transported to the spring over the course of one event. A sudden electrical conductivity drop, which may be indicative of freshly infiltrated water, is considered by many as a good tracer for the arrival of allochthonous turbidity (Ryan and Meiman, 1996; Valdes et al., 2006; Schiperski et al., 2015b). As surface soils are much richer in organic content than intrakarstic sediments, natural fluorescence of dissolved and suspended organic matter is another example of such tracers (Auckenthaler et al., 2002; Pronk et al., 2006). Fecal coliform concentrations at karst springs have also been of particular interest due to their sanitary implications. Issued on or just below the surface by agriculture and/or sceptic tanks, they are frequently found in karst groundwater and springs, even in catchments feed by diffuse autogenic recharge. Several authors reported that fecal coliforms are in fact stored in soils or at the soil/epikarst interface and are released to the aquifer by flood pulses (Pasquarell and Boyer, 1995; Gunn et al., 1997; Knierim et al., 2015). The particle size distribution (PSD) of suspended particles, although largely affected by the aquifer hydrodynamics (Atteia and Kozel, 1997; Reed et al., 2010), is in some cases useful to identify sediment sources (Lacroix et al., 2000; Pronk et al., 2007). Overall, a large panel of techniques to differentiate autochthonous and allochthonous turbidity exists, although their applicability varies depending on study sites (Schiperski et al., 2015a). What stands out is that theses methods are based solely on water chemistry and suspended matter composition at the spring and do not account for sedimentary processes taking place within the karst system.

This chapter presents a synthesis of the Saivu spring monitoring using the aforementioned methods. An annual monitoring with biweekly sampling was carried out, along with a flood event monitoring with a finer time resolution (hourly to bi-hourly). Furthermore, to assess whether the resulting interpretations are consistent with the sedimentary processes occurring inside the karst network, they are compared with the simulations produced by the hydro-sedimentary model developed in Chap. 2 and 3. Finally, the turbidity variations during flood events as recorded through a ten year monitoring in the underground stream and at the Saivu spring are also analyzed.

4.2 Methodology

4.2.1 Annual and event monitoring of suspended solids at the Saivu and Bâme springs

Discharge and water quality at the Saivu and at the Bâme springs have been monitored with a 5 minute time interval from February 2015 to February 2016. The water stage has been monitored (Solinst Levelogger and Barologger Edge Model 3001, overall accuracy of 6 mm) and converted to discharge using rating curves. An existing rating curve was used for the Saivu spring and a new one was established by salt dilution gauging at the Bâme spring (Chap. 2). The temperature was also measured by the Solinst Levelogger probes (resolution of 0.003°C and accuracy of 0.05°C). The electrical conductivity has been monitored with HOBO U24-001 loggers (resolution of 1 µS·cm^{-1} and accuracy of 18 µS·cm^{-1}). The turbidity and natural fluorescence have been monitored with GGUN-FL30 field fluorometers. Resolution and accuracy for turbidity measurement are 0.002 NTU and 0.5 NTU respectively. Fluorescence is measured at excitation and emission wavelengths of 365 nm and 430 nm, and is used as a proxy for organic matter concentration.

Suspended solids were analyzed using two techniques: particle size distribution of the suspended mineral grains and *E.coli* concentration. The analyses were performed on grab or automatic samples within 24 hours from sampling. For the annual monitoring, samples were taken and analyzed on average biweekly. For the flood event monitoring, automatic samples were taken hourly in the early stage of the event and then bi-hourly. The particle size distribution was measured using an Abakus mobil fluid particle counter (Klotz, Germany). Particles are sorted in 32 grain size classes between 0.9 to 139 µm. The size of the classes varies from 0.5 µm for finer particles to 39 µm for the larger ones. During the flood event, several samples were above the saturation threshold of the machine and were diluted 10 to 100 times in ultrapure water of total particle concentration below 300 particles per mL. For the bacterial analysis, 100 mL samples were filtered on Millipore 0.45 µm filter and then incubated for 2 hours on TSA (Trypticase soy agar) medium at 37°C and for 22 hours on TBX (Tryptone Bile X-Glucuronide) medium at 44°C. Annual monitoring values are given in CFU per 100 mL. During the flood event monitoring, several analyses were done on 10 mL samples due to high concentra-

tions which lead to a saturation of the filter. Results are then normalized in CFU per mL for all the measurements of the flood event monitoring.

4.2.2 Long term turbidity monitoring

As part of the environmental impact study of the construction of the A16 highway, several stations for flow rate and water quality monitoring have been set up in the Milandre system. In this chapter, flow rate and turbidity time series recorded at a 15 minute time interval from 2003 to 2015 at the Saivu and Bâme springs, at the most upstream station in the Milandrine and in the *Bure* tributary are analyzed. The location of these monitoring stations are shown in Fig. 4.1.

Water stage was monitored with MADD probes and converted to flow rate by rating curves. At the Saivu spring, the turbidity monitoring is provided by a Sigrist photometer (models KTJ25 and WTM500). In the underground stream, turbidity is measured with a GGUN-FL30 field fluorometer. Due to frequent and intense turbidity events, the measurement is affected by fouling — i.e. the measuring tube gets covered by sediment, leading to the reading of turbidity being overestimated (Fig. 4.2). The tube was cleaned on average every 3 months. A correction was applied by estimating the effect of fouling from the turbidity drop achieved by cleaning. As flood events are more frequent than probe cleaning, the total fouling after a flood event is not always known. In such cases, total fouling is assumed to be equal to the difference between the measured turbidity after the event, once stability is reached again, and the baseline turbidity signal. Fouling is then interpolated at each time step using the assumption that the fouling rate is proportional to instantaneous turbidity (Fig. 4.2).

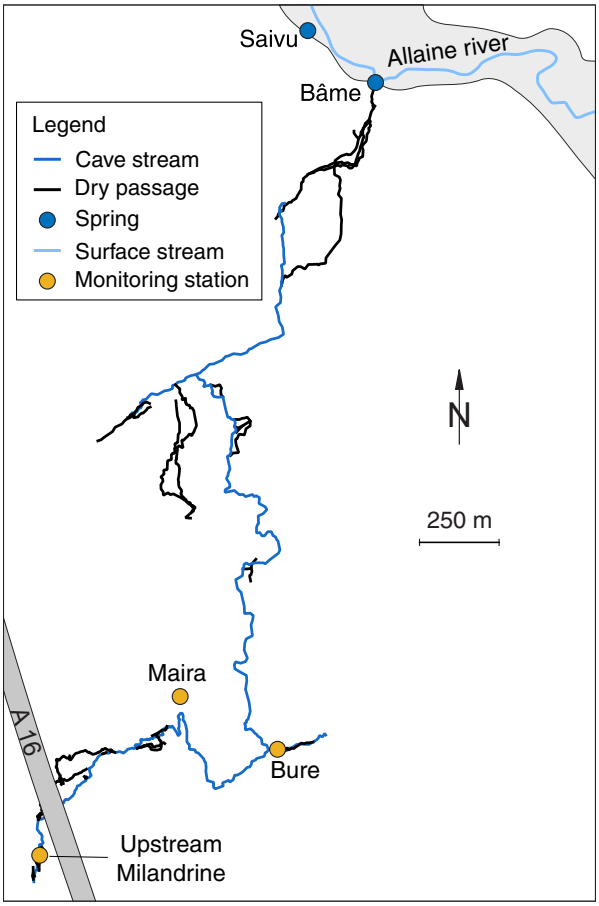

Figure 4.1: Location of the monitoring stations.

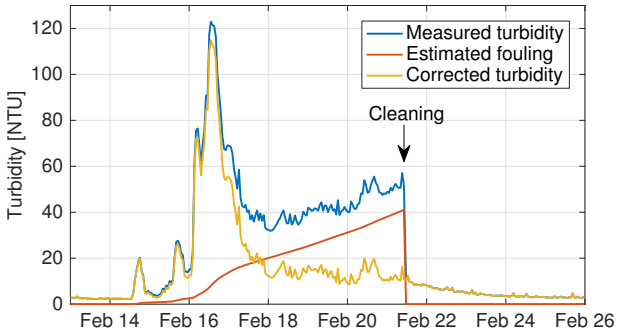

Figure 4.2: Fouling of the GGUN probe in the underground stream and the applied correction.

4.3 Results and interpretation

4.3.1 Annual suspended solids monitoring

The results of the annual monitoring of the Saivu and Bâme springs are plotted in Fig. 4.3 and 4.4. Additionally, daily rainfall at the Maira weather station, located in the middle of the catchment (Fig. 1.3), is also shown.

At the Saivu spring, the discharge varied between 15 and 200 $L{\cdot}s^{-1}$. The lowest discharge is observed during the end of October and in November, after particularly dry summer and fall seasons. The highest discharge peaks were reached during flood events in the spring and in the winter. The discharge threshold of about 90 $L{\cdot}s^{-1}$, above which the Bâme starts to flow, is well visible in the data. Indeed, the flow rate was between 80 and 100 $L{\cdot}s^{-1}$ during one third of the total monitoring period. In contrast, the Bâme spring was dry for half of the monitoring period, and some of its discharge peaks are equal to or greater than 2 $m^3{\cdot}s^{-1}$.

Recharge events are also associated with changes in water quality. At the Saivu spring, the electrical conductivity has a baseline value of approximately 610 $\mu S{\cdot}cm^{-1}$ and decreases by roughly 100 $\mu S{\cdot}cm^{-1}$ during flood events. The temperature is often stable at 10.2°C and generally, but not always, increases

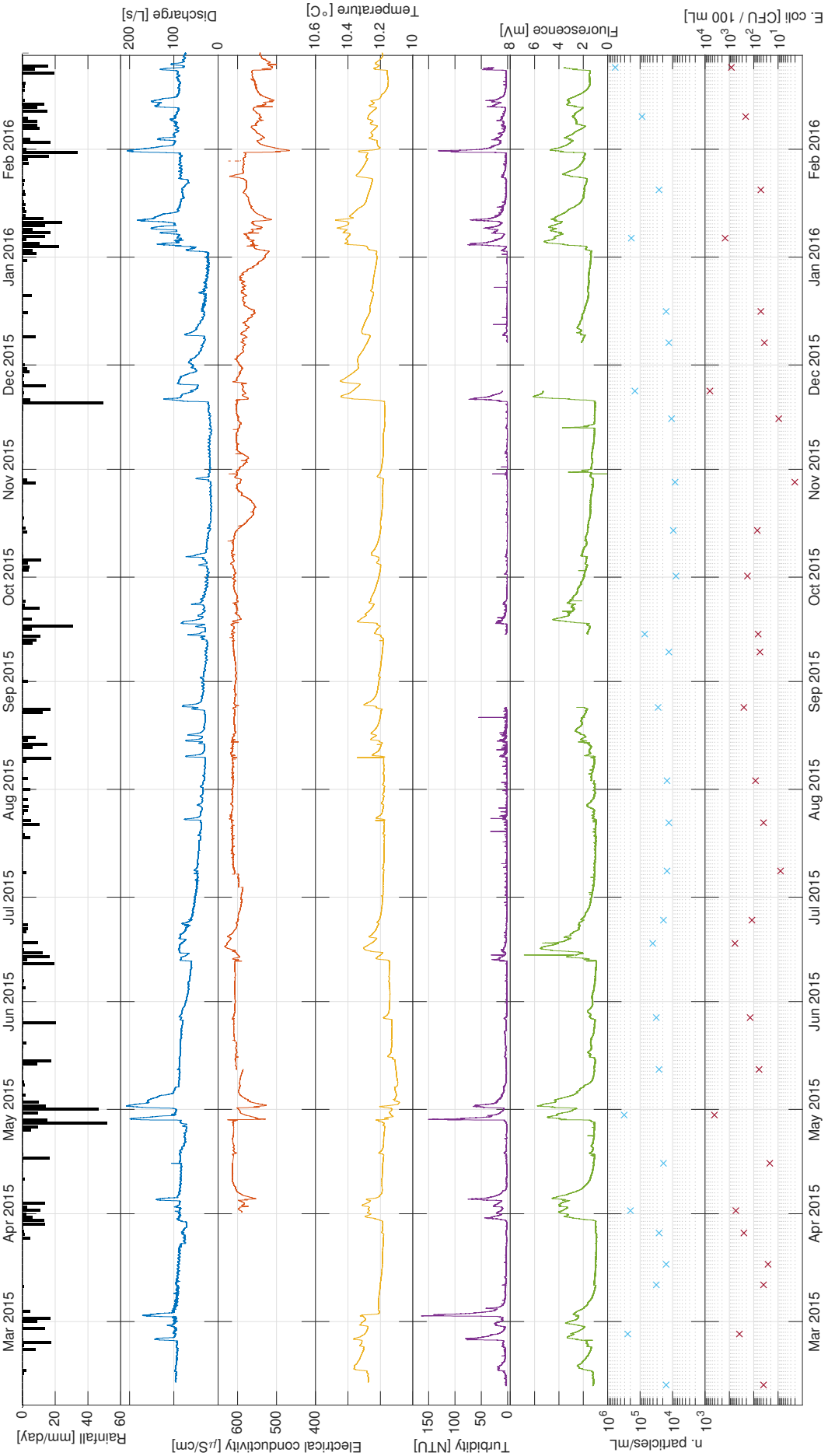

Figure 4.3: Annual monitoring of discharge, electrical conductivity, temperature, turbidity, natural fluorescence (15 minute time step), suspended sediment and *E. coli* concentrations (biweekly) at the Saivu spring.

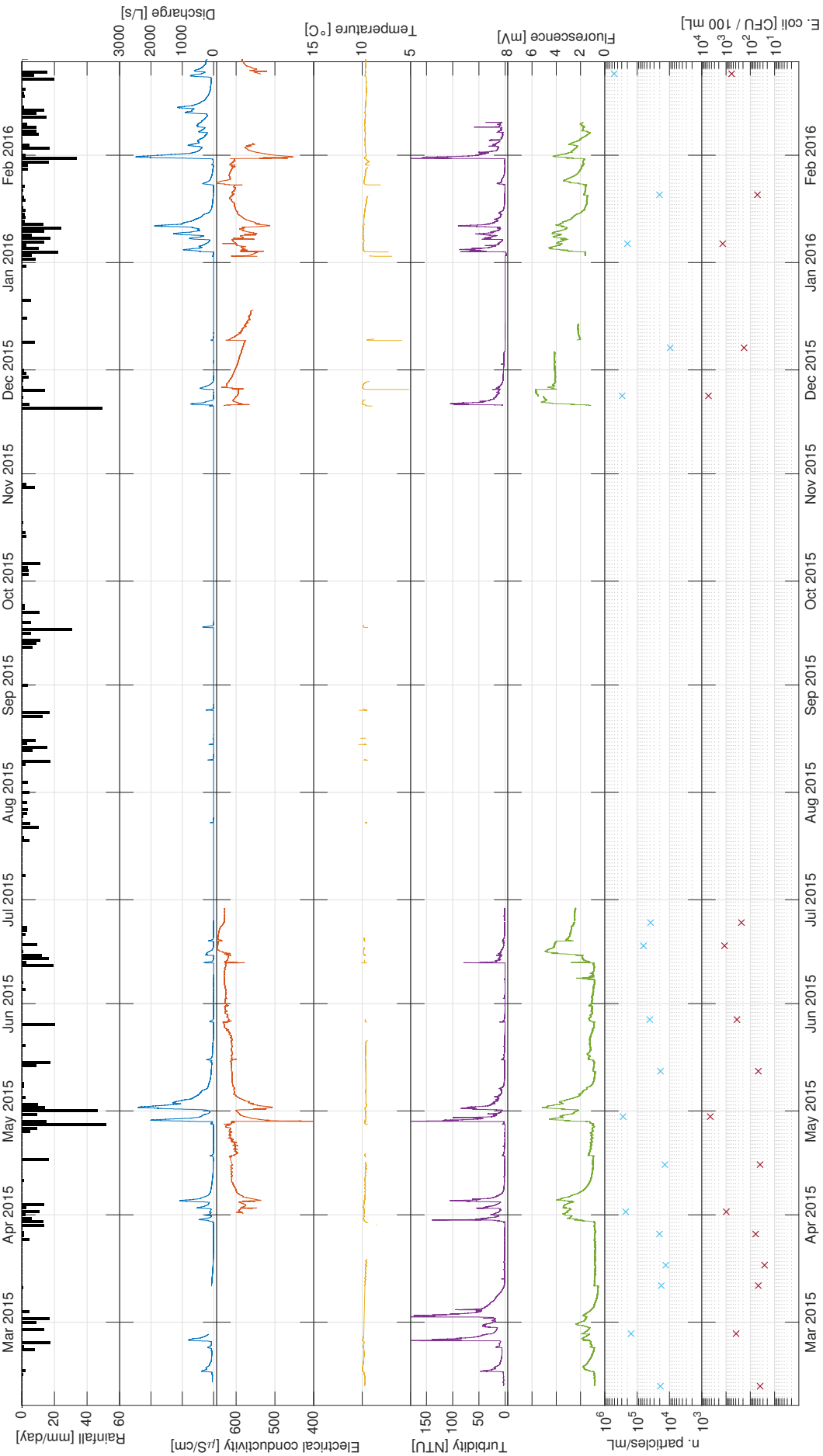

Figure 4.4: Annual monitoring of discharge, electrical conductivity, temperature, turbidity, natural fluorescence (15 minute time step), suspended sediment and *E. coli* concentrations (biweekly) at the Bâme overflow spring.

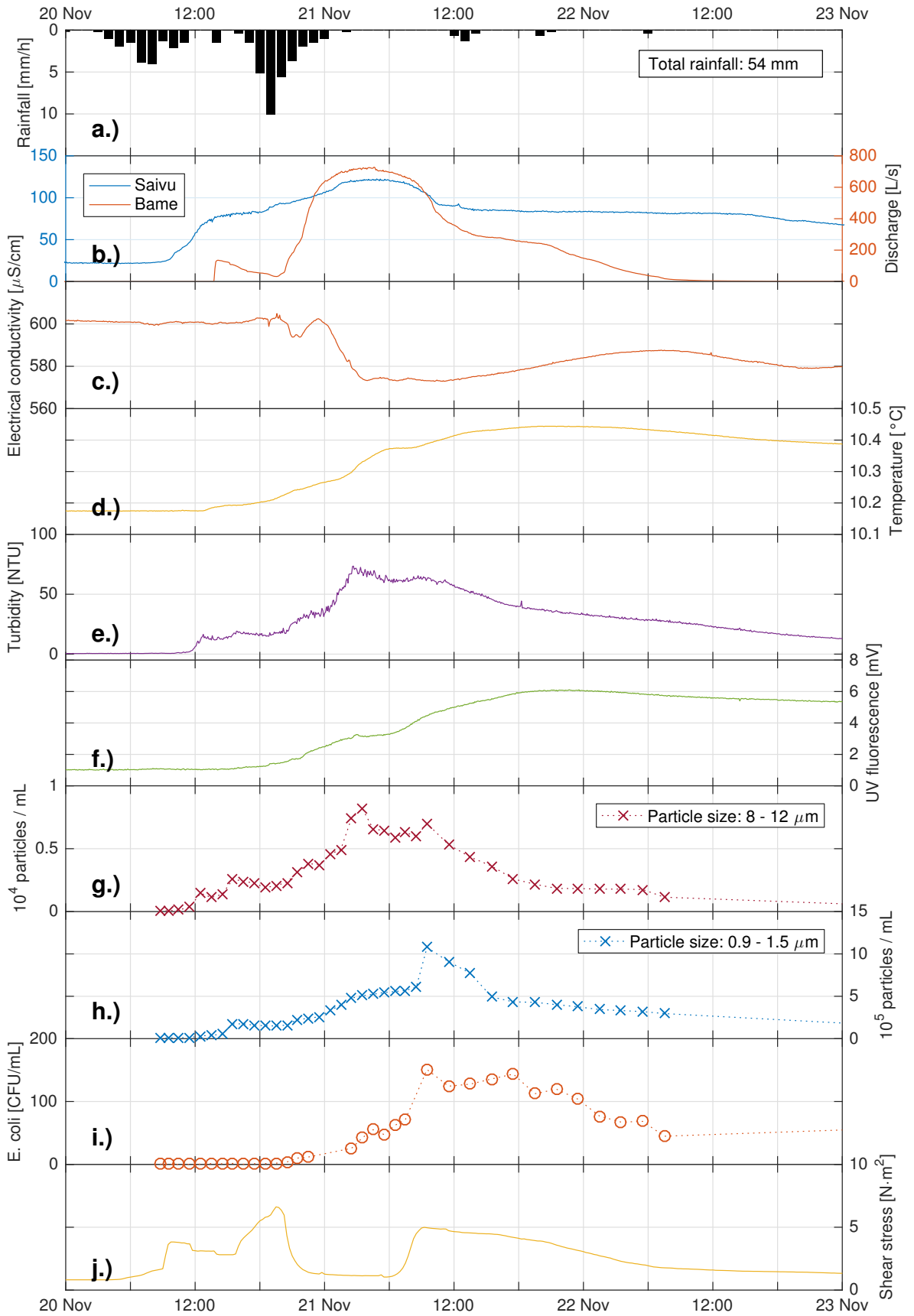

Figure 4.5: Flood event monitoring at the Saivu spring: spring discharge, electrical conductivity, temperature, turbidity, natural UV fluorescence, suspended particle concentration (8–12 µm and 0.9–1.5 µm), *E.coli* concentration and shear stress in the underground stream as computed by the hydraulic model (mean value of all the stream conduits).

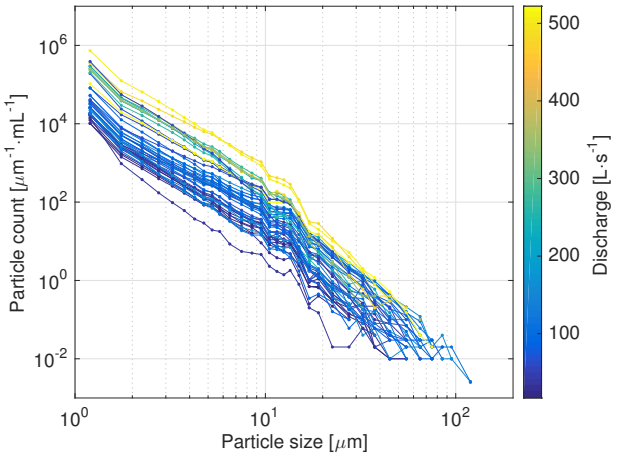

Figure 4.6: Particle size distribution in all the samples taken during the 2015 annual monitoring. On the x axis, the median grain size for each bin is plotted (dots). The y axis represents the concentration of particles measured in the corresponding bin (number of particle per mL), normalized by the size of the bin in µm. The lines are a linear interpolation between those points and the color scale corresponds to the total discharge of the system at the time of the sampling.

during high flow. The maximum amplitude of increase is 0.25°C. As for turbidity, it varies between 1 NTU during stable flow conditions to 150 NTU during the most intense events. Fluorescence also increases during flood events, going from 1 mV to maximum 6 mV. Fluorescence peaks are wider and smoother than turbidity peaks. Apart from temperature, physico-chemical parameter variations at the Bâme spring are in line with those of the perennial spring. As the overflow spring discharges in a natural pool, water temperature is affected by sunlight exposure and atmospheric temperature and is thus not always representative of groundwater temperature.

Fig. 4.6 shows the bin size normalized PSD for each sample taken during the annual monitoring. On average, 95% of the counted particles are smaller than 3.4 µm and particles seldom exceed a size of 70 µm. Accounting for both springs, the total number of suspended particles measured by PSD analyses (0.9 to 139 µm) on biweekly samples lies between $7.8{\cdot}10^3$ to $5.9{\cdot}10^5$ particles per mL (Fig. 4.3 and 4.4). The geometric mean is of $3.9{\cdot}10^4$. *E.coli* was detected in each sample, with concentrations varying between 2 to $6{\cdot}10^3$ CFU per 100 mL and a geometric mean of 145 CFU per 100 mL.

These variations by several orders of magnitude, both in suspended particles and fecal bacteria concentrations, appear to be largely influenced by the hydrodynamics of the karst system. In a log-log space, the correlation coefficient of particle concentration vs total discharge is 0.76, and 0.52 for *E.coli* concentration vs total discharge. At this sampling resolution, no seasonal patterns are visible. It rather seems that there is a constant availability in particles and fecal bacteria and that their fluxes are controlled by the hydrodynamics of the system. Regarding fecal bacteria, they are likely released by agriculture. Both pastures and cultivated areas are present in the Milandre catchment. Fecal bacteria input is thus expected to follow a seasonal pattern, as manure spreading is allowed only during the growth period — on average, from March to early November. As *E.coli* is present at the spring all year round, it is likely that a storage exists and that it is flushed towards the aquifer by storm events, as suggested by previous authors (Pasquarell and Boyer, 1995; Gunn et al., 1997; Knierim et al., 2015).

4.3.2 Monitoring of suspended solids during an event

Event description

To monitor the evolution of suspended matter content at the scale of a flood event, frequent samples (hourly to bi-hourly) were taken throughout an event in November 2015 (Fig. 4.5). Before the rain, low flow conditions prevailed in the aquifer, with a stable discharge of 22 $L{\cdot}s^{-1}$ at the Saivu spring and a dry Bâme spring. At the Maira weather station, rainfall started early in the morning on Nov 20 (Fig. 4.5a). Two rainfall pulses occurred throughout the day and in the following night, totalling 50.5 mm. The Fahy weather station recorded 50 mm of total and effective precipitation for the same time period. The discharge started to increase at 9:00 at the Saivu spring and peaked at 122 $L{\cdot}s^{-1}$ at 5:00 the next day (Fig. 4.5b). The Bâme spring started to flow at 14:00, Nov 20, and reached a maximum discharge of 725 $L{\cdot}s^{-1}$ at 16:00, Nov 21. Due to a failure of the automatic sampler at the Bâme spring, only the samples taken at the Saivu spring are discussed hereafter.

Interpreting PSD data

Fig. 4.7 shows the PSD for each sample taken during the Nov 2015 flood event monitoring. Particle concentrations are generally slightly higher than those measured during the annual monitoring (Fig. 4.6) and larger particles are relatively more abundant. On average, 95% of the particle were smaller than 5.4 µm. To try to extract information from the PSD data, the relationships between particle size class concentrations and other variables are investigated. Fig. 4.8a shows the correlation coefficient and the coefficient of determination between the total discharge (sum of Saivu and Bâme springs) and the particle concentration for 24 size classes (0.9 to 35 µm) throughout

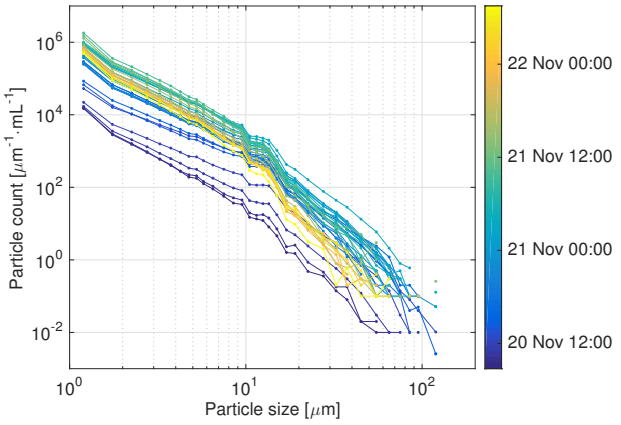

Figure 4.7: Particle size distribution in all the samples taken during the 2015 flood event monitoring. On the x axis, the median grain size for each bin is plotted (dots). The y axis represents the concentration of particles measured in the corresponding bin (number of particle per mL), normalized by the size of the bin in µm. The lines are a linear interpolation between those points and the color scale corresponds to the sampling time.

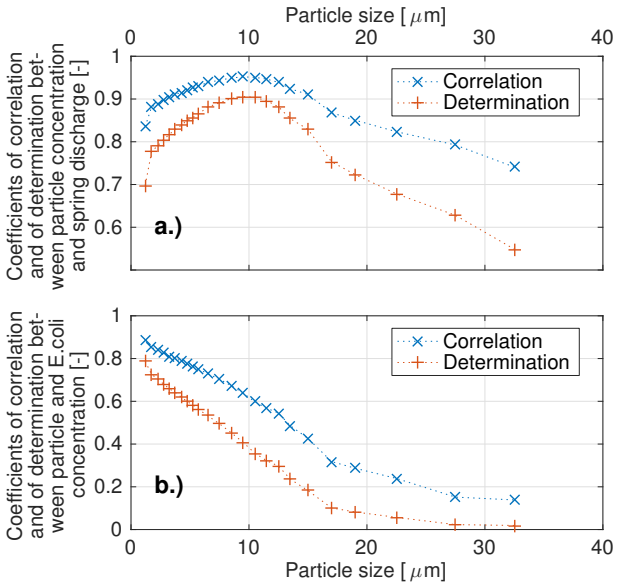

Figure 4.8: Coefficient of correlation and of determination between particle size class concentrations and spring discharge (a) and between particle size class concentrations and *E.coli* concentration (b). Log10 values are considered for particle and bacteria concentrations.

the flood event. Size classes above 35 µm are not considered due to very low particle counts, reaching zero in some samples. Log10 values are considered for particle concentrations, as they have a lognormal distribution. Although every class between 0.9 and 35 µm is well correlated with discharge (>0.5), a maximum of 0.95 is reached at classes 8–9, 9–10, 10–11 and 11–12 µm. They also have a high coefficient of determination of 0.9. Those four classes are thus mainly hydrodynamically controlled particles and are grouped together in Fig. 4.5g. Fig. 4.8b shows the correlation coefficient and the coefficient of determination between *E.coli* and particle size class concentrations. Log10 values are considered for each pair of variables. The smallest and most abundant particles (0.9–1.5 µm) are less correlated with discharge than with *E.coli* concentration. The correlation coefficient is of 0.89 for 0.9–1.5 µm particles and decreases gradually for larger particles. 30–35 µm particles are virtually not correlated with *E.coli* concentration (0.14). Similarly, the coefficient of determination goes from 0.79 (0.9–1.5 µm) to 0.02 (30–35 µm). As *E.coli* bacteria typically have a size of 1 µm, a high correlation with 0.9–1.5 µm is expected. This size class is thus selected as a variable highly correlated with *E. coli* concentration and its concentration evolution is plotted in Fig. 4.5h.

Suspended solids evolution

Fig. 4.5 shows the evolution of 10 variables throughout the event. At the spring, discharge is the first parameter to respond, around 9:00 on Nov 20. Turbidity starts to increase three hours later. As electrical conductivity and temperature are stable, this initial turbidity increase is likely caused by intra-karstic sediment remobilization. Both UV fluorescence and *E.coli* concentration stay at their baseline value at this stage, which further confirms the arrival of autochthonous turbidity. At the same time, a step wise increase in larger (8–12 µm) particles occurs, while finer (0.9–1.5 µm) particle concentration is stable. This is an indication that autochthonous turbidity is characterized by a relatively large grain size. Turbidity has a stable value around 15 NTU for the next ∼7 hours.

Around 21:00, as the Saivu spring discharge continues to rise, turbidity increases further. Simultaneously, UV fluorescence and *E.coli* concentration also rise, indicating the presence of allochthonous turbidity. At this stage, there is probably a mix of autochthonous and allochthonous turbidity at the spring. Turbidity reaches its peak value of 73 NTU at 02:30 on Nov 21, and stays at a high level until 12:00. PSD and *E.coli* data reveal more information on this high turbidity stage. The peak in larger particles was measured at 3:30, almost at the same time as the turbidity peak. Fine particles, on the other hand, peak several hours later, at 9:30, simultaneously with *E.coli* bacteria. Since 8–12 µm particles started to increase early in the event, they are considered to indicate the presence of autochthonous turbidity. The larger particle (8–12 µm) peak is thus interpreted as the peak contribution of autochthonous turbidity. Because of its simultaneity with the fecal bacteria, the fine parti-

cle peak is interpreted as the allochthonous turbidity peak. Shortly after, at 11:00, turbidity starts to recede, together with both fine and larger particles.

Indications from the hydraulic model

The PSD and *E.coli* data suggested that the turbidity pulse during the November 2015 flood is in fact an overlay of an autochthonous turbidity peak and an allochthonous one, the former slightly preceding the latter. Can the hydro-sedimentary model developed in Chap. 2 and 3 confirm this hypothesis? Fig. 4.5j shows the mean boundary shear stress in the underground stream throughout the flood event as computed by the model. For this plot, the simulated mean boundary shear stress in each conduit in the underground stream is averaged for each simulation time step. As described in Chap. 2, each conduit corresponds to a line-of-sight of the cave survey and the conduit cross sections are rectangles whose dimensions are read from the cave survey map. The results of the flow simulation described in Chap. 3 are used. This simulation covers the 2004–2015 period. The cumulative Saivu and Bâme spring discharge are used as the inflow applied at the upstream of the model. Here, the inflow is shifted earlier in time by 4:30 hours, in order that the initial discharge increase at the Saivu spring corresponds to what was actually observed at the spring.

Mean boundary stress in the conduits shows a two step increase in the initial stage of the event. This is probably caused by the two phased rainfall pulse (Fig. 4.5a). Between 10:00 and 16:00 on Nov 20, the average shear stress plateaus around 3 to 4 $N{\cdot}m^{-2}$, which is enough for significant erosion. This is in line with the initial turbidity plateau at the Saivu spring, which was interpreted as autochthonous in the previous section. The model predicts a maximum shear stress of 7 $N{\cdot}m^{-2}$ at 19:30. This corresponds to the time where the underground stream has the strongest erosive power. Taking into account the fact that the model predicts a 9 h transit time from the underground stream to the outlet at this stage of the event, this is compatible with the autochthonous peak observed at 3:30 at the spring. The shear stress peak is quite narrow and shear stress rapidly decreases although the flow rate is still increasing. Again, this does not contradict the arrival of the allochthonous peak detected at 9:00 at the spring, since it corresponds to a period of relatively low shear stress in the conduits. However, since the model includes only the downstream part of the conduit system and does not simulate the transfer of particles, it cannot give further insight into allochthonous turbidity transport. Later on, at 7:00, a secondary shear stress peak is predicted by the model at the onset of the event recession — as the system is draining, the stream regains erosive power. This is in line with the results from Chap. 3: at the sedimentation monitoring station, where on several instances, erosion was observed in the lower part of the conduit while deposition was visible in the upper part. This can be understood in the sense that the hydraulic gradient is higher during the flooding and draining of the system that at the flood peak. Hydraulic head monitoring in Chap. 2 indeed showed relatively low gradient in the karst network at the event maximum. However, no evidence for a secondary autochthonous peak was found at the spring through the flood event monitoring.

4.3.3 Long term turbidity monitoring

Milandrine upstream station

The monitoring station at the upstream end of the Milandrine is of interest with regards to event scale turbidity variations for several reasons. For instance, Blant et al. (2012) reported anomalous wide turbidity peaks appearing one or two days after recharge events and lasting for two days. These were not seen at the Saivu spring. Fig. 4.9a shows an example of one such event. They are of moderate intensity and occur during otherwise low flow conditions. They are characterized by a first narrow turbidity peak, lasting a few hours, which is simultaneous with the discharge peak. The secondary turbidity peak is of smaller intensity, lasts for one to two days and occurs once the flow rate is back to its pre-event value. They do not appear systematically and seem to be more frequent in the summer. Pronk (2008), analyzing two such events by monitoring turbidity and TOC, suggested that the wide turbidity peak is caused by the arrival of allochthonous sediment.

In the 10 year time series of flow rate and turbidity, another type of secondary turbidity peaks appears. They are produced during more intense flood events and have the distinctive feature of appearing during flow recession. An example is shown in Fig. 4.9b. Again, these secondary peaks are less intense than the primary ones, but they are relatively short, lasting for a few hours. And, in contrast with the first type of secondary peaks, they can occur up to one week after the mean discharge peak. Their common features is that they appear when the stream discharge starts to recede after a several days period where it had a stable value around 200 to 300 $L{\cdot}s^{-1}$. This flow rate threshold is visible in the flow relative frequency distribution, which has a local maximum around 270 $L{\cdot}s^{-1}$ (Fig. 4.10). It has already been described by Pantillon (1993) who explained it by the presence of a scree at the upstream end of the Milandre cave network. This scree impedes groundwater flow and induces an increase in hydraulic head on its upstream side, thus acting similarly to a dam.

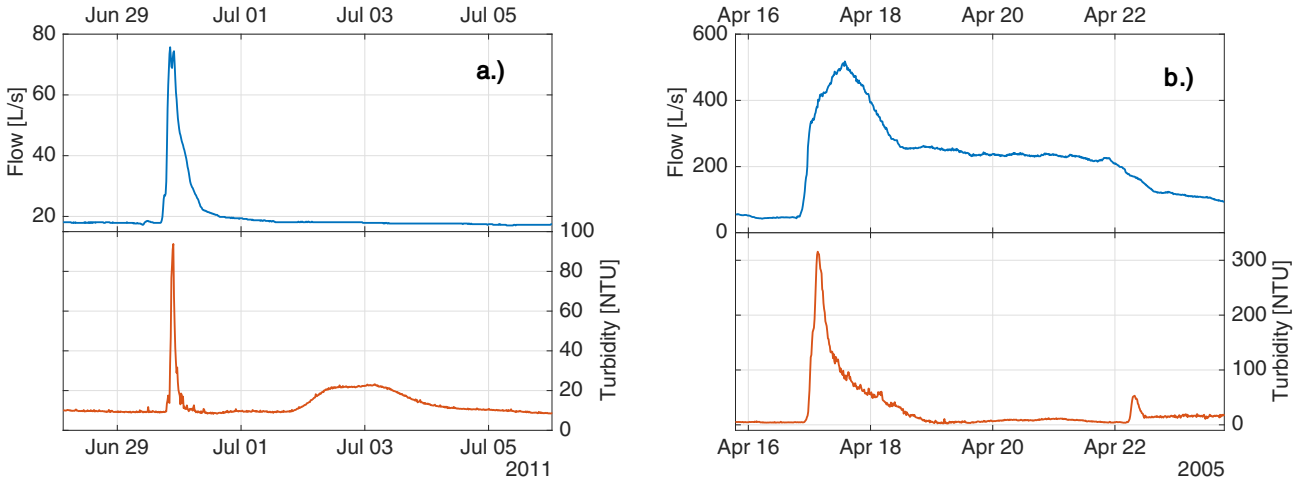

Figure 4.9: Flow rate and turbidity variations during two flood events at the upstream station in the Milandrine underground stream.

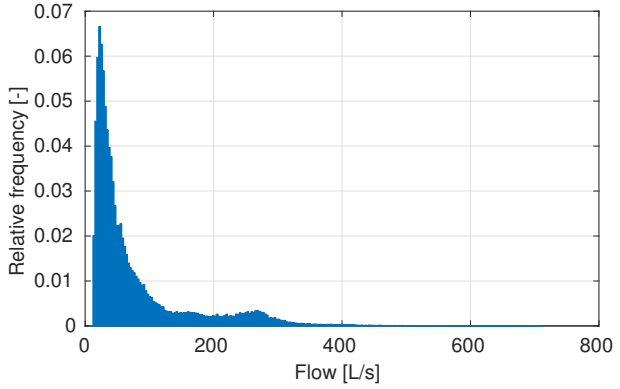

Figure 4.10: Flow relative frequency distribution of the upstream Milandrine discharge from 1998 to 2013.

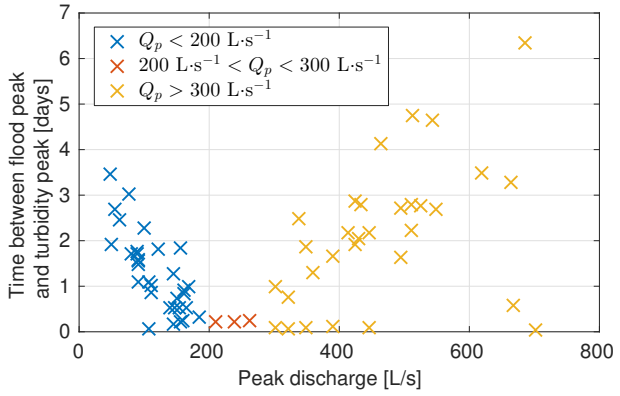

Figure 4.11: For 66 events recorded at the upstream Milandrine station, the event peak discharge (Q_p) is plotted against the time between the peak discharge and the secondary turbidity peak.

In an attempt to gain understanding on the mechanisms controlling the appearance of secondary turbidity peaks, discharge and turbidity time series were analyzed and the following variables were defined for each flood event displaying several turbidity peaks: initial discharge, peak discharge, primary turbidity peak and secondary turbidity peak, as well as the time of the initial flow increase, of the discharge peak and of the primary and secondary turbidity peaks. If the event displayed more than two turbidity peaks, the first peak is always considered the primary peak, and the following ones are successively regarded as secondary peaks, so that one flood event may appear several times in the data set. The total number of events is 66 and they are depicted in App. II. No strong relationship emerges between turbidity peak intensity and flow rate. However, an interesting pattern appears when plotting discharge peak value (Q_p) vs the time between the flood peak and the secondary turbidity peak (Fig. 4.11). Three groups of events can be distinguished:

$Q_p < 200$ L·s^{-1} The time between the flood peak and the secondary turbidity peak decreases when peak discharge increases

200 L·s^{-1} $< Q_p <$ 300 L·s^{-1} No visible effect of the peak discharge on the time between flood and secondary turbidity peak

$Q_p > 300$ L·s^{-1} The time between the flood peak and the secondary turbidity peak increases when peak discharge increases

The first category of events is compatible with the advection of soil sediment from the surface — the higher the flow rate, the faster the flow velocities. The wide shape of the peak also indicates a relatively long transport, which allows some dispersion. This implies that the primary turbidity peak is caused by

sediment remobilization in the aquifer, meaning that a sediment accumulation zone also exists upstream from the Milandrine. For peak discharge nearing 200 $L{\cdot}s^{-1}$, the delay between the flood peak and the secondary turbidity peak approaches zero. Autochthonous and allochthonous turbidity probably overlap at higher discharge, as observed at the spring in Sec. 4.3.2. However, this interpretation does not hold for the third category of events. More importantly, the secondary turbidity peak during those events is associated with the onset of flow recession (Fig. 4.9b and App. II). The higher the flood peak, the longer before flow recession, explaining the positive relationship between peak discharge and the time between flood peak and the secondary turbidity peak. Rather, as seen in Sec. 4.3.2, these peaks could be issued by a secondary erosive phase initiated by the flushing of the epiphreatic zone during flow recession.

Saivu and Bâme springs

To analyze the turbidity variations at the Saivu spring, the total discharge of the Bâme and Saivu springs is considered, as it represents almost the total discharge of the system. The turbidity response at the Saivu spring is often plurimodal and cannot be easily separated in different peaks such as at the upstream end of the Milandrine (Fig. 4.12). Indeed, while the turbidity observed at the uptream end of the Milandrine likely contributes to the turbidity at the Saivu spring, other turbidity inputs reach the cave stream: the *Bure* and the *Droite* tributaries, who each contributes to almost a third of the total discharge of the Milandrine, and the downstream epiphreatic zone, where previously deposited sediment are remobilized. As a result, the turbidity signal at the Saivu spring is a superimposition of these different contributions. Some insight can be gained into these processes by comparing the turbidity signal in the underground network and at the spring, as done in Fig. 4.12. In this figure, two events belonging to the data set described in the previous section are shown. At the upstream station, these events generated a primary turbidity peak during the flood event, which is interpreted as autochthonous, and a secondary, very dispersed peak which is interpreted as allochthonous. The turbidity signal in the *Bure* tributary is analogous to the upstream Milandrine signal, although the secondary peak is less delayed. At the Saivu spring, the primary turbidity peak has an irregular shape. No secondary peak is observed for the event represented in Fig. 4.12a, which is of low amplitude with a peak discharge at the springs of less than 200 $L{\cdot}s^{-1}$. For the event of Fig. 4.12b, of slightly higher amplitude with a peak discharge of 350 $L{\cdot}s^{-1}$ at the springs, a very dispersed secondary turbidity peak is detected at the spring two days after the flood peak. Four other events of the same data set, with peak discharges between 300 and 400 $L{\cdot}s^{-1}$ (09.2005, 05.2006, 06.2008, 03.2011), displayed a similarly delayed and flattened secondary turbidity peak appearing one or two days after the flood peak. The proposed interpretation of the turbidity response of the Saivu spring to low amplitude events is that the primary turbidity peak is composed of a superimposition of autochthonous turbidity contributions from the three subcatchments and from the

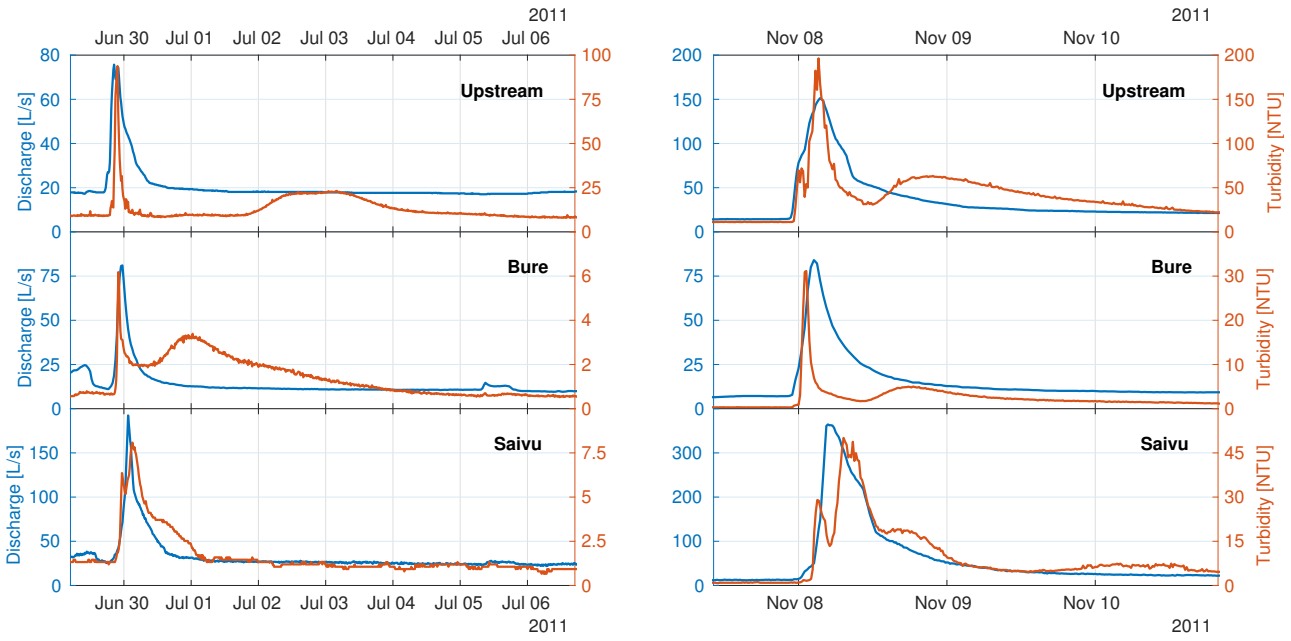

(a) July 2011 flood event

(b) November 2011 flood event

Figure 4.12: Discharge and turbidity variations during two flood events at the upstream end of the Milandrine, in the *Bure* tributary and at the Saivu spring. In the last case, the total Saivu and Bâme discharge is plotted.

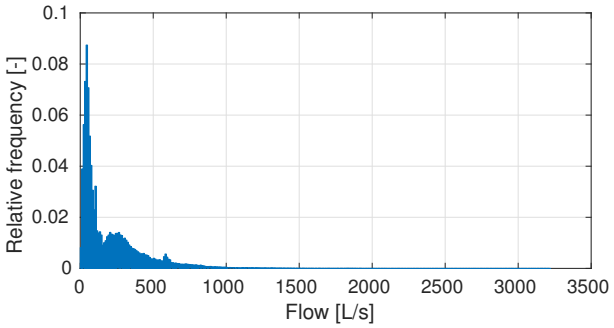

Figure 4.13: Flow relative frequency distribution of the total Saivu and Bâme discharge (2003–2015).

downstream epiphreactic zone, while the allochthonous turbidity is mostly redeposited in the conduit network or too dispersed to be detected at the spring.

Similarly to the upstream Milandrine, recession turbidity peaks may be observed during major flood events ($Q_p > 1$ m^3·s^{-1}) at the Saivu spring. They were already reported by Rodriguez (1996), who found that they regularly appeared when the recession starts to slow down around 600 L·s^{-1}. Indeed, similarly to the upstream Milandrine, the total spring discharge displays a threshold during recession, as evidenced by the local maximum at 585 L·s^{-1} in the flow frequency distribution in Fig. 4.13. It is also well visible during most of the events depicted in Fig. 4.14. Looking through the turbidity time series from 2003 to 2015, secondary peaks as described by Rodriguez (1996) were again found. They are marked with dashed vertical lines in Fig. 4.14. But even more delayed secondary peaks may get to the spring: they arise after the ∼600 L·s^{-1} threshold, when flow rate further drops. They are marked by dotted vertical lines in Fig. 4.14. The relationship between secondary peak occurrences and the hydrograph seems consistent between events. Their absolute and relative intensity however varies greatly. In both cases, they appear to be triggered by a sudden decrease in flow rate, similarly to the secondary turbidity peaks found at the upstream Milandrine station during major flood events. Again, this erosive phase may be caused by the emptying of epiphreatic conduits.

The hypothesis that those recession turbidity peaks have an autochthonous origin can be tested against the hydraulic simulation produced by the numerical model. As performed for the November 2015 flood event analysis (Sec. 4.3.2), the mean boundary shear stress simulated in the conduits for most of the events of Fig. 4.14 is plotted on the same figure. In contrast with Fig. 4.5j, the average is computed from the epiphreatic conduits — i.e. all the conduits in the model, excluding cave stream conduits and dry conduits. During the main flood peaks, there may be one or two shear stress peaks. Indeed, the pattern simulated for the November 2015 flood event, i.e. a shear stress peak during the onset of the event, followed by a phase of low shear stress during high stage, again followed by a shear stress peak, is found again during the events b, d, f, i, k. This corresponds to the flooding and the emptying of the upper epiphreatic passage flowing to the Bâme spring (∼ 390 m.a.s.l.). The absence of this pattern during the other events depicted in Fig. 4.14 is here attributed to a faster sequence of onset and recession phases. The simulated shear stress peaks during the flood peak are however not linked in an obvious way to the first type of recession turbidity peaks (dashed lines in 4.14). In contrast, the second type of recession turbidity peaks, which appears after the flow threshold at ∼585 L·s^{-1} (dotted lines in Fig. 4.14), are systematically associated with a marked and lasting rise in shear stress in the epiphreatic network, which corresponds to the emptying of lower epiphreatic passage flowing to the Bâme spring (∼ 382 m.a.s.l.). This further supports the hypothesis of autochthonous turbidity production by conduit drainage during flow recession. It is interesting to note, however, that not every of such shear stress rises produces a detectable turbidity peak at the Saivu spring. Also, similary to what was found at the Milandrine station, the intensity of the recession turbidity peaks varies greatly.

These findings can be compared to the turbidity signal at the Bâme spring, which has been monitored from February 2015 to February 2016. Eight major events ($Q_p \geqslant 1$ m^3·s^{-1}) are depicted in Fig. 4.15. Turbidity values during flood events are generally higher at the Bâme spring than at the Saivu spring. During the flood peak, the turbidity signal is very chaotic, often displaying several rapid increases followed by similary rapid decreases which do not appear at the Saivu spring. These extra peaks are thus attributed to sediment remobilization in the downstream part of the system, since the Bâme spring is the outlet of the epiphreatic conduits. The recession turbidity peaks found at the Saivu spring, both before the flow rate threshold (dashed lines in Fig. 4.15) and after (dotted lines), are still observed and are even more frequent compared to the perennial spring. This confirms that these peaks are generated in the downstream part of the karst system.

4.4 Conclusions

In this chapter, the turbidity variations at the scale of flood events in the Milandre system are investigated and mechanisms for the generation of turbidity are proposed. At the Saivu spring, the monitoring of PSD, *E.coli* and water quality during a flood event in November 2015 allowed to identify a mixed contribution of autochthonous and allochthonous sediment to the spring turbidity. This flood event was of

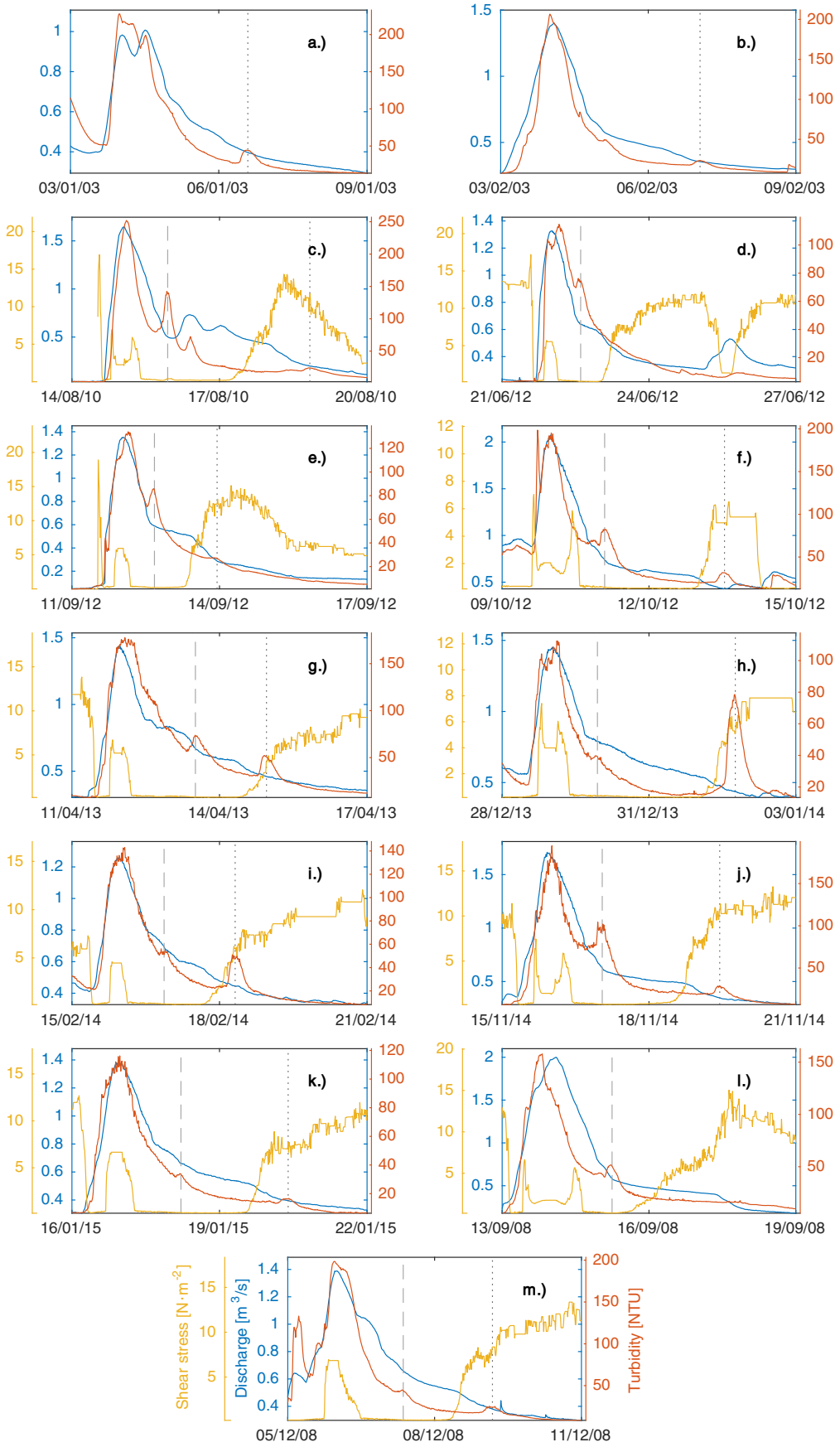

Figure 4.14: Discharge (blue), turbidity at the Saivu spring (orange) and simulated shear shear in the conduit system during a selection of major flood events. The discharge is the cumulative Bâme and Saivu flow rates. The shear stress is the mean value at each simulation time step over all the epiphreatic conduits of the model.

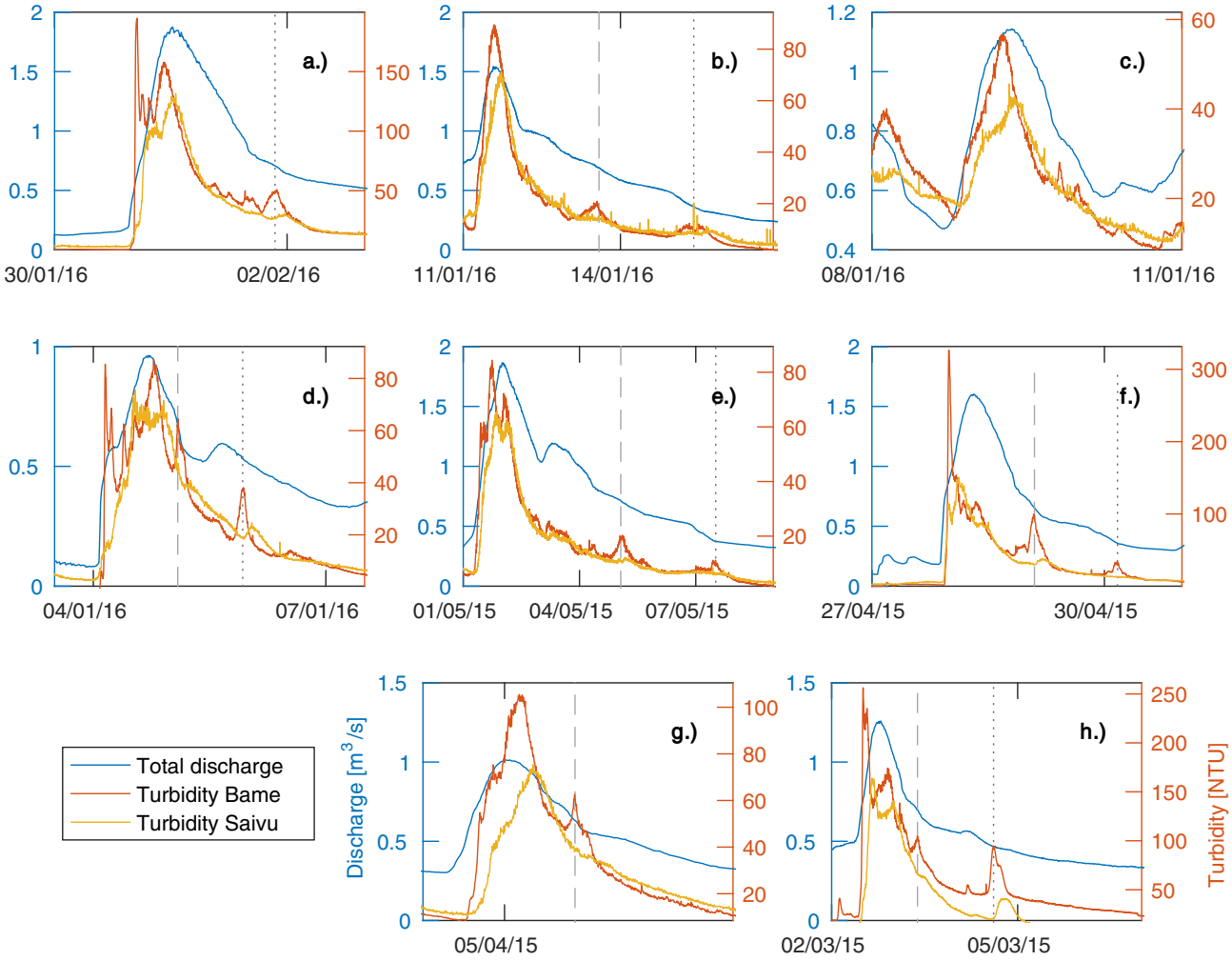

Figure 4.15: Turbidity variations during major flood events at the Bâme and Saivu springs. The discharge is the cumulative Bâme and Saivu flow rates. Recession turbidity peaks are marked by dashed and dotted lines.

medium intensity, with a cumulative peak discharge at the springs of 850 $L{\cdot}s^{-1}$ and total effective precipitation of 50 mm. While autochthonous turbidity slightly precedes allochthonous turbidity, their respective contributions seem to have been of similar intensities. Autochthonous turbidity was characterized by a relatively high content in 8–12 µm particles, low UV fluorescence and low *E.coli* concentration. Conversely, allochthonous turbidity was identified by a simultaneous breakthrough of 0.9–1.5 µm particles and *E.coli* concentration, and high UV fluorescence. Following the annual biweekly monitoring of *E.coli*, fecal bacteria are thought to be stored in soils and/or in the epikarst throughout the year and released to the aquifer during flood events. The arrival of allochthonous material to the spring during the November 2015 event is in line with the conceptual model of the system proposed by Perrin et al. (2003). Through stable isotope analyzes of rainfall and cave stream water, they stated that freshly infiltrated water may reach the saturated zone over the course of one event when infiltration is greater than 15 to 20 mm, such as for this event during which it reached 50 mm. Also, the fact the allochthonous sediment has a finer grain size than autochthonous sediment is consistent with the fact that it has been transported over longer distances, thus there is a higher probability for the potential larger allochthonous particles to have settled before reaching the spring.

The flow simulation presented in Chap. 3 yields an estimation of the mean boundary shear stress occurring in the conduits over the 2004 to 2015 period. It can thus inform on autochthonous turbidity generation during the November 2015 event. In line with the observations made at the spring, the model predicts an important erosive phase relatively early in the event, when water level increases in the conduits. Considering the transit time in the phreatic zone, there is a good match between the simulated erosive phase and the observed autochthonous peak at the spring. The model further predicts a decrease in boundary shear stress at the event maximum, which does not contradict the observed arrival

of allochthonous turbidity at the spring. During flow recession, the model indicates a secondary maximum in shear stress, which is caused by the drainage of the conduits. However, no effect of this potential secondary erosive phase was seen in the suspended sediment composition at the spring. Yet the erosive phase has a lower amplitude than the initial one. If this secondary erosive phase indeed exists, the absence of evidence at the spring could be explained either by an important re-deposition of the eroded sediment, flow velocity being receding, or because the monitoring was discontinued before this remobilized sediment reached the spring. This event scale pattern of erosion, with an initial erosive phase, followed by a quiescent phase at high stage, itself followed by a secondary erosive phase during recession is predicted by the model for other events each time a level of karst conduits is flooded and subsequently drained. This pattern is in agreement with the observations made at the sedimentation monitoring station in the main conduit of the cave stream. Indeed, there were several instances were erosion was observed on the lowest sedimentation plates in the conduit, whereas deposition was found on upper plates.

To gain insight into the overall turbidity dynamics in the Milandre system, 10 year time series of discharge and turbidity in the upstream part of the Milandrine, in the *Bure* and at the Saivu spring were analyzed. The 2015 monitoring of turbidity at the Bâme spring is also included in this data analysis. In the upstream Milandrine, a set of 66 events that generated a multi-peak response in turbidity were selected. The following observations were drawn: for minor flood events (peak discharge in the upstream of the Milandrine < 200 L·s^{-1}), an autochthonous turbidity peak occurs during the flood event, and a distinct — wider and longer — allochthonous peak may be observed up to several days after the event, once the flow rate is back to its pre-event value. The time shift between the discharge peak and the secondary turbidity peak consistently decreases as the peak discharge value increases. For more intense flood events (peak discharge in the upstream of the Milandrine > 200 L·s^{-1}), the arrival of allochthonous turbidity overlaps that of autochthonous turbidity. Again, this can be compared with the observations of Perrin et al. (2003) who sampled the cave stream at this location for their stable isotope analyzes. For a minor flood event (peak discharge of 180 L·s^{-1}), they found that no freshly infiltrated water reaches the cave stream over the course of the event. This is in line with the delay observed in the breakthrough of the allochthonous turbidity peak, which may arrive several days after the discharge went back to its pre-event value. Conversely, evidence for freshly infiltrated water in the cave stream was found during two more intense events (peak discharge in the upstream of the Milandrine of 260 and 400 L·s^{-1}), meaning that the direct transport of soil sediment is indeed possible for events of similar intensity.

The turbidity signal in the upstream Milandrine was compared to the one at the Saivu spring for a series a minor flood events (peak discharge at the Saivu and Bâme spring $\leqslant 500$ L·s^{-1}). This lead to the conclusion that most of the allochthonous sediment is deposited in the phreatic zone and does not reach the spring. In some cases, a very weak and dispersed peak was observed two days after the event. The turbidity signal during such events has an irregular shape with several secondary maximas. The turbidity signal at the Saivu spring during minor events is thus thought to be the superimposition of different autochthonous contributions coming from the subcatchment at the upstream of the Milandrine, the *Bure* and *Droite* tributaries subcatchments and in the downstream part of the Milandre catchment.

The spring turbidity during flood events of medium intensity are thought to have a mixed autochthonous and allochthonous origin, such as shown for the November 2015 event. During major flood events, the analysis highlighted the strong control of the sediment remobilization in the downstream epiphreatic conduits on the turbidity at the springs. For instance, several peaks appear in the Bâme spring turbidity signal, which is the outlet of the epiphreatic conduits, while they are absent at the Saivu spring. Furthermore, turbidity peaks associated with drops in the flow rate were identified. They appear mostly at the Bâme spring but are also visible at the Saivu spring, and are linked to the presence of a threshold in the hydrograph around 600 L·s^{-1}during flow recession. This threshold appears consistently during major flood events and is also visible in the flow frequency distribution, which indicates that it is controlled by the structure of the drainage system. These recession turbidity peaks appear both before and after the hydrograph reaches the threshold. They are thus thought to be generated by the emptying of epiphreatic conduits, which, as previously mentioned, causes a temporary increase in mean boundary shear stress. This effect is again confirmed with the hydraulic simulation for a series of those events at the Saivu spring. A similar observation is made at the upstream station in the Milandrine, where the flow threshold has a value of approximately 270 L·s^{-1}.

Chapter 5

Suspended sediment evolution on a pluri-annual scale

5.1 Introduction

The amount and the nature of the suspended matter discharged by a karst system may vary very quickly during flood events. This is the focus of Chap. 4 and of numerous studies found in the literature (Chap. 1). Fewer studies have focused on the pluriannual variations in particle fluxes through karst aquifers, and those that exist generally cover a relatively short time scale (2 to 3 years), with the exceptions of Currens (2002), who studied the impact of best management practices on fecal bacteria and sediment concentration in an agricultural catchment over 6 years, and of Chédeville et al. (2016), who managed to correlate a 20 year turbidity time series with an intrakarstic sediment core and with regional climatic events.

Moreover, several authors (Atteia and Kozel, 1997; Mavrocordatos et al., 2000; Shevenell and McCarthy, 2002; Reed et al., 2010) pointed out the dominant control of physico-chemical over hydrodynamical processes on fine particle fluxes in karst aquifers — fine particles, or colloids, generally refer to particles which diameter is smaller than 5 µm. Experiments using artificial particulate tracers (Sinreich et al., 2009; Flynn and Sinreich, 2010; Schiperski et al., 2016) showed that the hydrophobicity of the particle surface influences greatly their attenuation rate while transported through karst media. For naturally occurring suspended particles, Atteia and Kozel (1997); Shevenell and McCarthy (2002) pointed out an influence of pH and Mavrocordatos et al. (2000) suggested an effect of redox reactions. These physico-chemical processes are thus complex and have not been well characterized. In terms of groundwater vulnerability assessment, the identification of the transport processes affecting fine particles is key, because colloids are a powerful vector for contaminants (Atteia and Kozel, 1997).

This chapter presents the results of a 13 year monitoring of the suspended sediment concentration, mineralogical and granulometric content in the Milandre system. This monitoring was part of the environmental impact study of the construction work of the A16 highway. The results are analyzed with the aim of characterizing suspended sediment evolution and controlling processes in the Milandre system on a pluriannual time scale.

5.2 Methodology

The monitoring system for suspended sediment concentration and composition consists in a set of five stations, each of which is equipped with a turbidity monitoring device and a sediment trap (Fig. 5.1). Three of them are located in the Milandre underground stream network: the *Amont* and *Gal80* stations are in the upstream part of the main stream, while the *Bure* station is in the Bure tributary, one of the two main tributaries feeding the Milandrine stream. Another one is located at the Saivu spring, the perennial outlet of the system. A fifth station is set up at the Beuchire spring in Porrentruy, the outlet of an adjacent karstic catchment located south of the Milandre catchment. The Beuchire spring was chosen as a point for comparison with the Milandre system in order to assess a potential impact of the highway construction work on the groundwater suspended sediment content. The Beuchire catchment is also crossed by the A16 highway, but the major construction works occurred before and after those affecting the Milandre system. Potential impacts of the

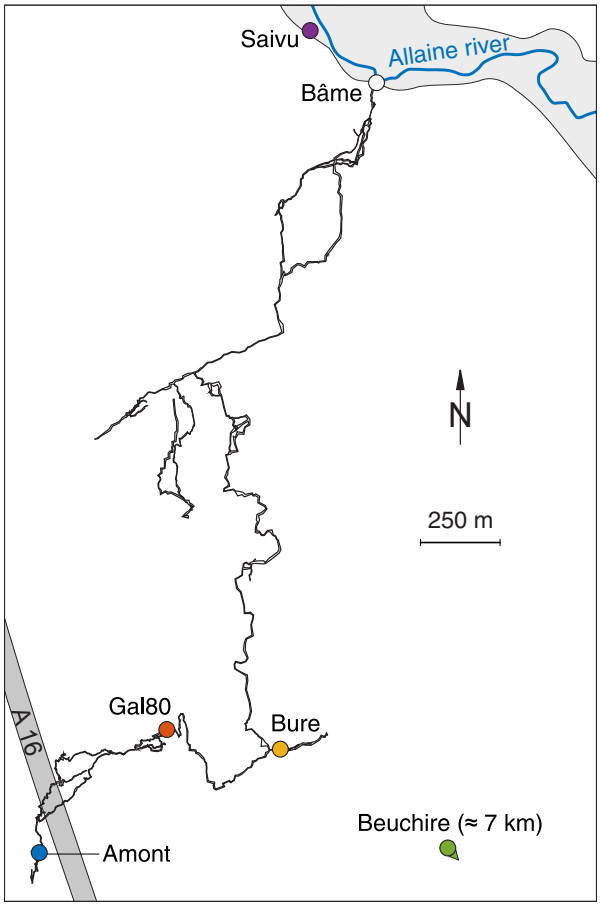

Figure 5.1: Map showing the location of the sediment traps (coloured circles) on the cave survey (black). In pale grey is the Allaine alluvial plain and in dark grey, the highway. The Bâme overflow spring (white circle) was not monitored for sediment composition and concentration but its discharge is used, in addition to the Saivu spring discharge, to estimate the sediment fluxes flowing out of the Milandre system. The Beuchire spring is the outlet of an adjacent karstic catchment and was monitored for sediment composition for comparison with the Milandre stations. Modified after Häuselmann et al. (2016).

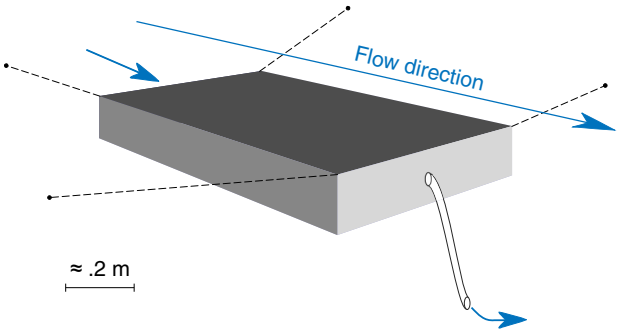

Figure 5.2: Schematized view of a sediment trap. Inner dimensions are 16.5 × 37 × 57 cm. A small opening on the upstream side and a tight tube on the downstream side restricts the flow rate and velocity through the sediment trap, causing the deposition of most of the suspended sediment.

highway works on the groundwater sediment fluxes should thus appear at different times in both systems.

Each sediment trap consists in a plastic box of dimensions 16.5 × 37 × 57 cm that is attached and maintained in the water flow (Fig. 5.2). It is designed to function as an integrative suspended sediment sampler: a small opening on the upstream side, and another one on the downstream side in which a tube is tucked, restrict water flow and velocity inside the box. This causes the deposition of most of the suspended sediment. The flow rate is controlled by the outflow tube diameter and the height difference between the box and the tube end. It is designed to allow a flow rate of maximum 1 L per minute in order to sample most of the suspended particles, down to the clay size range (<4 µm) (Atteia, 1998).

5.2.1 Sediment traps

The sediment accumulated in the traps was collected on average once every three months during the 2003 to 2015 period. Before collection, the sediment was thoroughly mixed inside the box in order to get a sample which is homogeneous and representative of the whole sampling period. Samples were analyzed for granulometry and mineralogical content at the University of Lausanne. Granulometry was analyzed with an Oriel Laser (2003–2008) and a Malvern Mastersizer (2009–2015). As the Malvern instrument has a much lower detection limit in terms of particle size, silt and clay measurements are not comparable between the two monitoring periods. The sand fraction however appeared to be consistent between the two periods based on a set of analyzes realized with both instruments (T. Adatte, personal communication). For the data analysis, particle sizes are sorted in three classes: clay (0.01–4 µm), silt (4–63 µm) and sand (63–150 µm). Only the 2009–2015 period is considered for the silt and clay data. Sediment mineralogy was analyzed by XRD with a Scintag XDS 2000 instrument during the whole monitoring period. Quartz and phyllosilicates, which are the most abundant minerals in the Milandre sediments, are considered in the present data analysis. Phyllosilicates are representative of the finer suspended particles, as they constitute 100% of the <16 µm particles in the insoluble particles (Häuselmann et al., 2016).

5.2.2 Sediment fluxes

In addition to the sediment traps, each monitoring station in the Milandre system was equipped with a turbidity monitoring device set at a 15 minute record time interval over the monitoring period (2003–2015). The underground stations (*Amont*, *Gal80* and *Bure*) used a GGUN-FL30 fluorometer. Due to the infrequent visits (every 3 months) and the relatively high suspended sediment content, these instruments were subject to important fouling of the measuring tube by sediment deposition, causing artificially high turbidity readings. This data is thus difficult to use in a quantitative manner, even after applying a correction (see Chap. 3). The Saivu spring, on another hand, was equipped with a Sigrist photometer which uses a pump and is thus not subject to sediment fouling. A relationship between the measured in-situ turbidity and the sediment concentration measured in the lab was established by collecting and analyzing regular samples over the monitoring period (3 to 4 samples per year, Fig 5.3). This allows to convert the turbidity record into an instantaneous sediment concentration time series which can be used to quantify sediment fluxes.

Sediment mass fluxes are estimated by multiplying sediment concentration with the flow rate. At

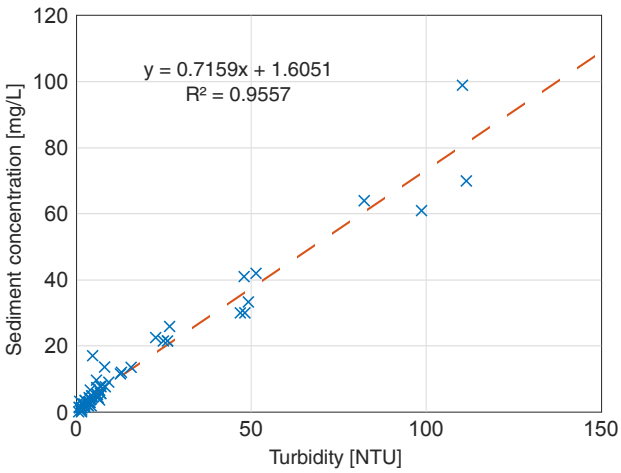

Figure 5.3: Empirical relation between turbidity and sediment concentration at the Saivu spring (after Häuselmann et al. (2016))

the Saivu spring, to quantify the total sediment mass outflowing from the Milandre system, the cumulative Saivu and Bâme spring discharge, monitored for the whole period at a 15 minute time step, is considered. Gaps in each spring flow rate time series are filled on the basis of the flow rate of the other spring with the help of the hydraulic model presented in Chap. 2 — since SWMM5 does not offer the possibility to constrain the flow rate at the outlets of the model, the ∼10 year flow simulation was used to establish a function of the Bâme discharge rate with respect to the Saivu discharge rate and vice versa. The mean sediment concentration for each sampling period is computed by dividing the integral of the sediment mass flux at the Saivu and Bâme springs by the cumulative discharged water volume. Sand, quartz and phyllosilicate concentrations are then obtained by multiplying the total sediment concentration by their respective contents in the sampled sediment.

5.2.3 Data analysis

To gain insight on the physical processes influencing the sediment fluxes through the Milandre system, the variations in sediment concentration and composition are analyzed together with other environmental variables. These variables are precipitation, effective precipitation (precipitation minus evapotranspiration, both measured at Fahy station (596 m.a.s.l.) by MeteoSwiss), mean discharge (sum of Saivu and Bâme discharge), mean water temperature, mean water electrical conductivity and mean pH at the Saivu spring. Mean values are computed from 15 minute time interval records. Further details are presented in Table 5.1. The sedimentary variables are total sediment concentration (computed from turbidity and discharge time series), sand, clay, quartz and phyllosilicate concentrations (total sediment concentration weighted by their respective content in the sedimen trap). Variables that have a log-normal distribution are log-transformed prior to the analysis (discharge, sand, clay, quartz and phyllosilicate concentrations). Each data point corresponds to a sampling period for the sediment trap of the Saivu spring (3 months on average). In total, there are 49 observations per variable, with the exception of pH (monitored from 2010 to 2015, 18 observations) and of clay (monitored from 2009 to 2015, 22 observations).

5.3 Results

5.3.1 Sediment composition

The evolution from 2003 to 2015 in the granulometric and mineralogical content at the 4 stations in the Milandre system and at the Beuchire spring are shown in Fig. 5.4. Values are given in weight fraction of the total accumulated sediment in the traps for each sampling period. At the Milandre stations, the overall mean values for the granulometric content in the 2009–2015 period are 7% for sand, 66% for silt and 27% for clay.

The spatial variability of the granulometric content appears to be limited, as the different stations display similar values and temporal evolutions. In contrast, the temporal variability is high, at least in sand content which is the only consistently measured granulometric variable over the whole monitoring period and which varies between 0 to more than 50%. These variations appear to be following the annual rainfall and mean annual discharge at the Saivu and Bâme spring (Fig. 5.4).

As for the mineralogical content, quartz shows a great inter-site and temporal variability, with values between less than 20 to more than 60%. The temporal variations appears to be linked to the hydrodynamics of the system, although less clearly than for the sand content. In constrast, the phyllosilicate content displays an upwards trend through the monitoring period. At the Milandre stations, mean values increase from 11.96±3.64% in 2003 to 24.16±6.52% in 2015. There is no apparent link between this evolution and the annual rainfall and discharge.

5.3.2 Sediment fluxes

The instantaneous sediment concentration at the Saivu is shown in Fig. 5.5. For the 2003–2015 period, it varied between 1.6 mg·L^{-1} during low flow to a max-

Symbol	Description	Units	log10-transformed
P	Total precipitation at Fahy station	mm	no
P_e	Effective precipitation (P-ETP) at Fahy station	mm	no
Q	Mean discharge at Saivu and Bâme springs	L·s^{-1}	yes
T_{gw}	Mean temperature at Saivu spring	°C	no
EC	Mean electrical conductivity at Saivu spring	µS·cm^{-1}	no
pH	Mean pH at Saivu spring	-	no

Table 5.1: Environmental variables considered for the data analysis

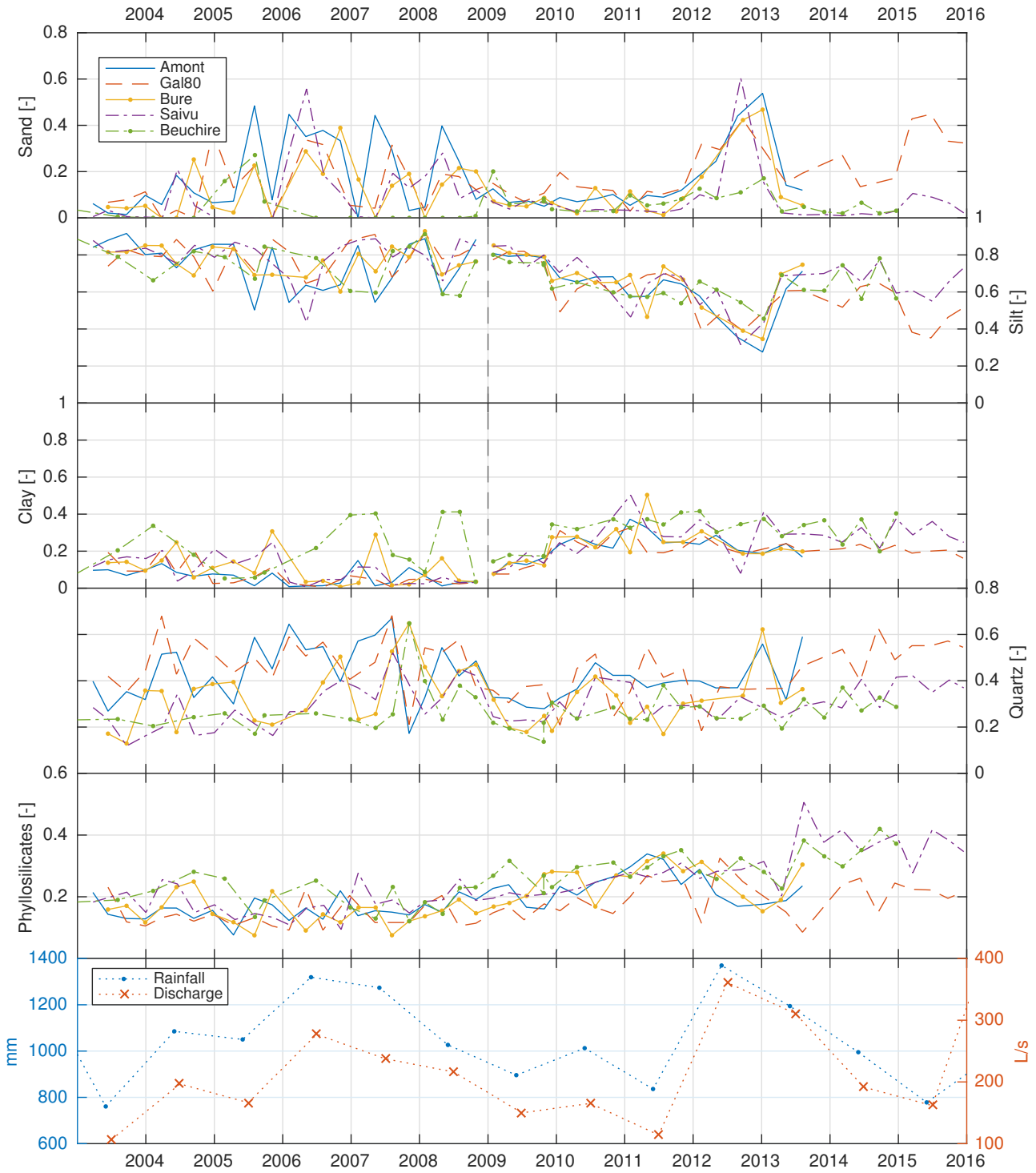

Figure 5.4: Temporal evolution of sand, silt, clay, quartz and phyllosilicate contents (expressed in weight fractions) in total suspended sediment at 5 monitoring stations (Fig 5.1), total annual rainfall at the Fahy station and mean annual discharge at the Saivu and Bâme springs. The vertical dashed lines indicate the change of instrument for granulometric analysis, which affects the silt and clay measurements.

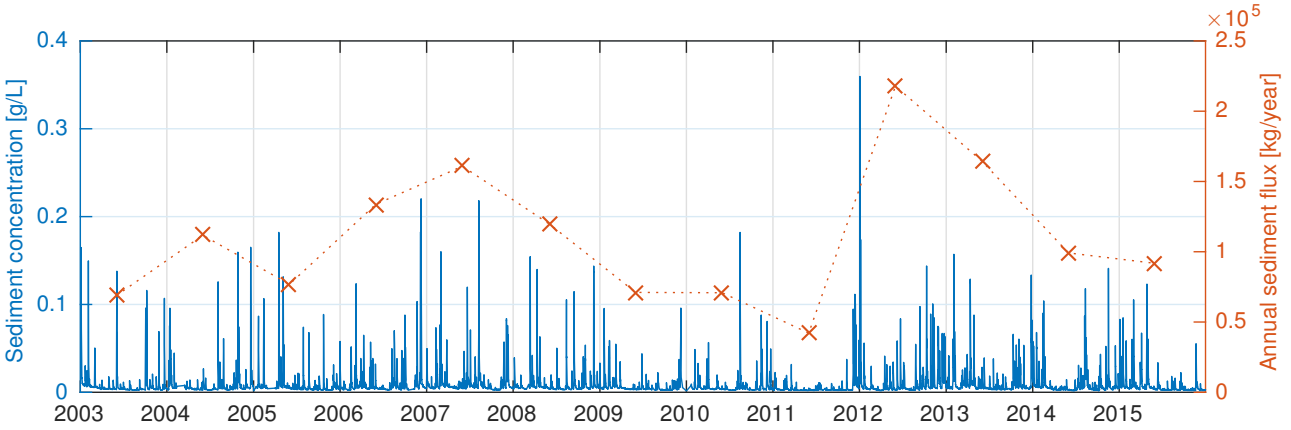

Figure 5.5: Instantaneous sediment concentration (blue) computed from the turbidity time series at the Saivu spring and annual sediment flux (orange) computed from the sediment concentration at the Saivu spring and the cumulative Bâme and Saivu discharge.

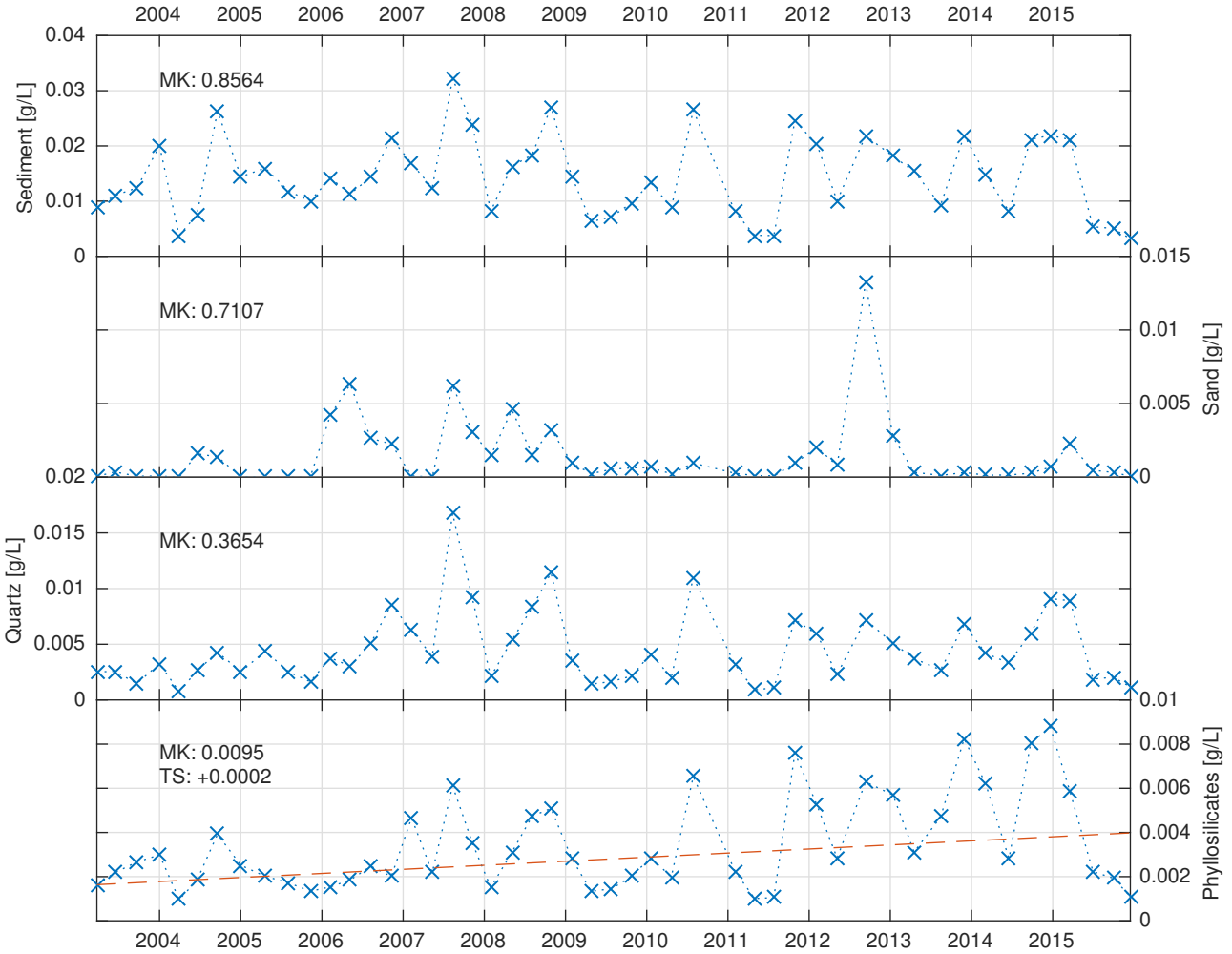

Figure 5.6: Temporal evolution of total suspended sediment, sand, quartz and phyllosilicate concentrations discharged by the Milandre system. Concentrations are obtained by dividing the cumulative sediment mass flux by the total discharged water volume for each sampling period. The sediment concentration was monitored at the Saivu spring and the flow rate takes into account both the Saivu and Bâme spring discharges. MK indicates the p-value of the Mann-Kendall test and TS, the Theil-Sen estimator ($g \cdot L^{-1} \cdot year^{-1}$) which is represented in the graph by the dashed line.

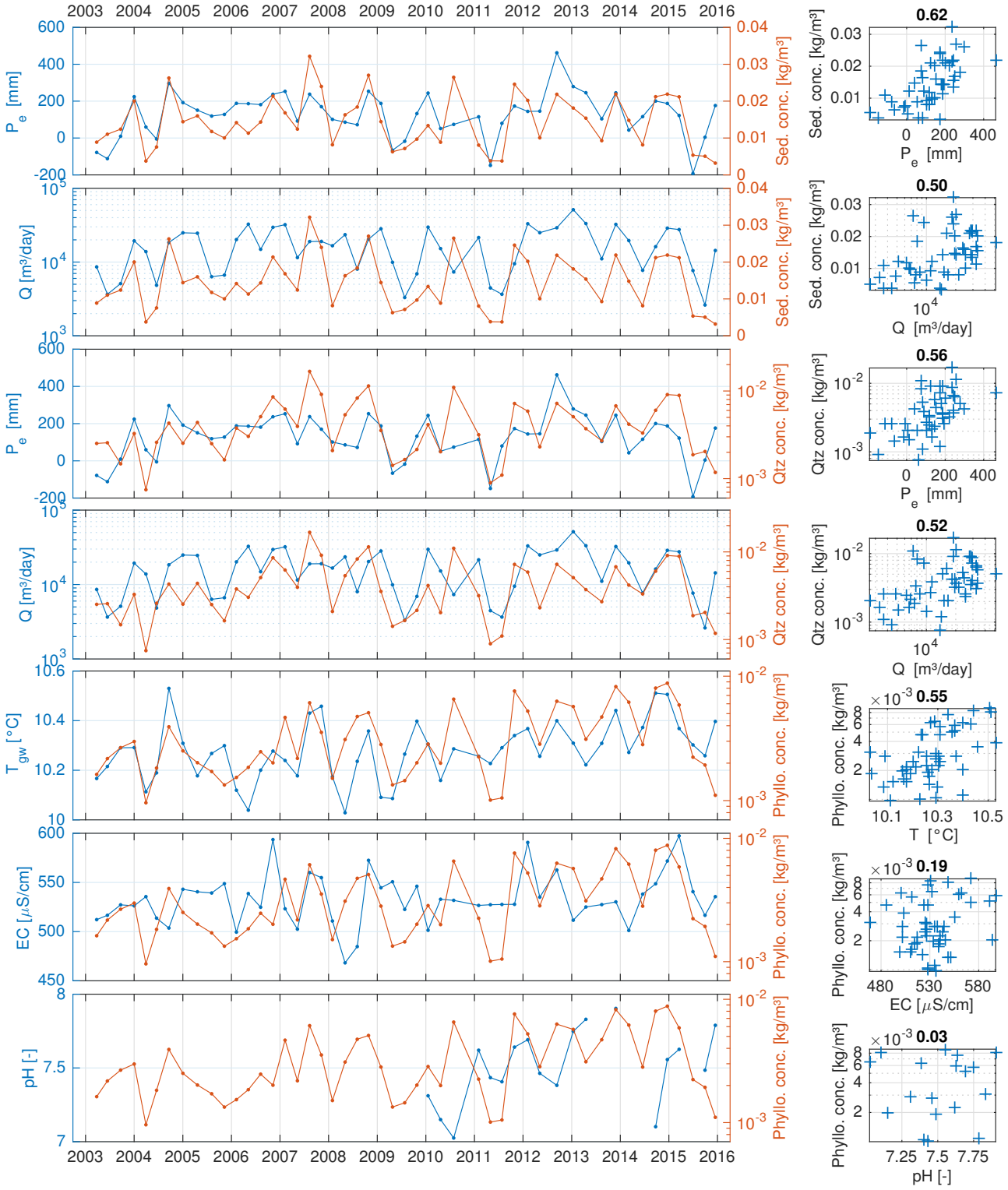

Figure 5.7: Time series (left) and scatter plots (right) of pairs of sedimentary vs environmental variables.

imum of 360 mg·L^{-1}. The mean annual sediment flux, obtained by the sediment concentration multiplied by the system's discharge (Saivu and Bâme discharge time series), is also plotted on Fig. 5.5. Values range from 4.2·10^4 to 2.2·10^5 kg per year. The evolution of the concentrations in total sediment, sand, quartz and phyllosilicates is shown in Fig. 5.6. Silt and clay concentrations are not considered for this analysis because of the lack of consistency in those two time series caused by the change of instrument.

The Mann-Kendall test, a distribution-free statistical test which assesses the existence of a monotonic trend in time series, was performed for each of those four variables. Neither total sediment, sand and quartz concentrations demonstrate any statistically significant trend. Similarly to the phyllosilicate content (Sec. 5.3.1), phyllosilicate concentration shows an upward trend, with a p-value of the Mann-Kendall test lower than 0.01. The Theil-Sen estimator indicates an overall increase in concentration of +0.2 mg·L^{-1} per year. With the mean annual discharge of 250 L·s^{-1}, this increase represents 1.6·10^3 kg of discharged phyllosilicate particles each year. In comparison, the mean annual sediment flux (Fig. 5.5) is 1.1·10^5 kg/year. Thus, the estimated phyllosilicate increase is ∼1% of the overall sediment flux.

5.3.3 Multivariate analysis

Correlation coefficients (ρ), coefficient of determination (R^2) and p-value of the linear model between sediment concentrations and selected environmental variables are shown in Table 5.2. The p-value of the linear model is the probability that there is no linear relationship between the two variables.

Almost all pairs of variables, with the notable exception of pH, are positively correlated, although in some cases the correlation coefficient is weak. Several pairs of variables are depicted in Fig. 5.7. Total sediment and quartz concentrations are well correlated ($\rho \geqslant 0.5$) with both effective precipitation and discharge. These two sedimentary variables also have a relatively high coefficient of determination ($R^2 \geqslant 0.3$) and significant linear relationship (p-value $< 10^{-4}$) with effective precipitation. The clay concentration is well correlated with discharge ($\rho = 0.55$). In contrast, phyllosilicate concentration has a stronger correlation coefficient (0.55) with water temperature than with any other environmental variable. Their linear relationship is also highly significant (p-value $= 3.7 \cdot 10^{-5}$). The temperature is also relatively well correlated with the total sediment concentration and with the clay concentration. Electrical conductivity is weakly positively correlated with each sedimentary variables, while pH shows no significant correlation with any. This could be due to the lower number of observations of this variable, since the monitoring started only in 2010 (18 observations vs 49 in other cases).

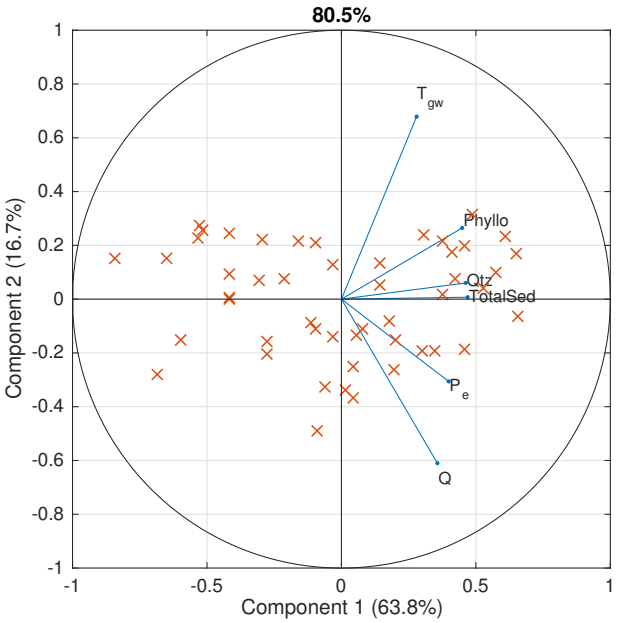

Figure 5.8: 1st and 2nd components of the principal component analysis

A principal component analysis of the data set is performed with total sediment, quartz and phyllosilicate concentrations as sedimentary variables, and effective precipitation, mean discharge, mean water temperature as environmental variables. Variables are standardized before the analysis. Precipitation is not taken into account to avoid redundancy with effective precipitation, as they are highly correlated. EC and pH are also left out as they are weakly correlated with the sedimentary variables. Results are plotted in Fig. 5.8. The first and second principal components explain respectively 63.8 and 16.7 % of the variance, totalling 80.5 %. For the first principal component, all variables have a coefficient between +0.28 (T_{gw}) and +0.47 (total sediment concentration). This suggests that, at the first order, all variables in the data set vary in a similar way. For the second principal component, the variables are more evenly distributed, with discharge (−0.61) and effective precipitation (−0.31) on one side, and water temperature (+0.68) on the other. Quartz and total sediment concentration are very close to 0 (+0.01 and and +0.06), while phyllosilicate concentration lies on the T_{gw} side at +0.26.

5.4 Interpretations and discussion

5.4.1 Overall dynamics

Due to the sampling duration of 3 months, there are some limitations in the interpretation of the data. For instance, the concentrations of the different min-

	P	P_e	Q	T_{gw}	EC	pH
	Correlation coefficient (ρ)					
Total sediment	0.41	**0.62**	**0.50**	0.49	0.29	-0.03
Sand	0.42	0.39	0.35	-0.02	0.17	0.01
Clay	0.12	0.39	**0.55**	0.47	0.17	0.17
Quartz	0.39	**0.56**	**0.52**	0.39	0.25	-0.02
Phyllosilicates	0.37	0.49	0.46	**0.55**	0.19	0.03
	Adjusted coefficient of determination (R^2)					
Total sediment	0.15	**0.37**	0.23	0.22	0.07	-0.06
Sand	0.16	0.14	0.10	-0.02	0.00	-0.06
Clay	-0.03	0.11	0.28	0.19	-0.01	-0.03
Quartz	0.14	**0.30**	0.25	0.13	0.04	-0.06
Phyllosilicates	0.12	0.22	0.20	0.29	0.02	-0.06
	p-value of the linear model					
Total sediment	0.0037	**2.2e-06**	0.00025	0.00035	0.043	0.89
Sand	0.0041	0.008	0.021	0.9	0.28	0.98
Clay	0.55	0.051	0.0034	0.016	0.41	0.5
Quartz	0.0054	**3e-05**	0.00015	0.006	0.082	0.95
Phyllosilicates	0.0093	0.00041	0.00084	**3.7e-05**	0.19	0.91

Table 5.2: Statistics of the relations between concentrations in sediment, in sand and silt and in clay and other environmental variables: precipitation (P), effective precipitation (P_e), discharge (Q), water temperature (T_{gw}), electrical conductivity (EC) and pH. Bold values indicate correlation coefficients greater or equal 0.5, coefficients of determination greater or equal to 0.3 and p-value of the linear model lower than 10^{-4}.

eralogical and granulometric fractions are rough approximations, since they are averaged over each sampling period. Similarly, to allow for the data analysis, the environmental variables (discharge, temperature, electrical conductivity and pH) were averaged according to the sampling scheme of the sediment traps, smoothing the fine scale variations which they are subject to. However, some relationships still emerge from the data analysis. For instance, the strong control of hydrodynamical conditions (quantified through precipitation, effective precipitation and discharge rate of the system) on sediment fluxes is highlighted. Furthermore, the finer particles (represented here by the phyllosilicate concentration) display a positive correlation with water temperature as well as a positive upwards trend over the 13 years monitoring period. The next two sections explore further these relationships.

5.4.2 Sediment fluxes

The multivariate analysis showed that, at the first order, the suspended sediment concentration is controlled by the hydrodynamics of the system. To see if the data set can reveal more details on this process, another analysis is performed at the daily scale, using the daily means of turbidity, water temperature and electrical conductivity at the Saivu spring, the daily mean discharge at Saivu and Bâme springs, and the daily sum of precipitation and effective precipitation at the Fahy station during the 2003–2015 period. Daily mean values are computed from 15 minute time interval records. Turbidity, a proxy for sediment concentration, and discharge are log10-transformed before the analysis. Coefficient of correlation, of determination and p-value of linear models between turbidity and every other variable are shown in Table 5.3. The highest coefficients ($\rho = 0.79$ and $R^2 = 0.62$) are obtained with daily discharge. Adding other variables or using other model functions (quadratic, power 3

	ρ	R^2	p-value
P	0.29	0.08	$< 10^{-10}$
P_e	0.35	0.12	$< 10^{-10}$
Q	0.79	0.62	$< 10^{-10}$
T_{gw}	0.29	0.09	$< 10^{-10}$
EC	-0.06	0.00	8.5904e-05

Table 5.3: Correlation coefficient (ρ), coefficient of determination (R^2) and p-value of the linear model of the daily mean turbidity value versus daily precipitation (P), daily effective precipitation (P_e), daily mean discharge (Q), daily mean water temperature (T_{gw}) and daily mean electrical conductivity (EC) at the Saivu spring for the 2003–2015 period.

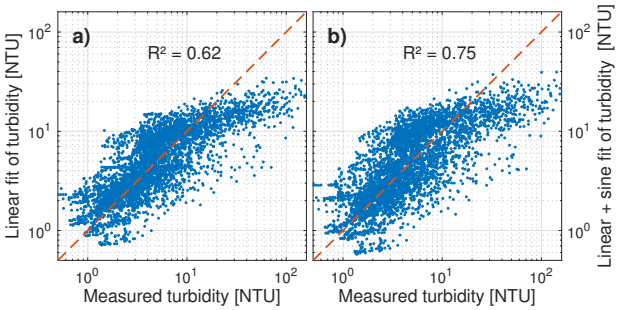

Figure 5.9: Scatter plots of observed vs fitted values. a) Linear model: linear fit of the daily mean turbidity as a function of the daily mean discharge at the Saivu and Bâme springs. b) Composite model: a sine function of a period of one year, obtained by a fit of the residuals of the first model (Fig. 5.10c), is added to the linear model.

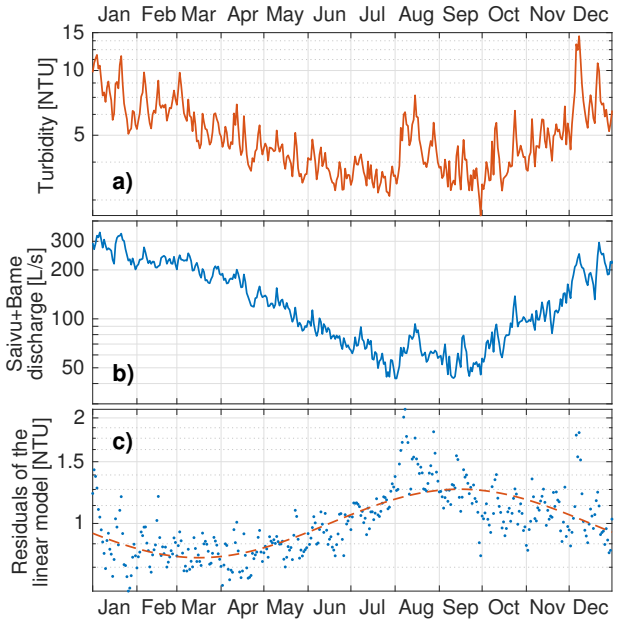

Figure 5.10: Seasonal variations: daily mean value for turbidity (a) and Saivu+Bâme spring discharge (b) for each day of the year during the 2003–2015 period. In c), the residuals (observed minus fitted values) of the linear model of turbidity vs discharge (Fig. 5.9a) are plotted as a function of the time of year (dots). The dashed line is a fitted sine function.

and exponential) did not provide significantly better statistical models than the linear model for daily turbidity as a function of daily discharge. A scatter plot of the measured vs fitted values for the linear model of daily turbidity as a function of daily discharge is shown is Fig. 5.9a. While the linear model performs well for value of turbidity lower than 10 NTU, higher values are systematically underestimated. This corresponds in the linear model to a discharge of 340 $L{\cdot}s^{-1}$. Thus, the linear model is valid only under low to intermediate flow conditions.

Atteia (1998) also proposed a statistical model of the turbidity at the Saivu spring. His model aims at estimating the peak turbidity value for each flood event during the 1993 to 1995 period. The input variables are the event initial discharge, the event peak discharge, and the time between the last flood peak and the start of the event. He also added a seasonal component by means of a sinusoidal function with a minimum in the end of January and a maximum at the end of July. By adding this component, the explained variance increases by 40% ($R^2 = 0.41$ to $R^2 = 0.81$). The explanation for this seasonal component is an enhanced availability of fine particles in soils during the summer time as a consequence of biological activity. Here, to test the hypothesis of a seasonally varying sediment availability on the present data set, the mean turbidity value for each day of the year over the 13 year monitoring period is computed. As depicted in Fig. 5.10a, a seasonality in sediment concentration is indeed marked, with a maximum during the months of December and January, and a minimum in the late summer — i.e. shifted by almost half a year compared with the seasonal component of Atteia (1998). However, this seasonality is very well explained ($R^2 = 0.72$) by the seasonality in discharge, which is shown in Fig. 5.10b. At the first order, the seasonality of the turbidity at the Saivu spring is thus caused by the hydrological seasonal pattern. To explore the variations in turbidity which are not explained by the variations in discharge, the residuals of the linear model of the daily turbidity as a function of the daily discharge (Fig. 5.9a) are plotted as a function of the time of year in Fig. 5.10c. The residuals, which are the measured values minus the fitted ones, are well described by a non-linear regression of a sine function ($R^2 = 0.55$ and p-value $< 10^{-10}$) with a maximum in mid-September and a minimum in mid-March. It means there is an excess in turbidity during fall which is not caused by hydrological events. This is thus consistent with the varying seasonal availability of sediment suggested by Atteia (1998). Adding this seasonal component to the initial linear model, the following non-linear model is obtained:

$$\begin{aligned}\log_{10}(\hat{\tau}_d) =& 0.7119 \cdot \log_{10}(Q_d) - 0.8005 \\ &+ 0.0977 \cdot \sin\left(\frac{2\pi t_d}{366} + 0.2746\right)\end{aligned} \tag{5.1}$$

where $\hat{\tau}_d$ is the fitted daily turbidity (NTU), Q_d is the daily discharge ($L{\cdot}s^{-1}$) and t_d is the day of year. Observed vs fitted values are plotted in Fig. 5.9b. Compared to the linear model, the explained variance is 13% greater ($R^2 = 0.62$ vs $R^2 = 0.75$). Yet the model still performs poorly for values of turbidity greater than ∼10 NTU. Furthermore, the model of Atteia (1998) has a higher R^2 of 0.81. However, Jeannin

et al. (2013) showed that Atteia's model, calibrated with the 1993–1995 time series, performs poorly for the 2003–2005 time series (R^2 = 0.39). Their explanation is that the model was calibrated on a period with unusually high turbidity values (e.g. several peaks higher than 300 NTU) compared to the 2003–2005 period (maximum peak value of 250 NTU). This could actually be partly caused by a sampling artifact. Indeed, the turbidity measuring device and its settings were changed in 1998. Although the record time interval has always been of 15 minutes, prior to mid-1998, the data logger recorded the mean value of 10 measurements done over the last 15 minutes. From mid-1998 on, the data logger recorded the mean value of 10 measurements done in the last 2 minutes. Since turbidity may vary very quickly, especially at high values (up to more than 50 NTU in 15 minutes in the 2003–2015 time series), it is possible that the later setting increases the probability to miss peak turbidity values. This highlights the limitations of models that aim at reproducing peak turbidity values — these peaks naturally have a great variability and they are not easy to measure.

In contrast, in the data presented here, the use of daily mean values should reduce this effect. In terms of instrumentation, the measuring device has been changed again in 2011, but the record settings stayed the same. Also, since it uses daily values on a 13 year time period, the proposed model has a much greater sample size than the model of Atteia (1998) and Jeannin et al. (2013) (∼4500 data points vs less than 100), and it is thus more robust. Furthermore, from the scatter plot in Fig. 5.9, it appears to be valid in the range of turbidity values within which lie most of the data points (<10 NTU). However, following Eq.5.1 and depending on the time of the year, a daily mean turbidity of 10 NTU corresponds to a daily mean discharge of 300 to 400 $L{\cdot}s^{-1}$, e.g. a minor flood event. During the 13 year study period, 25% of the daily mean discharge values are greater than this. The fact that high turbidity values are again underestimated points out the great variability of turbidity during high flow conditions and the limitations of simple statistical approaches for the characterization of these variations.

This brief analysis of the daily turbidity time series points out that the sediment concentration is, at the first order, mainly controlled by the system hydrodynamics. At the annual scale, the first order seasonal pattern is dictated by the hydrological cycle. There is however a second order seasonal component which is attributed to a greater sediment availability during the fall season. However, the resulting statistical model, which takes into account both the spring discharge and the seasonal cycle, is a poor predictor of turbidity under intermediate to high flow conditions and fails to explain the important variability in extreme turbidity values. Peak turbidity values, even at the daily scale, are systematically underestimated. A possible explanation for this erratic response of sediment concentration to flood events is the occurrence of complex sedimentary processes inside the karst system triggered by extreme flow conditions, such as collapses of sediment piles (Chap. 3) and hydraulically triggered erosive phases (Chap. 4).

5.4.3 Phyllosilicate evolution and relationship with groundwater temperature

Processes influencing groundwater temperature

The multivariate analysis pointed out a positive correlation between suspended phyllosilicate concentration and water temperature. A positive correlation with temperature is also present, to a lesser extent, for the total sediment concentration and the clay concentration. These positive correlations could be caused by a direct physical effect of temperature on fine particle concentration, by an underlying process affecting both of them, or by a coincidence. The correlation appears at the seasonal scale (Fig. 5.7) — especially in the years 2011 to 2015, both phyllosilicate and temperature have an annual peak in the late fall and/or in the winter. And on a pluriannual scale, the two variables display a similar upwards trend (Fig. 5.6 and 5.11). At the *Amont* station in the Milandrine, Jeannin et al. (2016) estimated an increase in temperature of +0.02 °C per year for the 1990 to 2011 period, which is attributed to global climate change. To try to highlight the processes influencing the temporal evolution of groundwater temperature, linear models for both the Saivu spring and the *Amont* station on a monthly scale were computed and are presented in Fig. 5.11.

The most significant models in both cases were found by combining the ground level atmospheric temperature (Fahy station) with a three months delay, a secular component for climate change, and the amount of precipitation received during the previous months of February to May. Every component of both models, apart from spring precipitation at the Saivu with 0.006, which is still significant at a 0.01 threshold, has an extremely low p-value (10^{-7} to 10^{-22}). The coefficients of determination (0.59 and 0.72) indicate that the temperature variations are well explained by the models. It is interesting to note that temperature at the *Amont* station is less influenced by the delayed surface temperature and more influenced by the secular increase and the precipitation fallen during spring.

Jeannin et al. (2016) associated the upward trend in groundwater temperature with an upward trend in electrical conductivity of +2.06 $\mu S \cdot cm^{-1}$ per year at the *Amont* station. Their explanation is that the

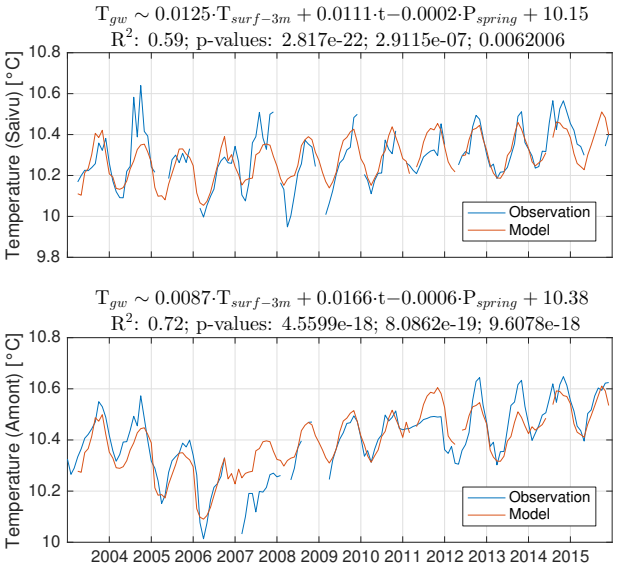

Figure 5.11: Linear model of water monthly temperature evolution at the Saivu spring and in the Milandrine (*Amont* station). T_{gw} is groundwater temperature (°C), $T_{surf-3m}$ is the atmospheric temperature at ground level with a 3 month delay (°C), t is the time in years, and P_{spring} is the precipiation received during the last February to May.

global increase in temperature enhances biological activity in soils, leading to an increase in partial CO_2 pressure in soils and in the infiltration water. As a consequence, the limestone dissolution intensifies and the groundwater mineralization increases. Could the insoluble residue of this added limestone dissolution be the origin of the increase in fine particle concentration in groundwater? At another spring of the Jura Mountains, Jeannin et al. (2016) saw a trend of +1.05 µS·cm^{-1}·year^{-1} and a corresponding increase of +1.74 mg·L^{-1}·year^{-1} in HCO_3^- concentration. If the correspondence from carbonate concentration to electrical conductivity is the same in Milandre, the trend in HCO_3^- concentration would be +1.74 mg·L^{-1}·year^{-1}. From the calcite dissolution equation, one mole of $CaCO_3$ gives two of HCO_3^-, and knowing that the purest limestone formation in the Jura contains ∼1% of insoluble residue (Kiraly et al., 1973), this would mean a trend of +0.03 mg ·L^{-1}·year^{-1}. This value is one order of magnitude smaller than the estimated phyllosilicate concentration increase (Fig. 5.6). This very rough calculation does not rule out the enhanced dissolution as contribution to the increase in phyllosilicate, but it suggests that it is probably not the dominant process.

The linear models also show that the annual distribution of precipitation affects groundwater temperature — the amount of precipitation received during the spring has a negative impact on groundwater temperature during the following year. This may lead to an indirect relationship between temperature and phyllosilicate concentration, e.g. if phyllosilicate particles are more available for erosion in the fall and in the winter, when recharge events have a positive effect on temperature. An enhanced availability of sediment during the fall season was already suggested by Atteia (1998) and by the statistical model presented in the previous section. Atteia (1998) further suggested that there is an increase in fine particle production in the summer because of the high biological activity in soils during this season. Observation of soil composition and texture, land use, agricultural practices and their annual cycle is needed in order to confirm this hypothesis.

Physical processes

In the literature, several studies report effects of water temperature on both the erodibility and the settling velocity of fine particles. For instance, Grissinger (1966) observed a twofold increase of the erosion rate of silt-loam mixture between 7 and 20°C (Fig. 5.12). Temperature variations in Milandre have a much smaller amplitude. However, over time, an enhanced erodibility of fine sediment could lead to a significant increase in fine particle concentration.

Other studies pointed out the influence of temperature on the settling velocity of fine particles. Owen (1976) measured the settling velocity of mud particles of size ranging from 2 to 100 µm in distilled water under varying water temperature. Results for 5.5 µm particles are shown in Fig. 5.13. With temperatures between 5 to 30 °C, he systematically found a positive linear relationship between settling velocity and

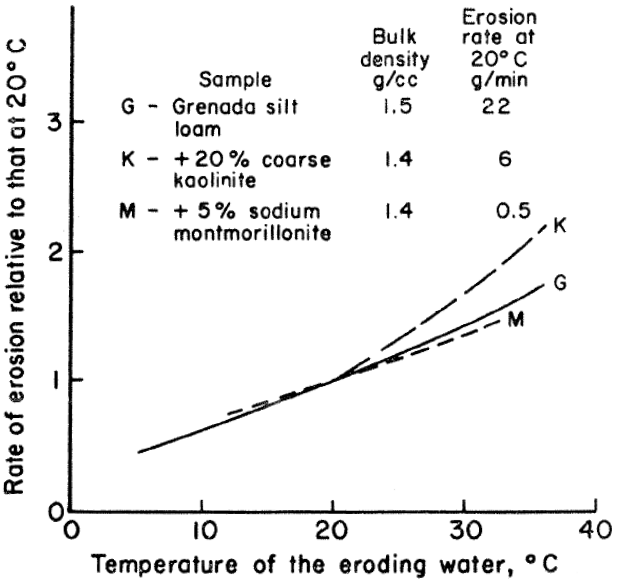

Figure 5.12: Experimental rate of erosion in three silt loam mixtures as a function of water temperature. From Grissinger (1966).

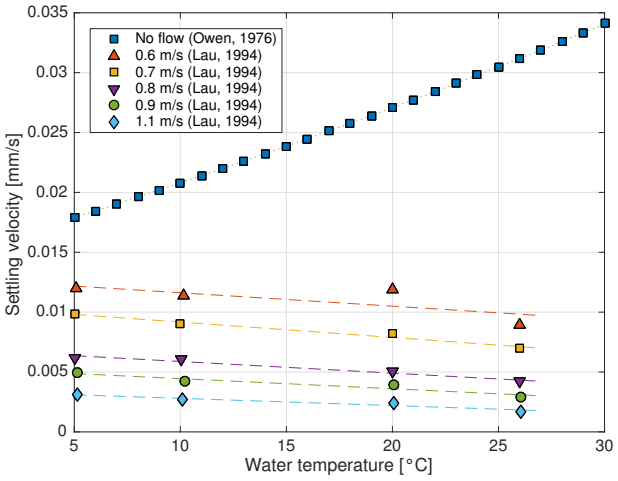

Figure 5.13: Settling velocity of fine particles (5.5 µm in blue and 5 µm diameter for other colors) vs water temperature in still water and under varying turbulent flow velocity as obtained by lab experiments. Data from Owen (1976) and Lau (1994).

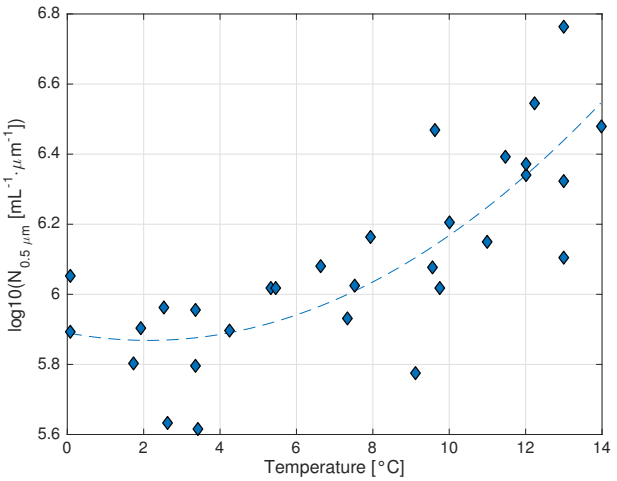

Figure 5.14: Concentration in 0.5 µm particles ($N_{0.5\mu m}$) vs temperature in a stream of the Jura Mountains. Modified from Atteia and Kozel (1997).

temperature. The main reason for this is the decrease in water viscosity with increasing temperature, which has a positive effect on settling velocity according to Stokes' law:

$$w = \frac{2}{9}\frac{(\rho_p - \rho_w)}{\mu} g R^2 \tag{5.2}$$

where w is the settling velocity ($m \cdot s^{-1}$), ρ_p and ρ_w the particle and water mass density ($kg \cdot m^{-3}$), μ the dynamic viscosity of water ($kg \cdot m^{-1} \cdot s^{-1}$), g the gravitational acceleration ($m \cdot s^{-2}$) and R the particle radius (m). Similar results are found in Naghipour et al. (2014) for 30 µm particles and in Wan et al. (2015) for ~8 µm particles.

However, all those experiments were realized in settling tubes under no flow conditions. Lau (1994) tested the effect of temperature on fine sediment settling velocity under turbulent flow conditions and observed a negative dependency. The results for 5 µm kaolinite particles under varying flow velocity in distilled water are depicted in Fig. 5.13. Similar trends were found for natural sediment with a mean diameter of 12 µm in river water. The reason invoked for this is linked with the ability of particles to flocculate, which is the main control on fine sediment settling velocity. Under turbulent flow, flocs are continuously formed and pulled apart, especially when reaching the highest shear stress zone near the bed. The attractive forces between particles, the Van der Waals forces, do not depend on temperature, while the repulsive forces have a positive linear dependency with temperature, hindering flocculation when the temperature increases (Lau, 1994). This phenomenon could thus explain the observed increase in phyllosilicate particles in groundwater with increased temperature in the Milandre system, where turbulent flow conditions are obvious. Although the temperature variations are relatively low — from 2003 to 2015, temperatures recorded at the Saivu spring and at the *Amont* station were comprised between 9.5 and 12 — this could still lead to a noticeable effect if the transit time of particles is sufficiently long.

In natural karst systems, no reports of a temperature influence on fine particle concentrations are found. Atteia and Kozel (1997) and Shevenell and McCarthy (2002) both observed an effect of pH on colloid concentration in karstic groundwater. However, in their study in the Jura mountains, Atteia and Kozel (1997) not only sampled a karst spring, but also its feed sinking stream, in which they found a positive link between temperature and fine particle concentration. Their data is reproduced in Fig. 5.14 and reveals a quadratic relationship between temperature and the log10 values of 0.5 µm particle concentration. Between 10 and 10.5 °C, that represents an increase of $1.4 \cdot 10^5$ particles $mL^{-1} \cdot \mu m^{-1}$. Although there is no direct evidence that the temperature and phyllosilicate concentration are causally linked, the fact that it has been observed both in lab and field experiments supports this hypothesis. This hypothesis, compared to the seasonal availability hypothesis, also has the benefit of explaining both the seasonal and pluri-annual correlation between the temperature and the phyllosilicate concentration.

Other potential causes for the increase in phyllosilicates

Highway construction works that could have had a potential impact on the suspended sediment fluxes in the Milandre system were carried out between 2005 and 2010 (Meury et al., 2006; Blant et al., 2011). As the increase in phyllosilicate is simultaneous in the

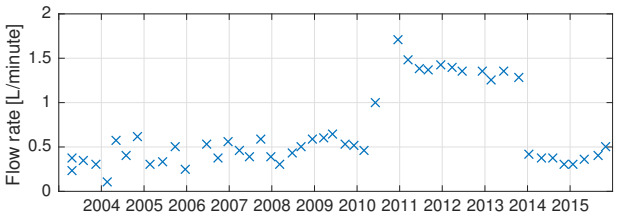

Figure 5.15: Flow rates measured in the Saivu sediment trap. Each point corresponds to the mean flow rate value for each sampling period. The high flow rate in 2010 to 2013 is caused by a temporary change in diameter of the outflowing tube

Milandre and Beuchire systems (Fig. 5.4), it is unlikely arising from the building of the highway, as the timelines for the construction works were different in both catchments. Furthermore, the increase is rather steady over 13 years, arguing against an impact of some construction works which would rather appear at a specific point in time.

Another potential cause for the phyllosilicate increase could be an instrumental drift. When sediment is accumulated on the inside of the outflowing tube of the sediment traps (Fig. 5.2), the decrease of the flow section leads to a restriction of flow through the trap. Slower flow velocities could decrease the size threshold for particle deposition. Flow rate through the trap has been measured at the beginning and at the end of each sampling period. From 2007 on, the outflowing tube has been cleaned at each visit, as a decrease in flow rate was indeed observed between the start and the end of each sampling period. Average values computed from the initial and final flow rate in the Saivu sediment trap are shown in Fig. 5.15. The mean flow rate for the monitoring period is 0.65±0.43 L per minute. It has not been constant through the years — especially, the 2011–2014 period has a high mean flow rate of 1.37 L per minute. This corresponds to a temporary change of the outflowing tube (Häuselmann et al., 2016). This however does not seem to have affected the collection of sediment, as it would mean an increase in large and/or a decrease in fine particles during this period, which is not observed (Fig. 5.4 and 5.6). Furthermore, it cannot explain the relative increase in phyllosilicate particles over the course of the monitoring period. The changes in sediment trap flow rate have thus no apparent effect on the composition of the collected sediment.

5.5 Conclusions

Through an analysis of the data obtained by the pluriannual monitoring of suspended sediment concentration and composition, this chapter highlights the physical processes that influence sediment fluxes in the karst system of Milandre. At the first order, the sediment concentration at the Saivu spring is mainly controlled by the discharge of the system. The seasonal variations in the sediment concentration are also mostly influenced by the hydrological cycle. There is however a second order seasonal component in the sediment concentration, which is thought to arise from an enhanced particle availability in soils during the late summer and the fall. A simple statistical model taking into account the system's discharge and the inferred seasonal cycle gives satisfactory estimates of the daily turbidity under low flow conditions and during minor flood events. However, there is an important variability in higher turbidity values which is not explained by the model. This confirms the findings presented in Chap. 3 and 4, i.e. that sedimentary processes taking place in the conduits during flood events may directly impact the spring turbidity and have a non-linear relationship with the system discharge. These processes include erosive phases triggered when a conduit is getting filled or emptied, as well as collapses of the piles of sediment that border the cave stream.

Similarly to the findings of previous karst studies, the data presented here argues for a significant effect of physico-chemical conditions on fine sediment concentration in karst aquifers. In particular, a strong correlation is found between water temperature and phyllosilicate particle concentration. The correlation appears on a seasonal scale, but also on a pluriannual scale, as both variables display an upwards trend over the monitoring period of 13 years. This relationship could arise from a greater availability in phyllosilicate during the late summer and the fall, because the annual maximum in groundwater temperature also occurs during fall. This link could also be of causal nature, warmer temperature allowing higher fine sediment concentrations in groundwater both by increasing their erodibility and decreasing their settling velocity under turbulent flow conditions. This explanation has the benefit that it explains both the seasonal and the pluri-annual patterns in the phyllosilicate concentration. Unlike Atteia and Kozel (1997) and Shevenell and McCarthy (2002), no influence of pH was found, but this may be due to the limited number of observations for this variable available in this study. Overall, the present observations provide some insight into the complex interplays between fine suspended sediment and the physico-chemical properties of water and how they might evolve on a pluriannual time scale.

The main shortcoming of the data analysis presented here is the sampling period of three months. Indeed, the discharge and the water quality vary rapidly in the Milandre system. To perform the data

analysis, these variables were averaged over the sampling periods, meaning that the fine scale temporal variations are lost. To overcome this issue, one could perform instantaneous measurements, for instance with the PSD device used for the flood event monitoring in Chap. 4. This would give more details on suspended sediment concentration variations and allow more detailed comparisons with other variables such as the pH and the water temperature.

Furthermore, direct observations on the surface are needed to confirm whether a seasonal cycle in sediment availability exists and whether it affects preferentially phyllosilicate particles. This could include soil texture and composition monitoring, investigations on agricultural practices and aerial photography surveying.

Chapter 6

Conclusion

6.1 Conceptual model of the sediment fluxes

6.1.1 Sedimentary dynamics at the event scale

From the observations and the flow simulations presented in this thesis, the following conceptual model of the sediment fluxes in the Milandre karst system is proposed. For flood events of minor intensity (peak discharge in the upstream Milandrine $Q_{up} \lesssim 200$ L·s^{-1} and peak discharge at the springs $Q_{out} \lesssim 400$ L·s^{-1}), the turbidity signal during the flood peak is mostly of autochthonous origin. Both the Milandrine and the *Bure* tributary show a sharp turbidity peak almost simultaneous with the discharge peak which is compatible with a remobilization of karstic sediment by the flood pulse. The turbidity evolution in the *Droite* tributary has not been monitored so far. At the Saivu spring, the turbidity signal during minor events is interpreted as a superimposition of the signal originating from the three main stream branches, to which is added the turbidity generated by sediment remobilization in the downstream epiphreatic zone. In the upstream Milandrine, the occurrence of a delayed, very dispersed peak after minor flood events is interpreted as the arrival of allochthonous turbidity. The delay between this secondary peak and the flood peak is approximately 3 days when $Q_{up} \approx 50$ L·s^{-1}and 1 day when $Q_{up} \approx 150$ L·s^{-1}. This allochthonous sediment can appear at the Saivu spring two days after the flood peak as a very dispersed, low amplitude peak, but is usually not detected, at least through turbidity monitoring. This can be caused by redeposition and/or dispersion.

As the intensity of the flood increases, the delay between the flood peak and the allochthonous turbidity peak decreases, while the intensity of the allochthonous turbidity increases. For moderate and high intensity events ($Q_{up} \gtrsim 200$ L·s^{-1} and peak discharge at the springs $Q_{out} \gtrsim 500$ L·s^{-1}), the allochthonous turbidity reaches the cave stream and the springs with only a small delay compared to the autochthonous turbidity. The monitoring of a moderate flood event ($Q_{out} = 850$ L·s^{-1}), which generated a single turbidity peak, revealed that the autochthonous and allochthonous contributions were of similar amplitude. During major events ($Q_{out} \gtrsim 1$ m^3·s^{-1}), erosive processes in the karst system have a strong control on the turbidity signal, which shows rapid and intense variations. The turbidity at the Bâme spring is more affected by these sediment remobilization processes than the turbidity at the Saivu spring: peak turbidity values are generally higher at the Bâme spring than at the Saivu spring. The model predicts a shear stress maximum when a level of conduits is flooded and subsequently when it is drained. As a result, secondary erosive phases occur during flow recession when the different epiphreatic levels of the downstrean part of the karst system are drained. Turbidity peaks associated with these recession erosive phases were observed at the Bâme spring and to a lesser extent at the Saivu spring. A similar mechanism was identified in the upstream part of the cave stream. Conversely, the hydraulic model predicts a local minimum in the mean boundary shear stress during the peak of flood events. Thus, in line with the observations gathered by the sedimentation monitoring station, the accumulation of sediment in the conduits is expected to be most effective at high stage.

6.1.2 Long term sedimentary dynamics

On a longer time scale (∼10 years), the suspended sediment concentration in the Milandre system appears to be mainly controlled by the hydrological conditions. The discharge of the system alone is however not a good predictor of the sediment concentration under intermediate and high flow conditions. This is here attributed to the complex processes of sediment remobilization in the karst system, which may induce intense turbidity peaks. In the second order, a seasonal component influences the sediment concentration. This effect is thought to arise from an enhanced sediment availability in the soils during the fall. In terms of suspended sediment composition, an upward trend in the phyllosilicate concentration was found. It is well correlated, both at the seasonal and at the pluriannual scale, with groundwater temperature.

Inside the karst system, the model predicts that both erosion and accumulation of sediment are frequent in the main conduit of the cave stream on a ∼10 year time scale. The sedimentation monitoring showed that erosion is active only in the first 1.5 meters above the stream base level, and accumulation is maximum a few meters above. Moreover, the sedimentation monitoring and occasional observations in the cave showed that the deposits on the stream banks are in some places sliding by gravity towards the stream, where they can be easily eroded during flood events. As a results, an equilibrium between erosion and accumulation is expected in the conduit of the cave stream. In intermediate epiphreatic passages, erosion is predicted to be less frequent, and deposition, more frequent, in comparison to the cave stream conduit. And finally, the model suggests a net sediment accumulation in the uppermost epiphreatic conduits, which is in accordance with anecdotal evidence gathered by visitors of the cave in the past decades.

6.2 Further results and outlook

6.2.1 Comparison with the model of Perrin (2003)

The sedimentary dynamics at the event scale as proposed in this thesis can be compared with the conceptual flow model proposed by Perrin (2003). On the basis of stable isotope and water chemistry variations in the cave stream and at the Saivu spring, Perrin (2003) developed a conceptual model hosting four compartments: the soil, the epikarst, the unsaturated zone and the phreatic zone. The soil and the epikarst act as storage compartments. During base flow conditions, the soil water is held by capillarity, and the epikarst water is steadily realeased towards the unsaturated and phreatic zones. Perrin (2003) describes the progress of a major flood event by four steps:

1. When rainfall starts, the soil water is pushed towards the epikarst. Subsequently, the discharge of the epikarst towards the saturated zone increases. The discharge in the phreatic zone and at the spring increases, but the water chemistry is stable.

2. If the rainfall input continues, the soil water may by-pass the epikarst to directly reach the phreatic zone. As a result, in the phreatic zone, the discharge continues to increase and water chemistry is affected by the input from soil water.

3. If the rainfall further continues, the soil becomes saturated and some freshly infiltrated water may by-pass the soil and the epikarst to reach the phreatic zone. The phreatic zone is thus fed by freshly infiltrated water, soil water and epikarst water. Freshly infiltrated water may constitute between 0 to 20% of the discharge, and soil water, between 60 to 70%, while the remainder comes from the epikarst.

4. When the rain stops, the soil water discharges to the epikarst, and the epikarst discharges to the phreatic zone.

Depending on the intensity of the rainfall pulse, flood events may reach stage 1, 2 or 3. In terms of quantification, Perrin (2003) states that the contribution of freshly infiltrated water to the flow in the phreactic zone is zero for a recharge event of 3 mm and 15-20% for a recharge event of 20 mm. Looking into his data set, Perrin (2003) describes the evolution of the stable isotope composition in rainfall water and at the upstream end of the cave stream throughout three flood events. For a flood event of $Q_{up} = 180$ L·s^{-1}, no influence of freshly infiltrated water was detected in the cave stream over the course of the flood peak. For another flood event of $Q_{up} = 270$ L·s^{-1}, the isotopic composition of water in the cave stream reacted to the rainfall with a delay of one day. And finally, during a flood event of $Q_{up} = 400$ L·s^{-1}, the isotopic composition in the cave stream reacted rapidly to the rainfall. The change in the isotopic composition of the phreatic water was simultaneous with the increase of the discharge. These numbers are in line with the proposed conceptual model of the sediment fluxes, which states that there is no direct allochthonous contribution to the turbidity signal during flood events of $Q_{up} \lesssim 200$ L·s^{-1}. During moderate flood events ($Q_{up} \sim 200-300$ L·s^{-1}), the proposed model suggests that the allochthonous turbidity contribution is more or less simultaneous with the discharge peak. Perrin's data suggests that there is still quite a delay between the flood peak and the arrival of freshly infiltrated water in the phreatic zone. These two observations are not necessarily contradictory. First, other parameters than the peak discharge value influence the solute and particle transport velocities during flood events. It would thus be interesting to analyze the turbidity dynamics during the events described by Perrin (which are older than the turbidity time series studied in this work), or to monitor new events in terms of both stable isotope and suspended sediment variations. Besides, following the conceptual flow model of Perrin (2003), there is an important distinction between freshly infiltrated water and soil water in the karst system of Milandre. This constrasts with karst systems that have a mostly allogenic recharge and limited soil storage. Here, allochthonous turbidity is defined as the turbidity directly derived from the soils. Following Perrin's model, allochtonous turbidity can thus be associated with soil water and with freshly infiltrated water. However, Perrin (2003) does not provide a quantification of the event intensity required to reach the stage 2 of his conceptual model, so a further comparison between the two models is so far not possible. Another question that needs to be adressed in this respect is whether soil erosion is limited to the surface or is also triggered inside soils during the stage 2 of flood events. Another possiblity to explain the discrepancy between both conceptual models is that the allochthonous turbidity is indeed produced on the soil surface, but that it reaches the phreatic zone earlier than the recharge water, as, because of exclusion processes, water molecules and particles are not advected in the same way in the underground media. And finally, it is also possible that the secondary turbidity peak that is here interpreted as allochthonous is in fact derived from sediment remobilization in a distal part of the aquifer. An important argument for the allochthonous origin of this delayed turbidity is that it is associated with a greater organic matter content than the primary turbidity peak. To verifiy this assumption, it would be insightful to analyze the composition of intrakarstic and surface sediments in terms of organic content.

6.2.2 Hydraulic modeling

The development of a hydraulic model of the downstream part of the Milandre system, described in the second chapter of this thesis, confirms the suitability of pipe flow model such as SWMM5 for the simulation of flow in karst system. By adjusting the conduit cross sectional areas, both the flow velocities and flow rates in the phreatic zone have been reproduced. The cave survey allowed to set strong constraints on the geometry of the conduit network in the epiphreatic zone. On the basis of two calibration points, the hydraulic head vs discharge relationships in the speleological network are satisfactorily reproduced at 7 out of 8 observation points. This physics based flow model has the benefit that the resulting model can inform spatially and temporally on the hydraulics of the karst system.

This hydraulic model allowed, using the 15 minute interval record of flow rates at the two main springs, to compute the mean boundary shear stress and the shear velocity in the conduit network during the 2004 to 2015 period. After estimating the critical shear stress for sediment mobilization, and the critical shear velocities for d_{50} and d_{95} grain size sediment deposition, flow simulations can thus inform on when and where erosion and deposition are occurring in the conduit network. The model reproduces the general sedimentary dynamics that was observed at the sedimentation monitoring station in the cave stream — i.e. erosion takes place in the direct neighbourhood of the stream, while deposition is maximum a few meters above the stream base level.

While the hydraulic model developed in this work appears to be generally in agreement with the available sedimentation observations, it could be further tested and refined. Indeed, the model prediction at the sedimentation monitoring station is accurate only for a bit more than the half of the observations. Some parameters lack a validation by direct measurement in the field — for example, the estimations of the critical boundary shear stress used to determine the occurrence of erosion, and the critical shear velocity, used to assess the deposition processes. Besides, the sedimentary processes are very simplified in the model. Indeed, they are based on threshold values and do not attempt to fully reproduce the mechanisms governing sediment transport — i.e., the approach does not consider whether there actually is suspended sediment to deposit, or conversely, deposited sediment to erode. A difficulty inherent to the modeling of sedimentary processes is that they are dependent on the sediment grain size. The sediment grain size is usually not unimodal, meaning that it is possible that deposition may occur for some particles of the suspended load while other stay in suspension. Furthermore, the sediment grain size distribution in the suspended load is variable in time, as seen with the flood event monitoring. In the cave deposits, sediment grain size distribution is also spatially variable, as can be seen by walking by the cave stream. While it would not be realistic to try to capture the entirety of these variations, some direct measurements of grain size distribution and critical shear stress on cave deposit samples would be an important step to improve the modeling approach presented here.

Furthermore, the estimations of the mean boundary shear stress and the shear velocity in the conduits, which are used in this work to infer whether erosion or deposition of sediment may occur, also lack a validation by direct measurements. They are dependent on water depth and flow velocity, which may not be reproduced at a fine enough scale in the current model. Indeed, conduit cross sections are considered rectangular and are averaged over the cave survey line-of-sights (length of $\sim$7 m). To assess the impact of this simplification on the estimation of the mean boundary shear stress and the shear velocity, one idea could be to perform a detailed survey of a conduit cross sections and to monitor the variations in water depth at a fine (e.g. a few meters) spatial resolution. The resulting estimations of the simulated shear stress and velocity could then be compared with the one computed by the simplified model. It is also important to note that the mean boundary shear stress used here represents the shear stress of the whole flow section over the conduit border. Lateral variations of the shear stress are expected throughout the flow section, and the shear stress close to the conduit bed is the most important in terms of erosion. Thus, another step to improve the modeling approach would be to characterize the lateral variations of the shear stress.

At the time scale of a single event, the flow simulation indicates that erosion is mostly active when the conduits are getting filled with flood water, and conversely, that a secondary erosive phase may take place when the conduits are drained. Evidences for this secondary erosive phase were found in the long term turbidity record at the springs and in the cave stream. In Milandre, these hypothetical secondary autochthonous turbidity peaks are simultaneous with a step wise decrease in flow rate after a discharge threshold, both in the upstream section of the Milandrine and at the Saivu and Bâme springs. These thresholds appear quite systematically in the spring and cave stream hydrographs and are thus considered as structural features of the karst system. To test whether these secondary turbidity peaks exist in other systems, a straightforward test is to check whether there are turbidity peaks when the discharge passes below a hydraulic threshold. These hydraulic thresholds are easily highlighted by plotting a spring's frequency flow distribution.

While the recession turbidity peaks are in line with the flow simulations, the autochthonous turbidity signal during the flood peak of major events is not well predicted by the model. In the present work, an important simplification was made by computing the average boundary shear stress in every epiphreatic conduit of the model at each simulation time step. Further information could be gained by analyzing shear stress variations at a more local scale, i.e. at the scale of the model conduits. Furthermore, the current model is not expected so far to perform well at a fine time resolution, such as during flood peaks, because the inflow boundary conditions is simply the cumulative discharge at the springs shifted earlier in time. As a result, the spring hydrographs is not reproduced precisely. To overcome this issue, either a rainfall–recharge model should be built, or a hydraulic model supporting the application of boundary conditions at the oulets should be used.

6.2.3 Origins of the turbidity

The monitoring of a moderate intensity flood event allowed to identify the mixed contribution of autochthonous and allochthonous sediment to the spring turbidity. The autochthonous turbidity arrives first at the spring and is characterized by a relatively large ($\sim$10 µm) grain size. The allochothonous turbidity is characterized by a greater portion of fine particles ($<$1.5 µm) and is identified by its simultaneity with high values of *E.coli* concentration and dissolved organic matter, which is estimated through UV fluorescence monitoring. The presence of allochthonous turbidity at the spring during the monitored event is also in line with the conceptual model proposed by Perrin et al. (2003), which states that event water may reach the saturated zone over the course of one event if the effective precipitation is greater than 15 to 20 mm, while it was of 50 mm during the studied event. Also, the timing of the arrival of the maximum in allochthonous turbidity at the spring is in agreement with the mean boundary shear stress simulated by the hydraulic model in the cave stream.

The use of *E.coli* and organic matter as tracers for allochthonous turbidity relies on the fact that they are generally much more abundant in surface soils than in the underground deposits. Direct measurements of soil and cave sediment organic and bacterial content could confirm this assumption. It would also be insightful to monitor the turbidity and the suspended sediment composition in the cave stream, upstream from the epiphreatic zone, in order to compare them with what is observed at the spring. This would allow to confirm the hypothesis on autochthonous sediment composition and to quantify how much sediment is remobilized in this part of the system.

6.2.4 Fine particle dynamics

Through the long term monitoring of the suspended sediment composition in the Milandre system, an upward trend in the phyllosilicate concentration was pointed out. The phyllosilicate concentration is well correlated with groundwater temperature both on a seasonal scale and on a $\sim$10 year scale. It is not yet clear if this relationship is of causal nature. While water temperature was shown in lab experiments to have a positive effect on fine sediment erodibility and a negative effect on fine particle settling velocity, this effect needs to be investigated in karst environments in order to confirm this hypothesis. Moreover, the data set did not indicate a relationship between pH and fine sediment concentration, although it was previously mentioned by karst authors (Atteia and Kozel, 1997; Shevenell and McCarthy, 2002). A limitation of the sediment trap methodology is that the sediment composition is averaged over each sampling period ($\sim$3 months). Further knowledge on the physico-chemical controls on fine particle concentration could be gained for instance by instantaneous measurements of the sediment composition and grain size and of the physico-chemical parameters of water (temperature, pH and electrical conductivity). Besides, the upward trend in phyllosilicate concentration may also arise from an enhanced availability of this material in soils, e.g. because of land use evolution, or by an indirect effect of climate change, which was shown to affect biological activity in soil in the Milandre catchment (Jeannin et al., 2016). This could be investigated by evaluating the effects of agricultural practices on sediment availability and by monitoring the evolution of land use and of the physical properties of soils.

Bibliography

Amraoui F., Razack M., and Bouchaou L. 2003. Turbidity dynamics in karstic systems. Example of Ribaa and Bittit springs in the Middle Atlas (Morocco). *Hydrological Sciences Journal*, 48(6):971–984. doi: 10.1623/hysj.48.6.971.51418.

Atteia O. Etude de la turbidité des sources de Milandre et de la Beuchire avant travaux. Unpublished report for MFR Géologie–Géotechnique SA, CHYN, Université de Neuchâtel, 1998.

Atteia O. and Kozel R. 1997. Particle size distributions in waters from a karstic aquifer: from particles to colloids. *Journal of Hydrology*, 201(1):102–119. doi: 10.1016/S0022-1694(97)00033-4.

Auckenthaler A., Raso G., and Huggenberger P. 2002. Particle transport in a karst aquifer: natural and artificial tracer experiments with bacteria, bacteriophages and microspheres. *Water Science and Technology*, 46(3):131–138.

Baker V. R. and Ritter D. F. 1975. Competence of rivers to transport coarse bedload material. *GSA Bulletin*, 86(7):975. doi: 10.1130/0016-7606(1975)86⟨975:CORTTC⟩2.0.CO;2.

Blant D., Jeannin P.-Y., Meury P. X., Eichenberger U., Hessenauer M., Häuselmann P., and Adatte T. A16 – Section 2: Etude d'impact sur la grotte de Milandre, rapport annuel 2007. Unpublished report for the Republic and Canton of the Jura, SISKA, 2008.

Blant D., Meury P. X., Eichenberger U., Hessenauer M., Häuselmann P., Weber E., and Adatte T. A16 – Section 2: Etude d'impact sur la grotte de Milandre, rapport annuel 2008. Unpublished report for the Republic and Canton of the Jura, SISKA, 2009.

Blant D., Meury P. X., Eichenberger U., Hessenauer M., Häuselmann P., Weber E., and Adatte T. A16 – Section 2: Etude d'impact sur la grotte de Milandre, rapport annuel 2009. Unpublished report for the Republic and Canton of the Jura, SISKA, 2010.

Blant D., Meury P. X., Eichenberger U., Hessenauer M., Häuselmann P., Weber E., and Adatte T. A16 – Section 2: Etude d'impact sur la grotte de Milandre, rapport annuel 2010. Unpublished report for the Republic and Canton of the Jura, SISKA, 2011.

Blant D., Hessenauer M., Eichenberger U., Häuselmann P., Weber E., and Adatte T. A16 – Section 2: Etude d'impact sur la grotte de Milandre, rapport annuel 2011. Unpublished report for the Republic and Canton of the Jura, SISKA, 2012.

Bosch R. F. and White W. B. *Studies of Cave Sediments*, chapter Lithofacies and Transport of Clastic Sediments in Karstic Aquifers, pages 1–22. Springer US, Boston, MA, 2004. ISBN 978-1-4419-9118-8. doi: 10.1007/978-1-4419-9118-8_1.

Bouchaou L., Mangin A., and Chauve P. 2002. Turbidity mechanism of water from a karstic spring: example of the Ain Asserdoune spring (Beni Mellal Atlas, Morocco). *Journal of Hydrology*, 265(1-4):34–42. doi: 10.1016/S0022-1694(02)00098-7.

Boyer D. G. and Pasquarell G. C. 1999. Agricultural land use impacts on bacterial water quality in a karst groundwater aquifer. *JAWRA Journal of the American Water Resources Association*, 35(2):291–300. doi: 10.1111/j.1752-1688.1999.tb03590.x.

Brennan F. P., O'Flaherty V., Kramers G., Grant J., and Richards K. G. March 2010. Long-term persistence and leaching of *Escherichia coli* in temperate maritime soils. *Applied and environmental microbiology*, 76(5):1449–1455. doi: 10.1128/aem.02335-09.

Butscher C., Auckenthaler A., Scheidler S., and Huggenberger P. 2011. Validation of a numerical indicator of microbial contamination for karst springs. *Ground Water*, 49(1):66–76. doi: 10.1111/j.1745-6584.2010.00687.x.

Campbell C. and Sullivan S. M. 2002. Simulating time-varying cave flow and water levels using the Storm Water Management Model. *Engineering Geology*, 65(2-3):133 – 139. ISSN 0013-7952. doi: 10.1016/S0013-7952(01)00120-X. Engineering and Environmental Impacts of Karst.

Chédeville S., Laignel B., Massei N., Hauchard E., Ladhui V., Todisco D., Hanin G., and Rodet J. 2016. Study of hydro-sedimentary variability of the Radicatel karst system influenced by climate signal fluctuations (Normandy, France). *Hydrological Sciences Journal*, 61(4):732–740. doi: 10.1080/02626667.2014.965171.

Chen Z. and Goldscheider N. 2014. Modeling spatially and temporally varied hydraulic behavior of a folded karst system with dominant conduit drainage at catchment scale, Hochifen–Gottesacker, Alps. *Journal of Hydrology*, 514:41 – 52. ISSN 0022-1694. doi: 10.1016/j.jhydrol.2014.04.005.

Chess D. L., Chess C. A., Sasowsky I. D., Schmidt V. A., and White W. B. 2010. Clastic sediments in the Butler Cave – Sinking Creek System, Virginia, USA. *Acta Carsologica*, 39(1):11–26. doi: 10.3986/ac.v39i1.109.

Cholet C., Steinmann M., Charlier J.-B., and Denimal S. Transport of solute and suspended matter elements during a flood event in a small karst aquifer. In *Eurokarst, 5–7 September 2016, Neuchâtel, Switzerland*, 2016.

Collins S., Reinhardt E., Werner C., Maillot C. L., Devos F., and Meacham S. 2015a. Regional response of the coastal aquifer to Hurricane Ingrid and sedimentation flux in the Yax Chen cave system (Ox Bel Ha) Yucatan, Mexico. *Palaeogeography, Palaeoclimatology, Palaeoecology*, 438:226–238. doi: 10.1016/j.palaeo.2015.07.030.

Collins S., Reinhardt E., Werner C., Maillot C. L., Devos F., and Rissolo D. 2015b. Late Holocene mangrove development and onset of sedimentation in the Yax Chen cave system (Ox Bel Ha) Yucatan, Mexico: Implications for using cave sediments as a sea-level indicator. *Palaeogeography, Palaeoclimatology, Palaeoecology*, 438:124–134. ISSN 0031-0182. doi: 10.1016/j.palaeo.2015.07.042.

Currens J. C. 2002. Changes in groundwater quality in a conduit-flow-dominated karst aquifer, following BMP implementation. *Environmental Geology*, 42(5):525–531. doi: 10.1007/s00254-001-0515-6.

Davies W. E. and Chao E. C. T. Report on sediments in Mammoth cave, Kentucky. Technical report, U.S. National Park Service, August 1959.

Davis R. K., Hamilton S., and Brahana J. V. 2005. *Escherichia coli* survival in mantled karst springs and streams, northwest Arkansas Ozarks, USA. *JAWRA Journal of the American Water Resources Association*, 41(6):1279–1287. doi: 10.1111/j.1752-1688.2005.tb03800.x.

Debnath K. M. and Chaudhuri S. 2010. Cohesive sediment erosion threshold: A review. *ISH Journal of Hydraulic Engineering*, 16(1):36–56. doi: 10.1080/09715010.2010.10514987.

Dogwiler T. and Wicks C. M. 2004. Sediment entrainment and transport in fluviokarst systems. *Journal of Hydrology*, 295(1-4):163 – 172. doi: 10.1016/j.jhydrol.2004.03.002.

Drysdale R., Pierotti L., Piccini L., and Baldacci F. 2001. Suspended sediments in karst spring waters near Massa (Tuscany), Italy. *Environmental Geology*, 40(8):1037–1050. doi: 10.1007/s002540100311.

Dussart L., Dupont J.-P., Zimmerlin I., Lacroix M., Saiter J., Junter G.-A., and Jouenne T. 2003. Occurrence of sessile pseudomonas oryzihabitans from a karstified chalk aquifer. *Water Research*, 37(7):1593 – 1600. ISSN 0043-1354. doi: 10.1016/S0043-1354(02)00555-9.

Dussart-Baptista L., Massei N., Dupont J.-P., and Jouenne T. 2003. Transfer of bacteria-contaminated particles in a karst aquifer: evolution of contaminated materials from a sinkhole to a spring. *Journal of Hydrology*, 284(1-4):285 – 295. doi: 10.1016/j.jhydrol.2003.08.007.

Favre I. Base de données des essais de traçage du plateau karstique de Bure (JU), SIG, interprétations statistiques. Master's thesis, University of Neuchâtel, 2001.

Flynn R. M. and Sinreich M. 2010. Characterisation of virus transport and attenuation in epikarst using short pulse and prolonged injection multi-tracer testing. *Water Research*, 44(4):1138 – 1149. doi: 10.1016/j.watres.2009.11.032. Transport and Fate of Colloids and Microbes in Granular Aqueous Environments.

Ford D. and Williams P. *Karst Hydrogeology and Geomorphology*, chapter 6, pages 145–208. John Wiley & Sons Ltd,., 2007a. ISBN 9781118684986. doi: 10.1002/9781118684986.ch6.

Ford D. and Williams P. D. *Karst hydrogeology and geomorphology*. John Wiley & Sons, 2007b.

Fournier M., Massei N., Bakalowicz M., and Dupont J.-P. 2007a. Use of univariate clustering to identify transport modalities in karst aquifers. *Comptes Rendus Geoscience*, 339(9):622 – 631. doi: 10.1016/j.crte.2007.07.009.

Fournier M., Massei N., Bakalowicz M., Dussart-Baptista L., Rodet J., and Dupont J. P. 2007b. Using turbidity dynamics and geochemical variability as a tool for understanding the behavior and vulnerability of a karst aquifer. *Hydrogeology Journal*, 15(4):689–704. doi: 10.1007/s10040-006-0116-2.

Gale S. J. 1984. The hydraulics of conduit flow in carbonate aquifers. *Journal of Hydrology*, 70(1-4):309–327. doi: 10.1016/0022-1694(84)90129-X.

Gigon R. and Wenger R. *Inventaire spéléologique de la Suisse. Tome II. Canton du Jura*. Commission de Spéléologie de la Société helvétique des Sciences naturelles, 1986.

Gillieson D. 1986. Cave sedimentation in the new Guinea highlands. *Earth Surface Processes and Landforms*, 11(5):533–543. doi: 10.1002/esp.3290110508.

Goldscheider N. and Drew D. *Methods in Karst Hydrogeology*. IAH: International Contributions to Hydrogeology, 26. CRC Press, June 2007.

Goldscheider N., Hötzl H., Käss W., and Ufrecht W. 2003. Combined tracer tests in the karst aquifer of the artesian mineral springs of stuttgart, germany. *Environmental Geology*, 43(8):922–929. ISSN 1432-0495. doi: 10.1007/s00254-002-0714-9.

Goldscheider N., Meiman J., Pronk M., and Smart C. 2008. Tracer tests in karst hydrogeology and speleology. *International Journal of speleology*, 37(1):3. doi: 10.5038/1827-806X.37.1.3.

Göppert N. and Goldscheider N. 2008. Solute and colloid transport in karst conduits under low- and high-flow conditions. *Ground Water*, 46(1):61–68. doi: 10.1111/j.1745-6584.2007.00373.x.

Grasso D. A. and Jeannin P.-Y. 1994. Estimation des pertes dans la partie aval du réseau karstique de la Milandrine : bilan hydrique au sein d'un aquifère karstique. *Bulletin d'Hydrogéologie*, 13:115–128.

Grissinger E. H. 1966. Resistance of selected clay systems to erosion by water. *Water Resources Research*, 2 (1):131–138. doi: 10.1029/WR002i001p00131.

Gunn J., Tranter J., Perkins J., and Hunter C. 1997. Sanitary bacterial dynamics in a mixed karst aquifer. *IAHS Publications-Series of Proceedings and Reports-Intern Assoc Hydrological Sciences*, 247:61–71.

Hauns M. *Modeling tracer and particle transport under turbulent flow conditions in karst conduit structures*. PhD thesis, University of Neuchâtel, 1999.

Häuselmann P., Blant D., Hessenauer M., Eichenberger U., Weber E., and Adatte T. A16 – Section 2: Etude d'impact sur la grotte de Milandre, rapport annuel 2013. Unpublished report for the Swiss Federal Roads Office, SISKA, 2014a.

Häuselmann P., Blant D., Hessenauer M., Eichenberger U., Weber E., and Adatte T. A16 – Section 2: Etude d'impact sur la grotte de Milandre, rapport annuel 2012. Unpublished report for the Swiss Federal Roads Office, SISKA, 2014b.

Häuselmann P., Blant D., Hessenauer M., Eichenberger U., Weber E., Jeannin P.-Y., and Adatte T. A16 – Section 2: Etude d'impact sur la grotte de Milandre, rapport annuel 2014. Unpublished report for the Swiss Federal Roads Office, SISKA, 2015.

Häuselmann P., Blant D., Hessenauer M., Eichenberger U., Weber E., Jeannin P.-Y., and Adatte T. A16 – Section 2: Etude d'impact sur la grotte de Milandre, rapport annuel 2015. Unpublished report for the Swiss Federal Roads Office, SISKA, 2016.

Herman E. K., Tancredi J. H., Toran L., and White W. B. 2007. Mineralogy of suspended sediment in three karst springs. *Hydrogeology Journal*, 15(2):255–266. doi: 10.1007/s10040-006-0108-2.

Herman E. K., Toran L., and White W. B. 2008. Threshold events in spring discharge: Evidence from sediment and continuous water level measurement. *Journal of Hydrology*, 351(1-2):98–106. doi: 10.1016/j.jhydrol.2007.12.001.

Herman E. K., Toran L., and White W. B. 2012. Clastic sediment transport and storage in fluviokarst aquifers: an essential component of karst hydrogeology. *Carbonates and Evaporites*, 27(3-4):211–241. doi: 10.1007/s13146-012-0112-7.

Hessenauer M., Christe R., Jeannin P.-Y., Meury P. X., and Adatte T. A16 – Section 2: Etude d'impact sur la grotte de Milandre. Unpublished report for the Republic and Canton of the Jura, SISKA, 2004.

Hessenauer M., Meury P. X., and Jeannin P.-Y. A16 – Section 2: Mesures de protection de la grotte de Milandre et de la rivière souterraine. Mesure no. 7: Étude des relations Milandrine – Lômennes. Multitraçages des 6 octobre 2002 et 28/30 septembre 2004. Unpublished report for the Republic and Canton of the Jura, MFR Géologie–Géotechnique SA, 2005.

James W., Rossman L., and James W. R. C. *User's guide to SWMM5*. Computational Hydraulics International, Guelph, Ontario, Canada, 13th edition, November 2010.

Jamieson R., Joy D. M., Lee H., Kostaschuk R., and Gordon R. 2005. Transport and deposition of sediment-associated *Escherichia coli* in natural streams. *Water Research*, 39(12):2665 – 2675. doi: 10.1016/j.watres.2005.04.040.

Jeannin P.-Y. 2001. Modeling flow in phreatic and epiphreatic karst conduits in the Hölloch Cave (Muotatal, Switzerland). *Water Resources Research*, 37(2):191–200. ISSN 1944-7973. doi: 10.1029/2000WR900257.

Jeannin P.-Y. and Maréchal J.-C. 1995. Lois de pertes de charges dans les conduits karstiques : base théorique et observations. *Bulletin d'Hydrogéologie*, 14:149–176.

Jeannin P.-Y., Hessenauer M., Eichenberger U., and Meury P. X. Can particle transport be modelled? Indications from the Milandre underground laboratory (Jura, Switzerland). In *2013 GSA Annual Meeting in Denver: 125th Anniversary of GSA*, 2013.

Jeannin P.-Y., Malard A., Rickerl D., and Weber E. 2015. Assessing karst-hydraulic hazards in tunneling – the Brunnmühle spring system – Bernese Jura, Switzerland. *Environmental Earth Sciences*, 74(12):7655–7670. ISSN 1866-6299. doi: 10.1007/s12665-015-4655-5.

Jeannin P.-Y., Hessenauer M., Malard A., and Chapuis V. 2016. Impact of global change on karst groundwater mineralization in the Jura Mountains. *Science of the Total Environment*, 541:1208–1221. doi: 10.1016/j.scitotenv.2015.10.008.

Jeannin P.-Y., Malard A., Häuselmann P., and Meury P.-X. *EuroKarst 2016, Neuchâtel*, chapter Effect of Cave Ventilation on Karst Water Chemographs, pages 129–139. Springer International Publishing, Cham, 2017. ISBN 978-3-319-45465-8. doi: 10.1007/978-3-319-45465-8_14.

Jianwei H. 1981. Experimental study of settling properties of cohesive sediment in still water. *Journal of Sediment Research*, 2:30–41.

Jones W. K. 1971. Characteristics of the underground floodplain. *The National Speleological Society Bulletin*, 33(3):105–114.

Julien P. *Erosion and Sedimentation*. Cambridge University Press, 1998. ISBN 9780521636391.

Kaufmann G., Gabrovšek F., and Turk J. 2016. Modelling cave flow hydraulics in Postojnska jama, Slovenia. *Acta Carsologica*, 45:57–70. doi: 10.3986/ac.v45i1.3059.

Kiraly L. 1995. Effect of the epikarst on the hydrograph of karst springs: a numerical approach. *Bulletin d'Hydrogéologie*, 14:199–220.

Kiraly L. et al. *Notice explicative de la carte hydrogéologique du canton de Neuchâtel*. Université de Neuchâtel, Institut de géologie, Centre d'hydrogéologie, 1973.

Knapp E. P., Terry D. O., Harbor D. J., and Thren R. C. *Studies of Cave Sediments*, chapter Reading Virginia's Paleoclimate from the Geochemistry and Sedimentology of Clastic Cave Sediments, pages 95–106. Springer US, Boston, MA, 2004. ISBN 978-1-4419-9118-8. doi: 10.1007/978-1-4419-9118-8_6.

Knierim K. J., Hays P. D., and Bowman D. 2015. Quantifying the variability in Escherichia coli (E. coli) throughout storm events at a karst spring in northwestern Arkansas, United States. *Environmental Earth Sciences*, 74(6):4607–4623. doi: 10.1007/s12665-015-4416-5.

Knighton D. *Fluvial Forms and Processes: A New Perspective*. A Hodder Arnold Publication. Arnold, 1998. ISBN 9780340663134.

Kovács A. and Jeannin P.-Y. 2003. Hydrogeological overview of the Bure plateau, Ajoie, Switzerland. *Eclogae Geologicae Helvetiae*, 96(3):367–380. doi: 10.1007/s00015-003-1099-9.

Lacroix M., Rodet J., Wang H. Q., Massei N., and Dupont J.-P. 2000. Origine des matières en suspension dans un système aquifère karstique : apports de la microgranulométrie. *Comptes Rendus de l'Académie des Sciences - Series IIA - Earth and Planetary Science*, 330(5):347–354. doi: 10.1016/S1251-8050(00)00161-0.

Laflen J. M., Beasley R. P., et al. 1960. Effects of compaction on critical tractive forces in cohesive soils. *Research Bulletin. Missouri Agricultural Experiment Station*, 749.

Lau Y. 1994. Temperature effect on settling velocity and deposition of cohesive sediments. *Journal of Hydraulic Research*, 32(1):41–51. doi: 10.1080/00221689409498788.

Luhmann A. J., Covington M. D., Alexander S. C., Chai S. Y., Schwartz B. F., Groten J. T., and Alexander Jr E. C. 2012. Comparing conservative and nonconservative tracers in karst and using them to estimate flow path geometry. *Journal of Hydrology*, 448-449:201–211. doi: 10.1016/j.jhydrol.2012.04.044.

Lynch F. L., Mahler B. J., and Hauwert N. N. *Studies of Cave Sediments*, chapter Provenance of Suspended Sediment Discharged from a Karst Aquifer Determined by Clay Mineralogy, pages 83–93. Springer US, Boston, MA, 2004. ISBN 978-1-4419-9118-8. doi: 10.1007/978-1-4419-9118-8_5.

Mahler B., Personné J.-C., Lods G., and Drogue C. 2000. Transport of free and particulate-associated bacteria in karst. *Journal of Hydrology*, 238(3-4):179–193. doi: 10.1016/S0022-1694(00)00324-3.

Mahler B. J. and Lynch F. L. 1999. Muddy waters: temporal variation in sediment discharging from a karst spring. *Journal of Hydrology*, 214(1-4):165 – 178. doi: 10.1016/S0022-1694(98)00287-X.

Mahler B. J., Bennett P. C., and Zimmerman M. 1998. Lanthanide-labeled clay: A new method for tracing sediment transport in karst. *Ground Water*, 36(5):835–843. doi: 10.1111/j.1745-6584.1998.tb02202.x.

Mahler B. J., Lynch L., and Bennett P. C. 1999. Mobile sediment in an urbanizing karst aquifer: implications for contaminant transport. *Environmental Geology*, 39(1):25–38. doi: 10.1007/s002540050434.

Mahler B. J., Personné J.-C., Lynch F. L., and Van Metre P. C. *Studies of Cave Sediments*, chapter Sediment and Sediment-Associated Contaminant Transport Through Karst, pages 23–46. Springer US, Boston, MA, 2004. ISBN 978-1-4419-9118-8. doi: 10.1007/978-1-4419-9118-8_2.

Maréchal J.-C. Étude et modélisation de l'hydraulique et du transport dans les drains karstiques. Master's thesis, Université de Neuchâtel, December 1994.

Marshall D., Brahana J., and Davis R. Resuspension of viable sediment-bound enteric pathogens in shallow karst aquifers. In Brahana J. V., Eckstein Y., Ongley L K S. R., and E M. J., editors, *Gambling With Groundwater – Physical, Chemical, and Biological Aspects of Aquifer-Stream Relations*, 1998.

Massei N., Lacroix M., Wang H., Mahler B., and Dupont J. 2002. Transport of suspended solids from a karstic to an alluvial aquifer: the role of the karst/alluvium interface. *Journal of Hydrology*, 260(1-4):88 – 101. doi: 10.1016/S0022-1694(01)00608-4.

Massei N., Wang H., Dupont J., Rodet J., and Laignel B. 2003. Assessment of direct transfer and resuspension of particles during turbid floods at a karstic spring. *Journal of Hydrology*, 275(1-2):109 – 121. doi: 10.1016/S0022-1694(03)00020-9.

Massei N., Dupont J., Mahler B., Laignel B., Fournier M., Valdes D., and Ogier S. 2006. Investigating transport properties and turbidity dynamics of a karst aquifer using correlation, spectral, and wavelet analyses. *Journal of Hydrology*, 329(1-2):244 – 257. doi: 10.1016/j.jhydrol.2006.02.021.

Mattson S. 1928. Cataphoresis and the electrical neutralization of colloidal material. *The Journal of Physical Chemistry*, 32(10):1532–1552. doi: 10.1021/j150292a011.

Mavrocordatos D., Mondi-Couture C., Atteia O., Leppard G., and Perret D. 2000. Formation of a distinct class of Fe–Ca(–Corg)-rich particles in a complex peat–karst system. *Journal of Hydrology*, 237(3-4):234–247. doi: 10.1016/S0022-1694(00)00309-7.

McDowell-Boyer L. M., Hunt J. R., and Sitar N. 1986. Particle transport through porous media. *Water Resources Research*, 22(13):1901–1921. ISSN 1944-7973. doi: 10.1029/WR022i013p01901.

McFarlane D. A. and Lundberg J. *Studies of Cave Sediments*, chapter Reliquiae Diluvianae Alter: Last Interglacial Flood Deposits in the Caves of the West Indies, pages 313–322. Springer US, Boston, MA, 2004. ISBN 978-1-4419-9118-8. doi: 10.1007/978-1-4419-9118-8_17.

Mehta A. J., Hayter E. J., Parker W. R., Krone R. B., and Teeter A. M. 1989. Cohesive sediment transport. i: Process description. *Journal of Hydraulic Engineering*, 115(8):1076–1093. doi: 10.1061/(ASCE)0733-9429(1989)115:8(1076).

Meury P. X., Hessenauer M., Eichenberger U., and Adatte T. A16 – Section 2: Etude d'impact sur la grotte de Milandre, rapport annuel 2004. Unpublished report for the Republic and Canton of the Jura, SISKA, 2005.

Meury P. X., Christe R., Hessenauer M., Eichenberger U., Jeannin P.-Y., Malard A., and Adatte T. A16 – Section 2: Etude d'impact sur la grotte de Milandre, rapport annuel 2005. Unpublished report for the Republic and Canton of the Jura, SISKA, 2006.

Murray A., Stanton R., Olley J., and Morton R. 1993. Determining the origins and history of sedimentation in an underground river system using natural and fallout radionuclides. *Journal of Hydrology*, 146:341–359. doi: 10.1016/0022-1694(93)90283-F.

Naghipour N., Ayyoubzadeh S. A., and Sedighkia M. 2014. Investigation on the effect of different factors on clay particle sedimentation in freshwaters. *Journal of Biodiversity and Environmental Sciences*, 5(5):75–81.

Owen M. W. Determination of the settling velocities of cohesive muds. Technical report, Hydraulics Research Station Wallingford, 1976.

Palmer A. N. and Palmer M. V. 2006. Hydraulic processes in the origin of tiankengs. *Speleogenesis and Evolution of Karst Aquifers*, 4(1):1–8.

Pantillon P. Etude hydrogéologique du site expérimental du Maira dans le projet COST 65. Master's thesis, University of Neuchâtel, 1993.

Pasquarell G. C. and Boyer D. G. 1995. Agricultural impacts on bacterial water quality in karst groundwater. *Journal of Environmental Quality*, 24(5):959–969. doi: 10.2134/jeq1995.00472425002400050026x.

Perrin J. *A conceptual model of flow and transport in a karst aquifer based on spatial and temporal variations of natural tracers*. PhD thesis, Université de Neuchâtel, 2003.

Perrin J., Jeannin P.-Y., and Zwahlen F. 2003. Epikarst storage in a karst aquifer: a conceptual model based on isotopic data, milandre test site, switzerland. *Journal of Hydrology*, 279(1–4):106 – 124. ISSN 0022-1694. doi: 10.1016/S0022-1694(03)00171-9.

Perrin J., Jeannin P.-Y., and Cornaton F. 2007. The role of tributary mixing in chemical variations at a karst spring, Milandre, Switzerland. *Journal of Hydrology*, 332(1–2):158 – 173. ISSN 0022-1694. doi: 10.1016/j.jhydrol.2006.06.027.

Personné J. C., Poty F., Vaute L., and Drogue C. 1998. Survival, transport and dissemination of *Escherichia coli* and enterococccci in a fissured environment. Study of a flood in a karstic aquifer. *Journal of Applied Microbiology*, 84(3):431–438. doi: 10.1046/j.1365-2672.1998.00366.x.

Peterson E. W. and Wicks C. M. 2006. Assessing the importance of conduit geometry and physical parameters in karst systems using the Storm Water Management Model (SWMM). *Journal of Hydrology*, 329(1–2):294 – 305. ISSN 0022-1694. doi: 10.1016/j.jhydrol.2006.02.017.

Pronk M. *Origin and Behaviour of Microorganisms and Particles in Selected Karst Aquifer Systems*. PhD thesis, University of Neuchâtel, 2008.

Pronk M., Goldscheider N., and Zopfi J. 2006. Dynamics and interaction of organic carbon, turbidity and bacteria in a karst aquifer system. *Hydrogeology Journal*, 14(4):473–484. doi: 10.1007/s10040-005-0454-5.

Pronk M., Goldscheider N., and Zopfi J. 2007. Particle-size distribution as indicator for fecal bacteria contamination of drinking water from karst springs. *Environmental Science & Technology*, 41(24):8400–8405. doi: 10.1021/es071976f. PMID: 18200870.

Pronk M., Goldscheider N., and Zopfi J. 2009. Microbial communities in karst groundwater and their potential use for biomonitoring. *Hydrogeology Journal*, 17(1):37–48. doi: 10.1007/s10040-008-0350-x.

Reed T. M., McFarland J. T., Fryar A. E., Fogle A. W., and Taraba J. L. 2010. Sediment discharges during storm flow from proximal urban and rural karst springs, central Kentucky, USA. *Journal of Hydrology*, 383 (3-4):280–290. doi: 10.1016/j.jhydrol.2009.12.043.

Reed T. M., Fryar A. E., Brion G. M., and Ward J. W. 2011. Differences in pathogen indicators between proximal urban and rural karst springs, central kentucky, usa. *Environmental Earth Sciences*, 64(1):47–55. ISSN 1866-6299. doi: 10.1007/s12665-010-0816-8.

Rodriguez A. Le transport des particules dans le karst : étude préliminaire dans le karst jurassien. Master's thesis, University of Neuchâtel, 1996.

Ryan M. and Meiman J. 1996. An examination of short-term variations in water quality at a karst spring in Kentucky. *Ground Water*, 34(1):23–30. doi: 10.1111/j.1745-6584.1996.tb01861.x.

Sasowsky I. D., Clotts R. A., Crowell B., Walko S. M., LaRock E. J., and Harbert W. *Studies of Cave Sediments*, chapter Paleomagnetic Analysis of a Long-Term Sediment Trap, Kooken Cave, Huntingdon County, Pennsylvania, USA, pages 71–81. Springer US, Boston, MA, 2004. ISBN 978-1-4419-9118-8. doi: 10.1007/978-1-4419-9118-8_4.

Savoy L., Meury P. X., Eichenberger U., Hessenauer M., Malard A., Häuselmann P., Jeannin P.-Y., and Adatte T. A16 – Section 2: Etude d'impact sur la grotte de Milandre, rapport annuel 2006. Unpublished report for the Republic and Canton of the Jura, SISKA, 2007.

Schiperski F., Zirlewagen J., Hillebrand O., Licha T., and Scheytt T. 5 2015a. Preliminary results on the dynamics of particles and their size distribution at a karst spring during a snowmelt event. *Journal of Hydrology*, 524:326–332. doi: 10.1016/j.jhydrol.2015.02.035.

Schiperski F., Zirlewagen J., Hillebrand O., Nödler K., Licha T., and Scheytt T. 2015b. Relationship between organic micropollutants and hydro-sedimentary processes at a karst spring in south-west Germany. *Science of The Total Environment*, 532:360–367. doi: 10.1016/j.scitotenv.2015.06.007.

Schiperski F., Zirlewagen J., and Scheytt T. 2016. Transport and attenuation of particles of different density and surface charge: A karst aquifer field study. *Environmental Science & Technology*, 50(15):8028–8035. doi: 10.1021/acs.est.6b00335. PMID: 27348254.

Schmassmann S. Analyses minéralogiques et géochimiques d'une carotte de sédiment karstique de la grotte de Milandre (Ajoie, JU), 2006.

Schroeder J. and Ford D. C. 1983. Clastic sediments in Castleguard Cave, Columbia Icefields, Alberta, Canada. *Arctic and Alpine Research*, 15:451–461. doi: 10.2307/1551232.

Shevenell L. and McCarthy J. F. 2002. Effects of precipitation events on colloids in a karst aquifer. *Journal of Hydrology*, 255(1-4):50–68. doi: 10.1016/S0022-1694(01)00510-8.

Sinreich M., Flynn R., and Zopfi J. 2009. Use of particulate surrogates for assessing microbial mobility in subsurface ecosystems. *Hydrogeology Journal*, 17(1):49–59. doi: 10.1007/s10040-008-0362-6.

Springer G. S. and Kite J. 1997. River-derived slackwater sediments in caves along Cheat River, West Virginia. *Geomorphology*, 18(2):91 – 100. doi: 10.1016/S0169-555X(96)00022-0.

Toran L., Tancredi J. H., Herman E. K., and White W. B. 2006. Conductivity and sediment variation during storms as evidence of pathways to karst springs. *Perspectives on Karst Geomorphology, Hydrology, and Geochemistry: A Tribute Volume to Derek C. Ford and William B. White*, 404:169. doi: 10.1130/2006.2404(14).

Valdes D., Dupont J.-P., Massei N., Laignel B., and Rodet J. 2005. Analysis of karst hydrodynamics through comparison of dissolved and suspended solids' transport. *Comptes Rendus Geoscience*, 337(15):1365 – 1374. doi: 10.1016/j.crte.2005.07.011.

Valdes D., Dupont J.-P., Massei N., Laignel B., and Rodet J. 2006. Investigation of karst hydrodynamics and organization using autocorrelations and t-c curves. *Journal of Hydrology*, 329(3-4):432 – 443. doi: 10.1016/j.jhydrol.2006.02.030.

VanderZaag A. C., Campbell K. J., Jamieson R. C., Sinclair A. C., and Hynes L. G. 2010. Survival of *Escherichia coli* in agricultural soil and presence in tile drainage and shallow groundwater. *Canadian Journal of Soil Science*, 90(3):495–505. doi: 10.4141/CJSS09113.

Vesper D. J. and White W. B. 2003. Metal transport to karst springs during storm flow: an example from Fort Campbell, Kentucky/Tennessee, USA. *Journal of Hydrology*, 276(1-4):20–36. doi: 10.1016/S0022-1694(03)00023-4.

Wan Y., Wu H., Roelvink D., and Gu F. 2015. Experimental study on fall velocity of fine sediment in the Yangtze Estuary, China. *Ocean Engineering*, 103:180 – 187. ISSN 0029-8018. doi: 10.1016/j.oceaneng.2015.04.076.

White E. L. and White W. B. October 1968. Dynamics of sediment transport in limestone caves. *Bulletin of the National Speleological Society*, 30(4):115–129.

White W. B. 1969. Conceptual models for carbonate aquifers. *Ground Water*, 7(3):15–21. ISSN 1745-6584. doi: 10.1111/j.1745-6584.1969.tb01279.x.

White W. B. 1977. Characterization of karst soils by near infrared spectroscopy. *The National Speleological Society Bulletin*, 39(1):27–31.

White W. B. and Hess J. W. July 1982. Geomorphology of Burnsville Cove and the Geology of the Butler Cave – Sinking Creek System. *The National Speleological Society Bulletin*, 44(3):67–77.

White W. B. and White E. L. Storm pulses, thresholds, and fluid mechanics in the transport of clastic sediments in limestone aquifers. In *Proceedings of the 12th International Congress of Speleology*, 1997.

Williams G. P. 1989. Sediment concentration versus water discharge during single hydrologic events in rivers. *Journal of Hydrology*, 111(1):89–106. doi: 10.1016/0022-1694(89)90254-0.

Worthington S. R. H. 2003. A comprehensive strategy for understanding flow in carbonate aquifer. *Speleogenesis and Evolution of Karst Aquifers*, 1(1):1–8.

Worthington S. R. H. 2009. Diagnostic hydrogeologic characteristics of a karst aquifer (Kentucky, USA). *Hydrogeology Journal*, 17(7):1665–1678. ISSN 1435-0157. doi: 10.1007/s10040-009-0489-0.

Worthington S. R. H., Smart C. C., and Ruland W. W. Assessment of groundwater velocities to the municipal wells at Walkerton. In D. Stolle A. P. and Crowder J., editors, *Ground and Water: Theory to Practice*. Southern Ontario Section of the Canadian Geotechnical Society, 2002.

Wu Y., Jiang Y., Yuan D., and Li L. 2008. Modeling hydrological responses of karst spring to storm events: example of the Shuifang spring (Jinfo Mt., Chongqing, China). *Environmental Geology*, 55(7):1545–1553. ISSN 1432-0495. doi: 10.1007/s00254-007-1105-z.

Zhang P., Johnson W. P., Piana M. J., Fuller C. C., and Naftz D. L. 2001. Potential artifacts in interpretation of differential breakthrough of colloids and dissolved tracers in the context of transport in a zero-valent iron permeable reactive barrier. *Groundwater*, 39(6):831–840. doi: 10.1111/j.1745-6584.2001.tb02471.x.

Appendix I

This appendix describes the tracer tests used for the calibration of the phreatic conduits of the hydraulic model (Sec. 2.3.1).

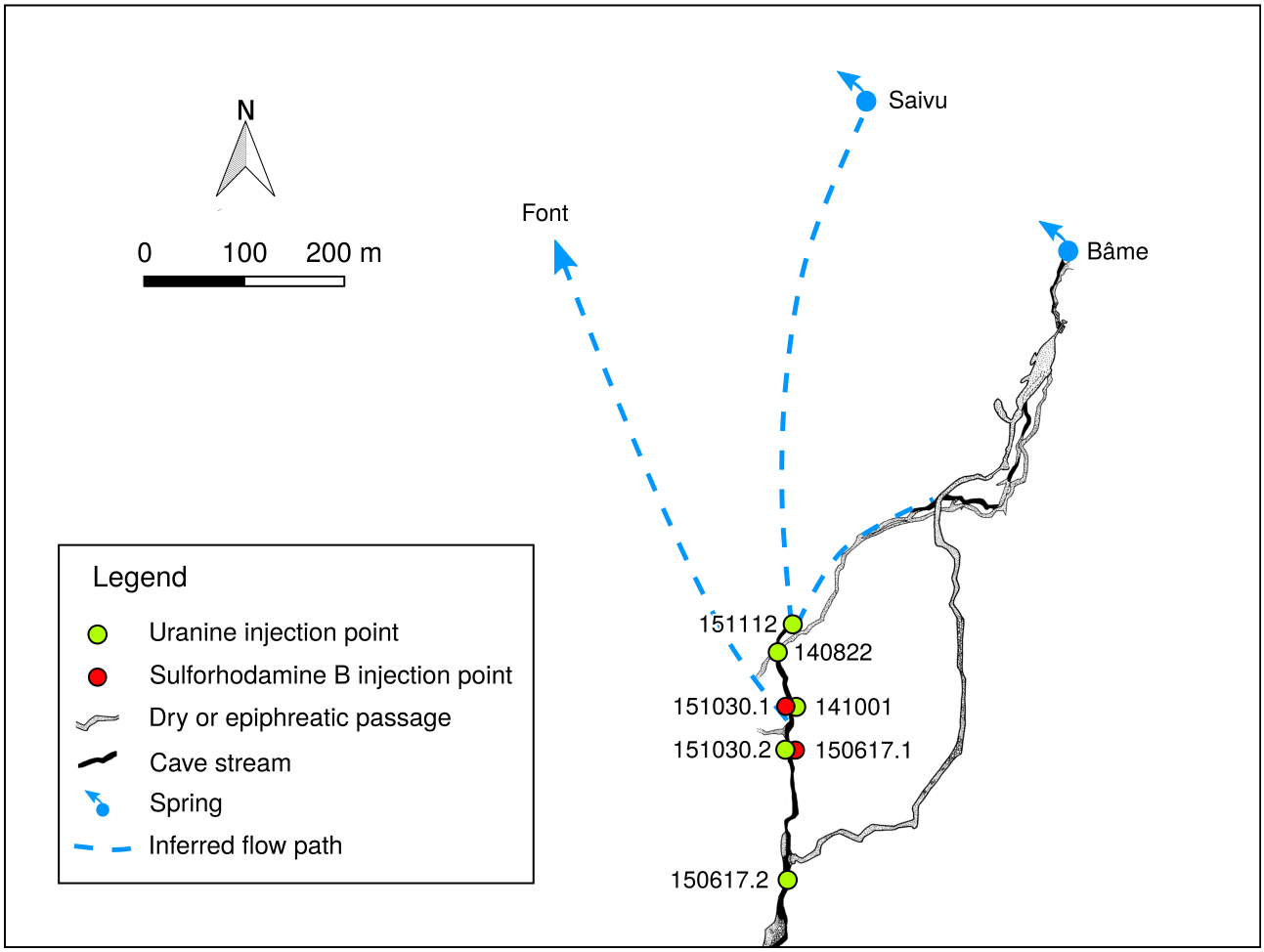

Figure 6.1: Map of the injection points of the tracer tests. Cave survey from Gigon and Wenger (1986).

Tracer test 151112

Injection			
Tracer	Uranine		
Injected mass	30.00 g		
Injection time	12 Nov 2015 14:15		
Coordinates	567869; 259161		
Distance to the Saivu spring	551 m		
Injection type	Tracer injected in the cave stream		
Tracer recovery at the Saivu spring			
Flow rate	19.8 $L \cdot s^{-1}$ (15 Nov 16:15)		
Recovery rate	85.0 %		
Transit time of first detection	06 h 15 min	**Maximum velocity**	88 $m \cdot h^{-1}$
Transit time of peak 1	08 h 40 min	**Modal velocity (peak 1)**	64 $m \cdot h^{-1}$
Transit time of peak 2	19 h 20 min	**Modal velocity (peak 2)**	29 $m \cdot h^{-1}$
Tracer recovery at the Bâme spring			
Flow rate	0 $L \cdot s^{-1}$		
Recovery rate	0 %		
Tracer recovery at the Font spring			
Transit time of first detection	3 d 1 h 5 min	**Maximum velocity**	16 $m \cdot h^{-1}$
Transit time of peak	3 d 2 h 35 min	**Modal velocity**	15 $m \cdot h^{-1}$

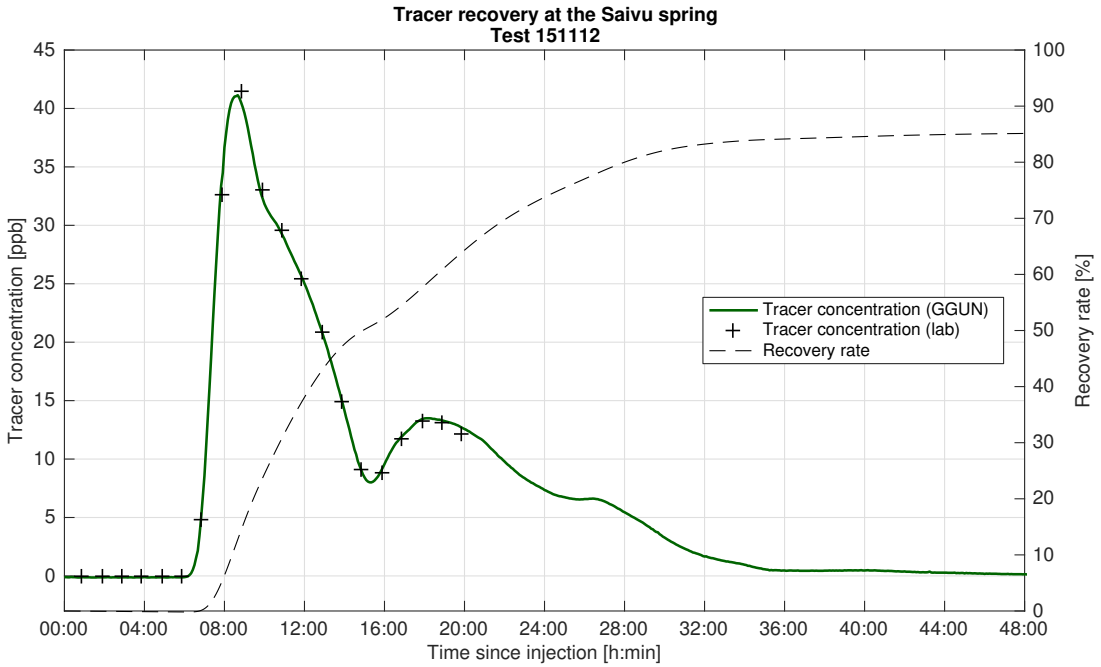

Tracer concentration at the Font spring (lab)	
12 Nov 2015 10:15	0 ppb
15 Nov 2015 15:20	2.42 ppb
15 Nov 2015 16:50	2.56 ppb

Tracer test 151030.1

Injection			
Tracer	Sulforhodamine B		
Injected mass	30.00 g		
Injection time	30 Oct 2015 19:06		
Coordinates	567866; 259072		
Distance to the Saivu spring	640 m		
Injection type	Tracer injected in the cave stream		
Tracer recovery at the Saivu spring			
Flow rate	18.8 $L \cdot s^{-1}$ (30 Oct 15:30)		
Recovery rate	80.9 %		
Transit time of first detection	06 h 39 min	**Maximum velocity**	96 $m \cdot h^{-1}$
Transit time of peak 1	08 h 49 min	**Modal velocity (peak 1)**	73 $m \cdot h^{-1}$
Transit time of peak 2	23 h 04 min	**Modal velocity (peak 2)**	28 $m \cdot h^{-1}$
Tracer recovery at the Bâme spring			
Flow rate	0 $L \cdot s^{-1}$		
Recovery rate	0 %		
Tracer recovery at the Font spring			
Transit time of first detection / of peak	3 d 15 h 24 min		
Maximum / modal velocity	14 $m \cdot h^{-1}$		

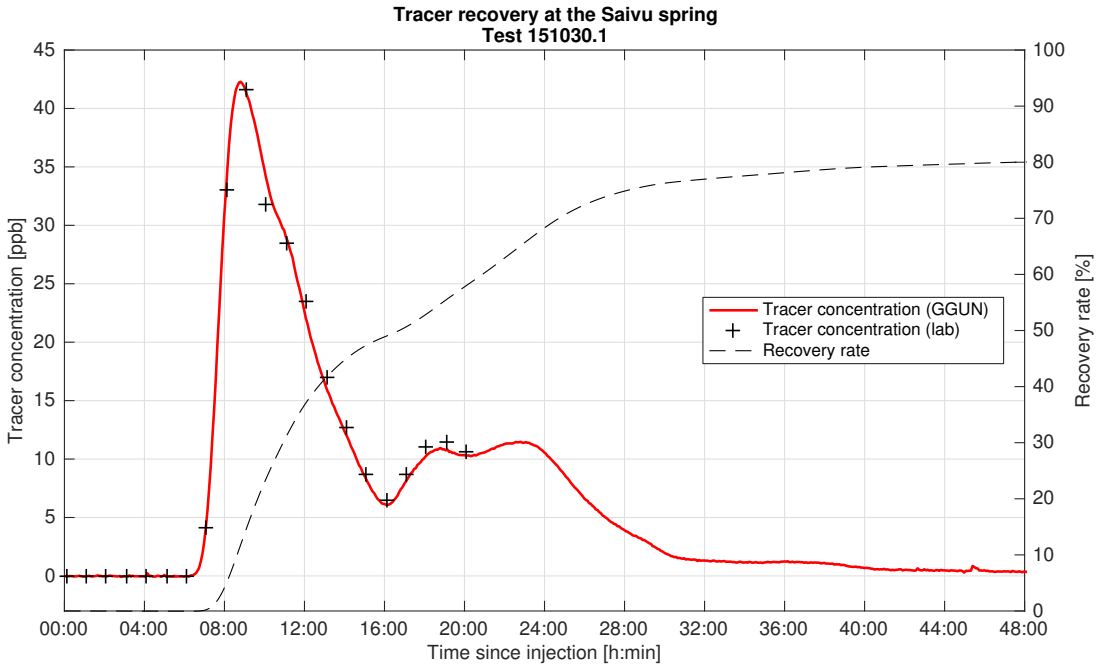

Tracer concentration at the Font spring (lab)	
3 Nov 2015 10:30	1.76 ppb
3 Nov 2015 12:30	1.39 ppb
5 Nov 2015 09:45	0 ppb

Tracer test 151030.2

Injection			
Tracer	Uranine		
Injected mass	30.00 g		
Injection time	30 Oct 2015 19:25		
Coordinates	567864; 259046		
Distance to the Saivu spring	666 m		
Injection type	Tracer injected in the cave stream		
Tracer recovery at the Saivu spring			
Flow rate	18.8 $L \cdot s^{-1}$ (30 Oct 15:30)		
Recovery rate	61.0 %		
Transit time of first detection	06 h 24 min	**Maximum velocity**	104 $m \cdot h^{-1}$
Transit time of peak 1	08 h 44 min	**Modal velocity (peak 1)**	76 $m \cdot h^{-1}$
Transit time of peak 2	22 h 34 min	**Modal velocity (peak 2)**	30 $m \cdot h^{-1}$
Tracer recovery at the Bâme spring			
Flow rate	0 $L \cdot s^{-1}$		
Recovery rate	0 %		
Tracer recovery at the Font spring			
Transit time of first detection / of peak	3 d 15 h 5 min		
Maximum / modal velocity	15 $m \cdot h^{-1}$		

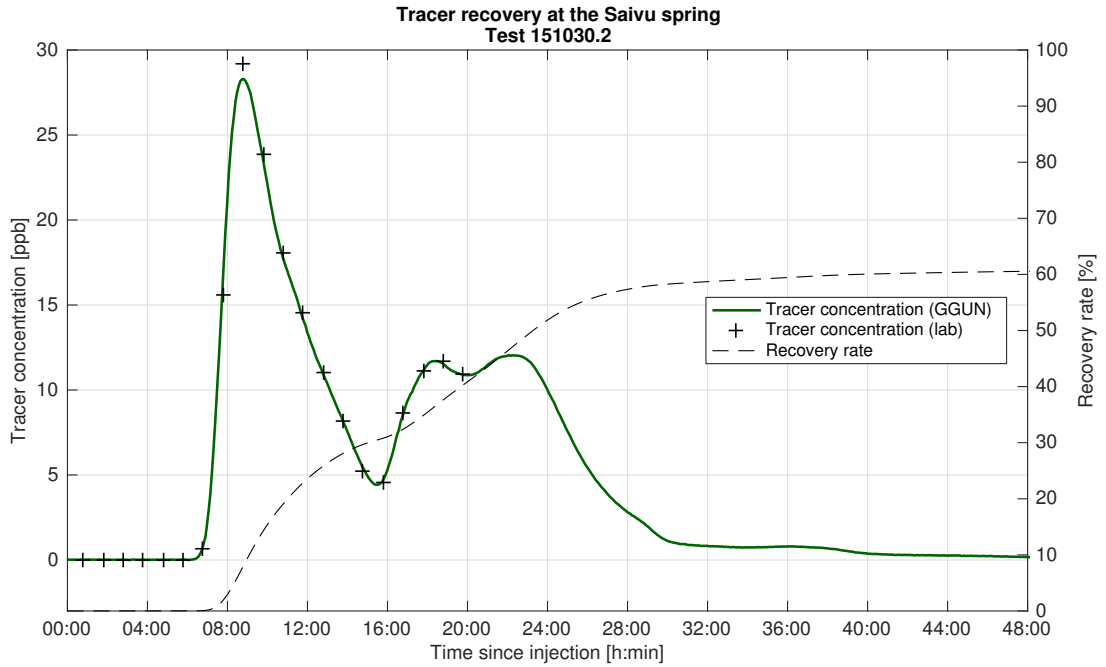

Tracer concentration at the Font spring (lab)	
3 Nov 2015 10:30	2.88 ppb
3 Nov 2015 12:30	2.39 ppb
5 Nov 2015 09:45	0 ppb

Tracer test 141001

Injection			
Tracer	Uranine		
Injected mass	30.00 g		
Injection time	01 Oct 2014 12:50		
Coordinates	567869; 259072		
Distance to the Saivu spring	640 m		
Injection type	Tracer injected in the cave stream		
Tracer recovery at the Saivu spring			
Flow rate	34.0 $L \cdot s^{-1}$ (01 Oct 10:30) 33.0 $L \cdot s^{-1}$ (01 Oct 17:30) 33.1 $L \cdot s^{-1}$ (02 Oct 15:30)		
Recovery rate	93.9 %		
Transit time of first detection	04 h 57 min	**Maximum velocity**	129 $m \cdot h^{-1}$
Transit time of peak 1	06 h 12 min	**Modal velocity (peak 1)**	103 $m \cdot h^{-1}$
Transit time of peak 2	10 h 45 min	**Modal velocity (peak 2)**	60 $m \cdot h^{-1}$
Tracer recovery at the Bâme spring			
Flow rate	0 $L \cdot s^{-1}$		
Recovery rate	0 %		
Tracer recovery at the Font spring			
The Font spring has not been monitored during the tracer test.			

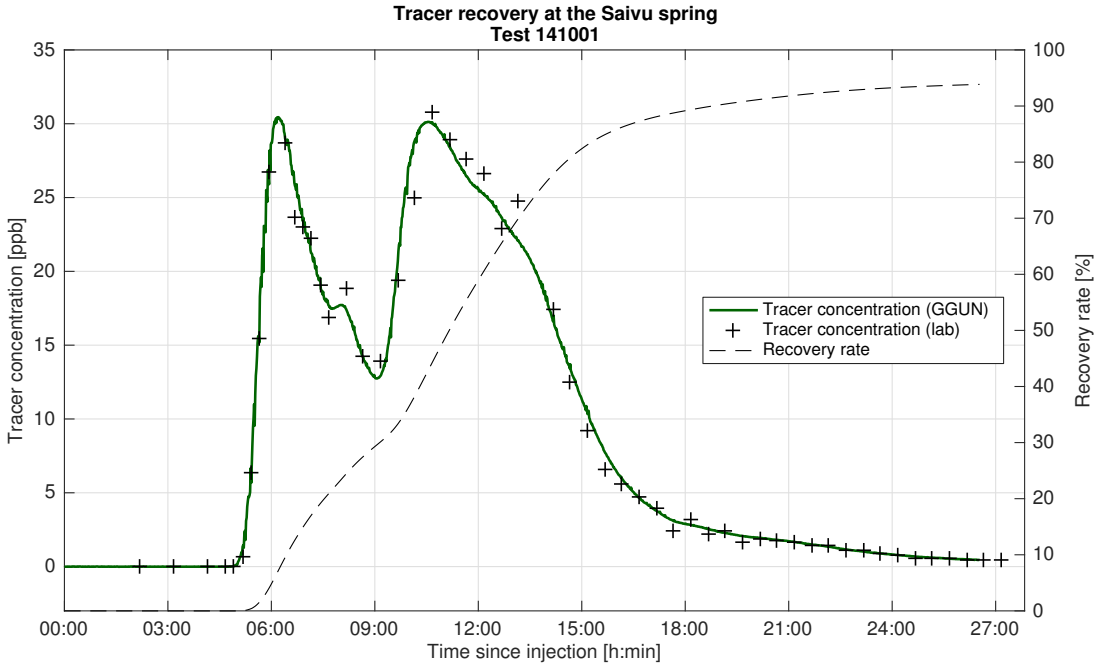

Tracer test 150617.1

Injection			
Tracer	Sulforhodamine B		
Injected mass	30.00 g		
Injection time	17 Jun 2015 11:00		
Coordinates	567866; 259046		
Distance to the Saivu spring	666 m		
Injection type	Tracer injected in the cave stream		
Tracer recovery at the Saivu spring			
Flow rate	85.6 $L \cdot s^{-1}$ (17 Jun 15:15) 80.7 $L \cdot s^{-1}$ (18 Jun 11:00)		
Recovery rate	84.4 %		
Transit time of first detection	05 h 15 min	**Maximum velocity**	127 $m \cdot h^{-1}$
Transit time of peak 1	06 h 49 min	**Modal velocity (peak 1)**	98 $m \cdot h^{-1}$
Transit time of peak 2	13 h 09 min	**Modal velocity (peak 2)**	51 $m \cdot h^{-1}$
Tracer recovery at the Bâme spring			
Flow rate	2.9 $L \cdot s^{-1}$ (17 Jun 13:45) 1.7 $L \cdot s^{-1}$ (17 Jun 14:20)		
Recovery rate	1.2 %		
Transit time of first detection	1 d 13 h 50 min	**Maximum velocity**	15 $m \cdot h^{-1}$
Transit time of peak	1 d 14 h 30 min	**Modal velocity**	15 $m \cdot h^{-1}$
Tracer recovery at the Font spring			
Recovery rate	15.6 %		
Transit time of first detection	1 d 7 h 0 min	**Maximum velocity**	41 $m \cdot h^{-1}$
Transit time of peak	1 d 18 h 40 min	**Modal velocity**	30 $m \cdot h^{-1}$

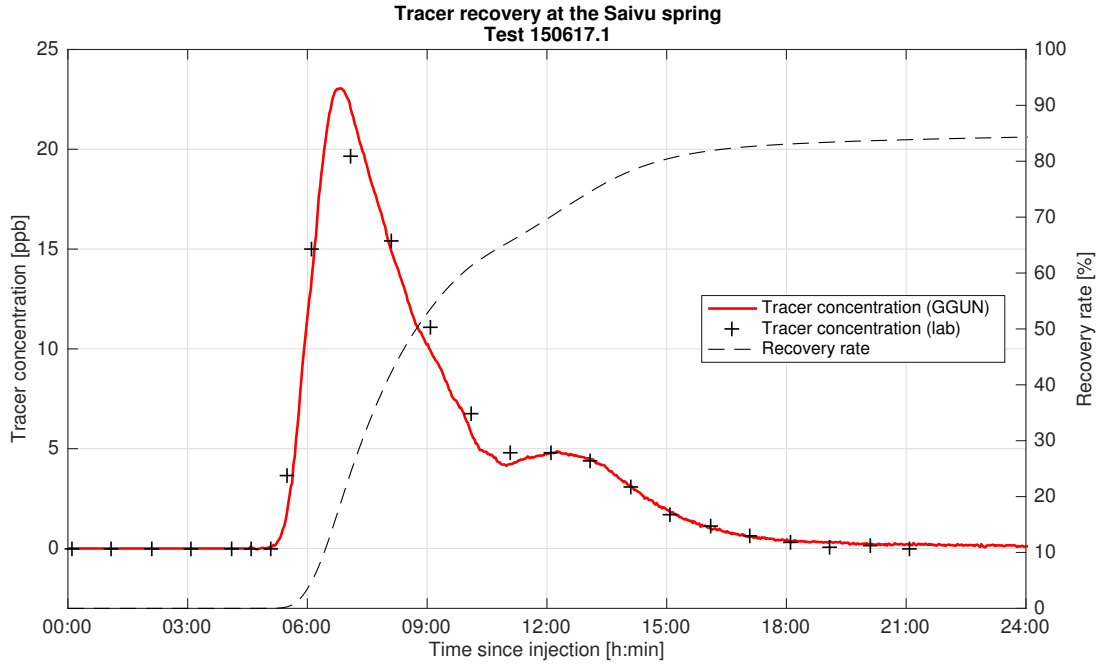

Tracer test 150617.2

Injection			
Tracer	Uranine		
Injected mass	30.00 g		
Injection time	17 Jun 2015 11:40		
Coordinates	567858; 258895		
Distance to the Saivu spring	816 m		
Injection type	Tracer injected in the cave stream		
Tracer recovery at the Saivu spring			
Flow rate	85.6 $L \cdot s^{-1}$ (17 Jun 15:15) 80.7 $L \cdot s^{-1}$ (18 Jun 11:00)		
Recovery rate	84.3 %		
Transit time of first detection	05 h 07 min	**Maximum velocity**	159 $m \cdot h^{-1}$
Transit time of peak 1	07 h 57 min	**Modal velocity (peak 1)**	103 $m \cdot h^{-1}$
Transit time of peak 2	13 h 43 min	**Modal velocity (peak 2)**	59 $m \cdot h^{-1}$
Tracer recovery at the Bâme spring			
Flow rate	2.9 $L \cdot s^{-1}$ (17 Jun 13:45) 1.7 $L \cdot s^{-1}$ (17 Jun 14:20)		
Recovery rate	0.8 %		
Transit time of first detection	1 d 13 h 50 min	**Maximum velocity**	19 $m \cdot h^{-1}$
Transit time of peak	1 d 14 h 28 min	**Modal velocity**	18 $m \cdot h^{-1}$
Tracer recovery at the Font spring			
Recovery rate	14.1 %		
Transit time of first detection	1 d 7 h 40 min	**Maximum velocity**	45 $m \cdot h^{-1}$
Transit time of peak	1 d 20 h 10 min	**Modal velocity**	32 $m \cdot h^{-1}$

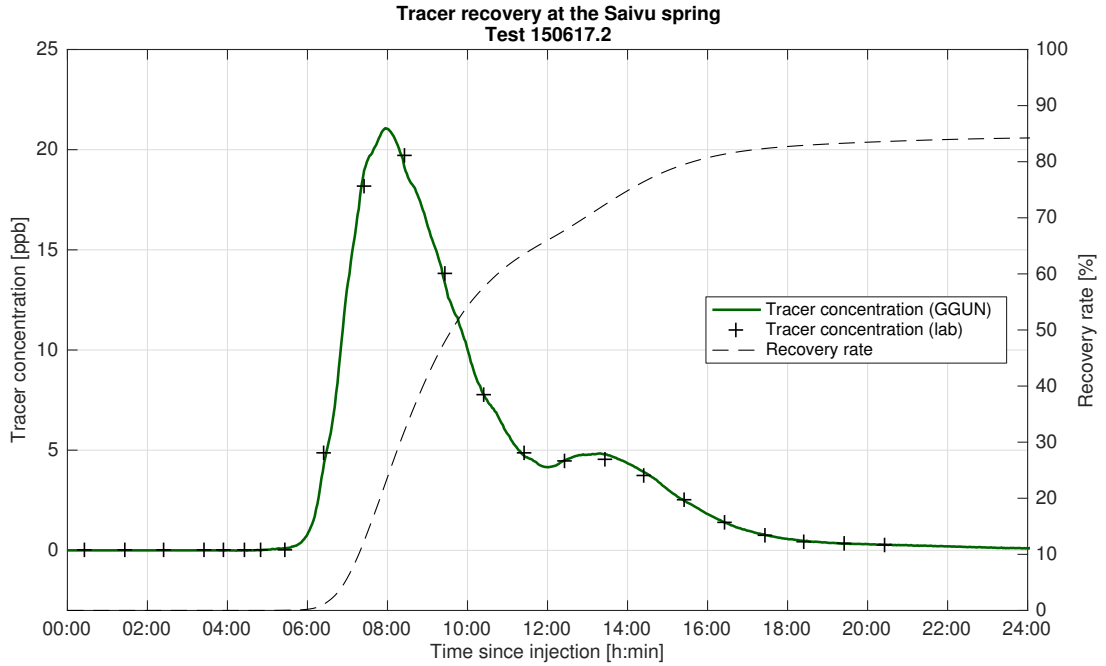

Recovery curves at the Bâme spring for tracer test 150617.1 and 150617.2

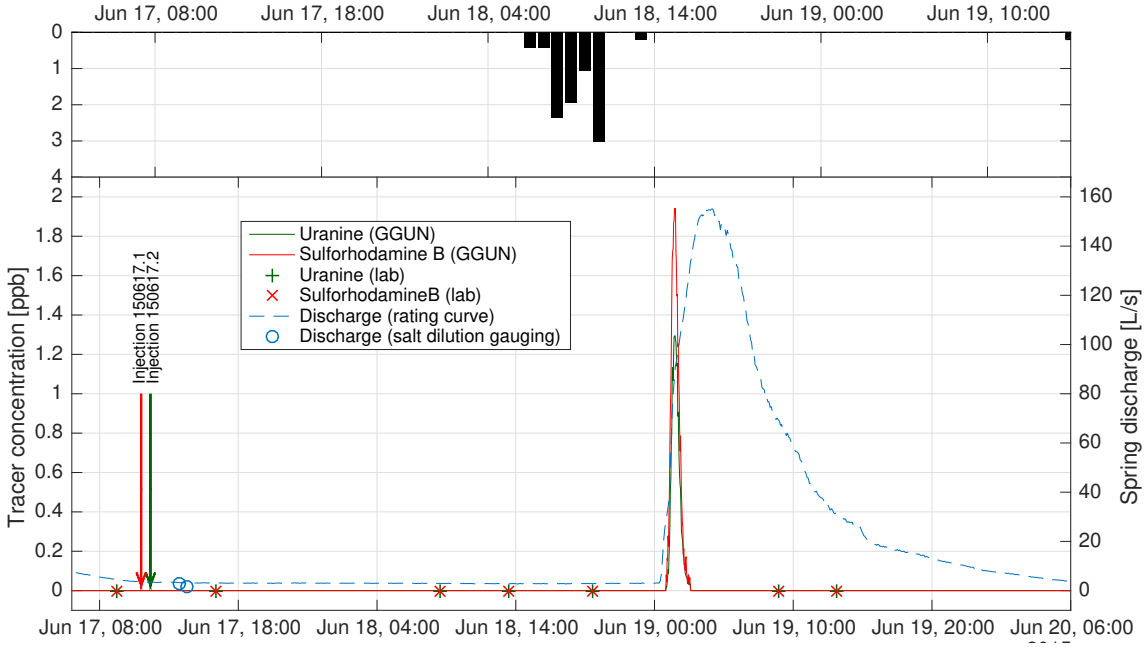

Recovery curves at the Font spring for tracer test 150617.1 and 150617.2

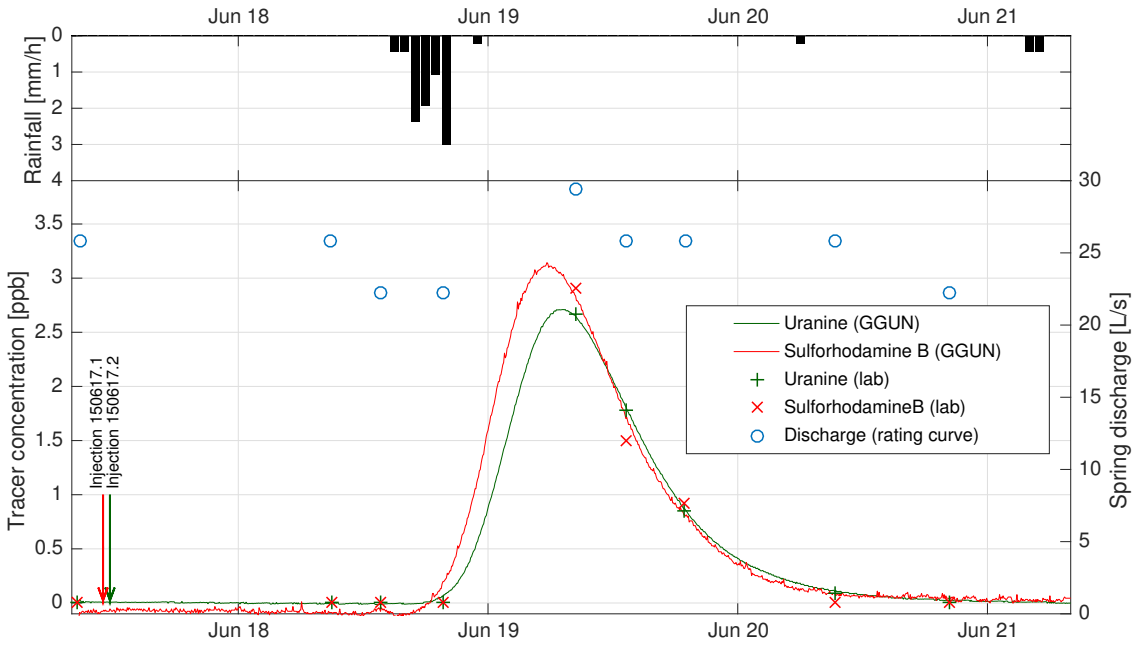

Tracer test 140822

Injection			
Tracer	Uranine		
Injected mass	30.00 g		
Injection time	22 Aug 2014 14:30		
Coordinates	567855; 259134		
Distance to the Saivu spring	581 m		
Injection type	Tracer injected in the cave stream		
Tracer recovery at the Saivu spring			
Flow rate	85.4 $L \cdot s^{-1}$ (22 Aug 10:42) 83.0 $L \cdot s^{-1}$ (22 Aug 10:54)		
Recovery rate	97.3 %		
Transit time of first detection	04 h 35 min	**Maximum velocity**	127 $m \cdot h^{-1}$
Transit time of peak 1	05 h 50 min	**Modal velocity (peak 1)**	100 $m \cdot h^{-1}$
Transit time of peak 2	11 h 45 min	**Modal velocity (peak 2)**	49 $m \cdot h^{-1}$
Tracer recovery at the Bâme spring			
Flow rate	1.8 $L \cdot s^{-1}$ (22 Aug 11:21) 2.4 $L \cdot s^{-1}$ (22 Aug 11:51)		
Recovery rate	Tracer not detected		
Tracer recovery at the Font spring			
The Font spring has not been monitored during the tracer test.			

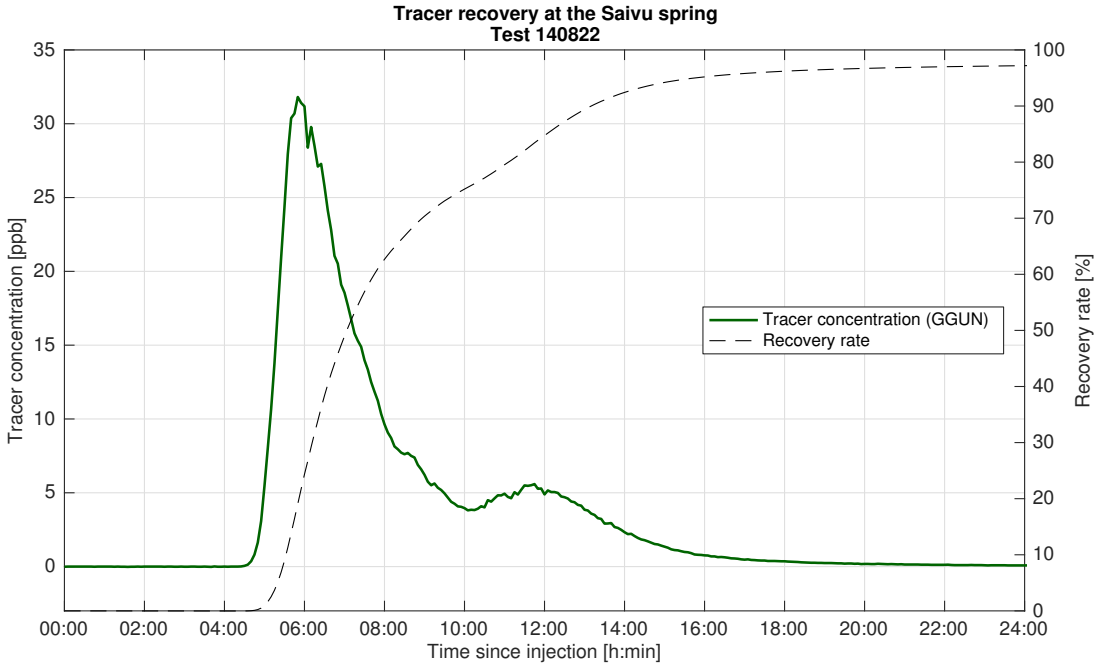

Appendix II

The following figures show the flood events used in the analysis of the turbidity time series in the upstream Milandrine (Sec. 4.3.3). For each event, the black circle shows the initial discharge, the black triangle, the peak discharge, the gray circle, the primary turbidity peak and the gray triangle, the secondary turbidity peak. For event displaying more than two turbidity peaks, the first peak is always considered as the primary peak and later peak are successively considered as the secondary peak. This data has been collected within the framework of the environmental impact study of the A16 highway construction (Hessenauer et al., 2004; Meury et al., 2005, 2006; Savoy et al., 2007; Blant et al., 2008, 2009, 2010, 2011, 2012; Häuselmann et al., 2014b,a, 2015, 2016).

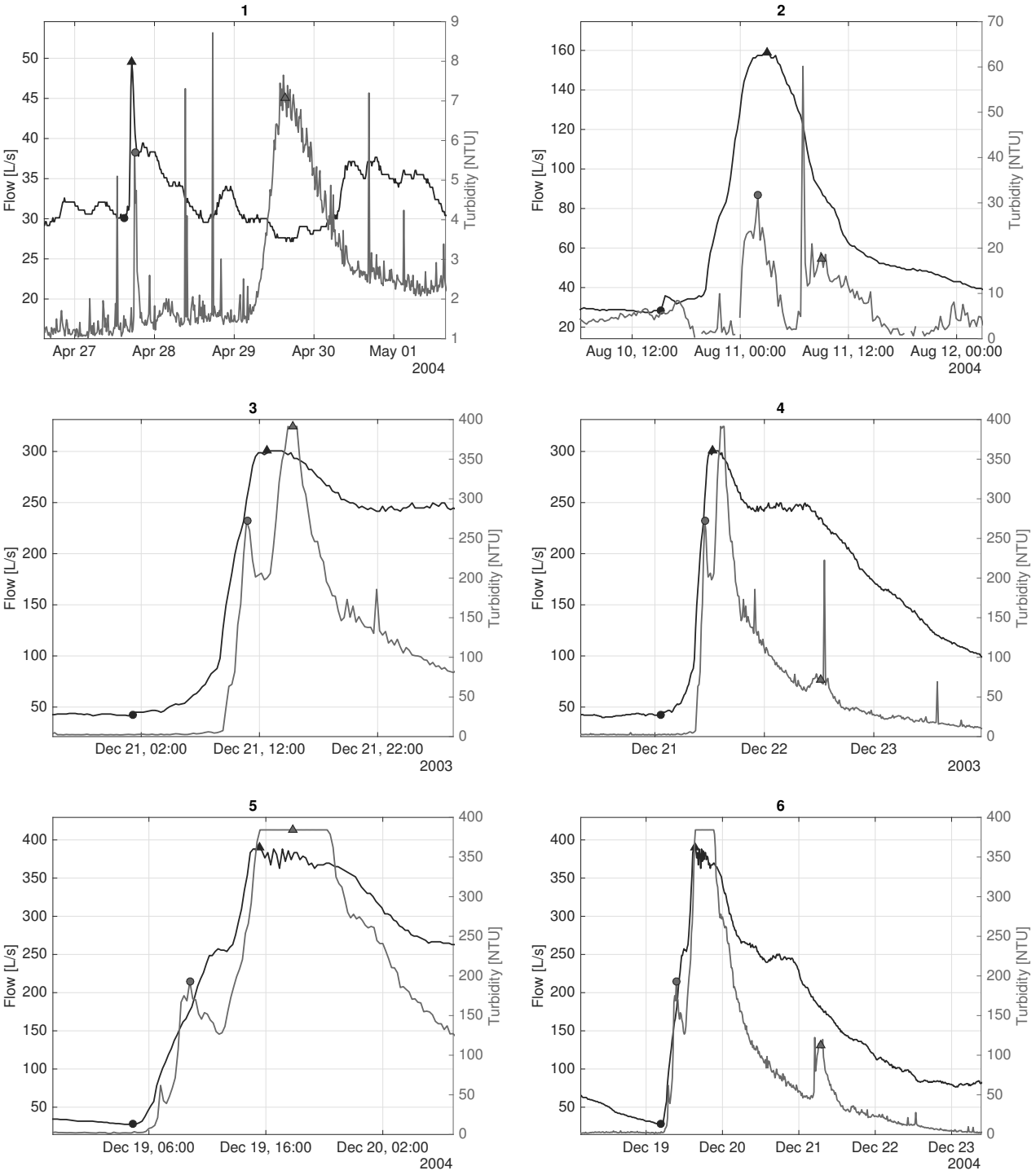
1
Flow [L/s]
Turbidity [NTU]
Apr 27
Apr 28
Apr 29
Apr 30
May 01
2004
2
Aug 10, 12:00
Aug 11, 00:00
Aug 11, 12:00
Aug 12, 00:00
2004
3
Dec 21, 02:00
Dec 21, 12:00
Dec 21, 22:00
2003
4
Dec 21
Dec 22
Dec 23
2003
5
Dec 19, 06:00
Dec 19, 16:00
Dec 20, 02:00
2004
6
Dec 19
Dec 20
Dec 21
Dec 22
Dec 23
2004

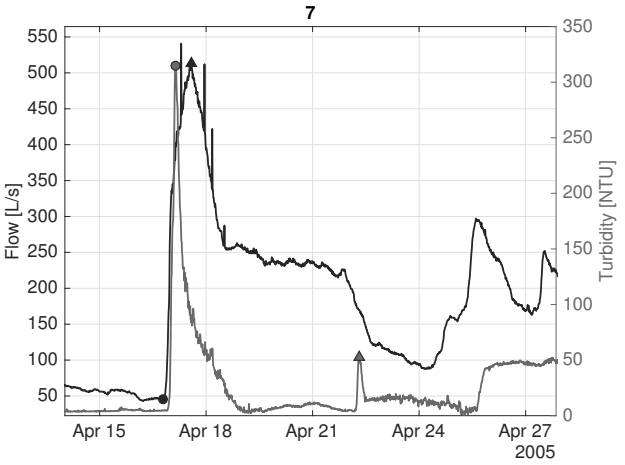
7
Flow [L/s]
Turbidity [NTU]
Apr 15
Apr 18
Apr 21
Apr 24
Apr 27
2005

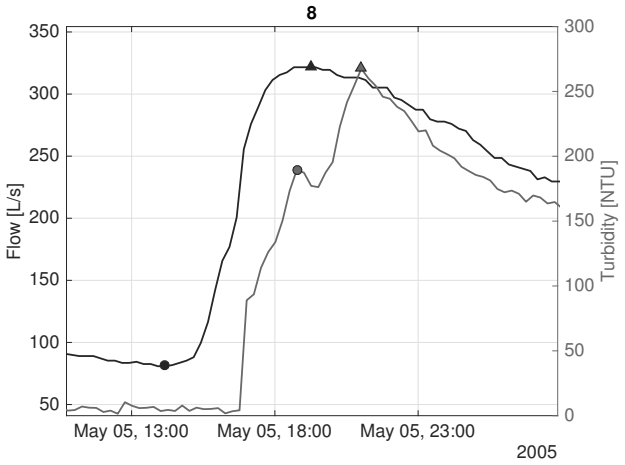
8
Flow [L/s]
Turbidity [NTU]
May 05, 13:00
May 05, 18:00
May 05, 23:00
2005

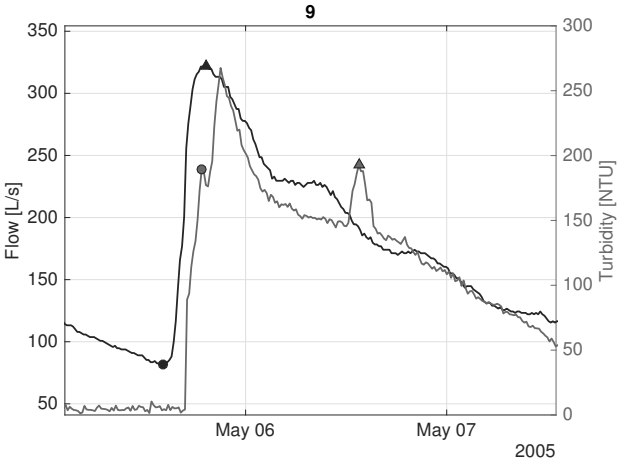
9
Flow [L/s]
Turbidity [NTU]
May 06
May 07
2005

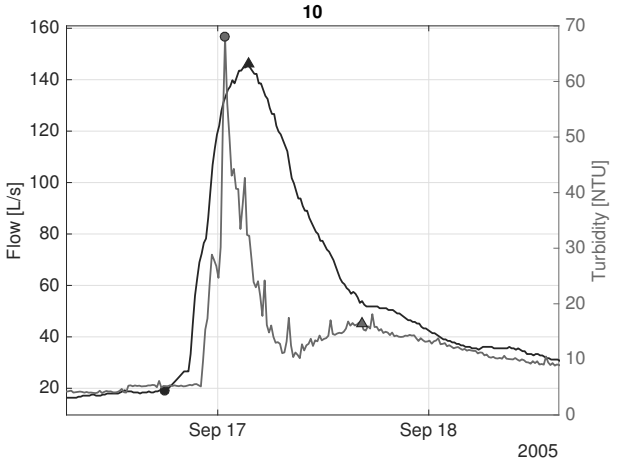
10
Flow [L/s]
Turbidity [NTU]
Sep 17
Sep 18
2005

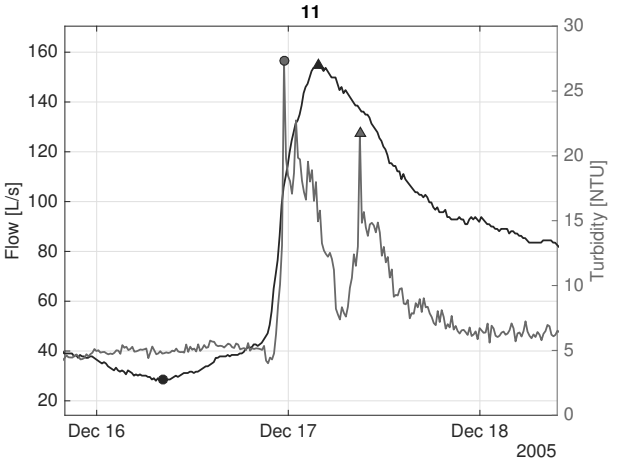
11
Flow [L/s]
Turbidity [NTU]
Dec 16
Dec 17
Dec 18
2005

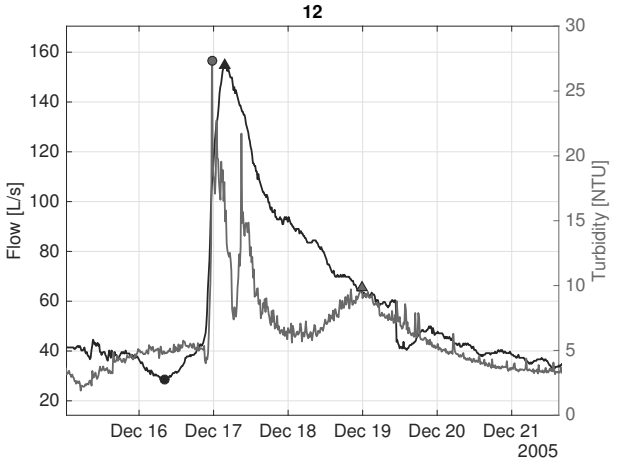
12
Flow [L/s]
Turbidity [NTU]
Dec 16
Dec 17
Dec 18
Dec 19
Dec 20
Dec 21
2005

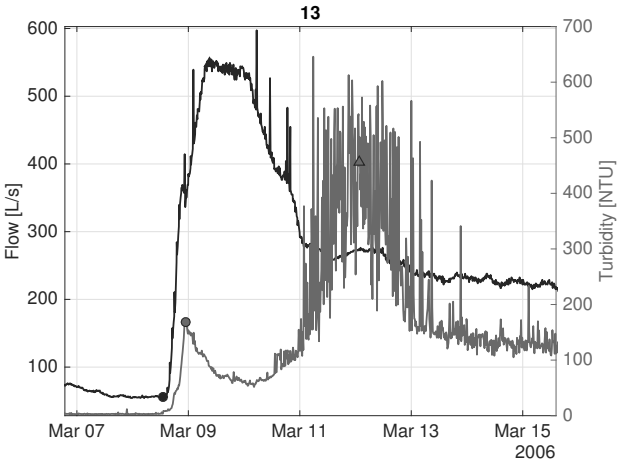
13
Flow [L/s]
Turbidity [NTU]
Mar 07
Mar 09
Mar 11
Mar 13
Mar 15
2006

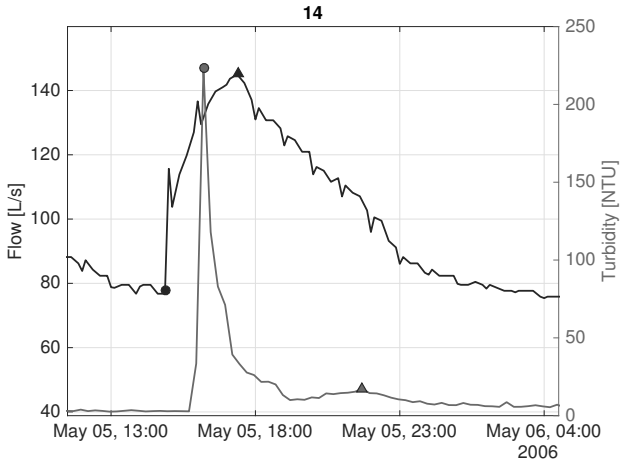
14
Flow [L/s]
Turbidity [NTU]
May 05, 13:00
May 05, 18:00
May 05, 23:00
May 06, 04:00
2006

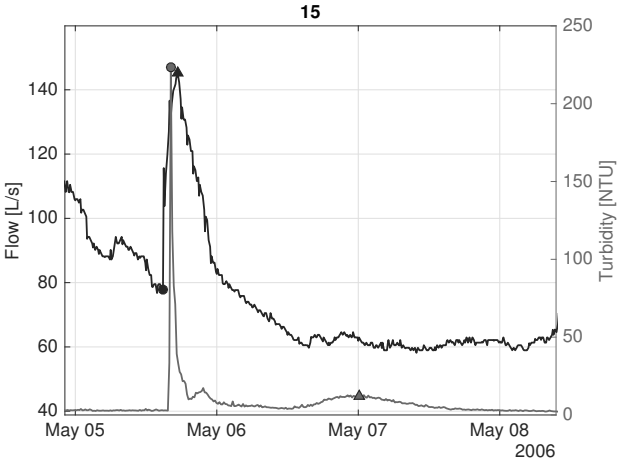
15
Flow [L/s]
Turbidity [NTU]
May 05
May 06
May 07
May 08
2006

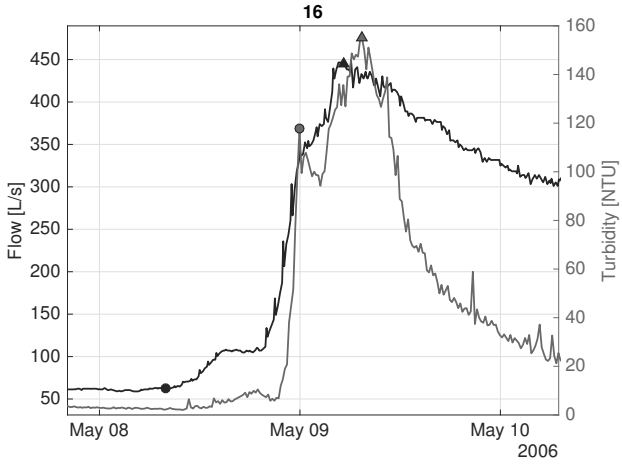
16
Flow [L/s]
Turbidity [NTU]
May 08
May 09
May 10
2006

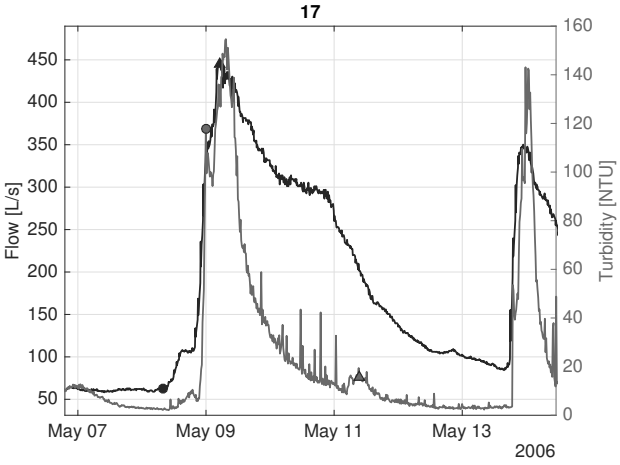
17
Flow [L/s]
Turbidity [NTU]
May 07
May 09
May 11
May 13
2006

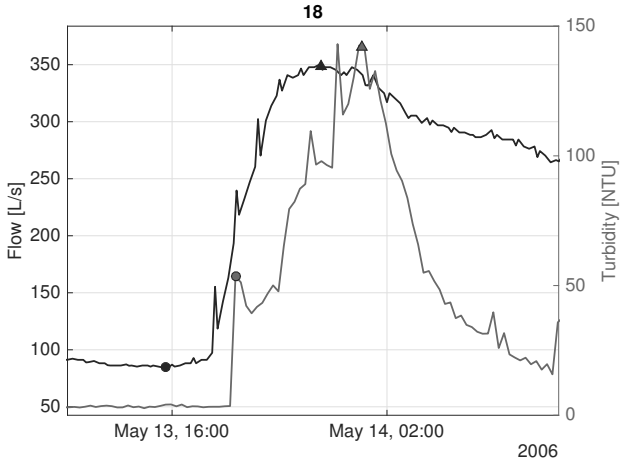
18
Flow [L/s]
Turbidity [NTU]
May 13, 16:00
May 14, 02:00
2006

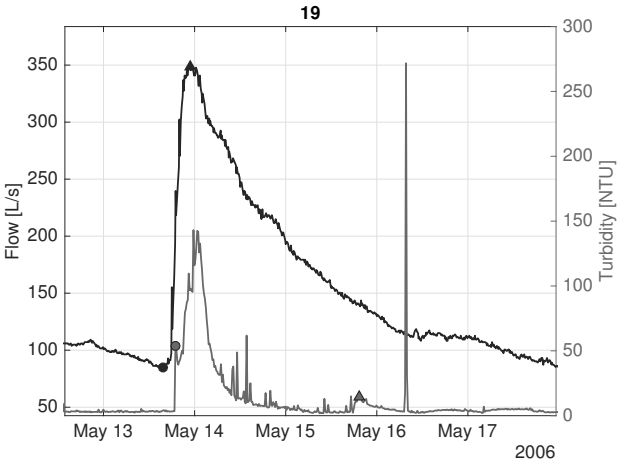
19
Flow [L/s]
Turbidity [NTU]
May 13
May 14
May 15
May 16
May 17
2006

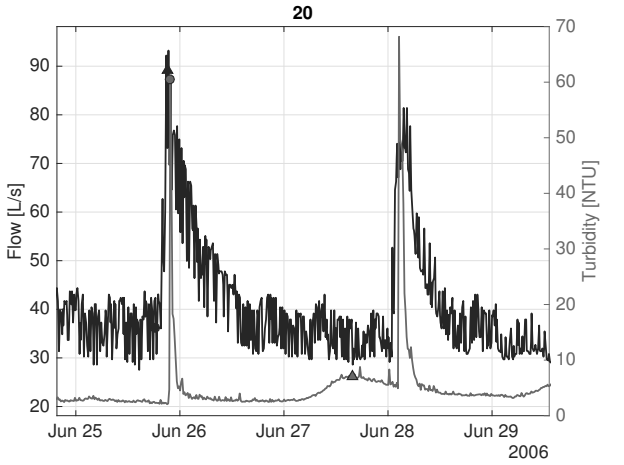
20
Flow [L/s]
Turbidity [NTU]
Jun 25
Jun 26
Jun 27
Jun 28
Jun 29
2006

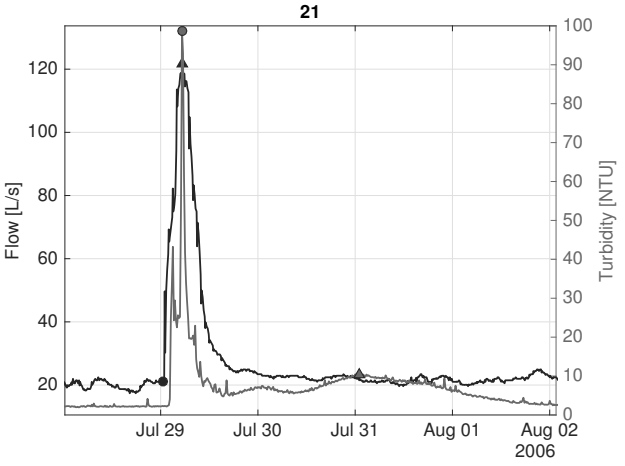
21
Flow [L/s]
Turbidity [NTU]
Jul 29
Jul 30
Jul 31
Aug 01
Aug 02
2006

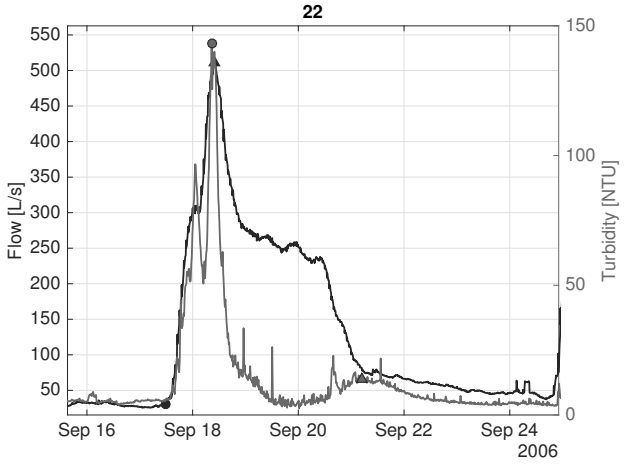
22
Flow [L/s]
Turbidity [NTU]
Sep 16
Sep 18
Sep 20
Sep 22
Sep 24
2006

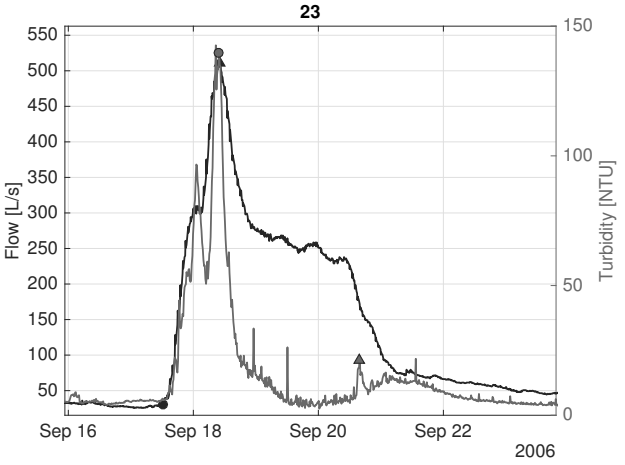
23
Flow [L/s]
Turbidity [NTU]
Sep 16
Sep 18
Sep 20
Sep 22
2006

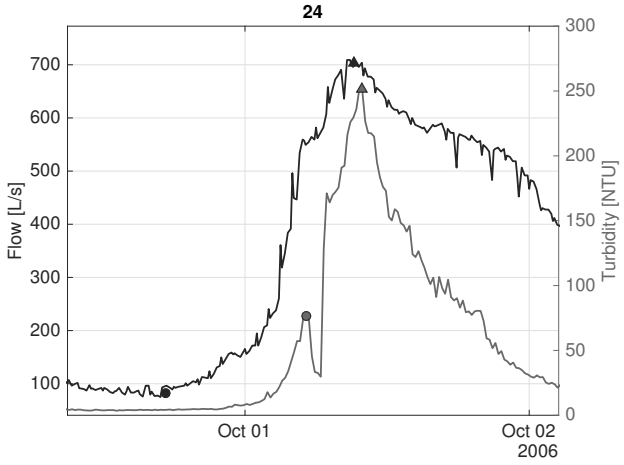
24
Flow [L/s]
Turbidity [NTU]
Oct 01
Oct 02
2006

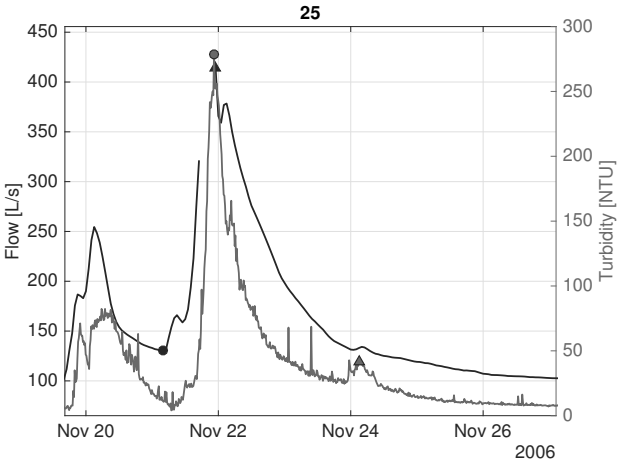
25
Flow [L/s]
Turbidity [NTU]
Nov 20
Nov 22
Nov 24
Nov 26
2006

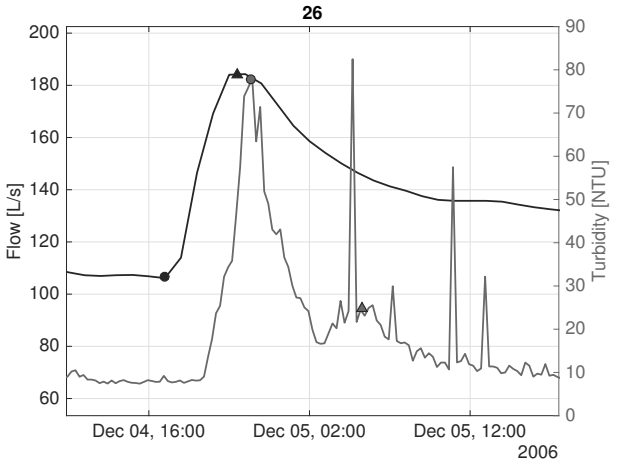
26
Flow [L/s]
Turbidity [NTU]
Dec 04, 16:00
Dec 05, 02:00
Dec 05, 12:00
2006

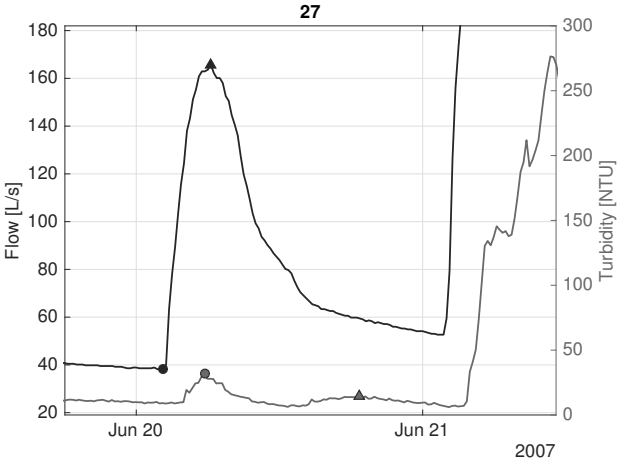
27
Flow [L/s]
Turbidity [NTU]
Jun 20
Jun 21
2007

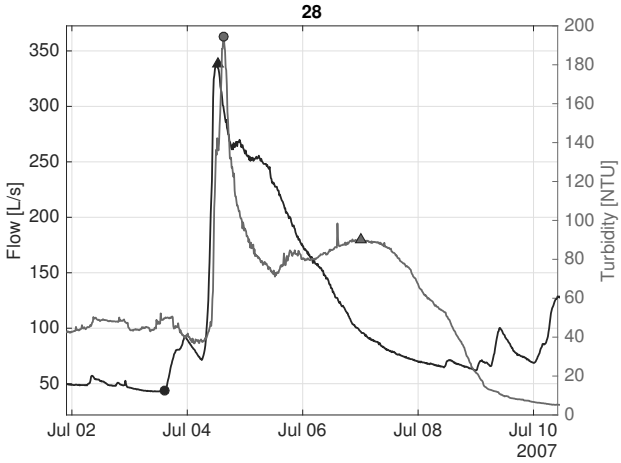
28
Flow [L/s]
Turbidity [NTU]
Jul 02
Jul 04
Jul 06
Jul 08
Jul 10
2007

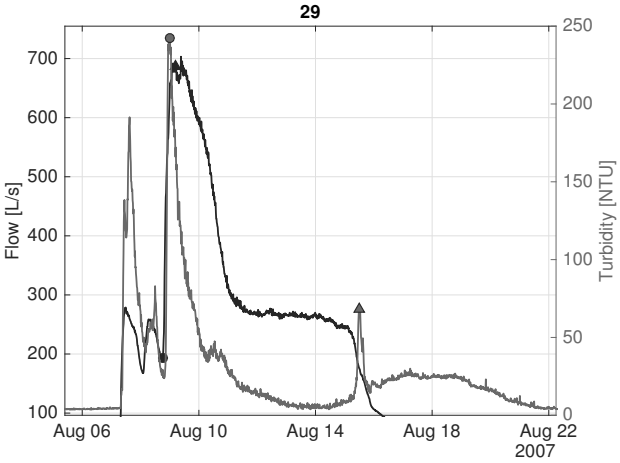
29
Flow [L/s]
Turbidity [NTU]
Aug 06
Aug 10
Aug 14
Aug 18
Aug 22
2007

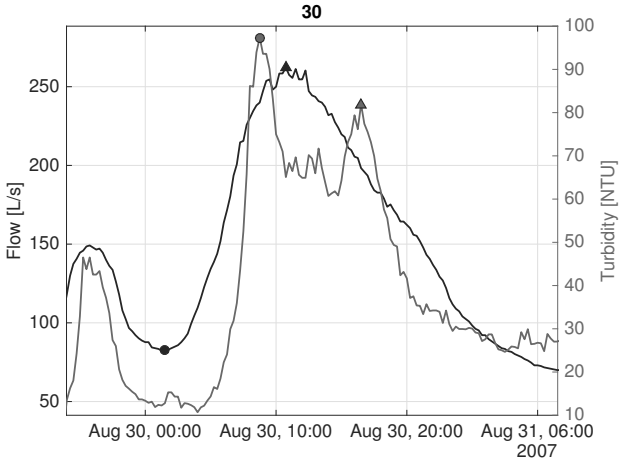
30
Flow [L/s]
Turbidity [NTU]
Aug 30, 00:00
Aug 30, 10:00
Aug 30, 20:00
Aug 31, 06:00
2007

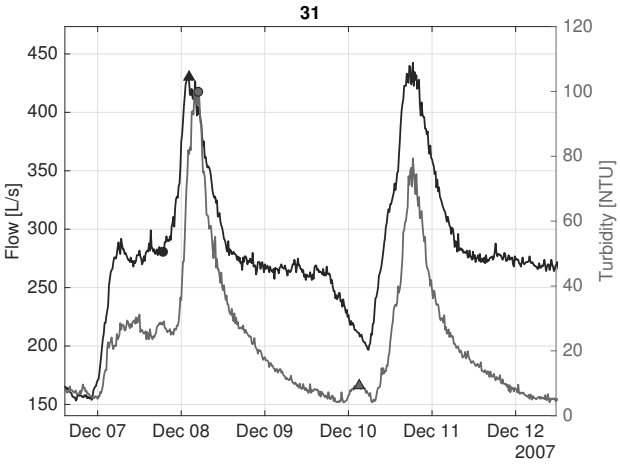
31
Flow [L/s]
Turbidity [NTU]
Dec 07
Dec 08
Dec 09
Dec 10
Dec 11
Dec 12
2007

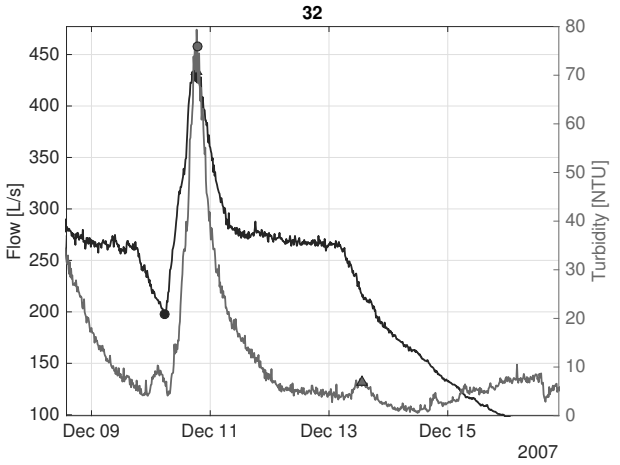
32
Flow [L/s]
Turbidity [NTU]
Dec 09
Dec 11
Dec 13
Dec 15
2007

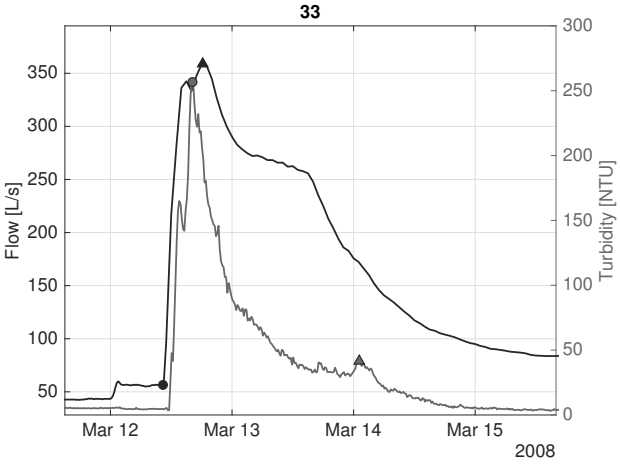
33
Flow [L/s]
Turbidity [NTU]
Mar 12
Mar 13
Mar 14
Mar 15
2008

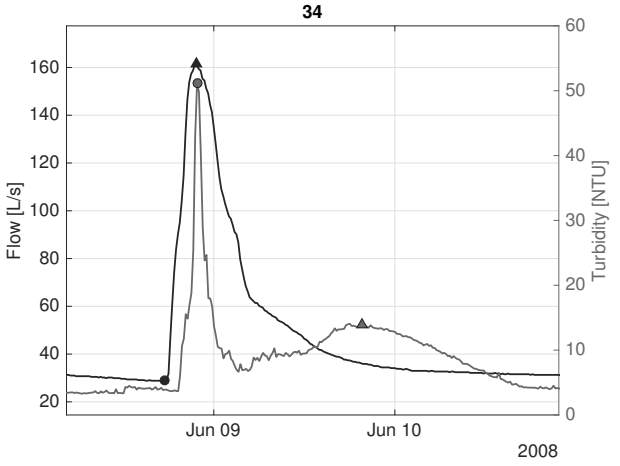
34
Flow [L/s]
Turbidity [NTU]
Jun 09
Jun 10
2008

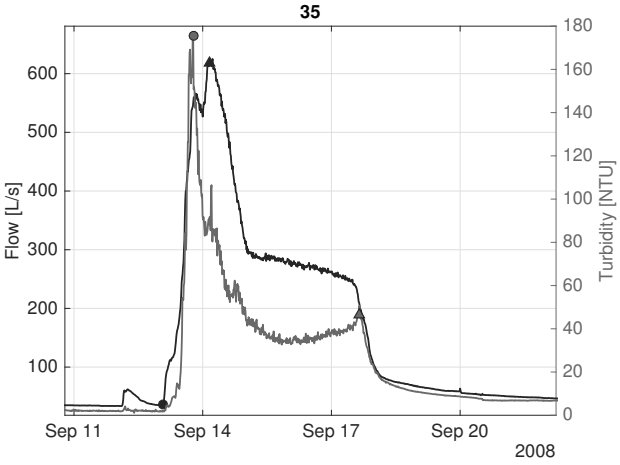
35
Flow [L/s]
Turbidity [NTU]
Sep 11
Sep 14
Sep 17
Sep 20
2008

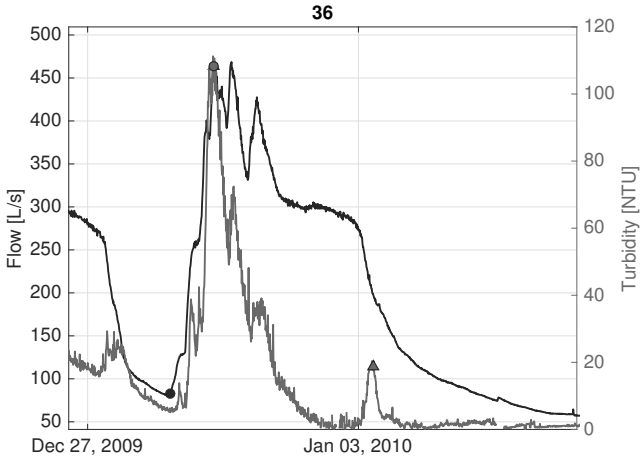
36
Flow [L/s]
Turbidity [NTU]
Dec 27, 2009
Jan 03, 2010

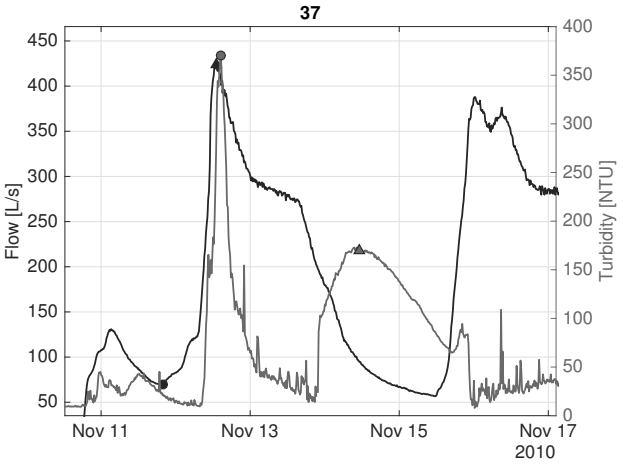
37
Flow [L/s]
Turbidity [NTU]
Nov 11
Nov 13
Nov 15
Nov 17
2010

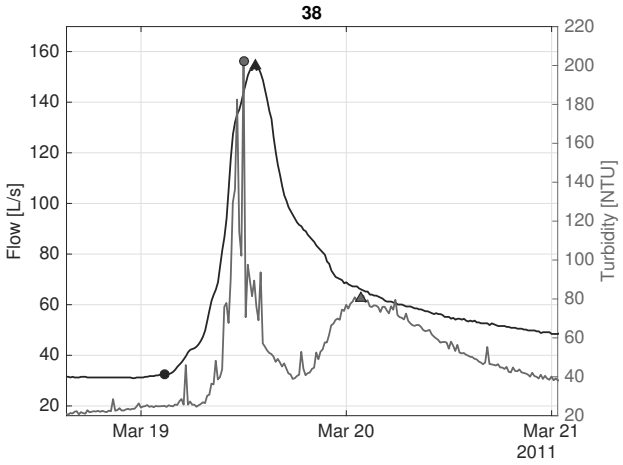
38
Flow [L/s]
Turbidity [NTU]
Mar 19
Mar 20
Mar 21
2011

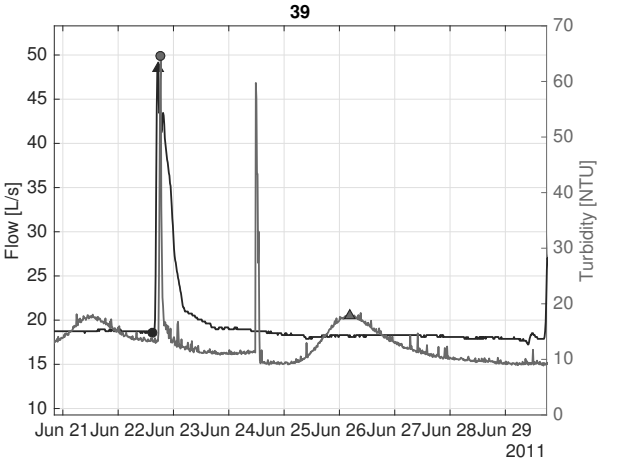
39
Flow [L/s]
Turbidity [NTU]
Jun 21Jun 22Jun 23Jun 24Jun 25Jun 26Jun 27Jun 28Jun 29
2011

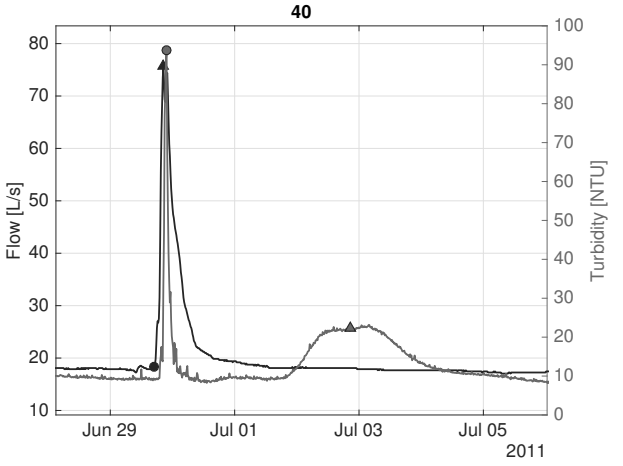
40
Flow [L/s]
Turbidity [NTU]
Jun 29
Jul 01
Jul 03
Jul 05
2011

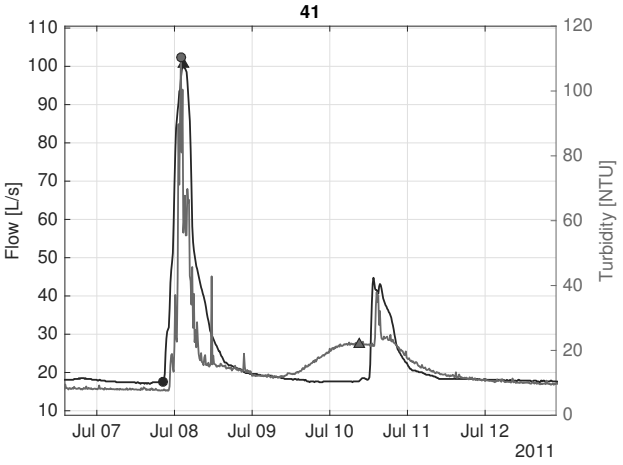
41
Flow [L/s]
Turbidity [NTU]
Jul 07
Jul 08
Jul 09
Jul 10
Jul 11
Jul 12
2011

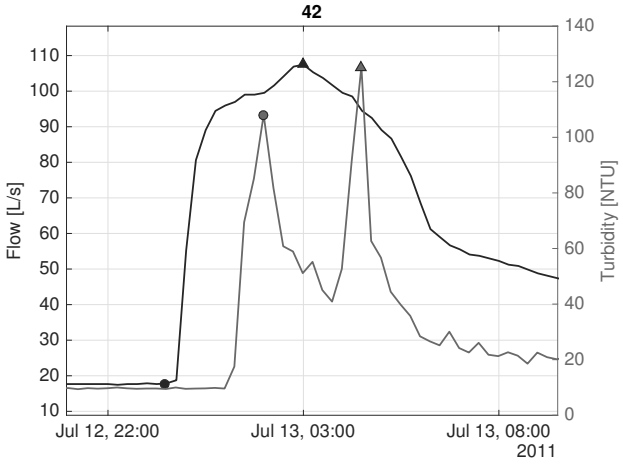
42
Flow [L/s]
Turbidity [NTU]
Jul 12, 22:00
Jul 13, 03:00
Jul 13, 08:00
2011

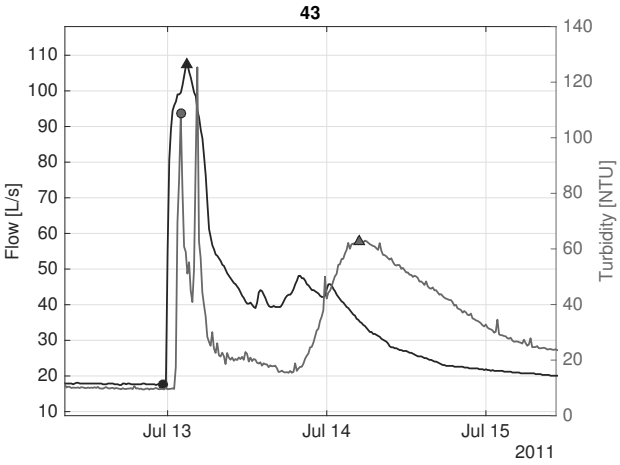
43
Flow [L/s]
Turbidity [NTU]
Jul 13
Jul 14
Jul 15
2011

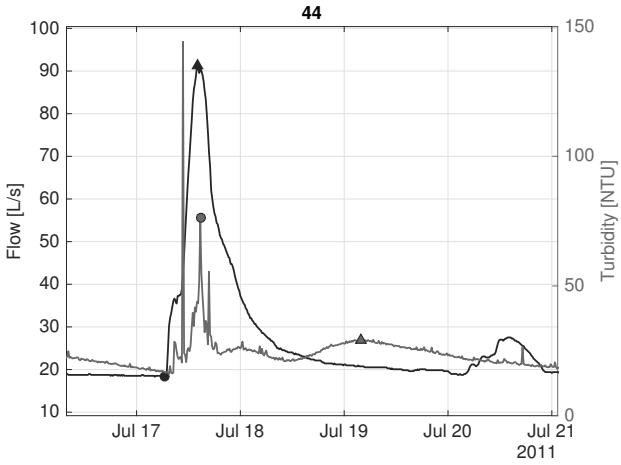
44
Flow [L/s]
Turbidity [NTU]
Jul 17
Jul 18
Jul 19
Jul 20
Jul 21
2011

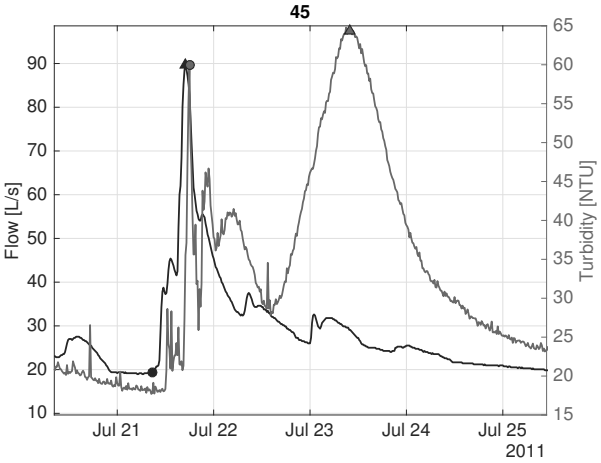
45
Flow [L/s]
Turbidity [NTU]
Jul 21
Jul 22
Jul 23
Jul 24
Jul 25
2011

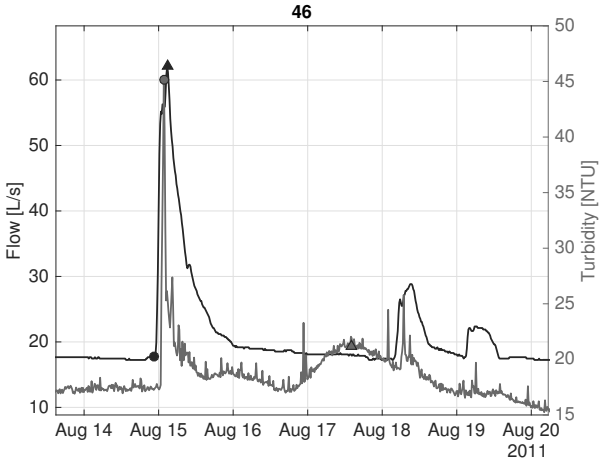
46
Flow [L/s]
Turbidity [NTU]
Aug 14
Aug 15
Aug 16
Aug 17
Aug 18
Aug 19
Aug 20
2011

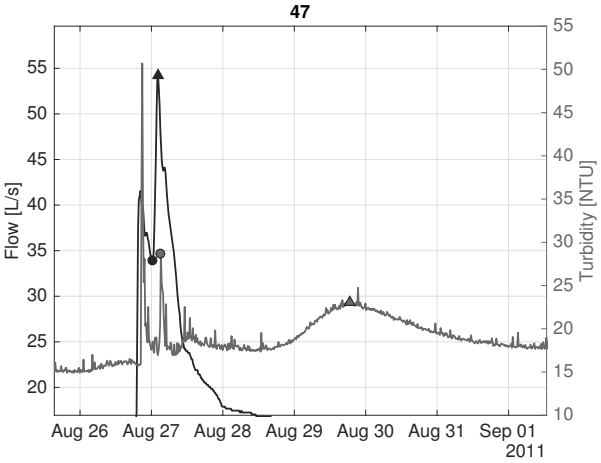
47
Flow [L/s]
Turbidity [NTU]
Aug 26
Aug 27
Aug 28
Aug 29
Aug 30
Aug 31
Sep 01
2011

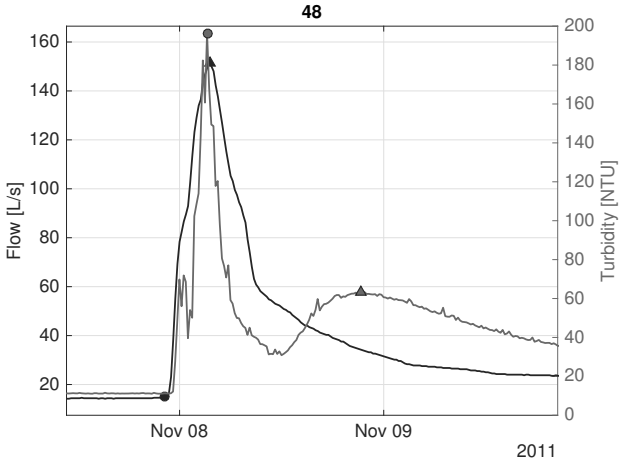
48
Flow [L/s]
Turbidity [NTU]
Nov 08
Nov 09
2011

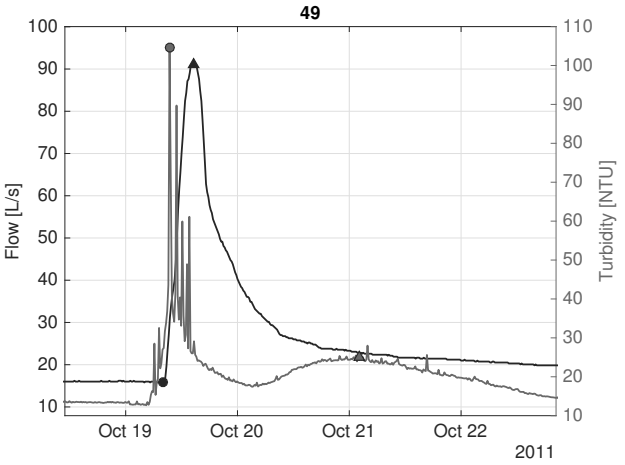
49
Flow [L/s]
Turbidity [NTU]
Oct 19
Oct 20
Oct 21
Oct 22
2011

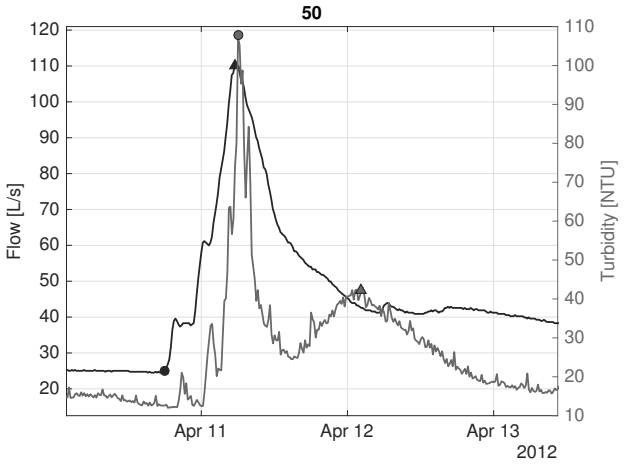
50
Flow [L/s]
Turbidity [NTU]
Apr 11
Apr 12
Apr 13
2012

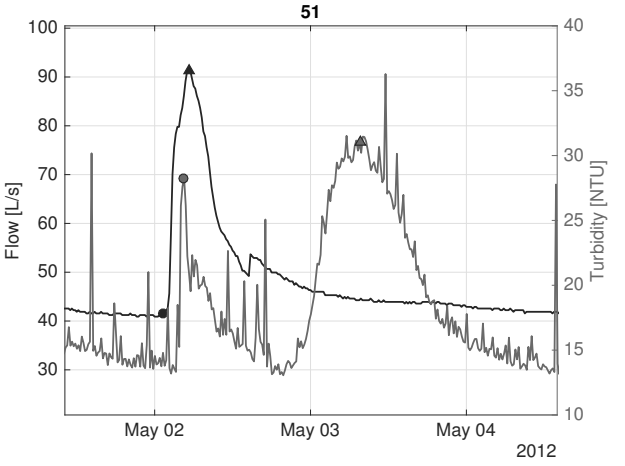
51
Flow [L/s]
Turbidity [NTU]
May 02
May 03
May 04
2012

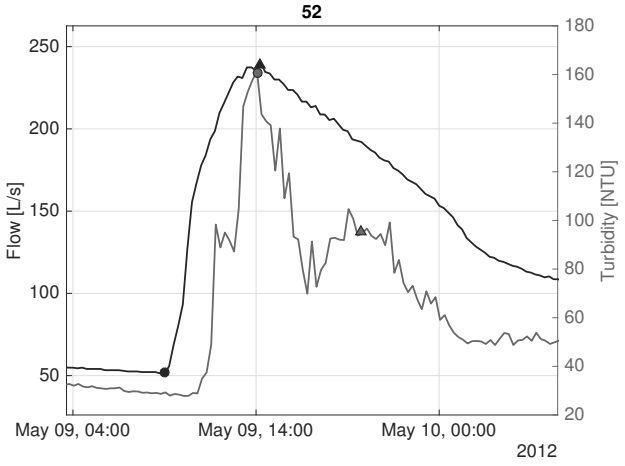
52
Flow [L/s]
Turbidity [NTU]
May 09, 04:00
May 09, 14:00
May 10, 00:00
2012

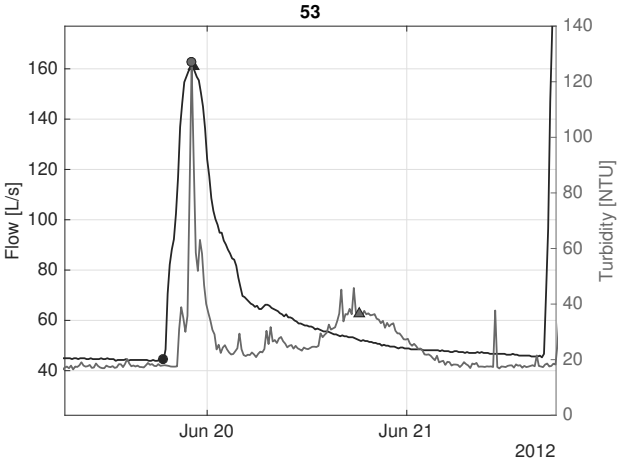
53
Flow [L/s]
Turbidity [NTU]
Jun 20
Jun 21
2012

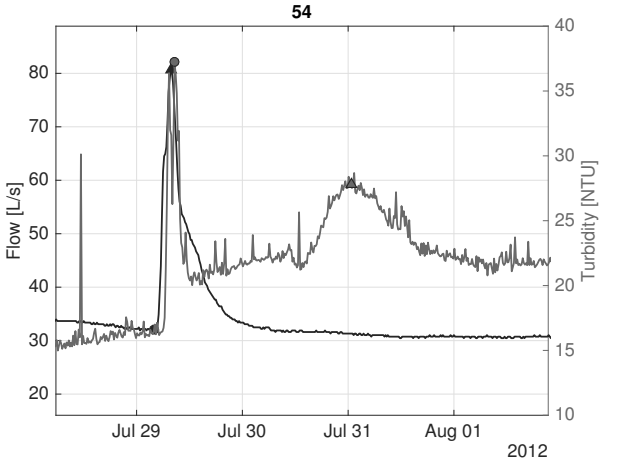
54
Flow [L/s]
Turbidity [NTU]
Jul 29
Jul 30
Jul 31
Aug 01
2012

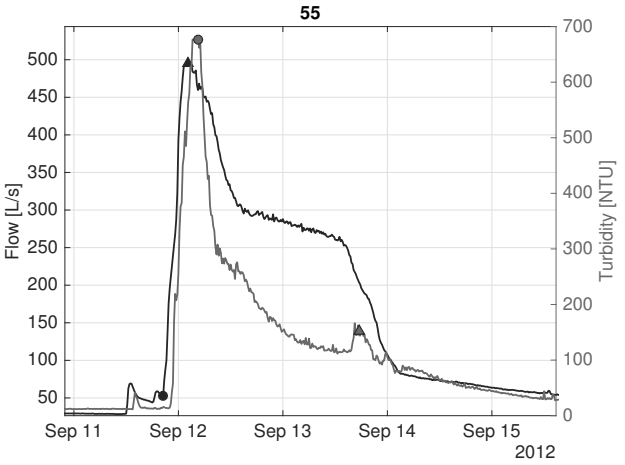
55
Flow [L/s]
Turbidity [NTU]
Sep 11
Sep 12
Sep 13
Sep 14
Sep 15
2012

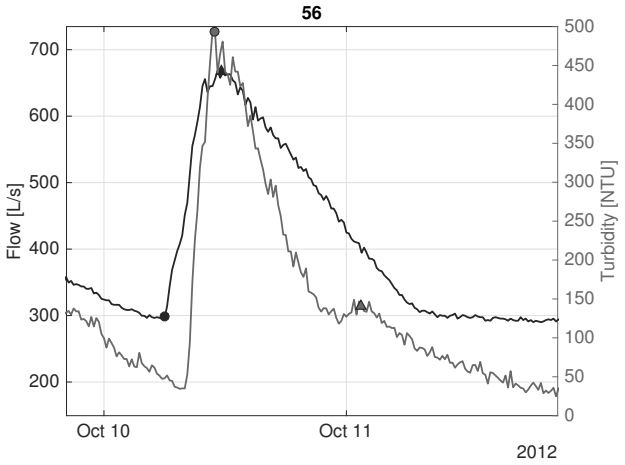
56
Flow [L/s]
Turbidity [NTU]
Oct 10
Oct 11
2012

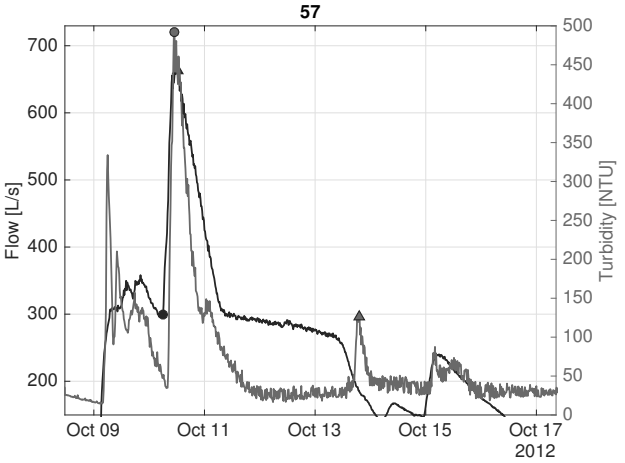
57
Flow [L/s]
Turbidity [NTU]
Oct 09
Oct 11
Oct 13
Oct 15
Oct 17
2012

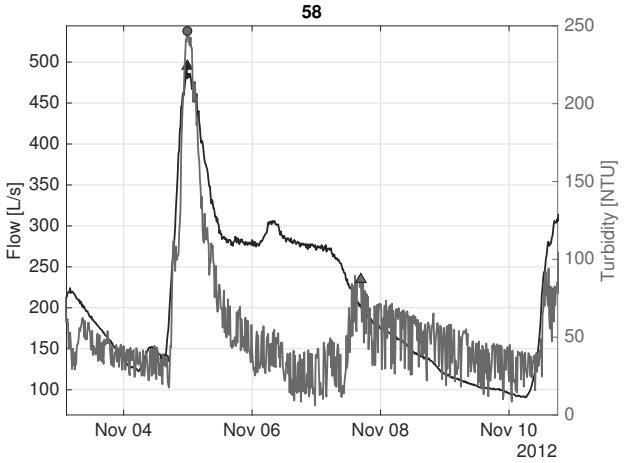
58
Flow [L/s]
Turbidity [NTU]
Nov 04
Nov 06
Nov 08
Nov 10
2012

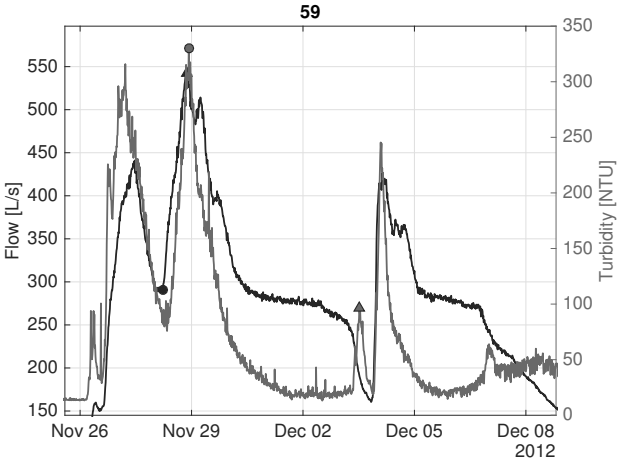
59
Flow [L/s]
Turbidity [NTU]
Nov 26
Nov 29
Dec 02
Dec 05
Dec 08
2012

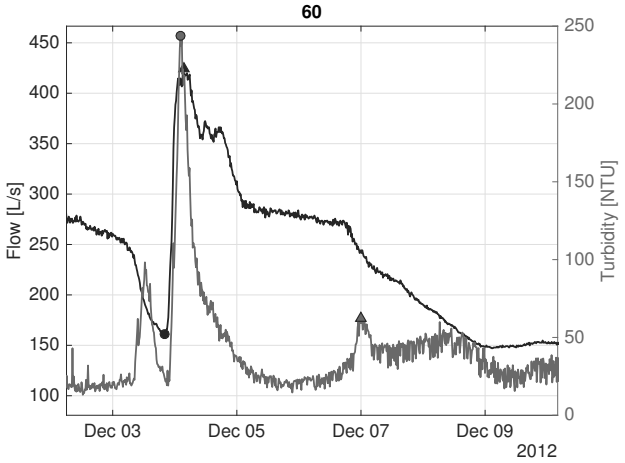
60
Flow [L/s]
Turbidity [NTU]
Dec 03
Dec 05
Dec 07
Dec 09
2012

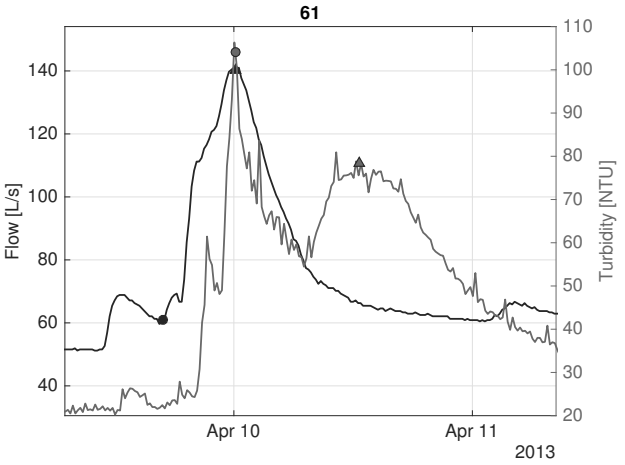
61
Flow [L/s]
Turbidity [NTU]
Apr 10
Apr 11
2013

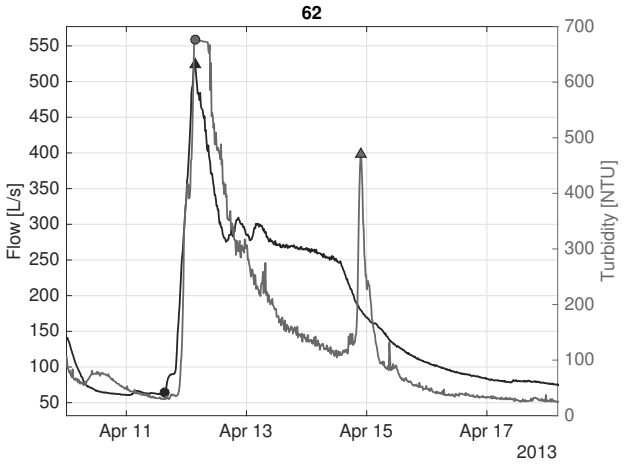
62
Flow [L/s]
Turbidity [NTU]
Apr 11
Apr 13
Apr 15
Apr 17
2013

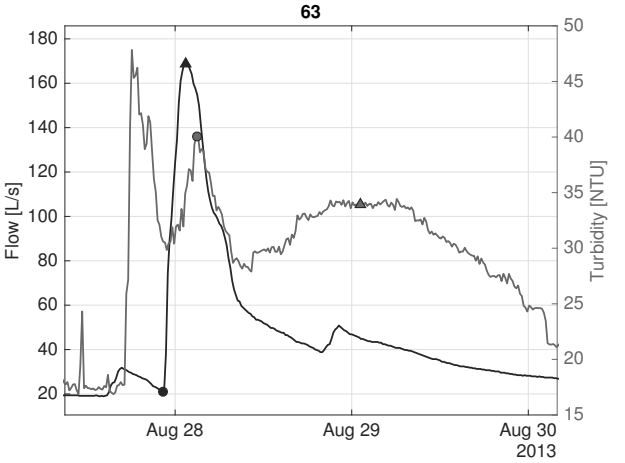
63
Flow [L/s]
Turbidity [NTU]
Aug 28
Aug 29
Aug 30
2013

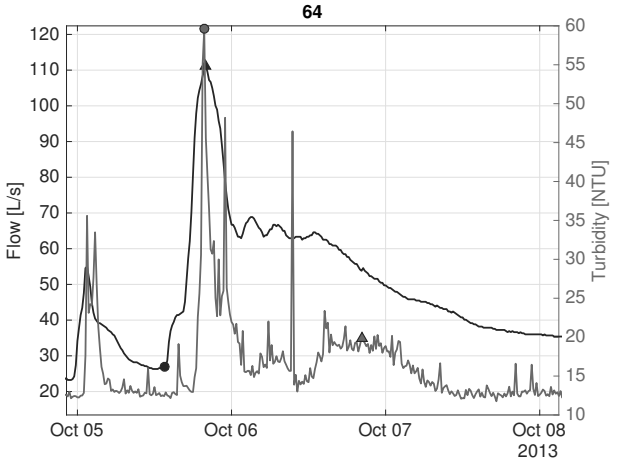
64
Flow [L/s]
Turbidity [NTU]
Oct 05
Oct 06
Oct 07
Oct 08
2013

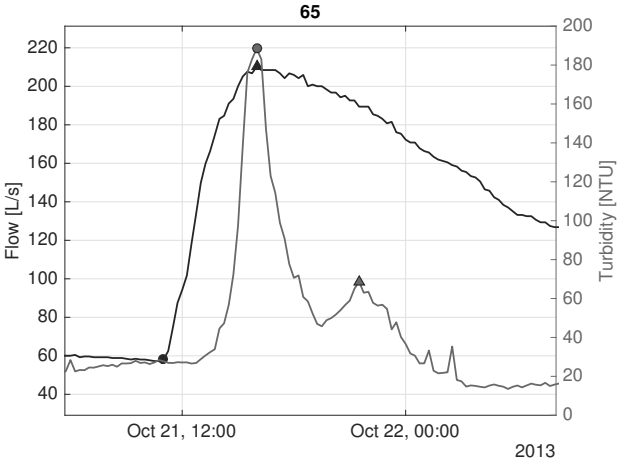
65
Flow [L/s]
Turbidity [NTU]
Oct 21, 12:00
Oct 22, 00:00
2013

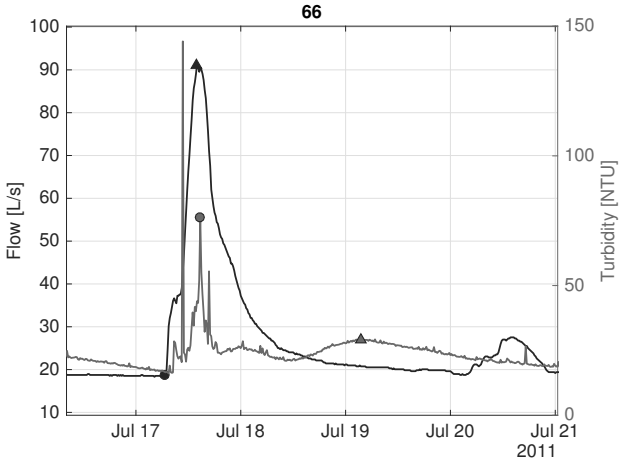
66
Flow [L/s]
Turbidity [NTU]
Jul 17
Jul 18
Jul 19
Jul 20
Jul 21
2011